

GEMS & GEMOLOGY

FALL 2022
VOLUME LVIII

THE QUARTERLY JOURNAL OF THE GEMOLOGICAL INSTITUTE OF AMERICA



Establishing the Geographic Origin of Diamonds

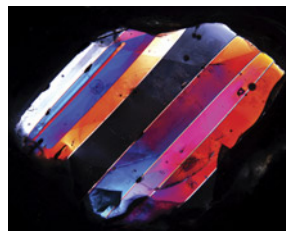
Sapphire from Muling, China

The History of Pigments Sourced from Gem Materials

Pink Spinel from Kuh-i-Lal, Tajikistan



p. 270



p. 302



p. 330



p. 359



p. 365



p. 385

EDITORIAL

269 The Geographic Origin of Diamonds, Sapphire from China, and Pigments Sourced from Gem Materials

Duncan Pay

FEATURE ARTICLES

270 Methods and Challenges of Establishing the Geographic Origin of Diamonds

Evan M. Smith, Karen V. Smit, and Steven B. Shirey

Examines the current available means of determining the geographic origin of gem-quality diamond, which are based largely on trace element and isotopic characteristics. For now, no method exists for determining the provenance of a random individual diamond.

290 Sapphire Beneath the Rich Black Soil of Muling, Northeastern China

Yimiao Liu and Ren Lu

A comprehensive look at the gemological features and advanced analysis of blue and fancy-color sapphire from the agricultural area of Muling, China.

318 Gems on Canvas: Pigments Historically Sourced from Gem Materials

Britni LeCroy

Explores the use of gem materials as pigments in works of art, from the earliest cave paintings to the modern era.

338 Color Mechanism and Spectroscopic Thermal Variation of Pink Spinel Reportedly from Kuh-i-Lal, Tajikistan

Yicen Liu, Lijian Qi, Dietmar Schwarz, and Zhengyu Zhou

A detailed spectroscopic investigation of the color of pink spinel reportedly from the Kuh-i-Lal deposit in the Pamir Mountains of Tajikistan.

REGULAR FEATURES

337 2022 Challenge Winners

354 Lab Notes

Exceptional fancy red diamond • Treated “nickel-rich” green diamond • *Gota de aceite*-like effect in a Brazilian emerald • Treated orange and pink CVD lab-grown diamonds • Non-nacreous pearl reportedly from *Telescopium telescopium* • Rare Kashmir star sapphire • Fraudulently inscribed synthetic moissanite • Synthetic moissanite presented as natural diamond rough • Cat’s-eye Paraiba tourmaline with copper inclusions

364 G&G Micro-World

Breyite in diamond • “Surprise” in elbaite tourmaline • Unusual purple fluid in quartz • Orange rutile inclusion in “chameleon” diamond • “Smoke rings” in sapphire • Stellate zircon in Paraiba tourmaline • Quarterly Crystal: Panasqueira quartz

370 Diamond Reflections

Examines the variety of fluid inclusions contained within diamond, which reflect the natural processes that created and modified these gems deep within the earth’s mantle.

376 Letters

378 Gem News International

Atypical “box bead” cultured pearls • Multi-colored quartz with oriented inclusions • Mozambique ruby mining update • Pressed amber imitation of “root amber” • Synthetic sapphire with Rose channels • Low-temperature “gel-filled” turquoise • Turquoise United conference • Ahmadjan Abduriyim receives JAMS Award for applied mineralogy • *Hidden Gems* at the San Diego Natural History Museum • *The Year of Mineralogy* at the Perot Museum • In Memoriam: Andrew Cody

Editorial Staff

Editor-in-Chief

Duncan Pay

Managing Editor

Stuart D. Overlin
soverlin@gia.edu

Editor

Brooke Goedert

Editorial Coordinator

Erica Zaidman

Technical Editors

Tao Z. Hsu
Jennifer Stone-Sundberg

Associate Technical Editor

Si Athena Chen

Editors, Lab Notes

Thomas M. Moses
Shane F. McClure

Editors, Micro-World

Nathan Renfro
Elise A. Skalwold
John I. Koivula

Editors, Gem News

Gagan Choudhary
Christopher M. Breeding
Guanghai Shi

Editors, Colored Stones Unearthed

Aaron C. Palke
James E. Shigley

Editor, Diamond Reflections

Evan M. Smith

Contributing Editors

James E. Shigley
Raquel Alonso-Perez

Editor-in-Chief Emeritus

Alice S. Keller

Assistant Editor

Erin Hogarth

Production Staff

Creative Director

Faizah Bhatti

Production and Multimedia Specialist

Michael Creighton

Photo/Video Producer

Kevin Schumacher

Photographer

Robert Weldon

Multimedia Associate

Christopher Bonine

Video Production

Albert Salvato

Editorial Review Board

Ahmadjan Abduriyim
Tokyo, Japan

Timothy Adams
San Diego, California

Edward W. Boehm
Chattanooga, Tennessee

James E. Butler
Washington, DC

Alan T. Collins
London, UK

Sally Eaton-Magaña
Carlsbad, California

John L. Emmett
Brush Prairie, Washington

Emmanuel Fritsch
Nantes, France

Eloïse Gaillou
Paris, France

Al Gilbertson
Carlsbad, California

Gaston Giuliani
Nancy, France

Lee A. Groat
Vancouver, Canada

Yunbin Guan
Pasadena, California

Peter Heaney
University Park, Pennsylvania

Richard W. Hughes
Bangkok, Thailand

Jaroslav Hyršl
Prague, Czech Republic

Dorrit Jacob
Canberra, Australia

A.J.A. (Bram) Janse
Perth, Australia

Mary L. Johnson
San Diego, California

Stefanos Karampelas
Paris, France

Lore Kiefert
Lucerne, Switzerland

Simon Lawson
Maidenhead, UK

Ren Lu
Wuhan, China

Thomas M. Moses
New York, New York

Laura Otter
Canberra, Australia

Aaron C. Palke
Carlsbad, California

Ilene Reinitz
Chicago, Illinois

Nathan Renfro
Carlsbad, California

Benjamin Rondeau
Nantes, France

George R. Rossman
Pasadena, California

Sudarat Saeseaw
Bangkok, Thailand

Karl Schmetzer
Petershausen, Germany

Andy Shen
Wuhan, China

Guanghai Shi
Beijing, China

James E. Shigley
Carlsbad, California

Elisabeth Strack
Hamburg, Germany

Nicholas Sturman
Bangkok, Thailand

D. Brian Thompson
Florence, Alabama

Fanus Viljoen
Johannesburg, South Africa

Wuyi Wang
New York, New York

Christopher M. Welbourn
Reading, UK

Chunhui Zhou
New York, New York

J.C. (Hanco) Zwaan
Leiden, The Netherlands

GEMS & GEMOLOGY®

gia.edu/gems-gemology

Customer Service

(760) 603-4200
gandg@gia.edu



Subscriptions

Copies of the current issue may be purchased for \$29.95 plus shipping. Subscriptions are \$79.99 for one year (4 issues) in the U.S. and \$99.99 elsewhere. Canadian subscribers should add GST. Discounts are available for renewals, group subscriptions, GIA alumni, and current GIA students. To purchase print subscriptions, visit store.gia.edu or contact Customer Service. For institutional rates, contact Customer Service.

Database Coverage

Gems & Gemology's impact factor is 2.045, according to the 2021 Journal Citation Reports by Clarivate Analytics (issued June 2022). *G&G* is abstracted in Thomson Reuters products (Current Contents: Physical, Chemical & Earth Sciences and Science Citation Index—Expanded, including the Web of Knowledge) and other databases. For a complete list of sources abstracting *G&G*, go to gia.edu/gems-gemology, and click on "Publication Information."

Manuscript Submissions

Gems & Gemology, a peer-reviewed journal, welcomes the submission of articles on all aspects of the field. Please see the Author Guidelines at gia.edu/gems-gemology or contact the Managing Editor. Letters on articles published in *G&G* are also welcome. Please note that Field Reports, Lab Notes, Gem News International, Micro-World, Colored Stones Unearthed, Diamond Reflections, and Charts are not peer-reviewed sections but do undergo technical and editorial review.

Copyright and Reprint Permission

Abstracting is permitted with credit to the source. Libraries are permitted to photocopy beyond the limits of U.S. copyright law for private use of patrons. Instructors are permitted to reproduce isolated articles and photographs/images owned by *G&G* for noncommercial classroom use without fee. Use of photographs/images under copyright by external parties is prohibited without the express permission of the photographer or owner of the image, as listed in the credits. For other copying, reprint, or republication permission, please contact the Managing Editor.

Gems & Gemology is published quarterly by the Gemological Institute of America, a nonprofit educational organization for the gem and jewelry industry.

Postmaster: Return undeliverable copies of *Gems & Gemology* to GIA, The Robert Mouawad Campus, 5345 Armada Drive, Carlsbad, CA 92008.

Our Canadian goods and service registration number is 126142892RT.

Any opinions expressed in signed articles are understood to be opinions of the authors and not of the publisher.

About the Cover

Developing an approach to determine the geographic origin of diamonds is a topic of growing interest and the subject of our lead article. The yellow diamond on the cover was sourced from Canada's Diavik mine in October 2018. Weighing a remarkable 552.7 ct, it remains the largest diamond discovered in North America. Photo by Evan M. Smith.

Printing is by L+L Printers, Carlsbad, CA.

GIA World Headquarters The Robert Mouawad Campus 5345 Armada Drive Carlsbad, CA 92008 USA
© 2022 Gemological Institute of America All rights reserved. ISSN 0016-626X



The Geographic Origin of Diamonds, Sapphire from China, and Pigments Sourced from Gem Materials



Welcome to the Fall 2022 edition of *Gems & Gemology*! This issue delivers fascinating new content, offering four feature articles ranging from the hot topic of diamond origin to an in-depth look at the role gem materials have played in art throughout history.

In our lead article, Evan Smith and coauthors explore the methods and challenges associated with determining the geographic origin of diamonds. Current approaches have attempted to associate trace element characteristics with specific origins, but there is still no scientifically robust method to determine the geographic origin of a given diamond. The authors conclude that the only definitive method to establish diamond origin depends on preserving and retaining origin information from the time of mining rather than determining it analytically.

“...the only definitive method to establish diamond origin depends on preserving and retaining origin information from the time of mining...”

diamond origin depends on preserving and retaining origin information from the time of mining rather than determining it analytically.

Next, authors Yimiao Liu and Ren Lu of the Gemmological Institute, China University of Geosciences in Wuhan, examine sapphire from a lesser-known source in Muling, China. Comparing their samples with sapphire from well-known sources worldwide, the authors report on the quality, gemological characteristics, and origin-related features with comprehensive analytical results. They determine that Muling sapphire is from a more diverse geological environment than the sapphire from many other regions.

In our third article, join Britni LeCroy for a lesson in art history as she researches pigments historically sourced from gem materials. Covering hematite, azurite, malachite, lapis lazuli, bone, ivory, and cinnabar, the study investigates the evolution of pigments in a wide array of artistic mediums, from ancient cave drawings to modern paintings.

Finally, Yicen Liu and coauthors present their spectroscopic investigation of the color mechanism of pink spinel reportedly from Kuh-i-Lal in the Pamir Mountains of Tajikistan. To determine the cause of color, the group examines the mechanism of color change from room temperature to 1000°C using spectroscopic techniques and trace element analysis.

Meanwhile, our regular features continue to deliver interesting findings from all over the globe. Highlights from the *Lab Notes* section include an exceptional natural-color 1.21 ct red diamond, a *gota de aceite*-like effect in a Brazilian emerald, and the first report of a natural pearl discovered in a *Telescopium* shell. *Micro-World* is packed with illuminating observations from the inner landscapes of gemstones, offering a glimpse at an unusual brightly colored purple fluid in quartz, “smoke ring” inclusions in heated blue sapphire, and a large orange rutile inclusion in a “chameleon” diamond. *Diamond Reflections* returns with an exploration of fluid inclusions in natural diamond, highlighting the scientific value these inclusions offer from the great depths of the earth. In *Gem News International*, you’ll find an update from Mozambique’s ruby mines, a report on the first-ever Turquoise United conference in Albuquerque, and highlights from current gem and mineral exhibits at the San Diego Natural History Museum and the Perot Museum of Nature and Science in Dallas.

We hope you enjoy the latest issue of *Gems & Gemology*!

Duncan Pay | Editor-in-Chief | dpay@gia.edu

METHODS AND CHALLENGES OF ESTABLISHING THE GEOGRAPHIC ORIGIN OF DIAMONDS

Evan M. Smith, Karen V. Smit, and Steven B. Shirey

There is growing interest in developing methods to deduce the geographic origin of diamonds. Most approaches have focused on trace elements within diamonds, which can be sensitive recorders of geological conditions during the growth of minerals. Gem-quality diamonds have ultra-low concentrations of trace elements, making them extremely challenging to analyze quantitatively. Nonetheless, high-quality trace element data from multiple studies reveal complex and variable patterns, but with striking similarities and overlap between worldwide deposits. Diamond properties such as trace element or isotopic characteristics vary as a function of geological conditions that are not necessarily distinct and resolvable between diamonds of different geographic origin. We conclude that there has been no study by any method demonstrating unique and measurable characteristics that would allow for independent provenance determination of a random individual diamond. For now and the foreseeable future, the only definitive method to establish diamond origin depends on preserving and retaining origin information from the time of mining.

Some famous diamonds, such as the Hope, the Cullinan, and the 404.2 ct “4 de Fevereiro” diamond in figure 1, have high-profile histories that include their geographic provenance. Other dia-

monds with a known origin can occasionally be sourced in the marketplace or directly from miners. But for the majority of diamonds, this information is not preserved, instead becoming obscured as they move through the supply chain. To some extent, diamond provenance has not been seen as a valuable piece of information and is not presented as a relevant pricing factor the way it sometimes is for some other gemstones. Rough diamonds are typically bought and sold in lots or parcels based on physical characteristics, including color, clarity, size, and morphology. In assembling these parcels, it is common practice to mix diamonds of similar character from different mines. Faceted diamonds are sold mainly on the basis of the 4Cs (color, cut, clarity, and carat weight) and may be mixed further.

Beyond the historical or scientific interest in provenance, several recent developments have put diamond origin at the forefront of conversations in the industry and among consumers. Initially, this was driven by a need to track conflict diamonds and prevent their entrance into the trade. Now, with mount-

Figure 1. A remarkable 404.2 ct type IIa rough diamond recovered at the Lulo mine in Angola in 2016. The main stone fashioned from it was a 163.4 ct D-color flawless emerald-cut diamond. Photo by Jian Xin (Jae) Liao.



See end of article for About the Authors and Acknowledgments.

GEMS & GEMOLOGY, Vol. 58, No. 3, pp. 270–288,

<http://dx.doi.org/10.5741/GEMS.58.3.270>

© 2022 Gemological Institute of America

BOX A: COMPARISON OF DIAMONDS TO OTHER GEMSTONES

Methodologies for geographic origin determination of rubies, emeralds, and other gem materials cannot readily be applied to diamonds. This is due to fundamental differences between diamonds and other gem materials. Diamonds form in the mantle, much deeper than most other gemstones. Except for some mantle-derived olivine/peridot, most other gemstones form in the earth's crust at relatively shallow depths.

Minerals in the crust are the product of multiple melting and differentiation processes that over time have created the crust. These processes concentrate certain elements (known as *incompatible elements*), which tend to partition into magma as rocks melt. Consequently, crustal rocks have relatively high concentrations of these otherwise rare incompatible elements. When gemstones form within crustal rocks, they naturally inherit higher concentrations of incompatible elements. Furthermore, the crust has great diversity in chemical composition, in contrast to the mantle's more uniform composition. Because of the chemical diversity of different geological environments in the crust, gemstones formed in different crustal environments often have markedly different trace element compositions. For example, rubies can exhibit differences in certain trace elements (magnesium, titanium, vanadium, iron, and gallium) based on their formation in igneous (basaltic and lamprophyric), metamorphic (granulitic and metalimestone), and metasomatic (skarn and pegmatitic) environments (Palke et al., 2019b).

In some cases, it is possible to relate specific compositional features in these gemstones to the compositions of known and exposed crustal rocks in the different geologic settings. Determining trace element concentrations within crustal gemstones allows constraints to be placed on the geological setting they formed in, potentially allowing their geographic origin to be inferred. However, distinguishing crustal gemstones that are from the same kind of geological setting but from different geographic locations remains

challenging. Multiple layers of evidence, including geochemical and inclusion characteristics, often must be combined in order to better assess a gemstone's origin.

This challenge is even more pronounced for diamonds. Diamonds formed in the same kinds of geological settings are found spread across many different geographic locations. The majority of diamonds form in the thick and ancient portions of the continental lithospheric mantle. There are three main host rock types—peridotite, eclogite, and websterite—that are composed primarily of different proportions of only four minerals: olivine, orthopyroxene, clinopyroxene, and garnet. Compared to crustal rocks, the rocks of the mantle have limited mineralogical and chemical variability. Furthermore, the covalently bonded diamond lattice is extremely compact and regular, composed of only one major element, and cannot easily accommodate the addition of substitutional and interstitial impurity elements. Only a few elements, such as hydrogen, boron, nitrogen, silicon, and nickel, fit into the diamond lattice. Other trace elements in diamond are thought to be present as nano-inclusions of fluid rather than occupying discrete crystal lattice sites (Melton et al., 2012; Krebs et al., 2019). Consequently, as a diamond grows, it incorporates extremely low levels of trace elements compared to other minerals. Nitrogen, however, is a notable exception.

Nitrogen is the most common impurity in natural diamond. It can substitute for carbon in the diamond lattice, typically at concentrations of tens to hundreds of parts per million (ppm). Diamond has a median nitrogen value of 160 ppm, with 99% being <1400 ppm (Stachel, 2014). It can occur as isolated nitrogen atoms (C centers), as aggregated pairs (A centers), or as groups of four atoms plus a vacancy (B centers) (Breeding and Shigley, 2009). Unfortunately, the nitrogen concentration and its degree of aggregation overlap completely among diamonds from around the world and cannot be used to determine geographic origin.

ing global sustainability efforts across all industries, consumers are interested in knowing the origin and impact of the goods they purchase. These social pressures have prompted direct efforts, by both privately and publicly funded research groups, to search for distinct geographic signatures among diamonds (e.g., Watling et al., 1995; McNeill et al., 2009; Dalpé et al., 2010; Rege et al., 2010; Coney et al., 2012; Melton et al., 2012; Brill et al., 2020; McManus et al., 2020).

A common goal has been to develop a database of measurable characteristics to compare diamonds from different sources. Trace element characteristics, in conjunction with other observations, have proven use-

ful for origin determination of other gem materials (see box A). Similarly, trace element analysis using mass spectrometry has been regarded as the most promising approach for diamonds (Watling et al., 1995; McNeill et al., 2009; Dalpé et al., 2010; Rege et al., 2010; Coney et al., 2012; Melton et al., 2012; Brill et al., 2020). One study has also used laser-induced breakdown spectroscopy (LIBS) for this application (McManus et al., 2020). This article will discuss these methods and the challenges they face. The reality at the moment is that there is no scientifically robust method to determine the geographic origin of any given diamond (Dalpé et al., 2010; Cartier et al., 2018;

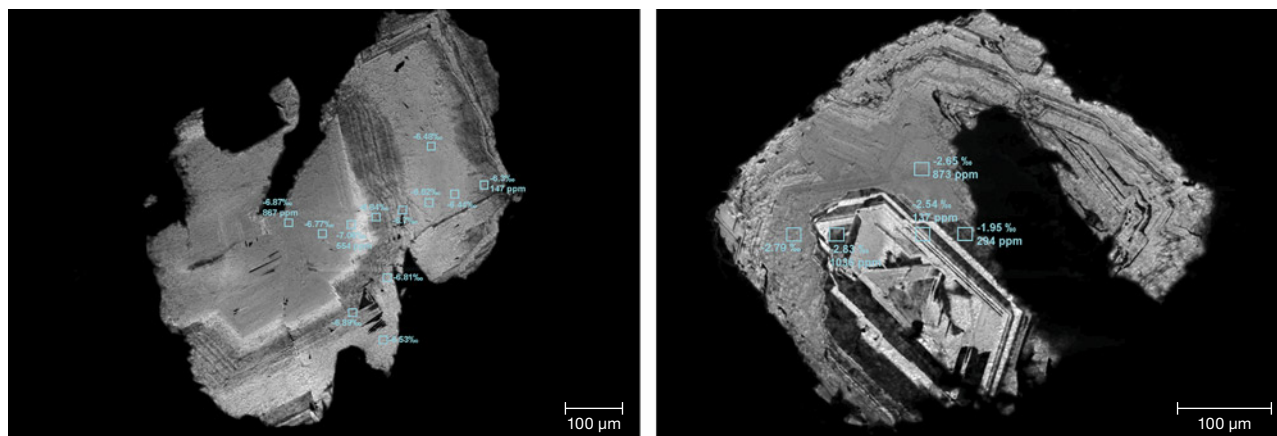


Figure 2. Cathodoluminescence (CL) images of polished surfaces through the interior of two diamonds from the Attawapiskat area of the Superior Craton (Canada), obtained by scanning electron microscopy (SEM). Both diamonds have a large internal range of nitrogen contents, which are governed by different fluid pulses—visible in CL as different growth zones with varying brightness. Secondary ion mass spectrometry (SIMS) spot analyses with $\delta^{13}\text{C}$ and nitrogen content (atomic ppm) are indicated. Images from Smit et al. (2014).

Krebs et al., 2019). All current, reliable, and available means of establishing provenance depend on retaining country-of-origin and/or mine-of-origin information, rather than determining this analytically.

DIAMOND FORMATION AND ITS GEOLOGICAL FRAMEWORK

One of the significant concepts emerging from the past century of diamond research is that there are many different ways diamonds can form, with the pertinent variables being the host rock type, the composition of the diamond-forming fluid or melt, and the depth of formation (lithospheric or sublithospheric) (Shirey et al., 2013). There are distinct varieties of diamond that arise in nature, and, crucially, these varieties do not appear to have unique geographic distributions overall.

In general, diamonds form as carbon-bearing fluids flow through rocks in the mantle and the carbon crystallizes due to chemical reactions or changes in pressure or temperature. Studying the interior of diamonds with cathodoluminescence has revealed that many diamonds exhibit multiple concentric growth layers, resulting from multiple fluid pulses and episodes of growth (figure 2; Shirey et al., 2013). The layers can have distinct carbon isotope compositions ($\delta^{13}\text{C}$), nitrogen concentrations, nitrogen isotope compositions ($\delta^{15}\text{N}$) (Stachel et al., 2022b), and perhaps other characteristics as well, such as trace element contents. Diamond trace element and isotopic composition are controlled by the elements present

in the parental carbon-bearing fluid, varying with the extent of interaction between the fluid and surrounding host rock minerals (Weiss et al., 2015).

The products of diamond formation in the earth's mantle are surprisingly similar across many different

In Brief

- Most diamonds have formed by geological conditions that are not unique to any one geographic location.
- Diamond characteristics have striking similarities and overlap on a global scale.
- Currently, there is no reliable way to independently determine the geographic origin of a random individual diamond.
- A feasible alternative, though not without challenges, is to retain origin information from the time of mining.

localities. Categorizing diamonds based on their mineral inclusions provides much of the basis for our understanding of different geological varieties of diamond. The major geological varieties defined by inclusion mineralogy are shown in table 1. These represent diamonds from the lithospheric mantle, formed at approximately 150–200 km, and exclude the rarer (<2%) sublithospheric or “superdeep” varieties of diamonds (Smith et al., 2017; Stachel et al., 2022a).

Diamonds we see at the earth's surface have been carried up in magmas that form kimberlites (or, less

commonly, lamproites). The magma rips up pieces of diamond-hosting mantle rocks hundreds of kilometers below the surface. During this journey, mantle rocks break apart and release diamonds into the magma, forming so-called xenocrysts (crystals foreign to the magma). Individual kimberlite deposits at the surface often contain multiple populations of diamonds mixed together, which could have originally crystallized in completely independent and episodic diamond-forming events within different host rocks. The spatial and temporal scale of diamond-forming events at depths in the mantle is not well understood because it is never exposed. Multiple eruption phases of a kimberlite may sample different portions of the lithosphere. Compiling a complete picture of diamond characteristics from any given deposit means taking into account multiple dissimilar populations. Depending on the nature

of the deposit, it could be difficult to judge whether a sample suite of diamonds is truly representative of that deposit. The situation may be more complex for alluvial deposits, which may contain diamonds eroded from multiple primary known or unknown kimberlite/lamproite sources.

The known geological varieties of diamond, including the major categories outlined in table 1, are not geographically restricted. Diamond properties are a function of geology, not geography, and the geological controls for the most common varieties of diamond result in broad, overlapping similarities between many geographic settings. For example, the most well-studied diamonds, found in most deposits around the world, formed within harzburgite (a type of peridotite) host rocks, at comparable pressure and temperature conditions, from carbon-bearing fluids of similar composition (Shirey et al., 2013). These are

TABLE 1. The most common geological varieties of diamond on the basis of mineral inclusions, modified from Stachel et al. (2022a).

	Peridotitic	Eclogitic	Websteritic	Uncertain/ Nonspecific
Common	Cr-pyrope Olivine Enstatite Cr-diopside Mg-chromite Fe-Ni sulfides ^a	Grossular-almandine-pyrope Omphacitic clinopyroxene Fe sulfides ^a	Almandine-pyrope Diopside-augite Enstatite	Graphite (epigenetic)
Occasional	—	Rutile Coesite Kyanite	Coesite Olivine	—
Rare		Corundum Ilmenite Magnetite Fe-Mg-chromite Phlogopite K-feldspar Titanite Staurolite Zircon Zircon Moissanite Calcite Dolomite	Phlogopite Goldschmidtite	Graphite (primary) Diamond Calcite Dolomite Perovskite Amphibole Apatite Eskolaite Sr-titanate Monazite

^apyrrhotite ± pentlandite ± chalcopyrite ± molybdenite (Kemppinen et al., 2018), with bulk Ni content >17 wt.% for peridotitic and <10 wt.% for eclogitic sulfides

the kinds of diamonds that contain rare vibrant purple Cr-pyropes. The diamond exploration strategy is to search for these garnets and other indicator minerals released by fragmentation of diamond-hosting rocks and dispersed in surficial sediments. The success of the strategy is underpinned by the fact that the predominant diamond formation processes are often similar from one deposit to the next worldwide. Searching for kimberlitic indicator minerals with the same composition as those from existing mines is an effective technique for finding new diamond-bearing kimberlites (Kjarsgaard et al., 2019).

Physical Characteristics and Traditional Gemological Observations. Each diamond deposit encompasses a range of diamond morphologies, surface textures, colors, and other characteristics. Some localities have more visually distinctive rough diamonds than others, which is noticeable upon examining parcels of diamonds from that locality. For example, the Ellendale mine in Australia produced a large proportion of resorbed, smooth-surfaced dodecahedral (or tetrahexahedral) yellow diamonds (Hall and Smith, 1984; Jaques et al., 1986). The Marange alluvial deposit in Zimbabwe has diamonds with a nontransparent coating and radiation damage (Smit et al., 2018), while the Victor mine in Canada has produced a high proportion of well-formed, near-colorless octahedral crystals with few mineral inclusions (“The real value of Victor Project,” 2007).

Of course, these are not the only examples of particular features associated with certain diamond localities. An unusual example is the porous, micro-polycrystalline diamond variety known as *carbonado*. Although not of gem quality, it is interesting because it is only recovered from placer deposits in Brazil and the Central African Republic (Heaney et al., 2005). As another example, the Cullinan mine in South Africa is known as a chief source of boron-bearing, type IIb diamonds (King et al., 1998). A random type IIb diamond circulating in the marketplace has a reasonable probability of being from Cullinan. The Argyle mine in Australia, which closed in 2020, was a leading producer of pink (and many brown) diamonds. Argyle’s pink diamonds generally have highly aggregated nitrogen (more B centers than A) and a color that is associated with slightly more diffuse pink graining compared to pink diamonds from most other localities, which tend to have less aggregated nitrogen and a pink color associated with sharply defined glide planes (Gaillou et al., 2012). Ar-

gyle was also an almost exclusive source of rare blue to violet diamonds whose color is related to hydrogen (Eaton-Magaña et al., 2018). The distinctive characteristics described here are helpful observations in terms of inferring the origin of some specific diamonds or representative and unmixed parcels, but they are certainly not definitive. Experienced professionals can reach an educated guess about the origin of diamond parcels, or even an individual diamond, but this judgment is highly subjective and cannot be easily verified. For the majority of polished or rough diamonds, there are no distinct characteristics that reveal the geographic origin.

Carbon and Nitrogen Characteristics. Carbon and nitrogen might seem to be a good way to fingerprint diamonds, given their high abundances and isotopic variations in this material. Such analyses could be performed on most diamonds. However, nitrogen abundance variations (measured by infrared absorbance spectroscopy or even imaged with luminescence-based techniques) reveal that the nitrogen content can vary greatly between the growth zones of each diamond (figure 2), not to mention on the scale of millions of diamonds in a single mine.

This variation in nitrogen content is due to the influx of different fluid pulses during diamond growth, each of which may have had a different nitrogen content. Diamonds with an internal tenfold difference in nitrogen content have been documented through secondary ion mass spectrometry (SIMS), a technique that can obtain spatially resolved measurements (see the measurement locations superimposed in figure 2) (Stachel et al., 2022b). These differences are averaged when using bulk analytical techniques such as infrared spectroscopy. Nitrogen abundance variability (within the limited range of possible concentrations) is so pervasive and occurs on such a small scale that nitrogen content alone is not a useful tool to distinguish diamonds from different geological environments.

Both carbon and nitrogen have two stable isotopes (^{12}C , ^{13}C and ^{14}N , ^{15}N), with the lighter atomic mass isotope of each element (^{12}C and ^{14}N) comprising ~99% of the isotopic composition of the respective element. Similar to nitrogen content, the entire global range of both $\delta^{13}\text{C}$ and $\delta^{15}\text{N}$ (the part per thousand variation of the $^{13}\text{C}/^{12}\text{C}$ and $^{15}\text{N}/^{14}\text{N}$ ratios, with respect to a standard) may be represented within one deposit (figures 3 and 4). The main mantle range of $\delta^{13}\text{C}$ is centered around -5‰, and the global $\delta^{13}\text{C}$ distributions of diamonds that form in the two main

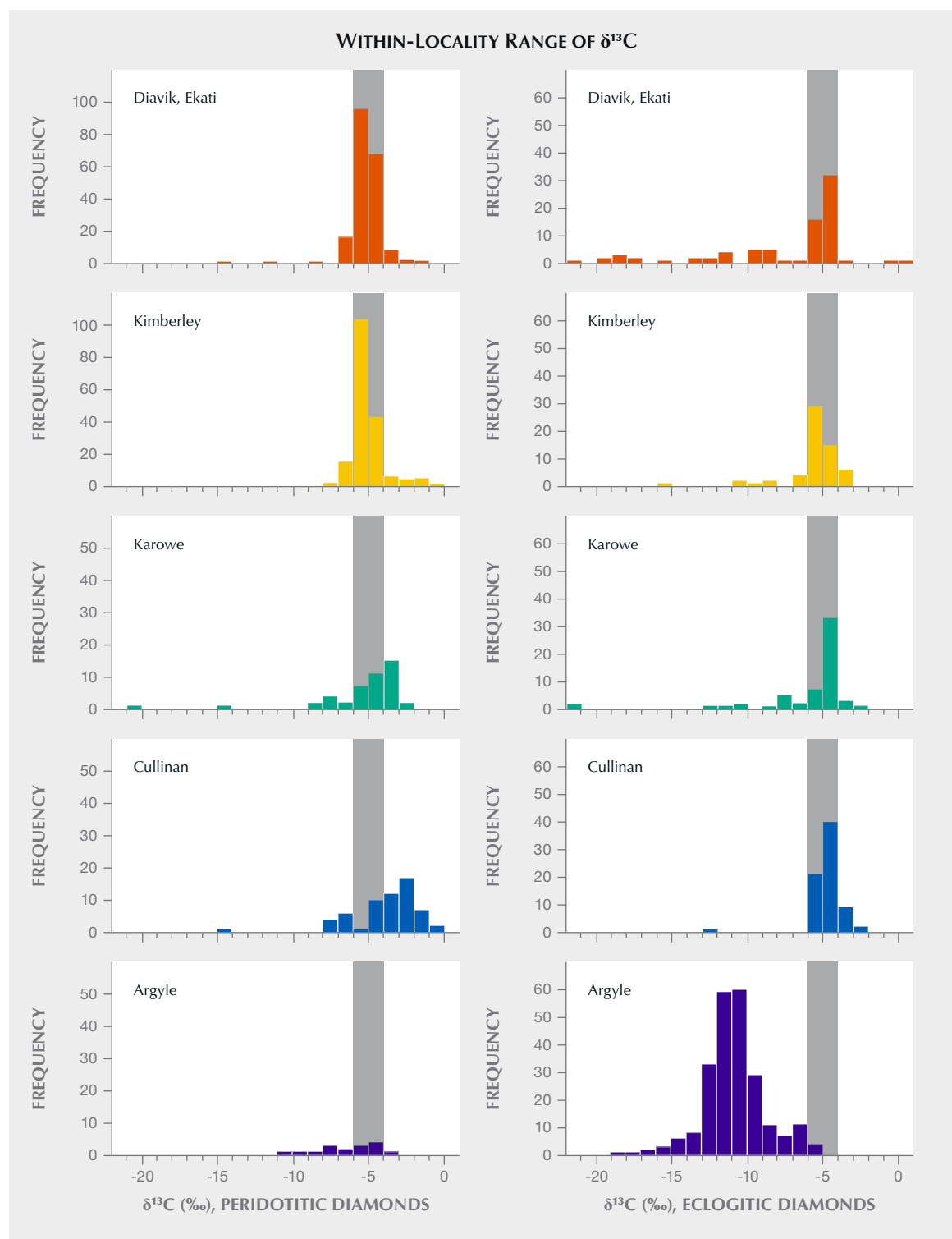


Figure 3. Within-locality range of $\delta^{13}\text{C}$ for five well-known localities: Diavik + Ekati (Lac de Gras), Kimberley, Karowe, Cullinan, and Argyle. Delta values ($\delta^{13}\text{C}$) express the deviation of the $^{13}\text{C}/^{12}\text{C}$ ratio of diamond samples relative to a known standard, expressed in permil (parts per thousand). At each locality, a range of values overlaps between peridotitic (histograms on the left) and eclogitic (histograms on the right) diamonds. There is also large overlap between localities, which makes it impossible to use $\delta^{13}\text{C}$ as a fingerprinting tool. The vertical gray band marks the main mantle range around -5‰. Data from Stachel et al. (2022b).

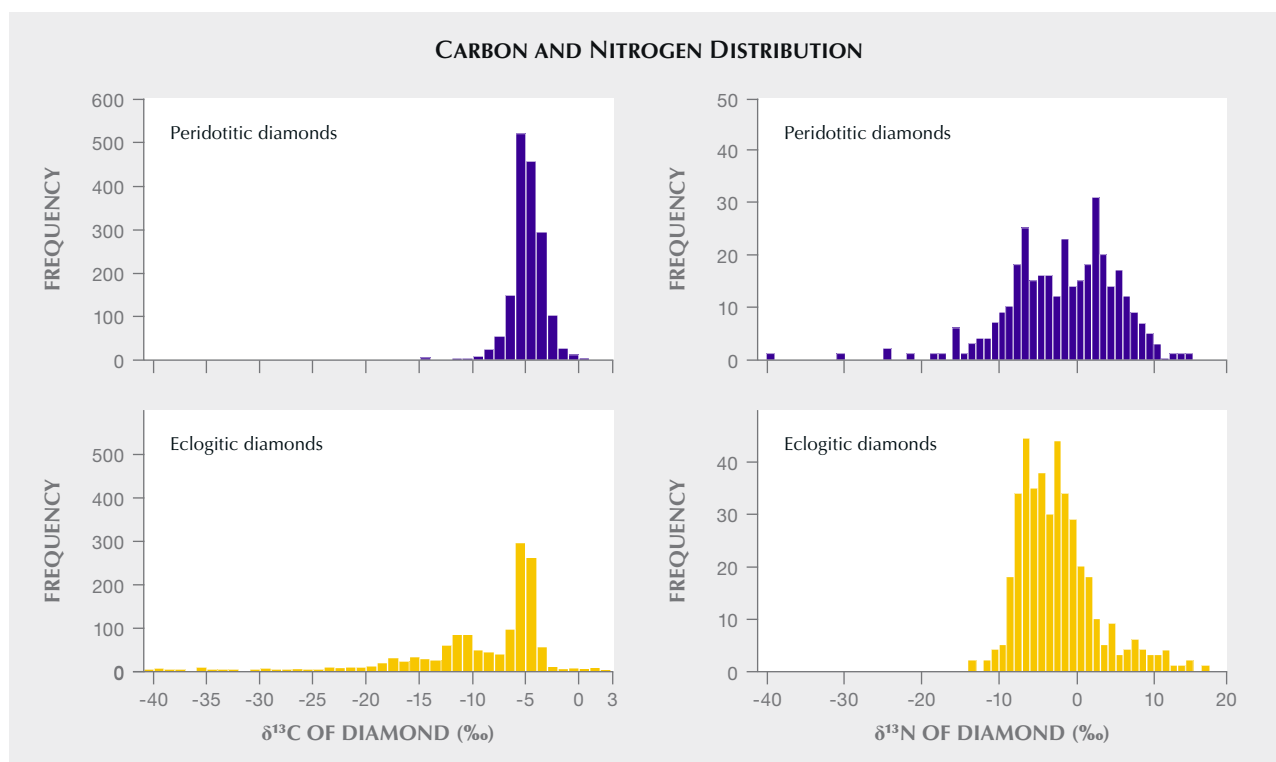


Figure 4. Distribution of carbon ($\delta^{13}\text{C}$) and nitrogen ($\delta^{15}\text{N}$) isotope compositions for worldwide peridotitic and eclogitic diamonds. Delta values ($\delta^{13}\text{C}$ and $\delta^{15}\text{N}$) express the deviation of the $^{13}\text{C}/^{12}\text{C}$ and $^{15}\text{N}/^{14}\text{N}$ ratios of diamond samples relative to a known standard. Carbon and nitrogen isotope data exhibit distributions that primarily reflect mantle host rock composition, irrespective of geographic origin. Generally, the same distributions are recorded from diamond deposits worldwide. Data from Stachel et al. (2022b).

host rocks—peridotite and eclogite—have modes that overlap with this mantle range (figure 4). Consequently, the stable isotope composition of a diamond lends insight into the host rock and fluids from which the crystal formed, but it is not a geographically distinct feature. Even if it were moderately helpful for origin determination, the time-consuming and expensive nature of stable isotope analysis, as well as the formation of ablation pits, makes it unsuitable for routine application to faceted diamonds.

Trace Element Characteristics. Like any mineral, diamond contains minute amounts of elements other than those stated in its mineral formula (see box B). These so-called trace elements may provide a rich geochemical record of the conditions of mineral growth, potentially revealing differences between different deposits. Trace elements can be present at concentrations from many parts per million (ppm) down to parts per billion (ppb), parts per trillion (ppt), or less, so there are enormous ranges of possible concentrations in natural materials. In transparent, gem-quality diamond, the concentrations of trace elements are extremely

low, often in the ppt range, making them especially difficult to measure compared to other minerals. The first pioneering measurements of trace elements in gem-quality diamond were made by instrumental neutron activation analysis (INAA) (Fesq et al., 1973; Bibby, 1982), but the amount and quality of data were limited. It is worth noting that the neutron bombardment of INAA severely damages the appearance of the whole diamond being analyzed.

Later studies have employed laser ablation–inductively coupled plasma–mass spectrometry (LA-ICP-MS), a widely used tool for measuring elemental compositions of many geological materials, including gemstones (Liu et al., 2013). Laser ablation involves vaporizing a small amount of the sample material by blasting a tiny crater into it with a laser. The liberated sample particles are ionized in a plasma to form a beam of atomic and small polyatomic ions, which are then continuously separated by mass/charge in a mass spectrometer (figure 5A). This technique has been applied to many gemstones (see review in Groat et al., 2019), including blue sapphire (Palke et al., 2019a), ruby (Palke et al., 2019b), and emerald, all of which

BOX B: WHAT ARE TRACE ELEMENTS?

Most of the rocks and minerals around us are made up of a relatively small selection of elements, including oxygen (O), silicon (Si), aluminum (Al), calcium (Ca), iron (Fe), magnesium (Mg), sodium (Na), and potassium (K), the most abundant elements in the earth's crust. Just consider the mineral formulas of some common rock-forming minerals: quartz (SiO_2), olivine ($[\text{Mg,Fe}]_2\text{SiO}_4$), potassium feldspar (KAlSi_3O_8), or what is regarded as the most abundant mineral at great depth within the earth, bridgmanite ($[\text{Mg,Fe}]\text{SiO}_3$). Many elements on the periodic table do not make an appearance as major defining components of minerals and are present only in trace quantities. In geology, the term *trace element* generally refers to those elements making up less than about 0.1% by weight (1000 ppm) of a mineral, rock, magma, or other system (Shaw, 2006). In a mineral, elements given in the mineral formula are essential structural constituents (Hanson and Langmuir, 1978) that impart distinct properties and make up the majority of the material. These are called *major elements*. The terms *major* and *trace* elements

can therefore refer to different elements depending on the material in question. Diamond is rather special, being composed solely of one major element, carbon. Other examples are gold, silver, and copper, all of which occur in their native form. In diamond, carbon is the only major element, whereas all other elements in this mineral are only present in trace quantities, often expressed in parts per million (ppm), billion (ppb), trillion (ppt), and so on, by weight.

The concentrations and relative abundances of trace elements can provide information about the way minerals formed. Trace element analysis of diamond has primarily focused on unraveling the geological settings and elements involved in diamond formation, but a secondary goal has been the forensic/gemological application of trying to distinguish geographic origin. The trace elements typically discussed in the context of diamonds include Cs, Rb, Ba, Th, U, Pb, Ta, Nb, La, Ce, Pr, Sr, Nd, Sm, Hf, Zr, Eu, Ti, Gd, Tb, Dy, Y, Ho, Er, Yb, and Lu, as well as the lighter elements H, B, N, O, Na, Mg, Al, Si, Cl, K, Ca, Fe, and Ni.

contain abundant trace elements that are relatively straightforward to measure.

When it comes to transparent, gem-quality diamond, however, the ultra-low concentration of most trace elements is problematic. The low bulk concentration of trace elements means that high-quality data cannot be obtained by routine “online” LA-ICP-MS analysis of gem-quality diamond because most elements fall near or below the limit of detection (McNeill et al., 2009). Increasing the laser energy to ablate more diamond in an effort to overcome the low concentration carries the risk of uncontrolled fractionation at the ablation site during sampling and increased diamond destruction. For these reasons, applying routine LA-ICP-MS techniques to gem-quality diamonds yields data that are generally not quantitative and whose uncertainties are difficult to evaluate (McNeill et al., 2009), making them of limited use for investigating diamond paragenesis and potential geographic variability. For example, in a study of 400 monocrystalline (nonfibrous) diamonds analyzed by LA-ICP-MS (Rege et al., 2010), the trace element patterns exhibited strong similarities regardless of geographic locality or geological paragenesis. Early attempts such as this struggled to accurately characterize detection limits or demonstrate that the data produced were significantly different from instrumental background.

Aside from carbon, most elements do not incorporate easily into the diamond crystal lattice as it grows, which is one of the reasons high-clarity diamond crystals have such low trace element concentrations. A few trace elements such as hydrogen, boron, nitrogen, silicon, and nickel (also common in laboratory-grown diamonds) may be incorporated as defects in the diamond lattice. But the majority of trace elements of geological interest, when they do occur in gem diamond, are thought to be hosted as fluid nano-inclusions that are simply too small and sparse to see (Melton et al., 2012; Krebs et al., 2019, 2020).

In contrast to the ultra-low trace element concentrations in gem-quality diamond, a particular growth habit called *fibrous diamond* has diamond trace element concentrations that are at least two to four orders of magnitude greater (Weiss et al., 2008). Fibrous diamond has a cloudy appearance due to abundant sub-micrometer-sized high-density fluid (HDF) inclusions (Navon et al., 1988) and is generally not considered gem-quality because of the diminished clarity. However, the abundance of HDF inclusions in fibrous diamond causes the bulk trace element contents to be high enough to analyze using LA-ICP-MS. Most trace element studies of diamond have focused on fibrous diamond (Tomlinson et al., 2005, 2009; Zedgenizov et al., 2007b; Rege et al., 2010;

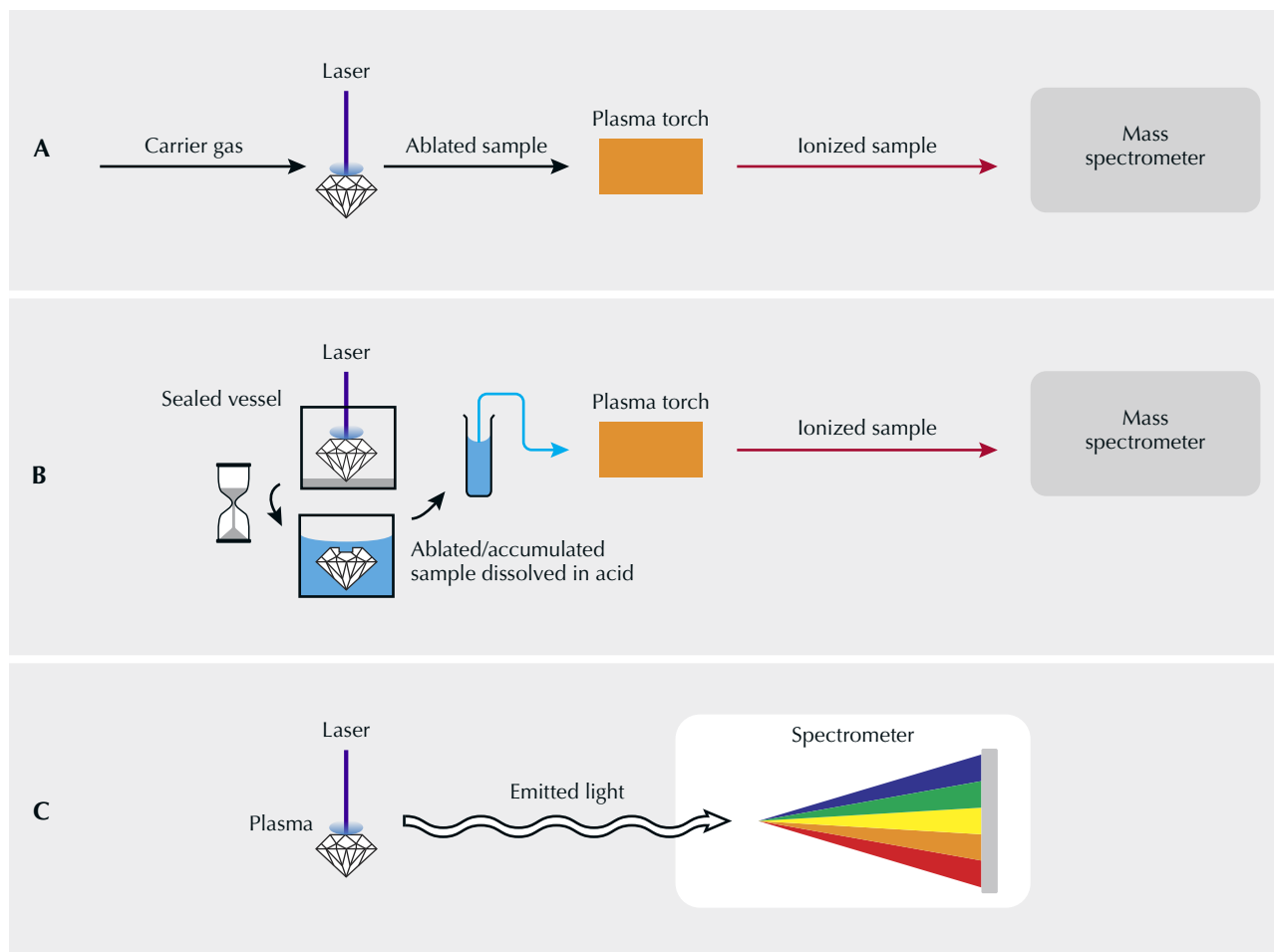


Figure 5. Simplified schematic of analytical methods. A: Conventional “online” LA-ICP-MS. A gas stream carries the ablated sample directly into the plasma torch, where it is ionized and accelerated as a beam. In the mass spectrometer, ions are separated based on mass/charge and their abundance can be quantified. B: “Offline” laser ablation combined with solution-based ICP-MS. Ablation takes place in a sealed vessel over an extended time, allowing a larger amount of ablated material to accumulate. Dissolving the ablated sample in acid allows it to be analyzed as a solution. C: The laser-induced breakdown spectroscopy (LIBS) technique. The laser striking the diamond creates a plasma, the emitted light of which can be separated into different wavelengths by a diffraction grating inside a spectrometer. The light spectrum can contain information about the elements and chemical bonding within the sample.

Smith et al., 2012; Weiss et al., 2013; Klein-BenDavid et al., 2014). Even though these analyses are based on micro-inclusions hosted in diamond and not the diamond itself, there is evidence that similar trace element characteristics exist at lower concentrations in gem-quality diamond that do not contain visible inclusions (Jablon and Navon, 2016; Krebs et al., 2019). This suggests that fibrous diamonds and their HDF inclusions are broadly informative of non-fibrous, gem-quality diamonds and provide an additional basis for discussing the prospect of origin

determination (see the section “Fibrous Diamonds Bolster Our Insight into Trace Elements”).

Returning to the more challenging analysis of gem-quality diamond, there is a modified laser ablation technique that can achieve superior results. McNeill et al. (2009) developed a sample pre-concentration technique involving “offline” laser ablation (see box C; figure 5B). This technique was developed as an improvement over conventional “online” LA-ICP-MS, specifically to measure trace elements and some radiogenic isotopes in gem-quality

BOX C: “OFFLINE” LASER ABLATION TECHNIQUE

This specialized method for measuring trace elements in diamond involves a pre-concentration step that allows a larger sample to be collected in a controlled fashion. It was developed by McNeill, Pearson, and colleagues at Durham University specifically for analyzing diamond (McNeill et al., 2009). The diamond is placed in an enclosed vessel with a window through which the laser can pass. Ablation takes place within this sealed vessel, allowing the ablated material to accumulate over the course of minutes or even hours. Compared to the direct uninterrupted ablation-to-analysis of LA-ICP-MS, this offline sampling technique means a much larger amount of diamond, and therefore a larger sample of trace elements, can be ablated in a controlled way. The accumulated sample is then taken up in acid and analyzed by conventional solution-based ICP-MS. Analyzing solutions greatly simplifies standardization, circumventing the need for a diamond standard. Appropriate solution standards with elemental concentrations similar to that expected in diamond can easily be prepared. Weighing the diamond before and after ablation gives the mass of diamond ablated, providing a way to recast results as elemental concentrations within the diamond. Offline ablation allows much higher volumes of analyte to be pre-concentrated before measurement rather than having the ablated material swept directly into a gas stream for analysis, as in LA-ICP-MS, effectively boosting what is known in analytical work as the *signal-to-noise ratio* by several orders of magnitude.

To measure a signal, having a strong signal and having low background noise are equally important. An example of low signal-to-noise ratio occurs when the *noise* from city lights prohibits the *signal* of distant stars from being seen by curious stargazers. In rural areas, background light is so low that even faint signals from stars can be seen.

In analytical work, scientists must pay special attention to the relative contributions of signal and noise. The limit of detection (LOD) provides a threshold level where weak signals cannot be confidently distinguished from background noise. One definition of the LOD is $3\times$ the standard deviation of the blank/background (Currie, 1968). However, we want to know how much of the element there is, not just that it can be detected. For the exceptionally low trace element contents of most gem-quality diamonds, which may be only marginally above

the background noise, McNeill et al. (2009) argued that a more stringent limit is needed: the limit of quantification (LOQ). This is defined as 7 to $10\times$ the standard deviation of the blank/background (Currie, 1968), and it is a better cutoff to ensure that the signal seen above the background can be used to calculate element concentration. Data must exceed the LOQ (the minimum accurate quantifiable value) to be considered truly quantitative. A number of studies have reported conventional online laser ablation results from gem-quality diamonds but with such low signal-to-noise ratios that LOQ criteria could not be met (Rege et al., 2005, 2010; Coney et al., 2012; Brill et al., 2020). If measurements do not exceed the LOQ, they may carry qualitative meaning, but large uncertainties will obscure comparison between samples, restricting their utility.

Offline laser ablation with ICP-MS enables quantitative trace element data for gem-quality diamond. However, the technique is not without drawbacks. The amount of diamond that must be ablated is large compared to the typical ablation crater involved in conventional LA-ICP-MS of other materials. For example, analyses of most colored gem materials using LA-ICP-MS would involve a spot size of 50–100 μm , meaning that an analysis can be performed on the girdle of a valuable ruby, sapphire, or emerald and would not be visible to the unaided eye. For offline ablation ICP-MS of diamond, larger raster patterns of $500 \times 500 \mu\text{m}$ are typical, extending several hundred micrometers deep into the diamond. In addition to being (partially) destructive, the technique is slow. Whereas ablation and analysis in conventional LA-ICP-MS might extend for 40–180 s, offline ablation for diamond normally requires up to 4 hours (and in some cases up to 20–30 hours). More time is needed to carefully clean the diamond with ultra-pure acids prior to ablation, to prepare the ablated sample into a solution, and ultimately to complete the ICP-MS analysis. A high-tech and expensive clean lab is necessary to minimize contamination. All samples are processed in parallel with total procedural blanks so that the combined background (or noise) of trace elements present in all acids and materials involved can be measured. The stringent requirements are such that only two laboratories have done this rigorous level of analysis for gem-quality diamond, first at Durham University and later at the University of Alberta by Pearson and colleagues.

ity diamond (McNeill et al., 2009; Klein-BenDavid et al., 2010). Part of the aim in developing this advanced methodology was to investigate whether trace elements can be linked to specific geographic origins (McNeill, 2011).

The offline laser ablation sampling technique permits meaningful quantitative measurement of trace elements in even the purest gem-quality diamonds, although it currently requires a substantial input of time, laboratory infrastructure, and analytical expert-

ise. This method is also moderately destructive, further barring its routine application to faceted gem diamonds. It involves ablating a relatively conspicuous “pit” on the order of 500 μm wide and several hundred micrometers deep. Only a limited number of diamond localities have been studied so far: 11 from Brazilian sublithospheric diamonds (Timmerman et al., 2019a); 10 from Koffiefontein, Letlhakane, and Orapa (Timmerman et al., 2019b); one from Udachnaya; one from Mir; one from Venezuela; 10 from Cullinan (McNeill et al., 2009); 24 from Finsch, Newlands, and Victor (Krebs et al., 2019); and 10 from Akwatia, Ghana, and the De Beers Kimberley Pool, South Africa (Melton et al., 2012). In small sample sets, statistical analysis of variance and logistic regression suggests significant differences between populations (e.g., McNeill, 2011), but these differences appear less distinct upon analysis of a wider variety of diamonds. Differences may be apparent when considering averaged trace element patterns from different localities, or even diamonds with sulfide versus silicate inclusions from a single locality, but comparing individual diamonds shows considerable overlap from one deposit to the next (Krebs et al., 2019). As discussed by Melton et al. (2012), some of these measurements may be skewed by the intersection of small mineral inclusions during the course of ablation, which may or may not be avoidable depending on the sample. This possibility requires additional care during ablation and later during interpretation.

Although the data are limited, a key outcome of this work is the finding that many gem diamonds have trace element patterns comparable to those of fibrous diamonds (Krebs et al., 2019; Timmerman et al., 2019b). In support of such a connection, HDF inclusions similar to those in fibrous diamonds have been reported within nonfibrous gem-quality diamonds (from the Voorspoed and Venetia mines in South Africa, for example) trapped along the twinning planes of macles (Jablon and Navon, 2016). These results allow us to draw on the existing literature on fibrous diamonds in the discussion of trace element use for geographic origin determination.

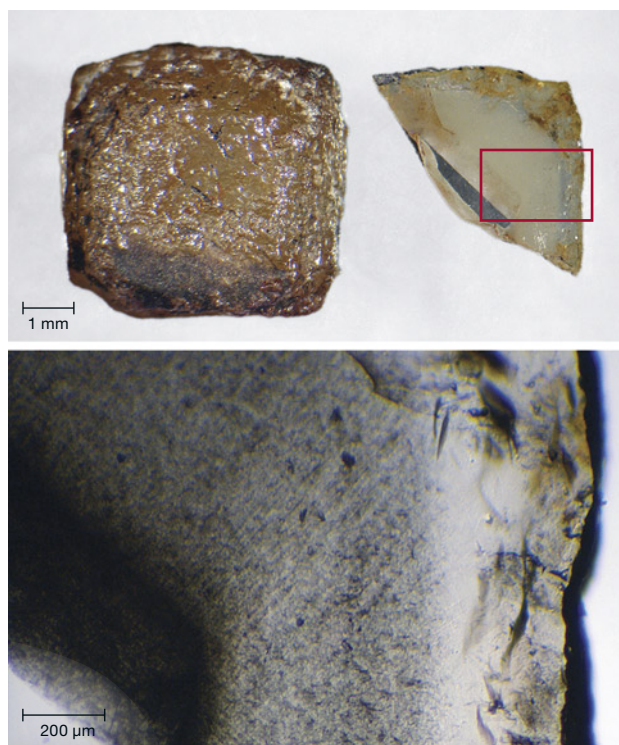
FIBROUS DIAMONDS BOLSTER OUR INSIGHT INTO TRACE ELEMENTS

There are marked similarities between fibrous diamonds and gem-quality nonfibrous diamonds upon comparing the major element compositions of fluid inclusions and trace element compositions of bulk diamond (Jablon and Navon, 2016; Krebs et al., 2019).

The similarities suggest that the more extensive work on trace elements in fibrous diamonds also offers insight into gem-quality diamonds. Fibrous diamond trace element properties cannot be claimed as a proxy for all diamonds, as some diamond varieties are thought to be formed from distinctly different fluids, such as methane-bearing reduced fluids (Smit et al., 2016, 2019) and metallic Fe-Ni-C-S liquids (Smith et al., 2016, 2017). However, the connection between fibrous diamonds and transparent, nonfibrous diamonds formed in the lithospheric mantle applies to many mined gem-quality diamonds derived from the lithospheric mantle.

Fibrous diamonds are fluid-rich diamonds that trap small droplets of the diamond-source fluid as inclusions during growth. They have a dendritic single-crystal growth habit (like a snowflake) that grows as

Figure 6. Cuboid diamond (5 mm edge length) consisting of a cloudy fibrous diamond coat over a transparent octahedral core. A partial slice has been cut through the middle, revealing the internal structure. The red rectangle outlines the region of the photomicrograph at bottom (field of view 1.5 mm), which shows a portion of the polished slice in transmitted light, with the micro-inclusions appearing as dark pinpoints. The reddish color is iron oxide staining in surface-reaching fractures. Photos by Evan M. Smith.



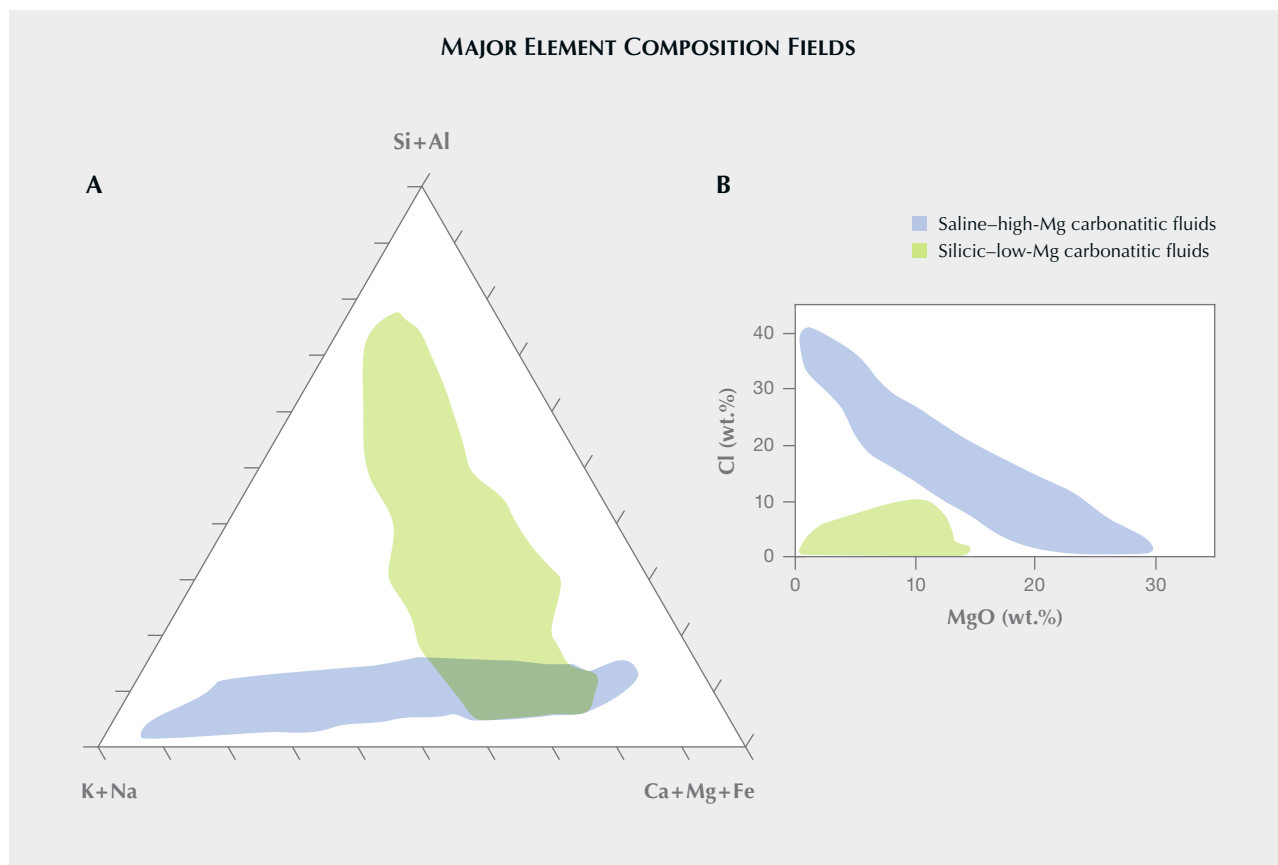


Figure 7. Fields of major element composition for fluids in fibrous diamonds worldwide, which are often plotted in a molar composition ternary plot (atomic proportions). A: Four major fluid end-member compositions have been identified in fibrous diamonds: saline, high-Mg carbonatitic, low-Mg carbonatitic, and silicic. B: The carbonatitic fluid compositions overlap in the ternary diagram but can be separated in a Cl vs. MgO plot. Data compiled from Izraeli et al. (2001); Klein-BenDavid et al. (2004, 2007, 2009); Kopylova et al. (2010); Schrauder and Navon (1994); Shiryayev et al. (2005); Smith et al. (2012); Tomlinson et al. (2006); Weiss et al. (2009); and Zedgenizov et al. (2007a).

a set of crystallographically controlled, space-filling branches in three dimensions, typically producing an overall cuboid shape (figure 6). The chemical composition of HDF inclusions in fibrous diamonds has been measured by several methods, with electron probe microanalysis (EPMA) being the most common. HDF compositions can be described in terms of four end members (figure 7). There is a silicic end member rich in Si, K, Al, Fe, and water; a low-Mg carbonatitic end member rich in Ca, Fe, K, Mg, and carbonate; a high-Mg carbonatitic end member rich in Mg, Ca, Fe, K, and carbonate; and a saline end member rich in Cl, K, Na, water, and carbonate (Navon et al., 1988; Izraeli et al., 2001; Tomlinson et al., 2006; Klein-BenDavid et al., 2007; Weiss et al., 2009). Compositional variability between end members defines

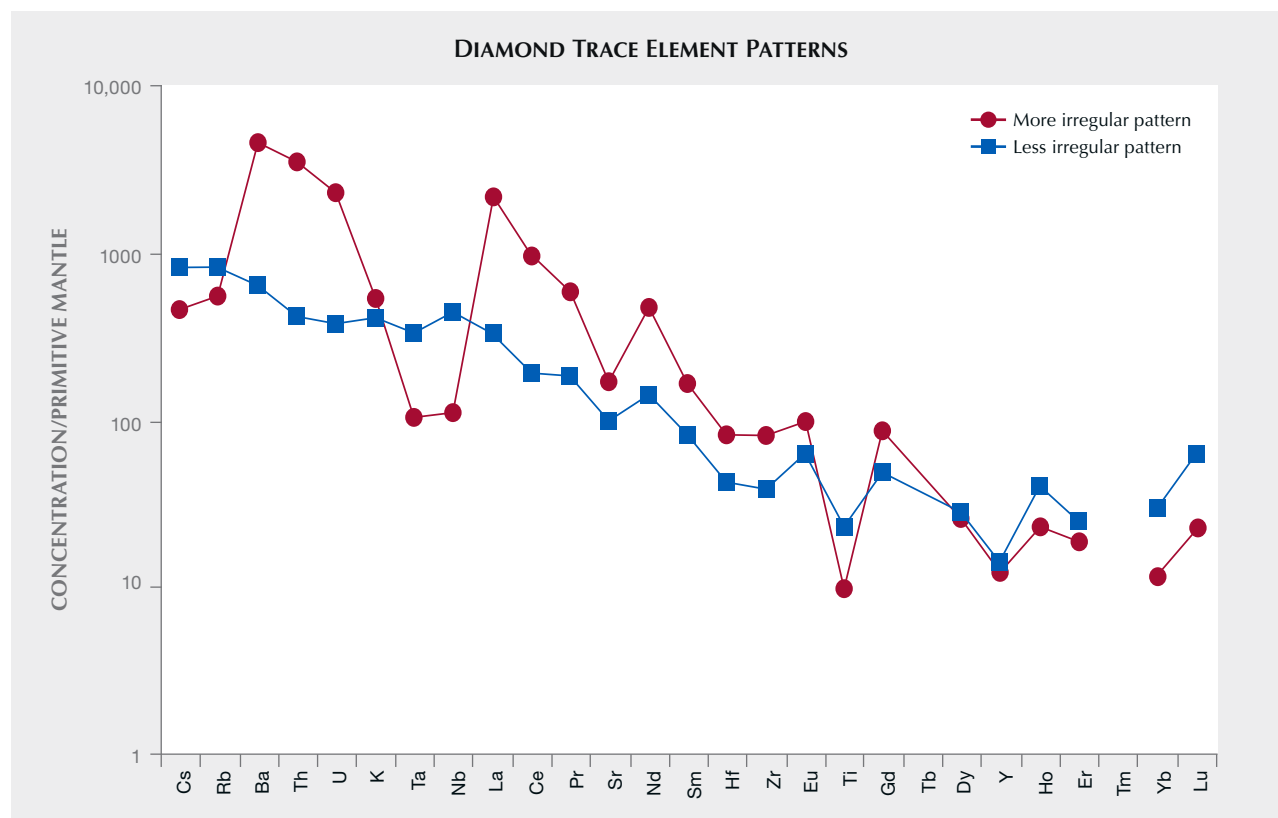
a transitional array bridging the silicic and low-Mg carbonatitic end members. The well-populated compositional array between silicic and low-Mg carbonatitic end members may be explained in terms of near-solidus melt compositions with varying H_2O/CO_2 ratios in eclogite host rocks leading up to diamond formation (Elazar et al., 2019). In contrast, the saline and high-Mg end members are more detached in compositional space. Only a few diamonds exhibit transitional compositions between saline and high-Mg carbonatitic end members (Klein-BenDavid et al., 2006) as well as between saline and silicic end members (Tomlinson et al., 2006; Weiss et al., 2009).

Trace element measurements by mass spectrometry, with both traditional LA-ICP-MS and offline laser ablation ICP-MS, reveal high degrees of trace el-

element enrichment in the fluids. Trace element patterns define two major groupings: one that is highly irregular, with prominent enrichments or depletions of particular elements, and another that is less irregular (figure 8). Specifically, the more irregular group has depleted compositions of alkali (e.g., K, Rb, Cs) and high field strength elements (e.g., Ta, Nb) and enriched large ion lithophile element concentrations (e.g., Ba, U, Th), while the less irregular group has lower large ion lithophile element concentrations (Tomlinson et al., 2009; Weiss et al., 2009, 2013; Klein-BenDavid et al., 2010; Smith et al., 2012;). The more irregular patterns are thought to relate to fluid interaction with the subcontinental lithospheric mantle, while the less irregular patterns may be a signature of the convecting mantle beneath the lithosphere (Weiss et al., 2013).

By combining trace elements with strontium isotope analyses, the origin of the saline fluid end member has been linked to the involvement of subducted oceanic crust altered by seawater, because seawater is known to have a very enriched $^{87}\text{Sr}/^{86}\text{Sr}$ isotope composition (Weiss et al., 2015). Furthermore, chemical evolution of such a fluid percolating through peridotitic and eclogitic rocks in the lithosphere is proposed to account for the compositional ranges of carbonatitic and silicic fluids (Weiss et al., 2015). High-Mg carbonatitic fluids may result from near-solidus melting in peridotite, while silicic-to-low-Mg carbonatitic fluids may reflect melting in eclogite (Tomlinson et al., 2009; Weiss et al., 2009, 2011; Klein-BenDavid et al., 2014; Elazar et al., 2019). Fibrous diamonds therefore provide a key signal of the input of subduction-derived seawater fluids for fi-

Figure 8. Trace element patterns in diamond define two prominent categories. One is a more irregular pattern with conspicuous enrichments or depletions of particular elements, while the other is less irregular. Trace element measurements from both fibrous diamonds and gem-quality diamonds can be highly variable, but they consistently exhibit characteristics of these two end members or their combinations, regardless of geographic provenance. The horizontal axis shows trace elements of geologic interest, while the vertical axis shows their concentration, normalized to primitive mantle model concentrations of McDonough and Sun (1995). Plotted data show fibrous diamond analyses from Weiss et al. (2013).



brous diamond growth. These fluids may also lead to metasomatism of the lithospheric mantle (Miller et al., 2014; Weiss et al., 2015).

Fibrous diamonds and their purer gem-quality diamond counterparts therefore reveal two overarching trace element patterns, thought to reflect two major geological processes governing their formation in the mantle. Measurements in both fibrous and gem diamonds show that diamonds from different deposits can have similar patterns. For example, a striking similarity in trace element patterns has been found between suites of fibrous diamonds from two different Canadian deposits: the Wawa area of Ontario and the Ekati mine in the Northwest Territories (Smith et al., 2012). These findings suggest it might not be uncommon to encounter instances where complete overlap precludes an origin determination on the basis of trace elements alone. Conversely, diamonds from the same deposit can have dissimilar patterns, which is not surprising given the fact that many deposits contain multiple diamond populations with geologically distinct sources in the mantle.

Laser-Induced Breakdown Spectroscopy. As a comparatively new analytical technique applied to diamond, LIBS might offer an alternative way to capture chemical characteristics. It involves focusing a rapidly pulsed laser (the same kind as used for LA-ICP-MS) onto the sample to form a plasma and analyzing the spectrum of light emitted to reveal the characteristic wavelengths from elemental and molecular emissions (figure 5C; Senesi, 2014; Harmon and Senesi, 2021). The laser spot size is normally tens to hundreds of micrometers in diameter. Typical detection limits for most elements are in the tens of ppm range (Harmon and Senesi, 2021), but modified techniques such as double-pulse LIBS or nanoparticle-enhanced LIBS can potentially increase the signal-to-noise ratio and lower the detection limits (Koral et al., 2018).

LIBS has a wide range of applications and has been used previously to characterize major and trace elements in a variety of gemstones (Rossi et al., 2014), including efforts toward origin determination of ruby and sapphire (Kochelek et al., 2015). For gem-quality diamonds, most element concentrations fall well below LIBS detection limits. Nevertheless, each spectrum captures a complex combination of signals whose peak shapes and positions are affected by many variables.

Multivariate statistical analysis can be used to recognize shared or differentiating features among

sample suites (Harmon and Senesi, 2021). It is possible to compare entire emission spectra for differences, which can potentially be used to recognize geological and geographical patterns, even if the spectra are not deconvoluted into properties such as trace element concentrations. This is a powerful capability of LIBS spectroscopy. Upon comparing spectra, however, it is crucial to account for the fact that spectra collected in multiple analytical sessions can have significant differences arising from day-to-day changes—for example, in temperature, humidity, laser stability, and so on. To ensure data reliability, for LIBS or any other technique, it should be possible to measure a specimen multiple times, independently, and reproduce the same result.

One pilot study has attempted to use LIBS to distinguish diamonds by their different geographic origins. In this initial study involving multiple suites of 30 natural diamonds each, sourced from 12 different localities, plus two suites of laboratory-grown diamonds, McManus et al. (2020) proposed that it was possible to discriminate between the diamonds from different sources. Variable elemental emissions were observed from H, C, N, Na, Mg, Al, Si, K, Ca, Ti, V, Cr, Fe, Co, Ni, Cu, Sr, Ba, O, Ne, and Ar (the carrier gas). However, these analyses were performed on natural rough surfaces cleaned only with isopropyl alcohol rather than extensive acid leaching (compare with McNeill et al., 2009), which means the LIBS spectra could include surface contamination (that could in itself be origin-specific). Even after apparently ablating down through the surface with successive laser pulses, lingering foreign materials on the diamond surface and in shallow surface-reaching fractures could overwhelm the comparatively scant abundance of trace elements actually inside a diamond.

Regardless, a significant differentiating factor in the McManus et al. (2020) LIBS data lies with molecular C-C and C-N emissions (from the two most abundant elements in diamond, C and N), not just trace element characteristics. It is not clear what information these C-C and C-N peaks contain. Potentially, the C-C and C-N molecular emissions vary as a function of carbon and nitrogen isotope composition. Isotopic shifts in optical features are orders of magnitude greater for molecular emissions than for atomic emissions (Harmon and Senesi, 2021). The C-C and C-N peaks may also vary with nitrogen concentration and nitrogen aggregation state. However, many measurements of these carbon- and nitrogen-related variables from previous studies using other

methods do not show geographic distinctions (e.g., figures 3 and 4). Although it is possible that C-C and C-N emissions, perhaps under the influence of trace elements or lattice defects, contain rich and complex information, the specific constituents with the potential to convey geographic differences remain uncertain. It is also unclear how to ensure data quality without first understanding the meaning of spectral features of interest.

Alternatively, the observed C-N peaks reported by McManus et al. (2020) could reflect small and variable contributions from atmospheric nitrogen contaminating the argon gas flowing over the sample surface. This possibility cannot be dismissed, because the study did not include any nitrogen-free diamond samples or standards or measurements of the possible dynamically variable trace nitrogen content of the atmosphere in the ablation chamber. Also, the sensitivity of LIBS to nitrogen in diamond remains unclear. An unrelated study comparing point analyses in different crystallographic sectors of a laboratory-grown diamond found differing C-C and C-N emission intensities that were argued to correlate with different assumed nitrogen concentrations (Lebedev et al., 2020), but again it is difficult to entirely rule out atmospheric influences. Without more details of the analytical routine and data handling, it is difficult to evaluate the results.

As with any spot analysis, LIBS spectra collected from a single point may fail to account for internal heterogeneity. Diamonds often have heterogeneous growth layers in terms of nitrogen concentration, nitrogen isotope composition, and carbon isotope composition that may lead to non-uniform C-C and C-N emissions. The pilot study of McManus et al. (2020) does not appear to have explored spatial variations within samples. In addition to heterogeneity within individual diamonds, it is also important to account for the fact that many diamond mines contain multiple populations with distinct properties. Future studies should attempt to capture these variables.

A further challenge with LIBS is that the spectra contain artifacts specific to the instrument used, meaning spectra collected on a given instrument are best compared against others collected with the same equipment (Harmon and Senesi, 2021). Although LIBS offers many appealing aspects as an analytical tool, such as speed and simplicity, its suitability for evaluating and comparing gem-quality diamonds remains to be demonstrated.

PRESERVING GEOGRAPHIC ORIGIN INFORMATION FROM THE TIME OF MINING

As an alternative to inferring origin based on an independent assessment of diamond properties, finding a way to preserve this information from mine to market offers some advantages. If the origin is retained and certified through documentation or other means, it can be stated as a fact rather than as an inference or opinion, and it avoids the potential problem of multiple localities having diamonds with unresolvable, overlapping physical and geochemical characteristics. Perhaps the greatest advantage is that it is a simple and straightforward approach that can be accomplished with existing tools, albeit with logistical challenges.

There are now several industry initiatives for diamond traceability, given increasing attention to corporate governance, environmental impact, and social responsibility. For example, De Beers has developed a traceability initiative called Tracr that uses blockchain, a secure digital record of transactions, to allow a given diamond to be traced from mine to market. Lucara has its own blockchain traceability with Clara Diamond Solutions. Alrosa has developed a laser nanomark (capable of being read at any time) to identify its rough diamonds in a way that survives cutting and polishing. Rio Tinto developed a traceability program to track diamonds from its Argyle mine (now closed) through the supply chain.

Ultimately, traceability initiatives should encompass diamonds from both large-scale and artisanal miners. There is arguably a need for independent verification of origin information by third parties not involved in the sale of diamonds. Several such companies offer ways to verify traceability from mines, through the supply chain, including Everledger, using blockchain; diamond technology company Sarine, with Diamond Journey Traceability; and SCS Global Services, through their SCS-007 standard, which involves verifying supply chain documentation as well as collecting chemical information (through a partnered laboratory using LA-ICP-MS). GIA also provides a provenance service called the Diamond Origin Report, which matches the physical and spectral characteristics of a polished stone with that of a previously submitted rough diamond from a disclosed locality. More recently, the Institute launched the GIA Source Verification Service, which verifies origin information using supply chain documents and invoices from vetted manufacturers and provides this information through its online GIA Report Check service.

This level of investment in traceability by multiple stakeholders is a promising step forward. Preserving the geographic origin information is an exciting prospect not only for consumers, but also for diamond geologists. Just like fossils, meteorites, and mineral specimens, diamonds have a greater value to the consumer and to the scientist when they can be tied back to a specific community, geological setting, age, or process.

CONCLUDING REMARKS

Relative to mantle-derived diamond, gem minerals that formed in the crust are more amenable to inferring provenance on the basis of trace element analysis. Crustal minerals tend to incorporate higher concentrations of trace elements as they grow, and there is inherently more geochemical variability in crustal rocks (see the *G&G* Winter 2019 special issue on origin determination for colored gemstones). For example, trace elements have been widely employed with reasonable success for discriminating the mine of origin for ruby and sapphire (Saminpanya et al., 2003; Abduriyim and Kitawaki, 2006; Peucat et al., 2007; Pornwilard et al., 2011; Harlow and Bender, 2013; Sutherland et al., 2015). But even under these more favorable circumstances, when two different localities offer similar geological settings there can still be problematic overlap in trace element characteristics, such as for deposits of marble-type ruby and metamorphic blue sapphire (Krebs et al., 2020).

The recognized and resolvable varieties of natural diamond based on all measurable properties correspond to geological variables such as host rock type, the pressure and temperature conditions of crystal growth, and the composition of diamond-forming fluids. Generally these resolvable varieties, such as gem-quality lithospheric peridotitic or eclogitic diamonds, are not restricted to a single geographic origin. Instead, they occur across multiple deposits on a global scale, and multiple varieties can be observed within a single deposit.

Diamonds from different deposits can have indistinguishable trace element characteristics, and diamonds from the same deposit can have marked dissimilarities. The underlying patterns that have been recognized within trace element data are associated with geological processes, irrespective of geographic origin. If there are features unique to individual deposits, they must be subtle features, masked by the more pronounced overarching geological variations that are responsible for characteristics

such as inclusion mineralogy or the appearance of enriched versus non-enriched trace element patterns.

Observations to date suggest that trace element analysis may not be a definitive approach for inferring diamond origin. Although current techniques to quantitatively analyze trace elements in diamond are time-consuming, expensive, and somewhat destructive to the sample, these are not the principal hindrances. Even well-controlled, quantitative measurements made using offline laser ablation techniques do not appear to show distinct signatures associated with different mines. In other words, future improvements to methods for measuring trace elements are not necessarily expected to resolve this issue—and even if they could, it might not translate into a feasible routine service for faceted gem-quality diamonds. Importantly, any methodology must be capable of scaling up from preliminary studies involving hundreds of diamonds to high-quality datasets involving hundreds of millions of diamonds in order to be viable for commercial origin determination.

Given the interest and importance of this issue, it may be worth further exploring a combination of techniques using large sample suites. GIA continues to actively investigate this challenge to see whether some level of origin determination is possible, even if the odds of success appear to be low. For now, however, all reliable and rigorous services to establish the geographic origin of a diamond depend on retaining country-of-origin and/or mine-of-origin information from mine to market, rather than attempting determination through independent geochemical analysis.

In short, the absence of a feasible method to accurately determine diamond origin is due to a combination of geological and analytical limitations:

1. Diamonds from different mines often form by comparable geological processes in the mantle and have overlapping physical and chemical characteristics.
2. Trace element data collected to date, though necessarily limited, show no clear evidence of distinct geographic signatures.
3. Even if the initial results were encouraging, the only proven method for quantitative trace element analysis of gem-quality diamond is prohibitively slow, expensive, high-tech, and destructive. These limitations preclude a large global-scale investigation into origin discrimination.

ABOUT THE AUTHORS

Dr. Smith is a research scientist specializing in diamond geology at GIA in New York. Dr. Smit is a senior lecturer in diamond geology and isotope geochemistry at the University of the Witwatersrand, South Africa. Dr. Shirey is a senior staff scientist in geology/isotope geochemistry at the Earth & Planets Laboratory at the Carnegie Institution for Science in Washington, DC.

ACKNOWLEDGMENTS

The authors wish to thank D. Graham Pearson, Ingrid Chinn, and an anonymous reviewer for their constructive comments, as well as Mandy Krebs, Michael C. Jollands, Barbara Dutrow, John Valley, Jeffrey Post, James Shigley, Catherine McManus, and R. John Watling for their valuable feedback and suggestions that helped to improve this manuscript.

REFERENCES

- Abduriyim A., Kitawaki H. (2006) Applications of laser ablation-inductively coupled plasma-mass spectrometry (LA-ICP-MS) to gemology. *G&G*, Vol. 42, No. 2, pp. 98–118, <http://dx.doi.org/10.5741/GEMS.42.2.98>
- Bibby D.M. (1982) Impurities in natural diamond. In P.A. Throver, Ed., *Chemistry and Physics of Carbon*, Vol. 18. Marcel Dekker, New York, pp. 1–91.
- Brill S., Lilimu N., Chetty D. (2020) Diamond fingerprinting for source discrimination using laser ablation inductively coupled plasma mass spectrometry (LA-ICP-MS) and Fourier transform infrared spectrometry (FTIR). *Heliyon*, Vol. 6, No. 12, article no. e05592, <http://dx.doi.org/10.1016/j.heliyon.2020.e05592>
- Breeding C.M., Shigley J.E. (2009) The “type” classification system of diamonds and its importance in gemology. *G&G*, Vol. 45, No. 2, pp. 96–111, <http://dx.doi.org/10.5741/GEMS.45.2.96>
- Cartier L.E., Ali S.H., Krzemnicki M.S. (2018) Blockchain, chain of custody and trace elements: An overview of tracking and traceability opportunities in the gem industry. *Journal of Gemmology*, Vol. 36, No. 3, pp. 212–227.
- Coney L., Moila A.V., Quadling A.G. (2012) Gem-quality diamonds: Source discrimination. *South African Journal of Geology*, Vol. 115, No. 1, pp. 33–46, <https://doi.org/10.2113/gssaig.115.1.33>
- Currie L.A. (1968) Limits for qualitative detection and quantitative determination. Application to radiochemistry. *Analytical Chemistry*, Vol. 40, No. 3, pp. 586–593, <http://dx.doi.org/10.1021/ac60259a007>
- Dalpé C., Hudon P., Ballantyne D.J., Williams D., Marcotte D. (2010) Trace element analysis of rough diamond by LA-ICP-MS: A case of source discrimination? *Journal of Forensic Sciences*, Vol. 55, No. 6, pp. 1443–1456, <https://doi.org/10.1111/j.1556-4029.2010.01509.x>
- Eaton-Magaña S., Breeding C.M., Shigley J.E. (2018) Natural-color blue, gray, and violet diamonds: Allure of the deep. *G&G*, Vol. 54, No. 2, pp. 112–131, <http://dx.doi.org/10.5741/GEMS.54.2.112>
- Elazar O., Frost D., Navon O., Kessel R. (2019) Melting of H₂O and CO₂-bearing eclogite at 4–6 GPa and 900–1200 °C: Implications for the generation of diamond-forming fluids. *Geochimica et Cosmochimica Acta*, Vol. 255, pp. 69–87, <http://dx.doi.org/https://doi.org/10.1016/j.gca.2019.03.025>
- Fesq H.W., Bibby D.M., Sellschop J.P.F., Watterson J.I.W. (1973) The determination of trace-element impurities in natural diamonds by instrumental neutron activation analysis. *Journal of Radioanalytical Chemistry*, Vol. 17, pp. 195–216, <https://doi.org/10.1007/BF02520785>
- Gaillou E., Post J.E., Rose T., Butler J.E. (2012) Cathodoluminescence of natural, plastically deformed pink diamonds. *Microscopy and Microanalysis*, Vol. 18, No. 6, pp. 1292–1302, <http://dx.doi.org/10.1017/S1431927612013542>
- Groat L.A., Giuliani G., Stone-Sundberg J., Sun Z., Renfro N.D., Palke A.C. (2019) A review of analytical methods used in geographic origin determination of gemstones. *G&G*, Vol. 55, No. 4, pp. 512–535, <http://dx.doi.org/10.5741/GEMS.55.4.512>
- Hall A.E., Smith C.B. (1984) Lampiroite diamonds - Are they different? In J. Glover and P. Harris, Eds., *Kimberlite Occurrence and Origin: A Basis for Conceptual Models in Exploration*, Vol. 8, University of Western Australia, Perth, pp. 167–212.
- Hanson G.N., Langmuir C.H. (1978) Modelling of major elements in mantle-melt systems using trace element approaches. *Geochimica et Cosmochimica Acta*, Vol. 42, No. 6, pp. 725–741, [https://doi.org/10.1016/0016-7037\(78\)90090-X](https://doi.org/10.1016/0016-7037(78)90090-X)
- Harlow G.E., Bender W. (2013) A study of ruby (corundum) compositions from the Mogok Belt, Myanmar: Searching for chemical fingerprints. *American Mineralogist*, Vol. 98, No. 7, pp. 1120–1132, <http://dx.doi.org/10.2138/am.2013.4388>
- Harmon R.S., Senesi G.S. (2021) Laser-induced breakdown spectroscopy – A geochemical tool for the 21st century. *Applied Geochemistry*, Vol. 128, article no. 104929, <http://dx.doi.org/10.1016/j.apgeochem.2021.104929>
- Heaney P.J., Vicenzi E.P., De S. (2005) Strange diamonds: The mysterious origins of carbonado and framesite. *Elements*, Vol. 1, No. 2, pp. 85–89, <http://dx.doi.org/10.2113/gselements.1.2.85>
- Izraeli E.S., Harris J.W., Navon O. (2001) Brine inclusions in diamonds: A new upper mantle fluid. *Earth and Planetary Science Letters*, Vol. 187, No. 3–4, pp. 323–332, [http://dx.doi.org/10.1016/S0012-821X\(01\)00291-6](http://dx.doi.org/10.1016/S0012-821X(01)00291-6)
- Jablon B.M., Navon O. (2016) Most diamonds were created equal. *Earth and Planetary Science Letters*, Vol. 443, pp. 41–47, <http://dx.doi.org/http://dx.doi.org/10.1016/j.epsl.2016.03.013>
- Jaques A.L., Sheraton J.W., Hall A.E., Smith C.B., Sun S.-S., Drew R.M., Foudoulis C. (1986) Composition of crystalline inclusions and C-isotopic composition of Argyle and Ellendale diamonds. *International Kimberlite Conference: Extended Abstracts*, Vol. 4, p. 426–428, <https://doi.org/10.29173/ikc1192>
- Kemppinen L.I., Kohn S.C., Parkinson I.J., Bulanova G.P., Howell D., Smith C.B. (2018) Identification of molybdenite in diamond-hosted sulphide inclusions: Implications for Re–Os radiometric dating. *Earth and Planetary Science Letters*, Vol. 495, pp. 101–111, <http://dx.doi.org/10.1016/j.epsl.2018.04.037>
- King J.M., Moses T.M., Shigley J.E., Welbourn C.M., Lawson S.C., Cooper M. (1998) Characterizing natural-color type IIb blue diamonds. *G&G*, Vol. 34, No. 4, pp. 246–268, <http://dx.doi.org/10.5741/GEMS.34.4.246>
- Kjarsgaard B.A., Januszczak N., Stiefenhofer J. (2019) Diamond exploration and resource evaluation of kimberlites. *Elements*, Vol. 15, No. 6, pp. 411–416, <http://dx.doi.org/10.2138/gselements.15.6.411>
- Klein-BenDavid O., Izraeli E.S., Hauri E., Navon O. (2004) Mantle fluid evolution—a tale of one diamond. *Lithos*, Vol. 77, No. 1–4, pp. 243–253, <http://dx.doi.org/10.1016/j.lithos.2004.04.003>
- Klein-BenDavid O., Wirth R., Navon O. (2006) TEM imaging and analysis of microinclusions in diamonds: A close look at dia-

- mond-growing fluids. *American Mineralogist*, Vol. 91, No. 2-3, pp. 353–365, <http://dx.doi.org/10.2138/am.2006.1864>
- Klein-BenDavid O., Izraeli E.S., Hauri E., Navon O. (2007) Fluid inclusions in diamonds from the Diavik mine, Canada and the evolution of diamond-forming fluids. *Geochimica et Cosmochimica Acta*, Vol. 71, No. 3, pp. 723–744, <http://dx.doi.org/10.1016/j.gca.2006.10.008>
- Klein-BenDavid O., Logvinova A.M., Schrauder M., Spetsius Z.V., Weiss Y., Hauri E.H., Kaminsky F.V., Sobolev N.V., Navon O. (2009) High-Mg carbonatitic microinclusions in some Yakutian diamonds—a new type of diamond-forming fluid. *Lithos*, Vol. 112, No. Supplement 2, pp. 648–659, <http://dx.doi.org/10.1016/j.lithos.2009.03.015>
- Klein-BenDavid O., Pearson D.G., Nowell G.M., Ottley C., McNeill J.C.R., Cartigny P. (2010) Mixed fluid sources involved in diamond growth constrained by Sr–Nd–Pb–C–N isotopes and trace elements. *Earth and Planetary Science Letters*, Vol. 289, No. 1-2, pp. 123–133, <http://dx.doi.org/10.1016/j.epsl.2009.10.035>
- Klein-BenDavid O., Pearson D.G., Nowell G.M., Ottley C., McNeill J.C.R., Logvinova A., Sobolev N.V. (2014) The sources and time-integrated evolution of diamond-forming fluids – Trace elements and Sr isotopic evidence. *Geochimica et Cosmochimica Acta*, Vol. 125, pp. 146–169, <http://dx.doi.org/10.1016/j.gca.2013.09.022>
- Kochelek K.A., McMillan N.J., McManus C.E., Daniel D.L. (2015) Provenance determination of sapphires and rubies using laser-induced breakdown spectroscopy and multivariate analysis. *American Mineralogist*, Vol. 100, No. 8-9, pp. 1921–1931, <http://dx.doi.org/10.2138/am-2015-5185>
- Kopylova M., Navon O., Dubrovinsky L., Khachatryan G. (2010) Carbonatitic mineralogy of natural diamond-forming fluids. *Earth and Planetary Science Letters*, Vol. 291, No. 1-4, pp. 126–137, <http://dx.doi.org/10.1016/j.epsl.2009.12.056>
- Koral C., Dell'Aglia M., Gaudiuso R., Alrifai R., Torelli M., De Giacomo A. (2018) Nanoparticle-enhanced laser induced breakdown spectroscopy for the noninvasive analysis of transparent samples and gemstones. *Talanta*, Vol. 182, pp. 253–258, <http://dx.doi.org/10.1016/j.talanta.2018.02.001>
- Krebs M.Y., Pearson D.G., Stachel T., Laiginhas F., Woodland S., Chinn I., Kong J. (2019) A common parentage-low abundance trace element data of gem diamonds reveals similar fluids to fibrous diamonds. *Lithos*, Vol. 324-325, pp. 356–370, <http://dx.doi.org/10.1016/j.lithos.2018.11.025>
- Krebs M.Y., Hardman M.F., Pearson D.G., Luo Y., Fagan A.J., Sarkar C. (2020) An evaluation of the potential for determination of the geographic origin of ruby and sapphire using an expanded trace element suite plus Sr–Pb isotope compositions. *Minerals*, Vol. 10, No. 5, article no. 447, <http://dx.doi.org/10.3390/min10050447>
- Lebedev V.F., Bulyga D.V., Koliadin A.V. (2020) Analysis of the impurity composition of synthetic HPHT diamonds by laser-induced breakdown spectroscopy under conditions of laser-induced surface modification. *Technical Physics Letters*, Vol. 46, No. 5, pp. 413–415, <http://dx.doi.org/10.1134/S1063785020050107>
- Liu Y., Hu Z., Li M., Gao S. (2013) Applications of LA-ICP-MS in the elemental analyses of geological samples. *Chinese Science Bulletin*, Vol. 58, No. 32, pp. 3863–3878, <http://dx.doi.org/10.1007/s11434-013-5901-4>
- McDonough W.F., Sun S.-S. (1995) The composition of the Earth. *Chemical Geology*, Vol. 120, No. 3-4, pp. 223–253, [https://doi.org/10.1016/0009-2541\(94\)00140-4](https://doi.org/10.1016/0009-2541(94)00140-4)
- McManus C.E., McMillan N.J., Dowe J., Bell J. (2020) Diamonds certify themselves: Multivariate statistical provenance analysis. *Minerals*, Vol. 10, No. 10, article no. 916, <http://dx.doi.org/10.3390/min10100916>
- McNeill J.C.R. (2011) New techniques for trace element and radiogenic isotope measurement of diamonds: Their application to diamond petrogenesis and source tracing. PhD thesis, Durham University, 281 pp.
- McNeill J.C.R., Pearson D.G., Klein-BenDavid O., Nowell G.M., Ottley C.J., Chinn I. (2009) Quantitative analysis of trace element concentrations in some gem-quality diamonds. *Journal of Physics: Condensed Matter*, Vol. 21, No. 36, pp. 364207–364220, <http://dx.doi.org/10.1088/0953-8984/21/36/364207>
- Melton G.L., McNeill J., Stachel T., Pearson D.G., Harris J.W. (2012) Trace elements in gem diamond from Akwatia, Ghana and DeBeers Pool, South Africa. *Chemical Geology*, Vol. 314-317, pp. 1–8, <http://dx.doi.org/10.1016/j.chemgeo.2012.04.025>
- Miller C.E., Kopylova M.G., Smith E.M. (2014) Mineral inclusions in fibrous diamonds: Constraints on cratonic mantle refertilization and diamond formation. *Mineralogy and Petrology*, Vol. 108, No. 3, pp. 317–331, <http://dx.doi.org/10.1007/s00710-013-0305-3>
- Navon O., Hutcheon I.D., Rossman G.R., Wasserburg G.J. (1988) Mantle-derived fluids in diamond micro-inclusions. *Nature*, Vol. 335, No. 6193, pp. 784–789, <http://dx.doi.org/10.1038/335784a0>
- Palke A.C., Saesaw S., Renfro N.D., Sun Z., McClure S.F. (2019a) Geographic origin determination of blue sapphire. *G&G*, Vol. 55, No. 4, pp. 536–579, <http://dx.doi.org/10.5741/GEMS.55.4.536>
- (2019b) Geographic origin determination of ruby. *G&G*, Vol. 55, No. 4, pp. 580–613, <http://dx.doi.org/10.5741/GEMS.55.4.580>
- Peucat J.-J., Ruffault P., Fritsch E., Bouhnik-Le Coz M., Simonet C., Lasnier B. (2007) Ga/Mg ratio as a new geochemical tool to differentiate magmatic from metamorphic blue sapphires. *Lithos*, Vol. 98, No. 1-4, pp. 261–274, <https://doi.org/10.1016/j.lithos.2007.05.001>
- Pornwilarad M.-M., Hansawek R., Shiowatana J., Siripinyanond A. (2011) Geographical origin classification of gem corundum using elemental fingerprint analysis by laser ablation inductively coupled plasma mass spectrometry. *International Journal of Mass Spectrometry*, Vol. 306, No. 1, pp. 57–62, <https://doi.org/10.1016/j.ijms.2011.06.010>
- The real value of Victor Project (2007) *Canadian Mining Journal*, January 1, <https://www.canadianminingjournal.com/featured-article/the-real-value-of-victor-project>
- Rege S., Jackson S., Griffin W.L., Davies R.M., Pearson N.J., O'Reilly S.Y. (2005) Quantitative trace-element analysis of diamond by laser ablation inductively coupled plasma mass spectrometry. *Journal of Analytical Atomic Spectrometry*, Vol. 20, No. 7, pp. 601–611, <https://doi.org/10.1039/B501374G>
- Rege S., Griffin W.L., Pearson N.J., Araujo D., Zedgenizov D., O'Reilly S.Y. (2010) Trace-element patterns of fibrous and monocrystalline diamonds: Insights into mantle fluids. *Lithos*, Vol. 118, No. 3-4, pp. 313–337, <https://doi.org/10.1016/j.lithos.2010.05.007>
- Rossi M., Dell'Aglia M., De Giacomo A., Gaudiuso R., Senesi G.S., De Pascale O., Capitelli F., Nestola F., Ghiara M.R. (2014) Multi-methodological investigation of kunzite, hiddenite, alexandrite, elbaite and topaz, based on laser-induced breakdown spectroscopy and conventional analytical techniques for supporting mineralogical characterization. *Physics and Chemistry of Minerals*, Vol. 41, No. 2, pp. 127–140, <http://dx.doi.org/10.1007/s00269-013-0631-3>
- Saminpanya S., Manning D.A.C., Droop G.T.R., Henderson C.M.B. (2003) Trace elements in Thai gem corundums. *Journal of Gemmology*, Vol. 28, No. 7, pp. 399–415.
- Schrauder M., Navon O. (1994) Hydrous and carbonatitic mantle fluids in fibrous diamonds from Jwaneng, Botswana. *Geochimica et Cosmochimica Acta*, Vol. 58, No. 2, pp. 761–771, [https://doi.org/10.1016/0016-7037\(94\)90504-5](https://doi.org/10.1016/0016-7037(94)90504-5)
- Senesi G.S. (2014) Laser-induced breakdown spectroscopy (LIBS) applied to terrestrial and extraterrestrial analogue geomaterials with emphasis to minerals and rocks. *Earth-Science Reviews*, Vol. 139, pp. 231–267, <http://dx.doi.org/10.1016/j.earscirev.2014.09.008>
- Shaw D.M. (2006) *Trace Elements in Magmas: A Theoretical Treatment*. Cambridge University Press, Cambridge, UK.
- Shirey S.B., Cartigny P., Frost D.J., Keshav S., Nestola F., Nimis P., Pearson D.G., Sobolev N.V., Walter M.J. (2013) Diamonds and the geology of mantle carbon. *Reviews in Mineralogy and Geochemistry*, Vol. 75, No. 1, pp. 355–421,

- <https://doi.org/10.2138/rmg.2013.75.12>
- Shiryaev A.A., Izraeli E.S., Hauri E.H., Zakharchenko O.D., Navon O. (2005) Chemical, optical, and isotopic investigations of fibrous diamonds from Brazil. *Russian Geology and Geophysics*, Vol. 46, No. 12, pp. 1207–1222.
- Smit K.V., Stachel T., Stern R.A. (2014) Diamonds in the Atawapiskat area of the Superior craton (Canada): Evidence for a major diamond-forming event younger than 1.1 Ga. *Contributions to Mineralogy and Petrology*, Vol. 167, No. 1, pp. 1–16, <http://dx.doi.org/10.1007/s00410-013-0962-6>
- Smit K.V., Shirey S.B., Stern R.A., Steele A., Wang W. (2016) Diamond growth from C–H–N–O recycled fluids in the lithosphere: Evidence from CH₄ micro-inclusions and $\delta^{13}\text{C}$ – $\delta^{15}\text{N}$ –N content in Marange mixed-habit diamonds. *Lithos*, Vol. 265, pp. 68–81, <http://dx.doi.org/10.1016/j.lithos.2016.03.015>
- Smit K.V., Myagkaya E., Persaud S., Wang W. (2018) Black diamonds from Marange (Zimbabwe): A result of natural irradiation and graphite inclusions. *G&G*, Vol. 54, No. 2, pp. 132–148, <http://dx.doi.org/10.5741/GEMS.54.2.132>
- Smit K.V., Stachel T., Luth R.W., Stern R.A. (2019) Evaluating mechanisms for eclogitic diamond growth: An example from Zimmi Neoproterozoic diamonds (West African craton). *Chemical Geology*, Vol. 520, pp. 21–32, <http://dx.doi.org/10.1016/j.chemgeo.2019.04.014>
- Smith E.M., Kopylova M.G., Nowell G.M., Pearson D.G., Ryder J. (2012) Archean mantle fluids preserved in fibrous diamonds from Wawa, Superior craton. *Geology*, Vol. 40, No. 12, pp. 1071–1074, <http://dx.doi.org/10.1130/g33231.1>
- Smith E.M., Shirey S.B., Nestola F., Bullock E.S., Wang J., Richardson S.H., Wang W. (2016) Large gem diamonds from metallic liquid in Earth's deep mantle. *Science*, Vol. 354, No. 6318, pp. 1403–1405, <http://dx.doi.org/10.1126/science.aal1303>
- Smith E.M., Shirey S.B., Wang W. (2017) The very deep origin of the world's biggest diamonds. *G&G*, Vol. 53, No. 4, pp. 388–403, <http://dx.doi.org/10.5741/gems.53.4.388>
- Stachel T. (2014) Diamond. In L.A. Groat, Ed., *Geology of Gem Deposits*, Second Edition, Mineralogical Association of Canada, Quebec, pp. 1–28.
- Stachel T., Aulbach S., Harris J.W. (2022a) Mineral inclusions in lithospheric diamonds. *Reviews in Mineralogy and Geochemistry*, Vol. 88, No. 1, pp. 307–391, <https://doi.org/10.2138/rmg.2022.88.06>
- Stachel T., Cartigny P., Chacko T., Pearson D.G. (2022b) Carbon and nitrogen in mantle-derived diamonds. *Reviews in Mineralogy and Geochemistry*, Vol. 88, No. 1, pp. 809–875, <https://doi.org/10.2138/rmg.2022.88.15>
- Sutherland F.L., Zaw K., Meffre S., Yui T.-F., Thu K. (2015) Advances in trace element “fingerprinting” of gem corundum, ruby and sapphire, Mogok area, Myanmar. *Minerals*, Vol. 5, No. 1, pp. 61–79, <https://doi.org/10.3390/min5010061>
- Timmerman S., Honda M., Burnham A.D., Amelin Y., Woodland S., Pearson D.G., Jaques A.L., Le Losq C., Bennett V.C., Bulanova G.P., Smith C.B., Harris J.W., Tohver E. (2019a) Primordial and recycled helium isotope signatures in the mantle transition zone. *Science*, Vol. 365, No. 6454, pp. 692–694, <http://dx.doi.org/doi:10.1126/science.aax5293>
- Timmerman S., Krebs M.Y., Pearson D.G., Honda M. (2019b) Diamond-forming media through time—Trace element and noble gas systematics of diamonds formed over 3 billion years of Earth's history. *Geochimica et Cosmochimica Acta*, Vol. 257, pp. 266–283, <https://doi.org/10.1016/j.gca.2019.05.014>
- Tomlinson E., De Schrijver I., De Corte K., Jones A.P., Moens L., Vanhaecke F. (2005) Trace element compositions of sub-microscopic inclusions in coated diamond: A tool for understanding diamond petrogenesis. *Geochimica et Cosmochimica Acta*, Vol. 69, No. 19, pp. 4719–4732, <https://doi.org/10.1016/j.gca.2005.06.014>
- Tomlinson E.L., Jones A.P., Harris J.W. (2006) Co-existing fluid and silicate inclusions in mantle diamond. *Earth and Planetary Science Letters*, Vol. 250, No. 3–4, pp. 581–595, <https://doi.org/10.1016/j.epsl.2006.08.005>
- Tomlinson E.L., Müller W., EIMF (2009) A snapshot of mantle metasomatism: Trace element analysis of coexisting fluid (LA-ICP-MS) and silicate (SIMS) inclusions in fibrous diamonds. *Earth and Planetary Science Letters*, Vol. 279, No. 3–4, pp. 362–372, <http://dx.doi.org/10.1016/j.epsl.2009.01.010>
- Watling R.J., Herbert H.K., Barrow I.S., Thomas A.G. (1995) Analysis of diamonds and indicator minerals for diamond exploration by laser ablation–inductively coupled plasma mass spectrometry. *Analyst*, Vol. 120, pp. 1357–1364, <https://doi.org/10.1039/AN9952001357>
- Weiss Y., Griffin W.L., Elhlou S., Navon O. (2008) Comparison between LA-ICP-MS and EPMA analysis of trace elements in diamonds. *Chemical Geology*, Vol. 252, No. 3–4, pp. 158–168, <https://doi.org/10.1016/j.chemgeo.2008.02.008>
- Weiss Y., Kessel R., Griffin W.L., Kiflawi I., Klein-BenDavid O., Bell D.R., Harris J.W., Navon O. (2009) A new model for the evolution of diamond-forming fluids: Evidence from microinclusion-bearing diamonds from Kankan, Guinea. *Lithos*, Vol. 112, Supplement 2, pp. 660–674, <https://doi.org/10.1016/j.lithos.2009.05.038>
- Weiss Y., Griffin W.L., Bell D.R., Navon O. (2011) High-Mg carbonatitic melts in diamonds, kimberlites and the sub-continental lithosphere. *Earth and Planetary Science Letters*, Vol. 309, No. 3–4, pp. 337–347, <https://doi.org/10.1016/j.epsl.2011.07.012>
- Weiss Y., Griffin W.L., Navon O. (2013) Diamond-forming fluids in fibrous diamonds: The trace-element perspective. *Earth and Planetary Science Letters*, Vol. 376, No. 2, pp. 110–125, <http://dx.doi.org/10.1016/j.epsl.2013.06.021>
- Weiss Y., McNeill J., Pearson D.G., Nowell G.M., Ottley C.J. (2015) Highly saline fluids from a subducting slab as the source for fluid-rich diamonds. *Nature*, Vol. 524, No. 7565, pp. 339–342, <https://doi.org/10.1038/nature14857>
- Zedgenizov D.A., Ragozin A.L., Shatsky V.S. (2007a) Chloride-carbonate fluid in diamonds from the eclogite xenolith. *Doklady Earth Sciences*, Vol. 415, No. 2, pp. 961–964, <http://dx.doi.org/10.1134/s1028334x07060293>
- Zedgenizov D.A., Rege S., Griffin W.L., Kagi H., Shatsky V.S. (2007b) Composition of trapped fluids in cuboid fibrous diamonds from the Udachnaya kimberlite: LAM-ICPMS analysis. *Chemical Geology*, Vol. 240, No. 1–2, pp. 151–162, <https://doi.org/10.1016/j.chemgeo.2007.02.003>

LGDR

GIA®

LABORATORY-GROWN DIAMOND REPORT

February 16, 2021

GIA Report Number..... 6213478953
 Identification..... Laboratory-Grown
 Shape and Cutting Style..... Square Modified Brilliant
 Measurements..... 5.58 x 5.46 x 3.98 mm

LABORATORY-GROWN DIAMOND SPECIFICATIONS*

Carat Weight..... 1.50 carat
 Color..... D
 Clarity..... SI1

ADDITIONAL INFORMATION

Polish..... Excellent
 Symmetry..... Excellent
 Fluorescence..... Medium Blue
 Inscription(s): GIA 6213478953, LABORATORY-GROWN
 Comments: "SAMPLE" "SAMPLE" "SAMPLE" "SAMPLE"
 This is a man-made diamond produced by HPHT (High Pressure High Temperature) growth process and has evidence of post-growth treatments to change the color.

PROPORTIONS

slightly
thick
-
thick

Profile is actual proportions

CLARITY CHARACTERISTICS

KEY TO SYMBOLS

Crystal Cloud Feather Natural
 Not symbols denote internal characteristics (inclusions). Some or all of these symbols denote external characteristics (blemishes).
 Diagram is an approximate representation of the diamond, and symbols show relative type, position, and approximate size of clarity characteristics. Not every characteristic may be shown. Details of clarity are not shown.

Verify this report at <https://www.gia.edu/verify>

GIA COLOR SCALE

D	E	F	G	H	I	J	K	L	M	N	O	P	Q	R	S	T	U	V	W	X	Y	Z
EXCELLENT	VERY GOOD	GOOD	FAIR	POOR																		

GIA CUT SCALE

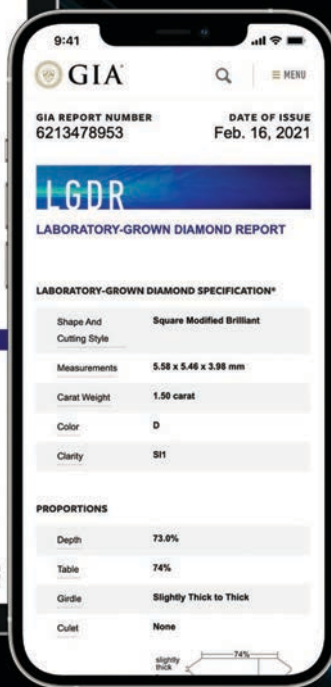
EXCELLENT	VERY GOOD	GOOD	FAIR	POOR
-----------	-----------	------	------	------

GIA CLARITY SCALE

FLAWLESS	FLAWLESS	FLAWLESS	FLAWLESS	FLAWLESS	FLAWLESS	FLAWLESS	FLAWLESS	FLAWLESS	FLAWLESS	FLAWLESS	FLAWLESS	FLAWLESS	FLAWLESS	FLAWLESS	FLAWLESS	FLAWLESS	FLAWLESS	FLAWLESS	FLAWLESS	FLAWLESS	FLAWLESS	FLAWLESS
FLAWLESS	FLAWLESS	FLAWLESS	FLAWLESS	FLAWLESS	FLAWLESS	FLAWLESS	FLAWLESS	FLAWLESS	FLAWLESS	FLAWLESS	FLAWLESS	FLAWLESS	FLAWLESS	FLAWLESS	FLAWLESS	FLAWLESS	FLAWLESS	FLAWLESS	FLAWLESS	FLAWLESS	FLAWLESS	FLAWLESS

*This GIA Laboratory-Grown Diamond Report describes color and clarity specifications on the same scale as the GIA Diamond Grading Report for natural diamonds. The specifications do not correlate to nature's continuum of clarity. To learn more about laboratory-grown diamonds, including how GIA differentiates them from natural diamonds, scan the QR code or visit www.gia.edu/LGDR.

This report is not a guarantee or valuation. For additional information and important limitations and disclosures, please see GIA's Laboratory-Grown Diamond Report. For more information, please contact GIA at 1-800-421-7229 or visit www.gia.edu.



LGDR by  **GIA®**



©2022 GIA. GIA® and the GIA logo are registered trademarks of Gemological Institute of America, Inc.

SAPPHIRE BENEATH THE RICH BLACK SOIL OF MULING, NORTHEASTERN CHINA

Yimiao Liu and Ren Lu

The rich black soil of Muling in northeastern China yields not only abundant crops but also glittering gem corundum. In this study, gemological quality and characteristics and provenance-related features of sapphire from Muling are first reported with comprehensive analytical results. Muling sapphire exhibits a wide spectrum of hue and saturation. Mineral inclusions (e.g., rutile, zircon, anorthite, and pyrope) as well as other distinctive internal features (e.g., polysynthetic twinning accompanied by intersecting tubes, iridescent hexagonal thin films, and angular color zoning) are identified by microscopic observation and Raman spectroscopy. Spectral features and trace element chemistry of the various colors of gem-quality Muling sapphire are analyzed by ultraviolet/visible/near-infrared spectroscopy and laser ablation–inductively coupled plasma–mass spectrometry. To assess the characteristics of Muling sapphire against well-known corundum sources worldwide, inclusion analysis and trace element discrimination diagrams are utilized. Analytical results indicate that Muling sapphire originated from a more diverse geological environment than typical magmatic or metamorphic origin. The Muling deposit shows great potential to produce fine gem-quality sapphire material.

China has become a strong force in both production and consumption of gems and jewelry in the past two decades, and it is the fastest-growing consumer market for fine gemstones. Chinese consumers have led the positive growth trend in the global luxury market and are on track to claim the largest share of the market by 2025, according to a Bain & Company study (Lannes and Zhang, 2020). Awareness of colored stones—particularly the classic “big three” of ruby, sapphire, and emerald—has reached unprecedented heights in China in less than a decade.

Despite its diverse geographic and geological landscapes, China has not been known historically as a producer of fine-quality gems such as ruby and sapphire. The only source of Chinese sapphire known to much of the world is Shandong, where large and clean but oversaturated blue sapphire is mined. During the 1980s and 1990s, other Chinese sources were also reported, mostly domestically, in-

cluding Penglai in Hainan Island and Mingxi in Fujian Province (all along the east coast of China) and described as classic magmatic sapphire deposits (Keller and Keller, 1986; Keller and Wang, 1986; Wang, 1988; Guo et al., 1992). Attempts to lighten the sapphire’s color from inky blue to a more marketable color (Wang et al., 1992; Cheng et al., 2009) have been unsuccessful. This Chinese sapphire material was therefore considered of little economic value on the global gem market. The situation is similar with ruby production. Ruby has been reported from the Ailaoshan area in Yunnan Province and the Xinjiang Uyghur Autonomous Region with little specific description of its quality or gemological characteristics (Galibert and Hughes, 1995; J. Zhang et al., 2003; Huang et al., 2021). The perception from such reports is that sapphire and ruby from China is not of fine quality.

The perceived scarcity of domestic gem resources in China motivated the authors to investigate identified corundum deposits for their potential. One is the Muling area, which lies on an exceptionally fertile black soil region (Sorokin et al., 2021). Our research reveals that hidden beneath this rich black soil is an underexplored resource of sapphire (figure 1).

See end of article for About the Authors and Acknowledgments.

GEMS & GEMOLOGY, Vol. 58, No. 3, pp. 290–317,

<http://dx.doi.org/10.5741/GEMS.58.3.290>

© 2022 Gemological Institute of America



Figure 1. These Muling sapphires (0.1–8.2 ct) in a variety of shapes and cuts demonstrate the full range of hue, saturation, and clarity coming from this deposit. Photo by Ren Lu.

Reports about Muling's mineral resources are limited compared with those about other Chinese corundum deposits. Su (1990) first reported sapphire production in this area. Galibert and Hughes (1995) also mentioned the deposit briefly. Jianxun Sun, who worked on a geological survey of Heilongjiang Province, published studies about the geological characteristics of corundum deposits in this region (Sun et al., 2005) and documented the mineralogical features of Muling sapphire from a geological perspective (Sun, 1995). Qiu et al. (2007) investigated the geological background of Muling by analyzing zircon megacrysts. Chen et al. (2011, 2013) studied the gemological features of gem-quality zircon and garnet. However, no publication has drawn conclusions about the quality and the provenance-related characteristics of Muling sapphire.

The present authors began systematic studies of Muling sapphire in 2014 and previously provided a brief introduction in *G&G* (Liu and Lu, 2016). Au-

thor RL's research team studied gem-quality megacrysts (garnet, clinopyroxene, and orthopyroxene) hosted by the Cenozoic alkali basalts in the

In Brief

- The Muling deposit, in Heilongjiang Province of northeastern China, produces fine sapphire material.
- Muling sapphire exhibits a wide variety of hues and saturations.
- Muling sapphire originated from a more diverse geological environment than typical magmatic or metamorphic origin.

Muling area, providing more information on the parental magmatic systems of this area (Hu et al., 2022). The comprehensive gemological features and



Figure 2. Geographic map of reported corundum occurrences in China. The red marker on the upper right represents the Muling area.

advanced analysis of Muling sapphire, including preliminary data to aid in origin determination, will be presented in this article.

GEOGRAPHY AND HISTORY

Muling, with a population of 320,000, is a very small community by Chinese standards. It lies in eastern Heilongjiang Province, near the Chinese-Russian border (figure 2). The Muling River flows through this mountainous city from north to south. Although small, Muling plays an important role. Located on exceptionally fertile land covered with black soil, the area has been referred to as the country's "grain basket" (Gu et al., 2018) (figure 3). Muling is famous for its richness in natural resources, with a saying of "Two yellow, two black, and one treasure." This refers to golden and yellow sun-cured tobacco ("two yellow"), coal and graphite ("two black"), and gemstones ("one treasure"). With the adjoining city of Suifenhe as one of the largest Sino-Russian centers, all of these products can be shipped across the country by highway. Although the high-latitude cold climate limits human activities, it protects the natural environment and wild animals. Muling is part of the Northeast China Tiger and

Figure 3. A vast expanse of brightly colored marigolds in a field of black soil in the Muling region. The gem-producing region lies in the distance. Photo by Ren Lu.





Figure 4. This photo of the Muling sapphire deposit, taken in April 2018, shows the trommel left unused. In this area, mining operations must cease for more than half the year because of freezing temperatures. The authors visited the mining site in June 2018, when weather conditions permitted mining activities. Photo by Aijun Yi.

Leopard National Park. These precious animals are listed on the International Union for Conservation of Nature (IUCN) Red List of Threatened Species (Miquelle et al., 2011), and their populations are even rarer than that of the giant panda. A rugged, warm, and generous character defines the people who live here.

The name *Muling* is a transliteration of a Manchurian word to contemporary Mandarin Chinese that means “horse breeding farm.” According to local annals (Editorial Committee of Muling, 1989), it was reserved as a “royal forbidden area” and served as a horse range for the royal army in the Qing Dynasty (1636–1912 CE). This pristine region was untouched until World War II. After the establishment of the People’s Republic of China in 1949, new geological surveys targeting strategic ore deposits began throughout the country. Potential gem resources in the Muling area were originally recorded in these geological reconnaissance surveys. But it was not until the late 1980s that the public took notice. A series of studies were conducted by the Geo-

logical Survey of Heilongjiang Province to search for gem resources.

Starting in the late 1990s, Muling attracted the attention of gem traders from Thailand, who forged an agreement with the local government and brought in mining machinery. One of the machines was left in Muling and is still fully functional today (figure 4). Aijun Yi, former director of the mineral resource administration in Muling, participated in cooperative exploitation. This cooperation continued until 2002, and he recalled that the total production of corundum during official mining activities from the late 1990s to 2002 was 10,000 carats (Yi A., pers. comm., 2018). After that, commercial mining activities ceased until small-scale mining was carried out by a domestic mining company for a few months in 2017. Due to the policy of prime farmland preservation, however, there is no mining in Muling as of the time of this writing. Local farmers usually collected gemstones such as corundum, garnet, and feldspar from the low-lying area downstream from the mountains, which is said to abound with precious stones.



Figure 5. Author YL sits on one of the local basalt columns measuring over 50 cm in diameter. Photo by Ren Lu.

GEOLOGICAL SETTING

Northeastern China belongs to the eastern segment of the Central Asian Orogenic Belt, which lies between the North China Craton and the Siberian Craton (Wilhem et al., 2012). This area underwent the tectonic evolution of the amalgamation during the Paleozoic (Wang et al., 2019), overprinted by circum-Pacific tectonic events since the early Mesozoic (Feng et al., 2019; Li et al., 2020), and then entered a phase of the extensive eruption of Cenozoic basalts (Pan et al., 2015). The Muling area lies at the northern section of the Dunhua-Mishan fault, a large thrust fault trending N50°E (Wang and Dou, 1997). The Dunhua-Mishan fault is a branch of the northern part of the N-S trending Tan-Lu fault (Wang et al., 2001; Y.Q. Zhang et al., 2003; Ling et al., 2017), cutting through the Shenyang, Dunhua, and Mishan areas and extending into Russia (Ling et al., 2017). The Tan-Lu fault is a classic example of lithospheric extension between the Xingmeng Orogenic Belt and

the Pacific subduction zone (Qiu et al., 2007; Ling et al., 2017).

The corundum-related rocks in the Muling area belong to Tertiary basalts, including dense massive olivine basalt, basaltic pumice, amygdaloidal basalt, and taxitic basalt (figure 5; Sun et al., 2005). Dayan Ridge was the main mining site operated by miners from Thailand, producing large amounts of sapphire of almost all colors as well as a small quantity of ruby material. Another mine is found in the small village of Guangming. Villagers can occasionally find high-quality rough (mainly ruby). Other places such as Li Mountain, Gangouzi, and Hanconggou are also accessible for villagers to collect rough gems (figure 6). These occurrences are all secondary deposits derived from basalts, which are regarded as the gem carrier (Sun, 1995). During the weathering process, heavy minerals are concentrated, including corundum, zircon, spinel, magnetite, ilmenite, augite, garnet (almandine, pyrope), and hematite.

MATERIALS AND METHODS

Samples. For this study, a few thousand pieces of rough corundum were gathered during and after the authors' three field trips to Muling between 2014 and 2018. More than 70% of these samples were donated by Mr. Yi, a lifelong resident who surveyed the Muling region throughout his career. The authors found 20% of the stones from the remnants of the Dayan Ridge deposit mined in the 1990s. Around 5% of the samples with high gem quality were purchased from local farmers through Mr. Yi, especially red samples (again, see figure 1).

From our few thousand pieces of rough, 1,030 were grouped according to color (see figures 7 and 8). Of these, 311 polished samples were used for more detailed studies. The 311 stones were grouped according to color: the red group ("R," including all samples with a dominant red hue—including pink, orangy pink, purple, and purplish red), the light blue group ("LB"), the deep blue group ("DB"), the yellow group ("Y"), and the green group ("G").

The subsequent naming convention for samples is color coded (e.g., DB2 for deep blue sample no. 2). Near-colorless sapphires are not discussed in this

paper. The analysis and discussion of low-saturation materials, including near-colorless sapphires, will be presented in a separate study.

After visually and microscopically examining all samples, 311 stones with suitable size (0.5–3.0 ct) were selected, covering a full range of color and not affected by open fissures. Of those, 115 were faceted and 196 were doubly polished into wafers for detailed gemological observation and spectroscopic analysis. In addition, 77 samples were analyzed for trace element compositions. These samples were chosen from polished samples of each color group with variations in hue and saturation. Sample numbers of both faceted and wafer sets can be seen in table 1. Among all wafers, only those with desirable optical homogeneity underwent a complete set of spectroscopic and *in situ* trace element chemical analysis. Most of the visually transparent and homogeneous crystals were further found to exhibit various levels of twinning structures when illuminated under cross-polarized light. Wafers that were optically near perfect or only contained minor optical imperfections were also analyzed for a relatively complete set of spectroscopic characterizations of each color group of samples.

Figure 6. Geological map of corundum deposits in Muling, captured from a 1:200,000 geological map. Modified after Sun (1995).

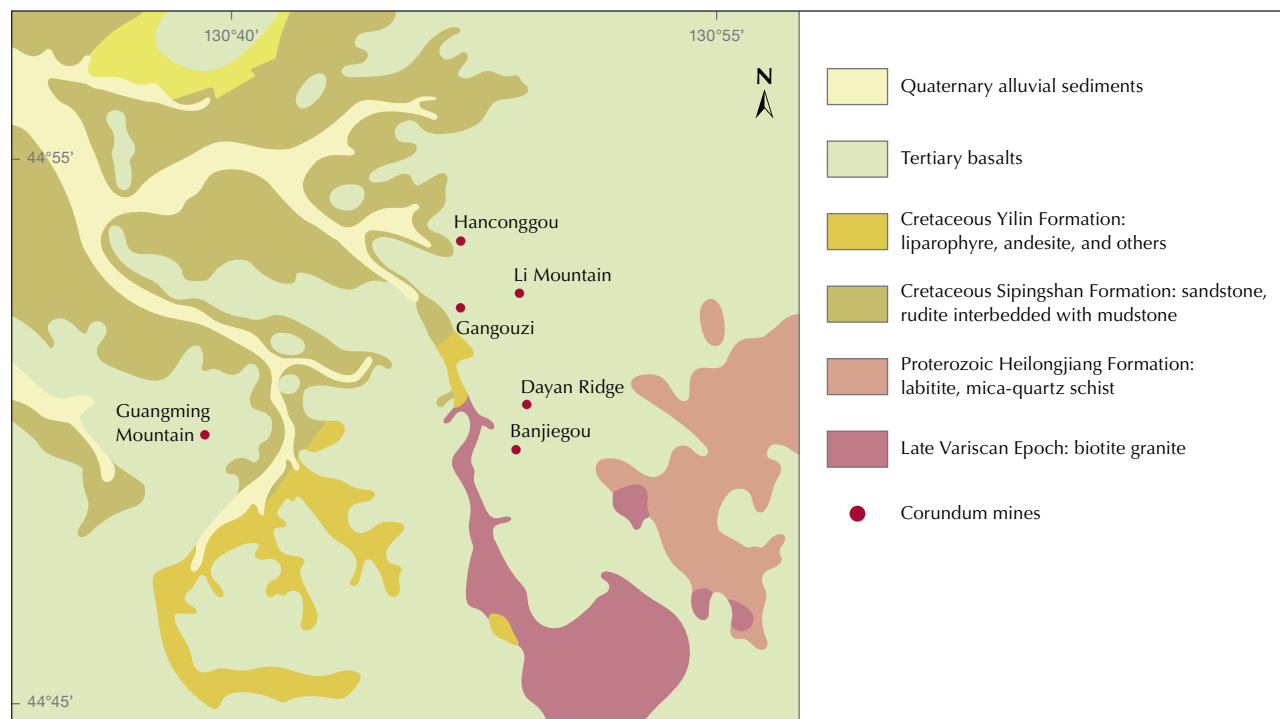


TABLE 1. Number of faceted and wafer samples from each color group of gem corundum from Muling, China.

Color group	Red ^a	Light blue	Deep blue	Yellow	Green	Total number
Wafers	78	43	52	13	10	196
Faceted stones	34	29	36	10	6	115
Wafers for trace element analysis	27	12	17	6	5	67
Faceted stones for trace element analysis	4	1	3	1	1	10

^aThe red group includes pink, orangy pink, purple, and purplish red.

Standard Gemological Testing. Standard gemological testing was performed at the gemological laboratory of the Gemmological Institute, China University of Geosciences in Wuhan. An optical duplex gem refractometer was used to measure the refractive index and birefringence of the polished stones. Fluorescence was observed with long- and short-wave UV lamps (365 and 254 nm, respectively) in a darkened room. Specific gravity was determined hydrostatically with an electronic balance.

Photomicrography. Internal features of the 311 polished wafer and faceted samples were observed and recorded under different magnifications with a Leica M205 A camera and a LAS V4.12 system. Various illuminations including darkfield, brightfield, diffused, and oblique, together with a fiber-optic light source, were utilized as necessary.

Raman Spectroscopy. To identify mineral inclusions, Raman spectra of all 311 samples were obtained at the gemological laboratory of the Gemmological Institute, China University of Geosciences in Wuhan, using a Bruker Senterra R200-L Raman spectrometer fitted with a 532 nm laser and magnifications of 20× and 50×. The laser power was set at 10 mW. The spectra were collected in the confocal mode with a spectral resolution of 5 cm⁻¹ and an integration time of 20 s. The accumulation was set at 5 times until the signal-to-noise ratio of the spectra was above 10. Calibration was performed using the 520.5 cm⁻¹ line of a silicon wafer. In all cases, the RRUFF database (rruff.info; Lafuente et al., 2015) was referenced when identifying inclusions.

FTIR Spectroscopy. To detect potential trace-level hydrogen in gem corundum and hydrous mineral inclu-

sions, Fourier-transform infrared (FTIR) spectroscopy was performed on all 196 wafered samples using a Bruker Vertex 80 spectrometer equipped with a Hyperion 3000 microscope and a combination of beam splitters and detectors for the mid- to near-infrared ranges (7000–400 cm⁻¹). The magnification of the objective lens was 15×. The spectral resolution was set at 2 cm⁻¹ with 64 accumulations.

UV-Vis-NIR Spectroscopy. To illustrate the major chromophores' features, 196 doubly polished wafers covering the main color groups—red (including pink, orangy pink, purple, and purplish red), light blue, deep blue, yellow, and green—were analyzed with ultraviolet/visible/near-infrared (UV-Vis-NIR) spectroscopy using a PerkinElmer 650s spectrometer with a 150 mm integrating sphere accessory. To further clarify the quantitative relationship between trace elements and spectral absorption, samples were further screened and prepared to obtain UV-visible spectra in a more focused sampling area. UV-Vis-NIR spectra were collected using a JASCO MSV-5200 spectrometer equipped with a microscope and a 16× objective. The sampling area of 400 μm diameter covered the same area as the laser spots resulting from laser ablation–inductively coupled plasma–mass spectrometry (LA-ICP-MS) analysis. Spectra were collected in the 300–1500 nm range. The spectral resolution was 0.1 nm with a scan speed of 200 nm/min.

Four deep blue sapphires with high clarity and no noticeable twinning structures (DB2, DB12, DB31, and DB35) were prepared as oriented wafers (perpendicular to the *c*-axis) and further studied for spectra in both orientations and for *in situ* chemical analysis. The optical qualities of samples in other color groups were affected by twinning to various degrees. Samples

with moderate or minor twinning were selected and cut into wafers for the analysis of microscopic-scale submillimeter spectroscopy and trace element chemistry. Efforts were made to obtain fully oriented spectra. However, the optical conditions of the crystals did not allow us to precisely determine the orientation of each optic axis due to the twinning. For the red and light blue groups, partially oriented spectra (o-ray) of nine samples were obtained (sample nos. R5, R12, R20, R28, R41, LB3, LB7, LB19, and LB29). For the yellow and green group samples, partial or non-oriented spectra were obtained (sample nos. Y3-7 and G1-5).

The absorbance was first corrected by subtracting the loss of multiple reflections. The Sellmeier equation for corundum was performed to determine a given sample's refractive index and calculate all the reflections between the two surfaces (Tatian, 1984). Except for reflection, the internal scatter of inclusions (Lu, 2012) may impact the spectral baseline of natural corundum samples, unlike the high-purity synthetic corundum materials. Considering the potential near-infrared absorption centered at 880 nm, the spectral baseline was then corrected by subtracting the spectral offset at 1500 nm, where the chromophore's features were insignificant. The spectroscopic data was converted to show absorption coefficient (α , cm^{-1}) using $\alpha = 2.303A/d$, where A is absorbance and d is the path length in centimeters.

Trace Element Analysis. LA-ICP-MS analysis was carried out at the State Key Laboratory of Geological Processes and Mineral Resources, China University of Geosciences in Wuhan. The instrument used was an Agilent 7500 ICP-MS combined with a GeoLas 193 nm laser. Laser ablation conditions included a 44 μm diameter laser spot size, a fluence of 12 J/cm^2 , and a 6 Hz repetition rate. Each analysis incorporated a background acquisition of approximately 20 s (gas blank), followed by 50 s of main acquisition time and 30 s of washout phase. Three spot analyses were performed on each sample. The widely used quantitative calibration standards of National Institute of Standards and Technology (NIST) glass SRM 610 and U.S. Geological Survey (USGS) synthetic glasses BCR-2G, BHVO-2G, and BIR-1G (Jochum et al., 2005) were used as reference materials. The preferred values of element concentrations for the USGS reference glasses are from the GeoReM database (<http://georem.mpch-mainz.gwdg.de>). Each analysis was first normalized by aluminum, and then a time-drift correction was applied using a linear interpolation (with

time) for every nine analyses according to the variations of SRM 610 (Liu et al., 2008). Offline selection, integration of background, analyte signals, and quantitative calibration were performed by ICPMSDataCal (Liu et al., 2008).

Units of ppmw and ppma were both used for the trace element content in this study. The unit ppmw was applied in the discrimination diagrams. One ppmw means that there is one microgram of trace element in one gram of crystal. The unit ppma was applied to discuss the impact of trace elements on coloration. One ppma means that there is one trace element atom for every million atoms of the host crystal (Emmett et al., 2003).

RESULTS

Sample Grouping Rules. Grouping of samples was mainly based on dominant chromophore series: Cr^{3+} for red (including pink, orangy pink, purple, and purplish red), $\text{Fe}^{2+}\text{-Ti}^{4+}$ pair for blue, and Fe^{3+} for yellow. Samples in the $\text{Fe}^{2+}\text{-Ti}^{4+}$ series were further divided into light and deep blue, which exhibited differences in their crystal morphology and inclusion scenes and suggested differences in geological formation processes. Samples with Fe^{3+} and combined chromophores of Fe^{3+} and $\text{Fe}^{2+}\text{-Ti}^{4+}$ were separated into yellow and green categories, respectively. Analytical data from spectroscopy and trace element chemistry are presented following the above chromophore categories.

Gemological Properties. The Muling gem corundum samples in this study covered a wide spectrum of hue, encompassing blue, green, yellow, and red series (including pink, orangy pink, purple, and purplish red) and saturation ranging from light to deep. Samples were divided into five groups according to the grouping rules above. Deep blue sapphire refers to those with a strong saturation (e.g., the faceted blue sapphire in the bottom center of figure 1). By contrast, the light blue sapphire material had lower saturation and high transparency. Other color groups (red, yellow, and green) were within a narrower range of saturation than the spread between the deep blue and light blue groups. In addition to the grouping mentioned above, there were a few distinctively bi-color samples (less than 0.1%) that combined deep blue and yellow within a single stone.

Samples in the different color groups generally displayed distinct crystal morphology. Samples with high saturation (i.e., those in the deep blue group and the green group, and the very few deep blue and yellow



Figure 7. Rough stones from Muling, representing the five color groups from this study: two light blue sapphires (top left), four deep blue sapphires (bottom left), seven from the red group (including pink and purple samples; right), one green sample (bottom center), and one yellow sample (bottom right). The deep blue sapphires displayed well-developed barrel or tabular crystal shapes and predominantly hexagonal prisms. The light blue sapphires showed rounded shapes and erosion surfaces, while the red group consisted mainly of broken pieces with erosion surfaces or tabular crystals. The green and yellow samples were all broken pieces. Photo by Yimiao Liu.

low bicolor samples) showed little effect from weathering and appeared mainly as broken pieces with relatively sharp edges or retained their original crystal shapes. Most of the deep blue rough exhibited euhedral and subhedral crystal shapes (such as barrel or tabular) with hexagonal prisms as the dominant crystal form (figure 7). Some showed six-ray trapiche patterns. The red group samples mainly displayed tabular rounded morphology, while a few showed a euhedral hexagonal shape. For the light blue and yellow groups, the rough stones usually exhibited erosion surfaces with rounded shapes.

Among all the samples collected from Muling, the largest rough stone reached 51 ct (a deep blue sample), with the weight of most stones in the 1–3 ct range. The calculated proportions for each color group are provided in figure 8. The red group samples (including pink, orangy pink, purple, and purplish red) made up the largest proportion of all Muling gem

corundum, at 57%. Light blue and deep blue sapphires accounted for 15% and 16%, respectively. Yellow sapphires made up 6% of all samples, and green sapphires accounted for 3% (figure 8).

PROPORTION OF MULING GEM CORUNDUM BY COLOR

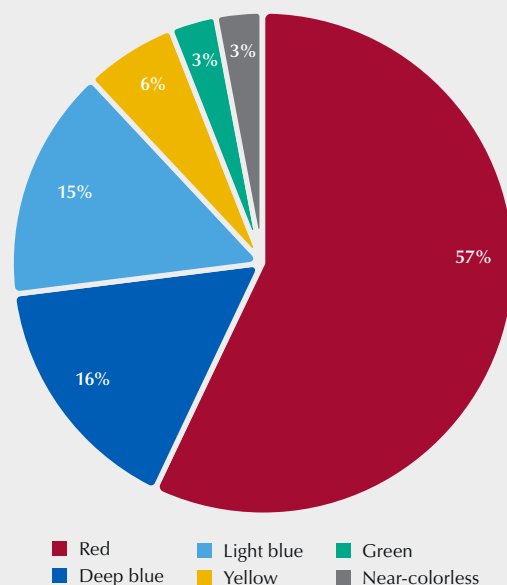


Figure 8. A pie chart of the five color groups (plus near-colorless) among the randomly selected ~1,030 Muling corundum samples. Among them, the red group (pink, orangy pink, purple, and purplish red) has the largest share, with 57%. Deep blue and light blue samples account for 16% and 15%, respectively. The rest consist of yellow, green, and near-colorless samples (6%, 3%, and 3%, respectively).

TABLE 2. Gemological characteristics of studied wafer and faceted gem corundum samples from Muling, China.

Color group		Red ^a	Light blue	Deep blue	Yellow	Green
Number of samples		112	72	88	23	16
Transparency		Transparent to semitransparent	Transparent to semitransparent	Transparent to semitransparent	Transparent	Transparent
Refractive index	n _o	1.758–1.760	1.758–1.760	1.760–1.762	1.759–1.762	1.760–1.762
	n _e	1.769–1.771	1.768–1.771	1.768–1.770	1.768–1.770	1.768–1.770
Birefringence		0.008–0.009	0.008–0.010	0.008	0.008	0.008
Dichroism		Medium: pink to purplish red	Medium: light blue to blue	Strong: blue to greenish blue	Weak: yellow to colorless	Strong: green to bluish green
Specific gravity		3.99–4.00	3.97–4.12	3.98–4.00	3.97–4.10	3.97–4.05
Fluorescence		Long-wave: Medium red Short-wave: Weak red	Inert	Inert	Inert	Inert

^aThe red group includes pink, orangy pink, purple, and purplish red.

Gemological characteristics by color group are summarized in table 2. The sample clarity ranged from transparent to semitransparent. Those crystals with high clarity and desirable color exhibited obvious commercial potential after cutting (again, see figure 1). Refractive index ranged from 1.760 to 1.769, and specific gravity was around 4.0 ± 0.2 . Samples in the red group showed medium red fluorescence under long-wave UV radiation and weak red under short-wave UV. Other color groups were inert under both long-wave and short-wave UV.

Internal Features. Representative photos were chosen to exhibit both common and rare internal features of the Muling sapphire after thoroughly examining the 311 faceted and wafer samples and documenting their microscopic characteristics.

Microscopic examination combined with Raman spectroscopy revealed various mineral inclusions such as rutile, zircon, anorthite, and pyrope. Rutile needles were the most common mineral inclusion, occurring in a short arrowhead shape and displaying iridescence along certain orientations (see figure 9;

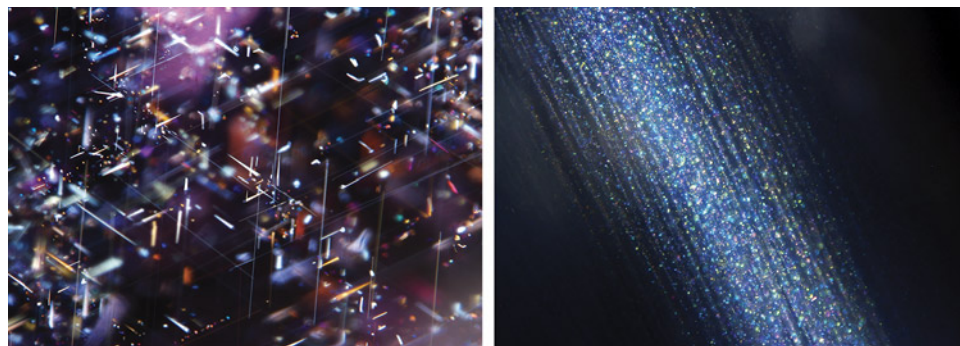


Figure 9. Left: Long silk and short arrowhead needles in a pink sapphire, at 60°/120° angles. Right: Densely packed reflective particles in a light blue sapphire observed under oblique illumination. Photomicrographs by Yimiao Liu; fields of view 0.98 and 1.56 mm, respectively.

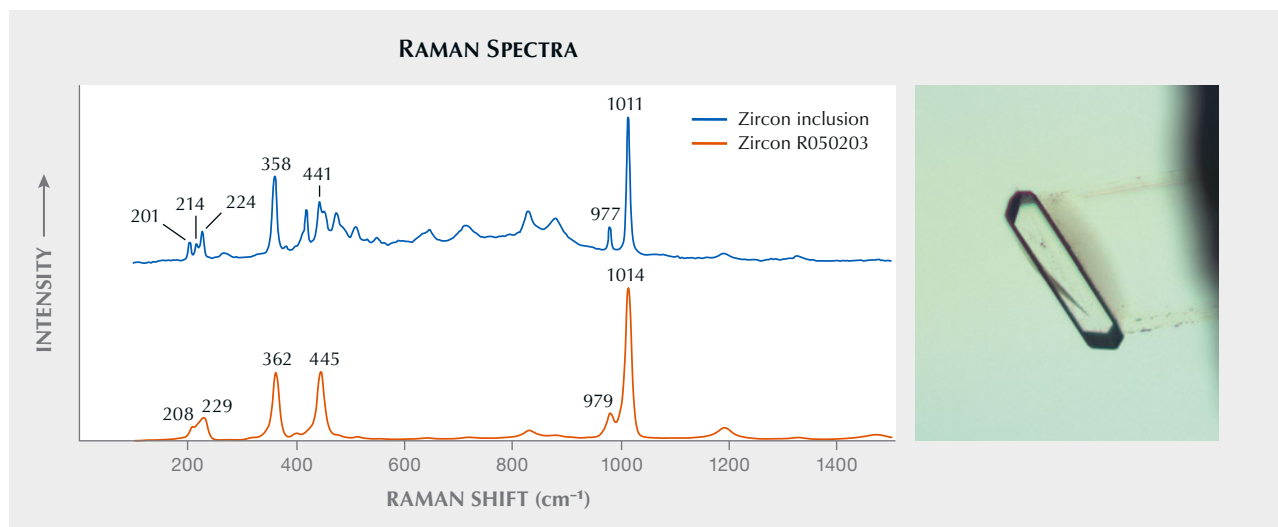


Figure 10. The Raman spectrum of a zircon inclusion in a deep blue sapphire sample matched the reference spectrum for zircon in the RRUFF database. Spectra are offset vertically for clarity. The inclusion is shown in the inset photo. Photomicrograph by Yimiao Liu; field of view 0.31 mm.

this inclusion image comes from the top middle purple sapphire in figure 1). Long silk was also common in Muling sapphire.

Zircon inclusions were occasionally encountered in deep blue sapphire. These were transparent, well-developed prismatic crystals (figure 10), typically isolated and rarely clustered. Most of them measured up to 200 μm long.

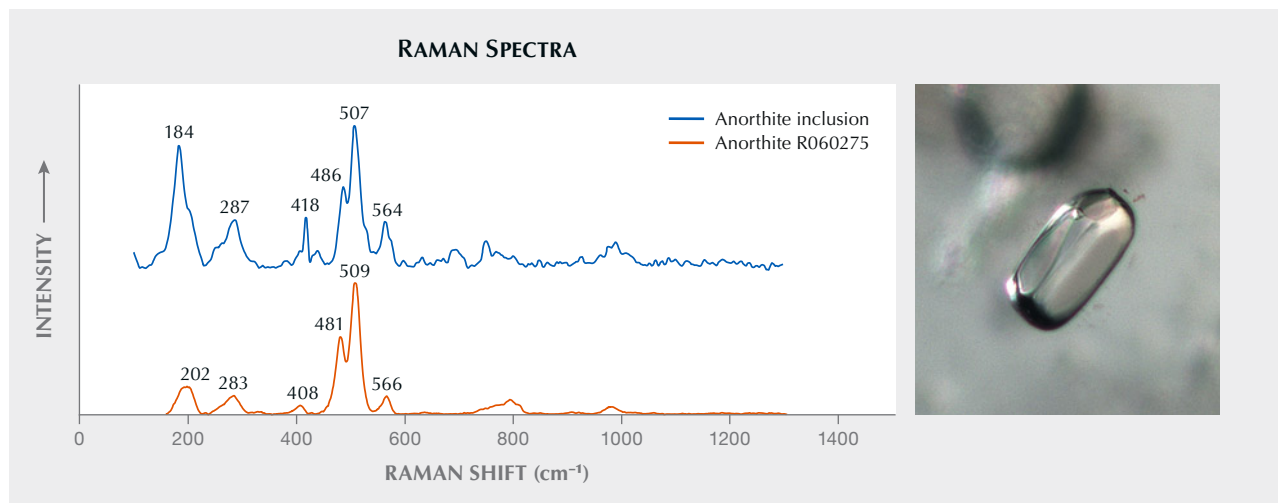
Prismatic and rounded, transparent calcium-rich plagioclase crystals (whose Raman spectra matched with anorthite) were discovered in a number of light

blue sapphires (figure 11). Both the mineral identity and crystal morphology suggest a protogenetic origin (Koivula and Fryer, 1987).

Garnet, identified by Raman spectroscopy as pyrope, rarely occurred as an inclusion and was only observed in two stones from the red group and one from the yellow group, all with well-developed crystal forms (figure 12). The size measured up to 200–300 μm .

An unusual multicomponent inclusion was discovered in one purplish red sample. Micro-sized clus-

Figure 11. The Raman spectrum of an anorthite crystal inclusion observed in a Muling light blue sapphire matched the reference spectrum for anorthite in the RRUFF database. Spectra are offset vertically for clarity. The inclusion is shown in the inset photo. Photomicrograph by Yimiao Liu; field of view 0.20 mm.



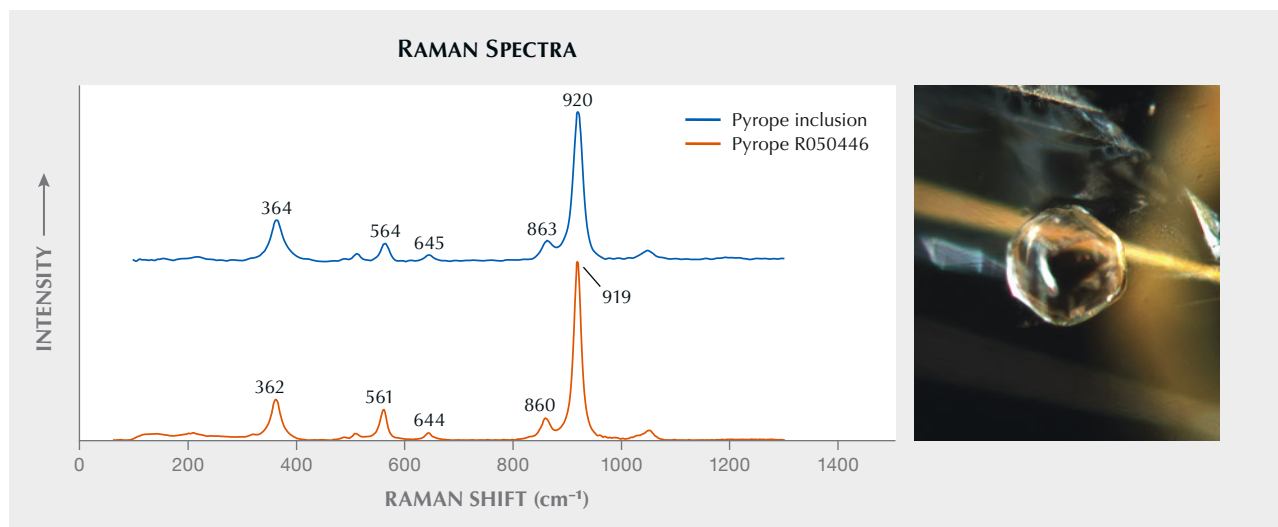
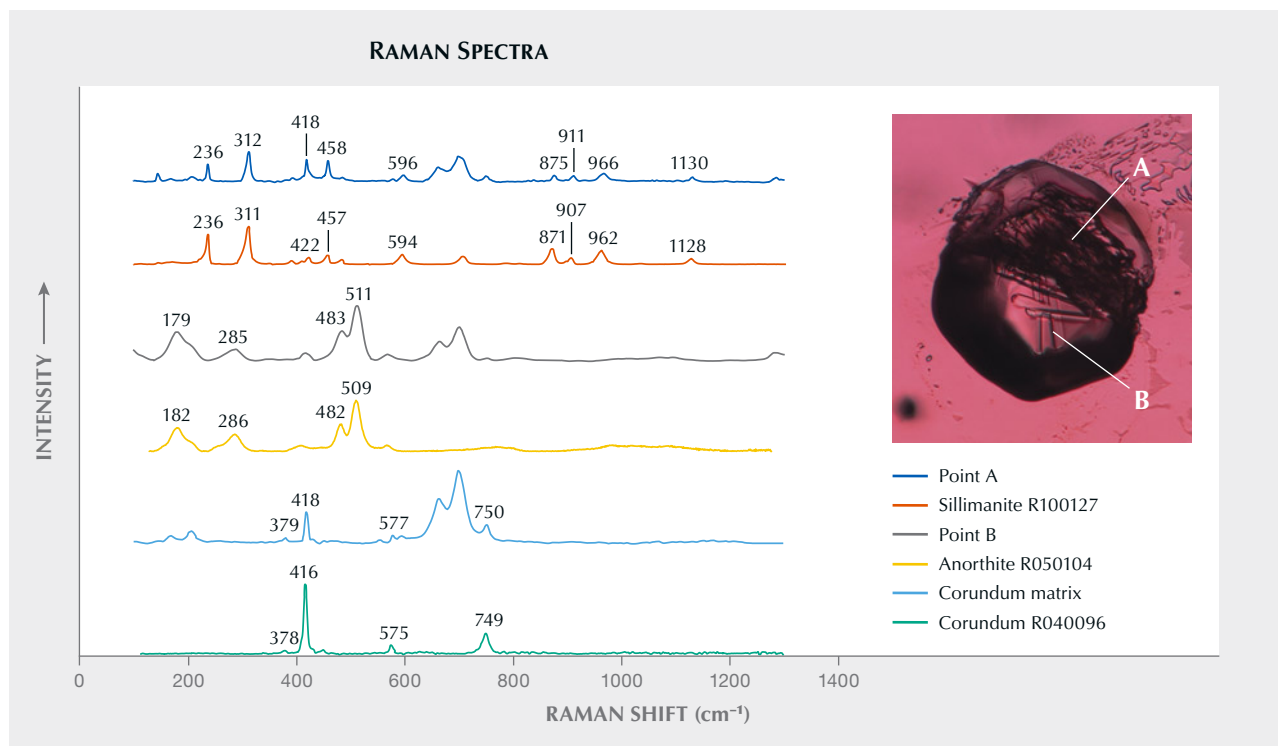


Figure 12. The Raman spectrum of a garnet inclusion observed in a Muling yellow sapphire matched the reference spectrum for pyrope in the RRUFF database. Spectra are offset vertically for clarity. The inclusion is shown in the inset photo. Photomicrograph by Yimiao Liu; field of view 0.59 mm.

ters of crystals arranged in different orientations were observed inside a hexagonal negative crystal (figure

13). Various clusters had different Raman spectra. The spectra for points A and B matched with sillimanite

Figure 13. The Raman spectra of a multicomponent inclusion observed in a Muling purplish red sample, identified using Raman spectroscopy and referencing the RRUFF database. Spectra are offset vertically for clarity. The spectrum of point A matched sillimanite, while point B matched anorthite. Double peaks near 700 cm^{-1} were present in the corundum matrix and in the other regions of this corundum sample and are not from inclusions. The inclusion is shown in the inset photo. Photomicrograph by Yimiao Liu; field of view 0.15 mm.



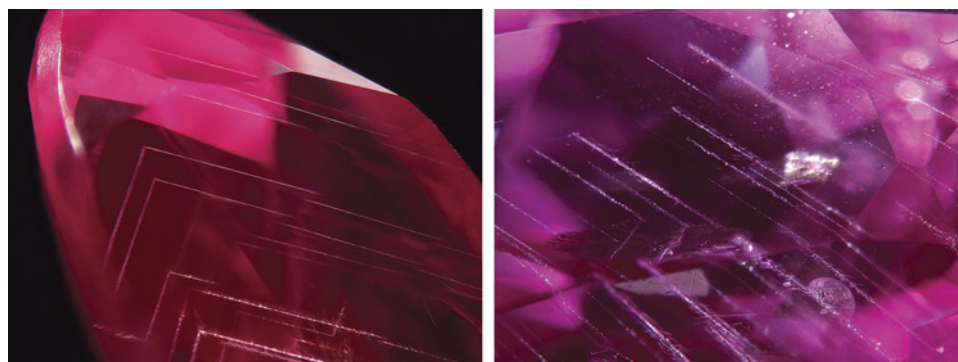


Figure 14. Left: Unidentified whitish linear inclusions intersect in an angular-shaped pattern in a Muling purple sample; field of view 3.16 mm. Right: A pink sapphire showed sub-parallel dotted lines with fringes; field of view 3.25 mm. Photomicrographs by Yimiao Liu.

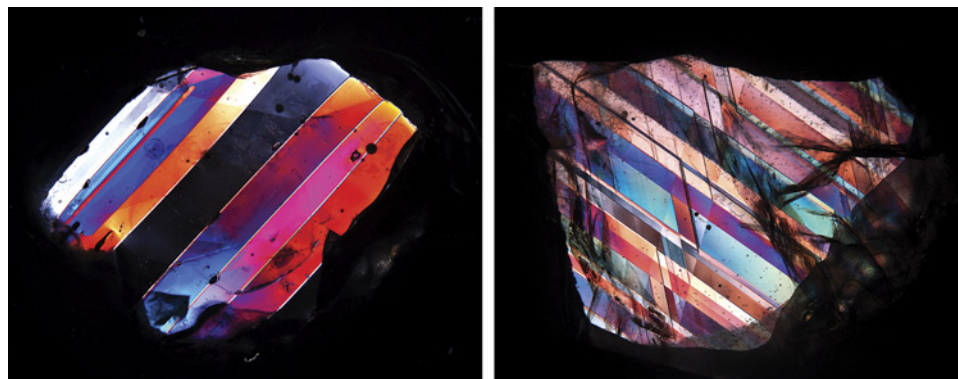


Figure 15. Left: Between crossed polarizers, this purple sample shows polysynthetic twinning. The inner-lamellar spacing measured ~0.9 mm. Right: A doubly polished purple sapphire wafer shows two sets of twinning planes with a 54° angle under cross-polarized light. Photos by Yimiao Liu.

and anorthite, respectively. These two cluster types were most likely daughter minerals that crystallized from the included fluids as temperature decreased.

Whitish linear inclusions were frequently observed in red and light blue samples. They occurred in specific directions: subparallel or intersecting with

each other (figure 14). Magnification showed dotted lines with fringes (figure 14, right). These linear features were not positively identified by FTIR and Raman spectroscopy. Polysynthetic twinning was also common in red and light blue samples (figure 15). Under cross-polarized light, multiple sets of twinning sometimes intersected with each other where linear inclusions occurred along the intersections (figure 15, right).

There are some other notable internal features in Muling sapphire. Angular color zoning was observed only in deep blue sapphire (figure 16), which has not been observed in the other color groups.

Thin films occurred in both green and light blue sapphires (figure 17). Their hexagonal shapes or angular iridescent patterns were closely related to the crystallographic symmetry of the host sapphire. All of the thin films reflected light at the same time because the crystal planes were identically oriented. Most were accompanied by a round elongated inclusion in the center. However, Raman spectroscopy failed to positively identify this type of inclusion.

Fissures and fingerprints as secondary inclusions were usually observed in the edge area of rough stones (figure 18, left). Triangular growth features were also common on the surfaces of samples from all color groups (figure 18, right).

Figure 16. Well-defined hexagonal color zones in this deep blue stone indicate the crystallization process of the host sapphire. Photomicrograph by Yimiao Liu; field of view 3.94 mm.



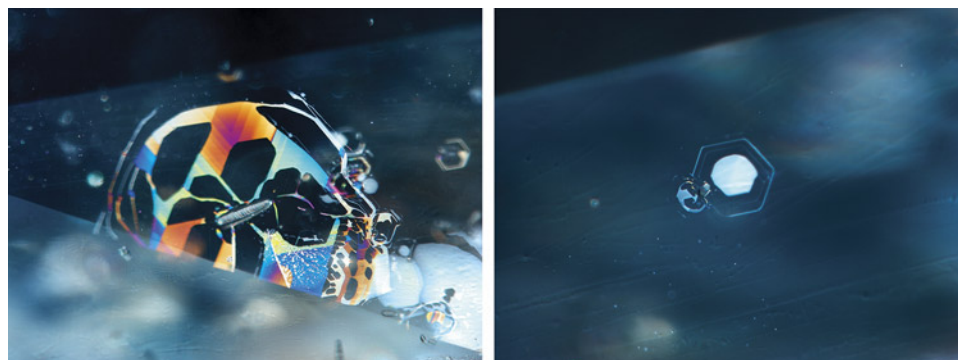


Figure 17. Left: An elongated crystal inclusion within a thin-film decrepitation halo in a green sapphire, showing a geometric distribution of interference colors; field of view 0.42 mm. Right: An orthohexagonal thin film conforming to the sapphire's crystal symmetry; field of view 0.86 mm. Photomicrographs by Yimiao Liu.

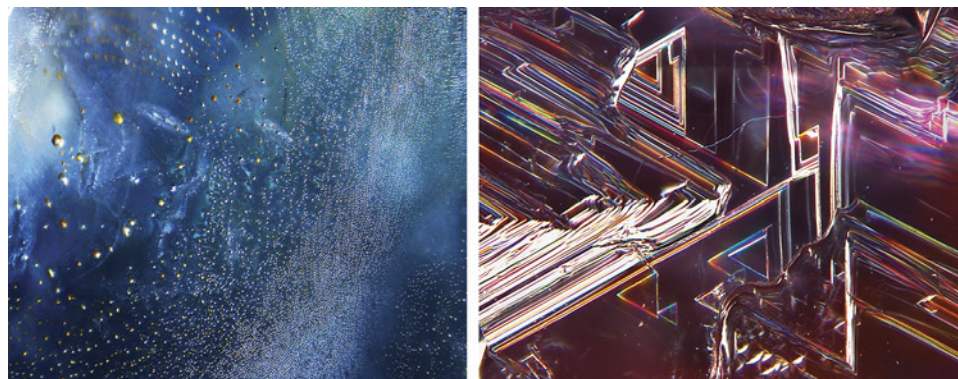


Figure 18. Left: Fingerprints with tiny negative crystals in a light blue sapphire, observed under oblique illumination; field of view 1.82 mm. Right: Surface details of a pink sapphire, showing triangular crystal growth terraces; field of view 2.28 mm. Photomicrographs by Yimiao Liu.

FTIR Spectral Features. FTIR spectroscopy was performed on 196 wafer samples in each color group. Ten percent of 52 deep blue wafers studied displayed peaks at 3310 and 3233 cm^{-1} (see sample DB3 in figure 19),

which can be assigned to the intrinsic OH defects (Beran and Rossman, 2006). Nevertheless, 90% of deep blue samples and samples from other color groups showed no significant peaks (again, see figure 19).

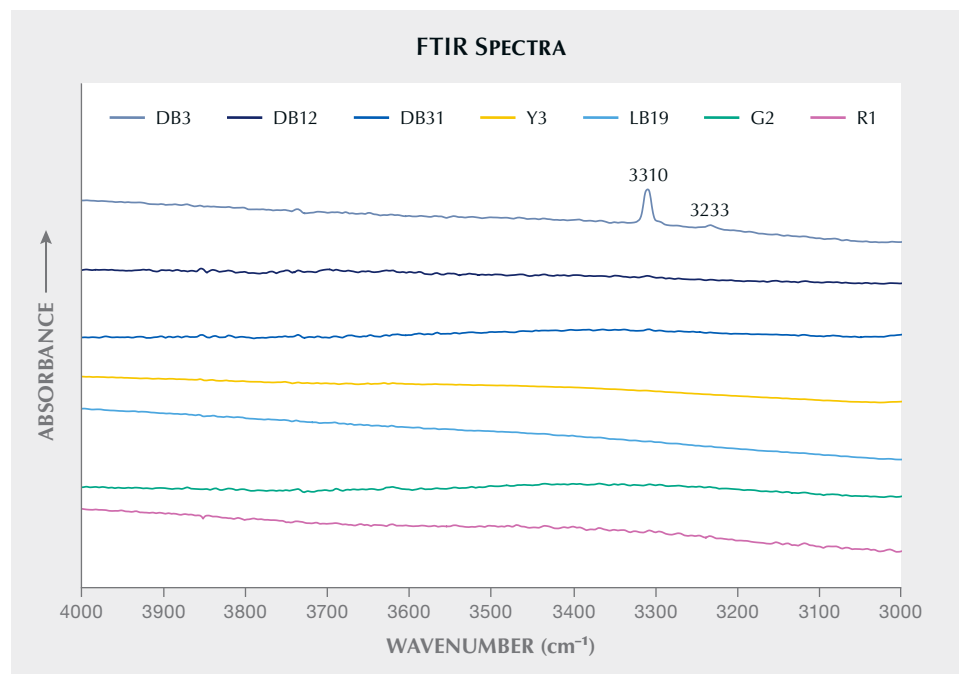


Figure 19. The FTIR spectra of representative samples from each group. Samples DB3, DB12, and DB31 were selected to represent the deep blue group, in which DB3 displayed sharp peaks at 3310 and 3233 cm^{-1} . Samples Y3, LB19, G2, and R1 represented other groups with no significant peaks shown in the 4000–3000 cm^{-1} range. Spectra are offset vertically for clarity.

TABLE 3. Concentrations of key trace elements in gem corundum from Muling, China.

Color group	Red ^a		Light blue		Deep blue		Yellow		Green		
Number of samples	31		13		20		7		6		
Number of analyses	102		42		72		24		21		
Trace elements	Range	Mean	Range	Mean	Range	Mean	Range	Mean	Range	Mean	Detection limits
ppmw ^b											
Mg	21–139	60	27–182	86	bdl–212	40	5–71	34	33–63	49	3
Ti	16–203	74	28–261	128	41–1162	323	5–199	52	51–90	72	1.5
V	bdl–49.3	14.6	3.3–59.7	23.6	bdl–75.3	30.5	1.4–9.6	4.9	3.1–41.9	16.2	0.2
Cr	140–10274	970	bdl–293	35	bdl–74	14	bdl–94	30	bdl–33	9	4.9
Fe	1939–7192	4251	2948–9133	5651	1834–13162	4958	4530–12151	7155	4753–8337	6380	25
Ni	bdl–46	—	bdl–56	6	bdl–31	—	bdl–848 ^d	71	bdl–12	—	4.5
Ga	21.6–56.9	37.2	23.0–75.5	41.9	119.8–201.9	158.8	20.2–336.2	115.7	28.6–69.3	42.4	0.6
ppma ^e											
Mg	17–113	49	22–149	70	bdl–173	33	4–58	28	27–51	40	2
Ti	7–88	32	12–113	54	17–505	137	2–86	22	21–39	31	0.7
V	bdl–19.7	5.9	1.3–23.9	9.4	bdl–30.1	12.2	0.6–3.8	1.9	1.3–16.8	6.5	0.08
Cr	54–3958	329	bdl–113	14	bdl–28	6	bdl–36	12	bdl–13	4	1.9
Fe	695–2576	1523	1056–3271	2024	657–4714	1776	1623–4352	2563	1702–2986	2285	9
Ni	bdl–16	—	bdl–19	2	bdl–10	—	bdl–288	24	bdl–4	—	1.5
Ga	6.2–16.4	10.7	6.6–21.7	12.0	34.4–58.1	45.7	5.8–96.7	33.3	8.2–19.9	12.2	0.2

^aThe red group includes pink, orangy pink, purple, and purplish red.^bppmw = parts per million by weight or µg/g^cbdl = below the detection limit of the analysis; mean values below the relevant detection limits are omitted.^dOne abnormal high nickel value for yellow might have been caused by the instability of the instrument.^eppma = parts per million atomic; $ppma = \frac{(\text{molecular weight of } Al_2O_3)/5}{\text{atomic weight of the element}} \times ppmw$

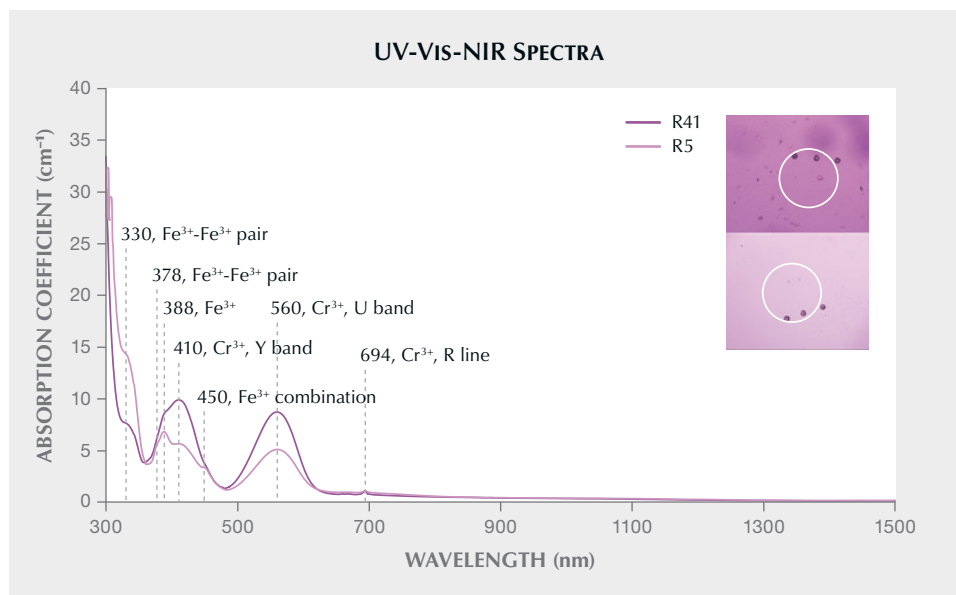


Figure 20. UV-Vis-NIR spectra comparing two pink sapphires with different saturations (sample nos. R41 and R5). The areas analyzed are shown in the inset photos, indicated by the white circles (400 μm diameter).

Chemical Analysis. Seventy-eight samples from Muling were measured by LA-ICP-MS, and the trace element composition varied according to bodycolor. Table 3 shows regular concentrations and atomic concentrations of trace elements (magnesium, titanium, vanadium, chromium, iron, nickel, and gallium) that may directly or indirectly impact the samples' coloration or origin determination (for individual stone data, see supplementary information at <https://www.gia.edu/gems-gemology/fall-2022-sapphire-from-china>). Value ranges and corresponding mean values and detection limits are displayed in this table. Elements such as magnesium, titanium, vanadium, iron, and gallium, although with various concentrations, occurred in all groups regardless of color, while chromium occurred mainly in the red group. When the average value of elements was below the relevant detection limit, the data was omitted. Some isotopes such as ^9Be , ^{90}Zr , ^{93}Nb , and ^{181}Ta displayed detectable values near detection limits sporadically, with one or two spots among all data. It is likely that laser-ablated microscopic particulates contained these elements (Lu and Shen, 2011; Pardieu, 2013; Emori et al., 2014). This data is not presented in table 3 because it is not directly related to the corundum.

Other measured isotopes (^7Li , ^{11}B , ^{45}Sc , ^{55}Mn , ^{59}Co , ^{66}Zn , ^{85}Rb , ^{88}Sr , ^{89}Y , ^{97}Mo , ^{118}Sn , ^{133}Cs , ^{137}Ba , ^{139}La , ^{140}Ce , ^{146}Nd , ^{147}Sm , ^{153}Eu , ^{178}Hf , ^{182}W , and ^{232}Th) were generally below detection limits or less than a few ppmw. Although silicon is common in corundum (Emmett et al., 2017), it is beyond the scope of this article due to the poor detection limit caused by the mass interference. Furthermore, the explanation of coloration would be affected by the unaccounted incorporation of Si^{4+} .

UV-Vis-NIR Spectral Features. The main color hues and saturations of Muling sapphire were examined using quantitative UV-Vis-NIR spectroscopy. Data were collected in the range extending to 1500 nm in the infrared region, beyond which no known chromophores exist (see, e.g., figure 22). All trace element analyses were performed over the spectrally analyzed local areas. The two sets of data (spectral and chemical) are highly correlated via the application of a UV-visible spectrometer equipped with a microscope. The real chromophore mechanisms of samples from each color group were then determined according to the rules of impurity interactions in corundum (Emmett et al., 2003, 2017).

Red Group (Pink, Orangy Pink, Purple, and Purplish Red Sapphire). The main chromophore features of red group samples in different saturations are shown in figure 20. Non-oriented UV-Vis-NIR spectra were acquired due to the twinning structures in the red group samples. Pink sapphires R5 and R41, with chromium contents of 197 and 473 ppma, respectively, were selected as representative of the red group to demonstrate variations in saturation. As seen in figure 20, these absorption spectra show evident Cr^{3+} features (i.e., Y band at 410 nm, U band at 560 nm, and R-line at 694 nm; Powell, 1998) superimposed by the Fe^{3+} absorptions (peaks at 378, 388, and 450 nm and a shoulder at 330 nm; Ferguson and Fielding, 1971 and 1972). The heights of the U band and Y band are positively associated with chromium content (table 4). Since the $\text{Fe}^{2+}\text{-Ti}^{4+}$ pair is an effective chromophore with a strong absorption cross section (Dubinsky et

TABLE 4. Trace element compositions (in ppma) of representative red group samples (R41 and R5) from Muling, China.^a

Sample no.	Mg	Ti	V	Cr	Fe
R41	27 (4)	12 (1)	3.4 (0.2)	473 (7)	910 (11)
R5	30 (1)	15 (2)	3.3 (0.4)	197 (5)	1821 (34)

^aAverage concentrations of three LA-ICP-MS data in each sample are shown with the standard deviation (ppma) in parentheses.

al., 2020), concentrations of a few ppma will produce observable coloration. The titanium in these two samples with concentrations above 10 ppma (table 4) showed little effect on the spectra, perhaps due to the existence of magnesium (Emmett et al., 2003, 2017). Low amounts of other elements such as vanadium (table 4) had limited effect on the spectra.

Light Blue Group. After carefully examining all 43 light blue samples, the absorption spectra showed relatively consistent characteristics, as represented by sample LB19 (figure 21). Only non-oriented spectra were acquired because of the twinning structure in this group. The UV-Vis-NIR spectrum of LB19 displayed typical Fe^{3+} absorptions (Ferguson and Fielding, 1972; Hänni, 1994) as well as evident $\text{Fe}^{2+}\text{-Ti}^{4+}$ intervalence charge transfer absorption (i.e., $\text{Fe}^{2+}\text{-Ti}^{4+}$ IVCT, band center at approximately 580 nm). The

trace element composition of LB19 demonstrates that the sample contains 100 ppma titanium, 2264 ppma iron, and 142 ppma magnesium (table 5). The elements that could cause the sample to produce a blue color (i.e., titanium and iron) are all present in significant concentrations. And such concentration (i.e., 100 ppma, if all titanium is paired with iron) of the $\text{Fe}^{2+}\text{-Ti}^{4+}$ pair would produce a strong saturation (Dubinsky et al., 2020). However, both the visual appearance and the absorption coefficient of the $\text{Fe}^{2+}\text{-Ti}^{4+}$ IVCT indicated a weak coloration of the stone. This is most likely due to the presence of the element magnesium. According to the rules of impurity interactions in corundum (Emmett et al., 2003, 2017), titanium will preferentially pair with magnesium before iron. In this case, the atomic content of the magnesium (142 ppma) is higher than that of titanium (100 ppma). If all the titanium paired with

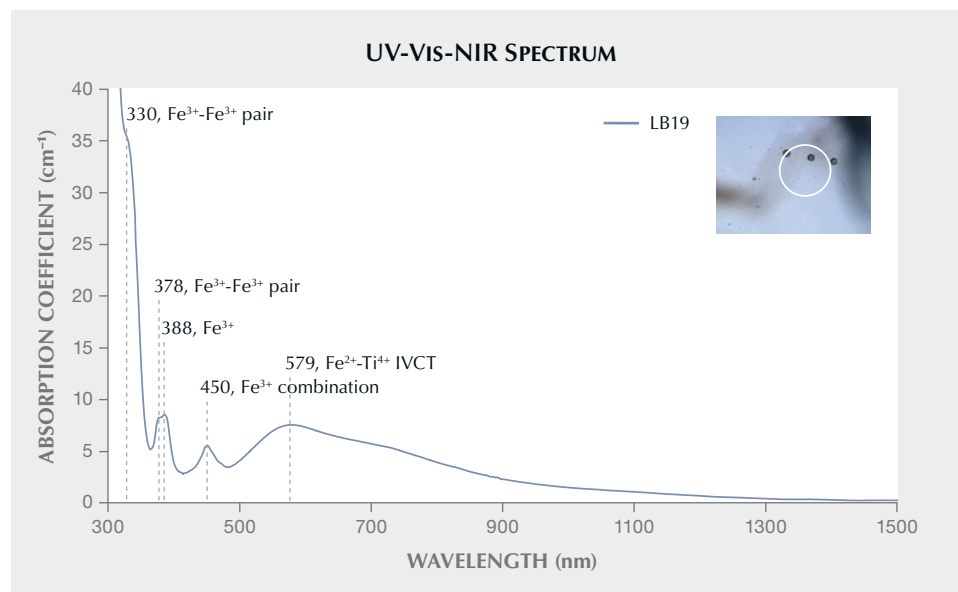


Figure 21. UV-Vis-NIR spectrum of sample LB19 representing the chromophore features of the light blue group. The area analyzed is shown in the inset photo, indicated by the white circle (400 μm diameter).

TABLE 5. Trace element composition (in ppma) of the light blue sapphire LB19 from Muling, China.^a

Sample no.	Mg	Ti	V	Cr	Fe
LB19	142 (5)	100 (2)	4.2 (0.3)	4 (1)	2264 (49)

^aAverage concentrations of three LA-ICP-MS data of trace elements are shown with the standard deviation (ppma) in parentheses.

magnesium, the stone would theoretically exhibit no blue color and there would be no absorption at 580 nm. Therefore, elements (such as silicon) with higher energy levels than titanium probably exist in the crystal lattice and preferentially pair with magnesium, allowing the remaining titanium to pair with iron and produce a light blue color.

Deep Blue Group. The high clarity and homogeneous structure without twinning of the 52 Muling deep blue sapphires allowed us to prepare high-quality oriented wafers. Therefore, oriented quantitative spectra could be obtained in both o-ray and e-ray directions for the full range from 300 to 1500 nm. Two different types of UV-Vis-NIR spectra were found among all tested spectra of deep blue sapphire wafers. Both types of spectra exhibited significant Fe^{2+} - Ti^{4+} pair features and Fe^{3+} features in the ultraviolet and visible regions. Oriented UV-Vis-NIR spectra of the first type, as represented by sample DB31, are displayed in figure 22. This type is the most common

in more than 90% of the 52 deep blue wafers, with a strong and wide band in the near-infrared region (centered at 880 nm). This strong absorption is a typical feature of basalt-related sapphire (Smith, 1978). Figure 23 shows the oriented UV-Vis-NIR spectra of sample DB12, which illustrates the second type of spectra. Observed in less than 10% of deep blue samples, this second type of spectra lacks the strong absorption in the near-infrared region.

The absorption coefficients for the 580 nm band were similar for samples DB31 and DB12. In oriented quantitative spectra, the height of a certain absorption is related to the chromophore concentrations, as the two stones are both deep blue with similar saturation. This suggests that the true Fe^{2+} - Ti^{4+} IVCT concentrations are of similar levels. Combined with the trace element data (table 6), sample DB31 has contents of 224 ppma titanium, 1694 ppma iron, and 16 ppma magnesium. When magnesium content is scarce and titanium content is sufficient to pair with iron, a strong absorption occurs and a deep color is produced.

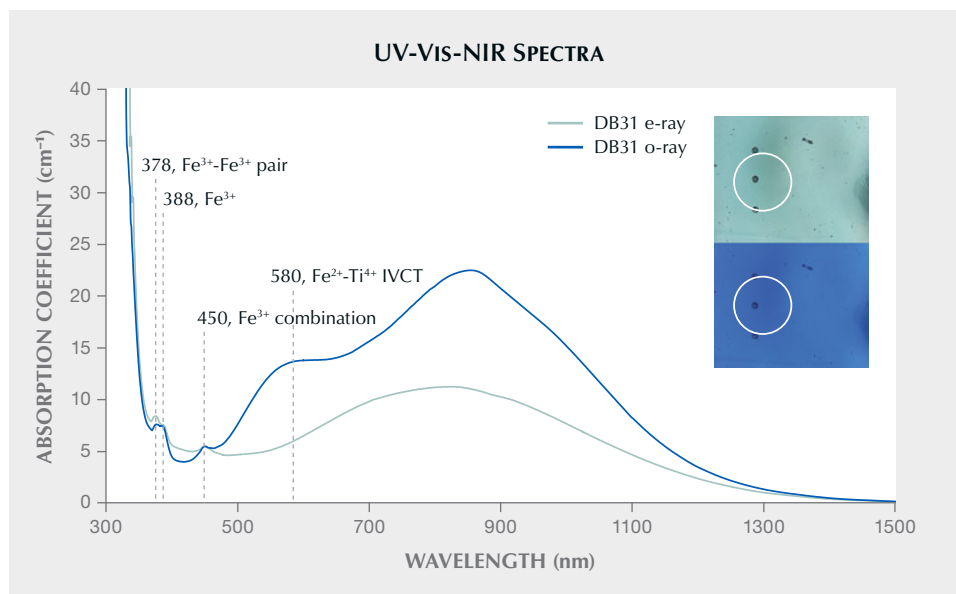


Figure 22. Oriented UV-Vis-NIR spectra of sample DB31 representing features of the first type of spectrum from the deep blue group, with inset photos of the different directions. The white circles indicate the areas analyzed (400 μm diameter).

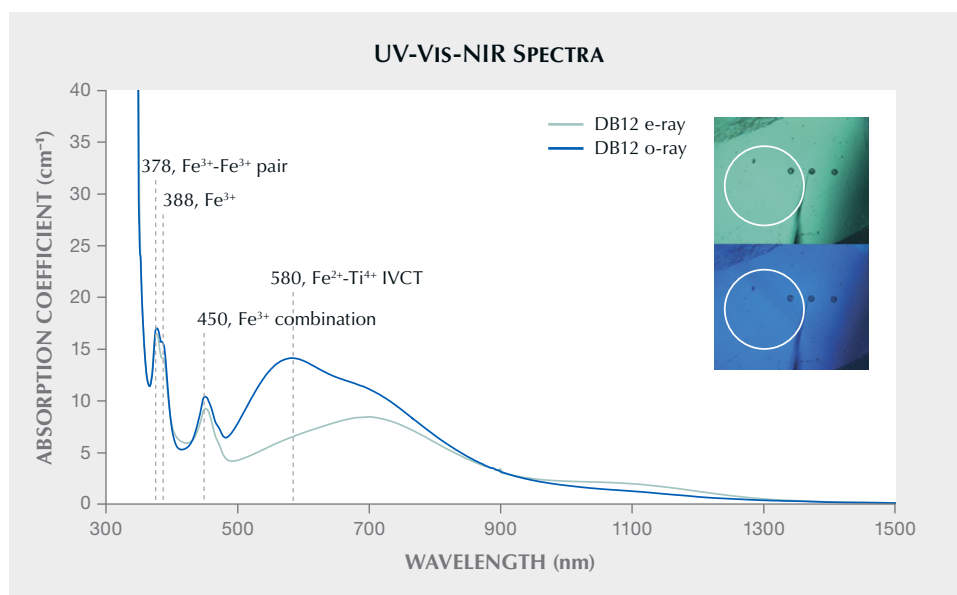


Figure 23. Oriented UV-Vis-NIR spectra of sample DB12 representing features of the second type of spectrum from the deep blue group, with inset photos showing the different directions. The white circles indicate the areas analyzed (400 μm diameter).

The trace element compositions of sample DB12 showed contents of 149 ppma titanium, 3690 ppma iron, and 169 ppma magnesium. The atomic concentrations of magnesium were analyzed to be higher than the concentrations of titanium. The high color saturation of this deep blue sapphire, caused by Fe^{2+} - Ti^{4+} IVCT, implies a large amount of titanium paired with iron instead of magnesium. It is deduced that there is a large depletion of magnesium by silicon. Furthermore, the weak bands at 700 and 1100 nm in the oriented spectra of sample DB12 (figure 23) might be related to the high Fe^{3+} concentrations (Dubinsky et al., 2020). LA-ICP-MS confirmed sample DB12's iron concentration of 3690 ppma (table 6).

Yellow and Green Groups. Samples in the yellow and green groups mainly exhibited Fe^{3+} features in their non-oriented UV-Vis-NIR spectra. Samples Y3

and G5 were selected as representative to exhibit the chromophore features (figure 24). The spectrum of yellow sapphire (sample Y3) showed weak absorption in the visible light region with mainly Fe^{3+} features and a weak broad band at 570 nm. Compared to the yellow sample, the green sapphire (sample G5) showed relatively strong absorptions at Fe^{3+} peaks (377, 388, and 450 nm) and the 570 nm band (which might be associated with the V^{3+} transition; Schmetzer and Bank, 1981), giving the stone a bluish green hue. The trace element data of these two samples (table 7) showed consistent results in their spectra, with iron the most significant impurity in both samples. Other elements showed only minor concentrations in both the yellow and green samples. The existence of vanadium and titanium in sample G5 might be the reason for the absorption at 570 nm, which would cause the green hue to appear.

TABLE 6. Trace element composition (in ppma) of two deep blue sapphires (DB31 and DB12) from Muling, China.^a

Sample no.	Mg	Ti	V	Cr	Fe
DB31	16 (4)	224 (10)	6.7 (0.3)	0 (0)	1694 (47)
DB12	169 (4)	149 (3)	20.9 (0.5)	15 (2)	3690 (92)

^aAverage concentrations of three LA-ICP-MS data in each sample are shown with the standard deviation (ppma) in parentheses.

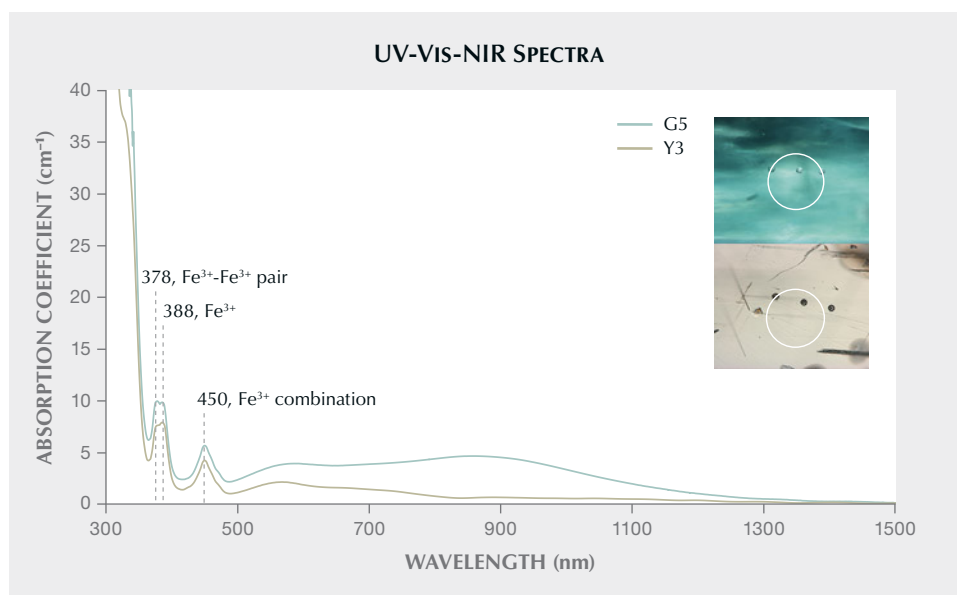


Figure 24. UV-Vis-NIR spectra comparing a yellow and a green sample (sample nos. Y3 and G5) from Muling. The areas analyzed are shown in the inset photos, indicated by the white circle (400 μm diameter).

DISCUSSION

Provenance Characteristics of Muling Sapphire. Muling sapphire comes in a wide range of colors and can display vivid color and high clarity, unlike sapphire from other magmatic deposits in China (Guo et al., 1992; Wang et al., 1992; Cheng et al., 2009; Zhang et al., 2018). The high color saturation of unheated Muling sapphire also reveals distinctive appearances compared to Montana sapphire (Emmett and Douthit, 1993; Hsu et al., 2017). The appearance is comparable to sapphire from other classic deposits such as Thailand or Madagascar. Therefore, additional evidence is needed to identify the provenance features of Muling sapphire.

Internal Features. Mineral inclusions in the Muling samples consisted of short rutile needles, euhedral prismatic zircon crystals, rounded prismatic calcium-

rich plagioclase, and garnet. These internal features (figures 9–15) are essential evidence of geographic origin. Comparison with published papers and the GIA classification system (<https://www.gia.edu/corundum-report-cover-source-type>) confirms that Muling sapphire inclusions overlap with typical metamorphic and magmatic sapphires.

Long to short rutile needles were common in samples of almost all colors except for yellow (table 8). Short arrow-headed needles, which were mainly encountered in light blue and red group samples from Muling, are regarded as the hallmark of Burmese origin and classic in Madagascar sapphire (Palke et al., 2019a,b) (table 5). However, rutile cannot be considered a decisive indicator of locality, as it is known to occur in corundum from various geological origins (e.g., Gübelin and Koivula, 1986; Palke et al., 2017, 2019a).

TABLE 7. Trace element composition (in ppma) of a yellow sapphire (Y3) and a green sapphire (G5) from Muling, China.^a

Sample no.	Mg	Ti	V	Cr	Fe
Y3	41 (1)	20 (2)	2.2 (0.2)	11 (1)	1730 (25)
G5	39 (3)	29 (3)	6.7 (0.2)	1 (0)	2199 (6)

^aAverage concentrations of three LA-ICP-MS data in each sample are shown with the standard deviation (ppma) in parentheses.

The presence of polysynthetic twinning and linear tubes or dotted lines in samples (figures 14 and 15) other than the deep blue sapphire indicates a possible high-pressure geological event that affected the corundum crystals during or after their crystallization. These inclusion combinations in light blue sapphire as well as red group samples might lead to an association with metamorphic sapphire at first glance with the microscope.

Zircon inclusions appeared only in deep blue sapphires and exhibited magmatic features (detailed chemical composition and morphology information will be presented in a forthcoming paper by the authors). The hexagonal color banding in deep blue sapphire is also reminiscent of magmatic sapphire (e.g., Cambodian and Ethiopian; Palke et al., 2019a).

Chemical Features. Various discrimination diagrams of trace element concentrations and ratios have been used to distinguish corundum from different geographic localities (e.g., Sutherland et al., 1998; Zaw et al., 2006; Abduriyim and Kitawaki, 2006; Peucat et al., 2007; Sutherland and Abduriyim, 2009; Zwaan et al., 2015). To explore the similarities and differ-

ences between Muling sapphire and material from other deposits, chemical data are plotted with these diagrams against sapphire datasets from around the world. Recognizing the distinct differences in proportions of trace elements in the different color groups, discussions on blue samples and red samples (including pink to purple sapphire) are documented separately below.

Blue Samples. The Ga/Mg ratio vs. Fe diagram and the Fe-Mg-Ti diagram proposed by Peucat et al. (2007) have been applied to geological typing of various sapphire deposits (Schwarz et al., 2008; Zwaan et al., 2015).

In the diagram of Ga/Mg ratio vs. Fe (figure 25), 13 light blue sapphires plot in a relatively restricted area, showing overlap with Yogo Gulch sapphire from Montana and metamorphic (and metasomatic) sapphire. Considering their high iron content (3170–9130 ppmw), the likelihood of a typical metamorphic origin (such as Sri Lanka) is rather low. The Ga/Mg ratio is 0.2–1.5. The 20 deep blue sapphires tend to be much more dispersed in between the fields of magmatic and metamorphic sapphire, with the

TABLE 8. Inclusion type and frequency in different color groups of gem corundum from Muling, China.

Color group	Red ^a	Light blue	Deep blue	Yellow	Green
Number of samples	112	72	88	23	16
Rutile needles	74%	75%	77%	—	31%
Zircon	—	—	9%	—	—
Feldspar	—	17%	—	—	—
Garnet	2%	—	—	4%	—
Twinning	100%	100%	—	100%	100%
Linear/tubes	52%	75%	—	91%	—
Color zoning	—	—	85%	—	—

^aThe red group includes pink, orangy pink, purple, and purplish red.

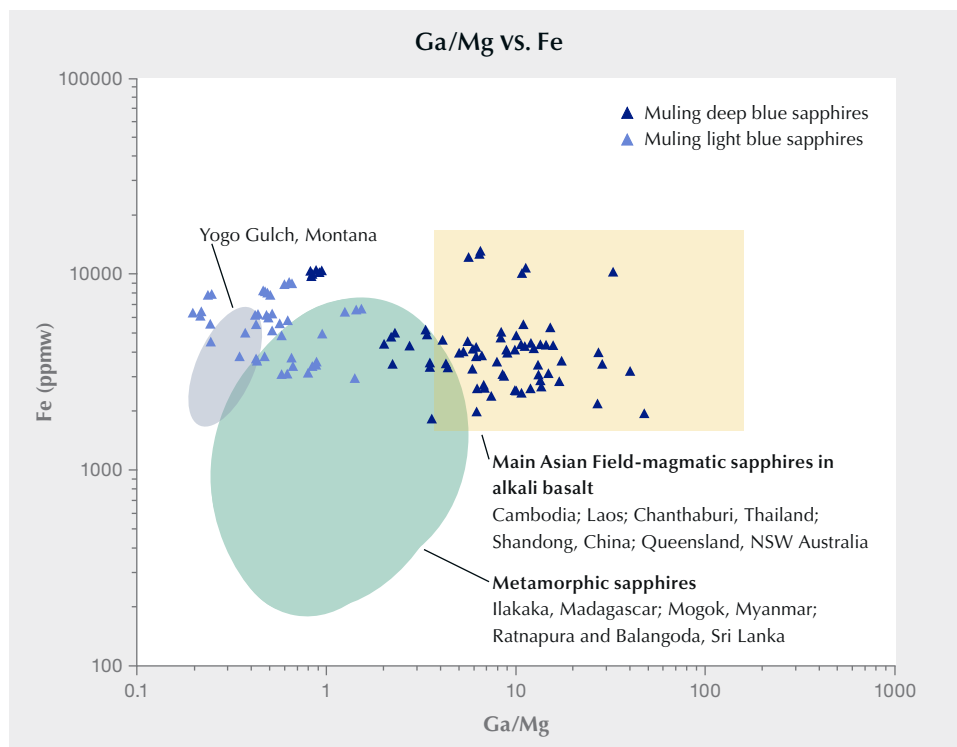


Figure 25. Comparison of Ga/Mg ratio vs. Fe between Muling blue sapphire and metamorphic, magmatic, and Yogo Gulch (Montana) blue sapphire, modified after Peucat et al. (2007) and Zwaan et al. (2015). The 13 Muling light blue sapphires overlap with metamorphic and Yogo sapphires at their higher level of Fe concentration. The 20 Muling deep blue sapphires are plotted in the fields of both magmatic and metamorphic sapphire. Note that both horizontal and vertical axes are displayed in log units rather than linear coordinates to display the data distribution in a more compact form.

Ga/Mg ratio varying from 0.8 to 47 and iron content of 1834–13162 ppmw. In the Fe-Mg-Ti diagram (fig-

ure 26), the chemical fingerprint of Muling light blue and deep blue sapphire exhibits a consistent trend

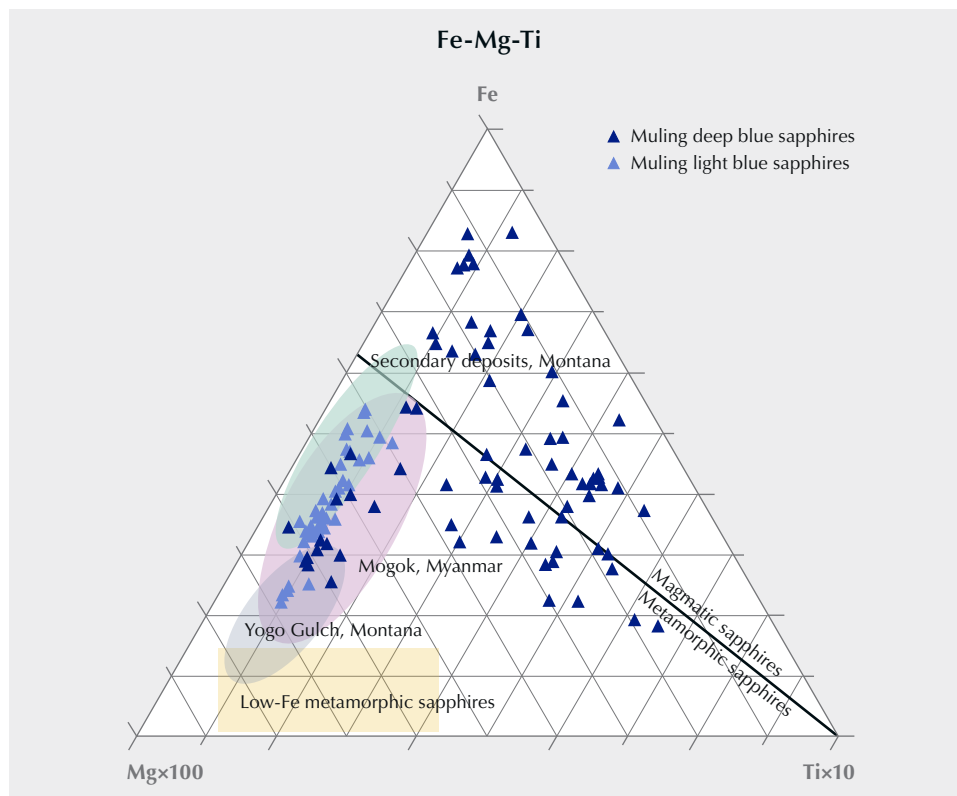


Figure 26. Fe-Mg-Ti diagram, modified after those of Peucat et al. (2007) and Zwaan et al. (2015), plotted in ppmw. The gray area indicates Yogo sapphire, while the green area refers to sapphire from secondary deposits elsewhere in Montana. Sapphire from Mogok exhibits a distribution typical of metamorphic origins (pink area). The yellow rectangle indicates classic metamorphic sapphire with low iron content.

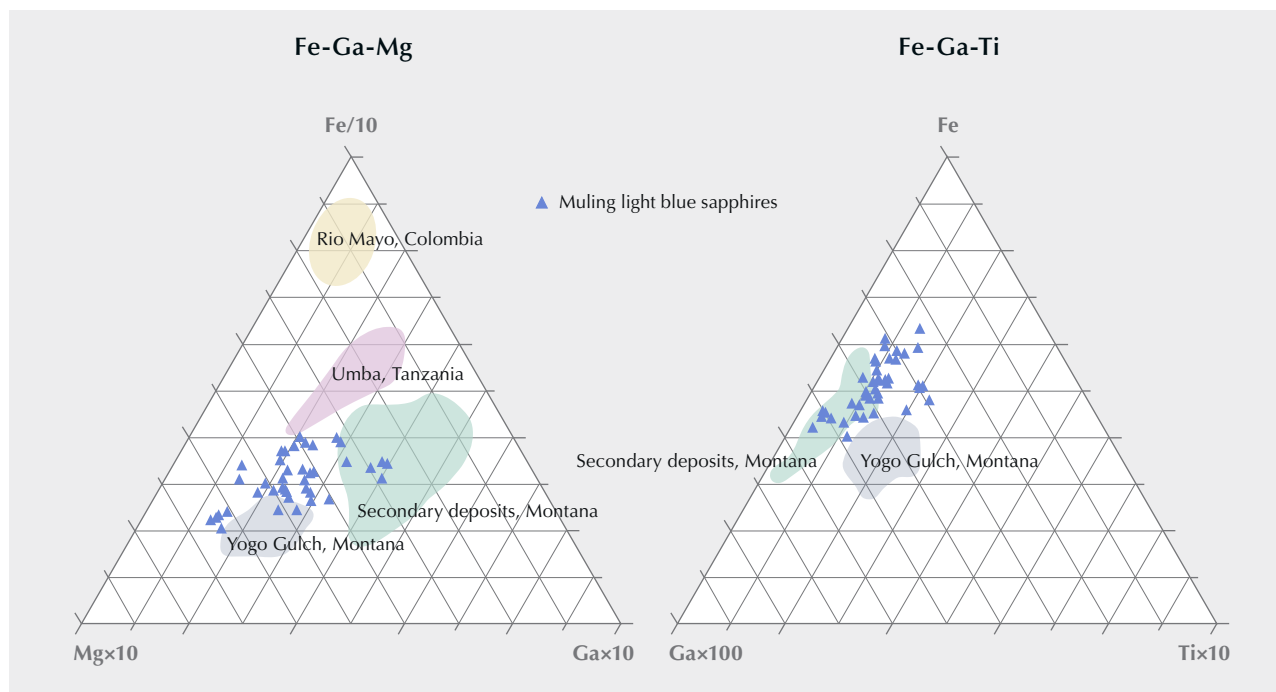


Figure 27. Left: The Fe-Ga-Mg diagram to separate Muling light blue sapphire from Montana secondary deposit sapphire, modified after Peucat et al. (2007) and Zwaan et al. (2015), plotted in ppmw. Right: The Fe-Ga-Ti diagram to distinguish Muling light blue sapphire from Montana Yogo sapphire. Data for Montana sapphire from Renfro et al. (2018).

from the Ga/Mg ratio vs. Fe diagram: Light blue sapphire falls into the area of metamorphic sapphire (e.g., Mogok, Myanmar) and Yogo Gulch (Montana) sapphire along the iron-magnesium axis, while the deep blue sapphire is distributed in both magmatic and metamorphic areas. Since Muling's light blue sapphire exhibits similarities with Montana sapphire (figures 25 and 26), two additional mathematical models are applied for further separation (figure 27). In an Fe-Ga-Mg diagram, Muling samples can be distinguished partially from Montana sapphire—from both secondary deposits and the primary deposit at Yogo Gulch. And in an Fe-Ga-Ti diagram, Muling sapphire shows a somewhat different distribution from that of Yogo sapphire.

Red Group Samples (Pink, Orangy Pink, Purple, and Purplish Red). Binary and ternary plots of the significant trace elements chromium, titanium, iron, and gallium are the most widely used discriminants for geological formation environments (Garnier et al., 2002; Rankin et al., 2003; Schwarz et al., 2008). In the plot of Fe_2O_3 vs. Cr_2O_3 proposed by Schwarz et al. (2008) to distinguish geological types, chemical fingerprints of Muling red group samples are mainly distributed in the field of magmatic-related ruby,

with high iron contents (figure 28). This plot also shows that the 31 red, pink, and purple samples overlap with ruby from Winza, Tanzania. A few spots with higher chromium content overlap with Malawi ruby. Most of the analyzed samples in this group consisted of pink sapphire; only a limited number of highly saturated red samples were collected and analyzed due to their rarity in the surveyed locations. Thus, in general, the chromium levels for the entire group of Muling red samples appear low.

Geological Origins of Muling Sapphire. Over the past 30 years, corundum specimens from the Muling area have only been found in alluvial sediments, and the ultimate source rocks have not yet been located. The crystallization conditions for corundum are much too difficult to ascertain for these secondary deposits (Giuliani et al., 2014).

Although the source rock of Muling sapphire needs further exploration, the internal features and the spectral and chemical analyses in this study provide some hints to their origin. The study of syngenetic and protogenetic inclusions makes it possible to extract valuable information about the growth environment. Zircon inclusions in the deep blue samples can provide age information on Muling sapphire (related in-

formation will be published in a forthcoming paper by the authors). Rounded anorthite inclusions in light blue sapphire revealed a higher formation temperature for the inclusion compared to the ideal crystallization point. The multiphase inclusion in a red group sample with daughter minerals (figure 13) indicated crystallization from a saturated liquid after it was trapped. And chemical compositions of sillimanite and anorthite (daughter minerals) reflected a sample of the fluid in which the host crystal grew (Roedder, 1962).

The UV-Vis-NIR spectra of the two types of deep blue sapphire display the diversity of the formation history of Muling sapphire. By observing the presence or absence of the absorption band (related to the basaltic environment; Smith, 1978) in the near-infrared range centered around 880 nm of the UV-Vis-NIR spectra (figures 22 and 23), it is possible to quickly distinguish between two sapphires of different geological origins, even though they might be very similar in appearance and have been discovered from the same deposit.

As for chemical characteristics, the plots in figures 25–28 provide some information related to the growth environment of Muling sapphire. The light blue sapphire material exhibits atypical metamorphic features with high iron concentrations. The deep blue sapphire material is distributed in the fields of both magmatic and metamorphic sapphire. However, these trace element diagrams should be used with caution since the

corundum coloration may strongly influence the results of the discrimination (Wong et al., 2017; Sorokina et al., 2019), which may conflict with other evidence in deciphering the geological origin (Palke et al., 2018). Therefore, the $\text{FeO-Cr}_2\text{O}_3\text{-MgO-V}_2\text{O}_3$ vs. $\text{FeO} + \text{TiO}_2 + \text{Ga}_2\text{O}_3$ chemical classification diagram proposed by Giuliani et al. (2015) is applied for light blue and deep blue sapphire in figure 29 and for pink and purple sapphire in figure 30. As shown in figure 29, most of the light blue sapphire is confined within the “metasomatic corundum” field, while few spots lie in the typical magmatic field. The deep blue sapphire is divided into two parts. One part lies in the “metasomatic corundum” field. Other deep blue sapphire lies in the overlapping area of the “sapphire in alkali basalts” field and the “sapphire in alkali basalts” field. Considering the overall geological background and the information on zircon inclusions, deep blue sapphire showed a closer relationship with basalts. The red group samples lie mainly in the “metasomatic” field in this plot (figure 26), similar to the result for light blue sapphire. Only a few spots lie in the “ruby in mafic-ultramafics” field. Thus, the $\text{FeO-Cr}_2\text{O}_3\text{-MgO-V}_2\text{O}_3$ vs. $\text{FeO} + \text{TiO}_2 + \text{Ga}_2\text{O}_3$ diagram suggests the possibility of a metasomatic origin for Muling light blue sapphires and red group samples.

However, there are still some uncertainties about the origins of geological formation conditions. The deep blue sapphire material exhibits two types of UV-

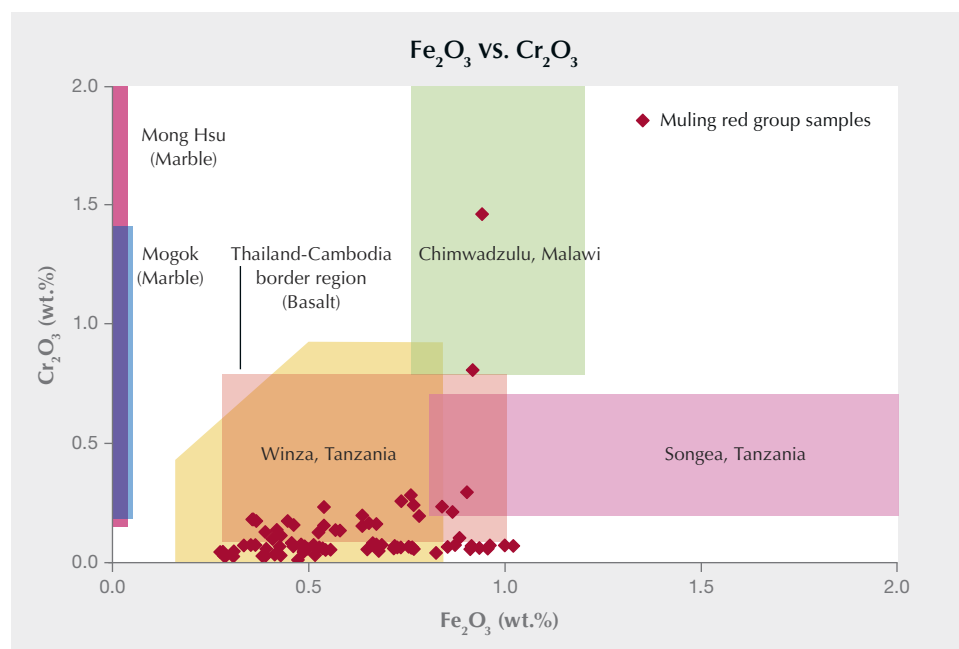


Figure 28. A binary plot of Fe_2O_3 vs. Cr_2O_3 , modified after Schwarzer et al. (2008). The chemical distribution of the 31 reddish samples from Muling overlaps mainly with magmatic ruby from Thailand and Tanzania.

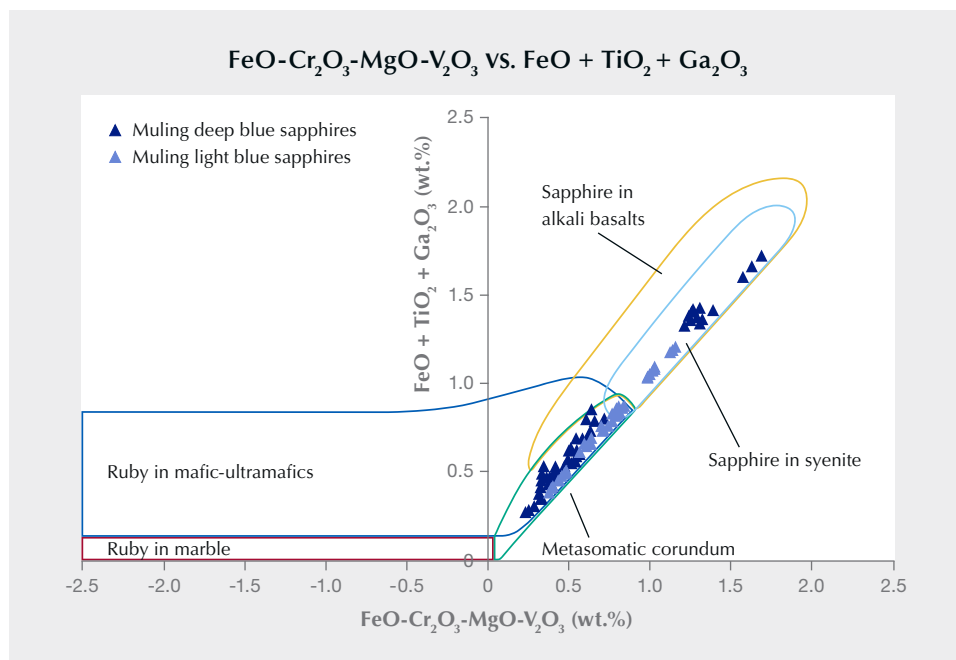


Figure 29. Trace element chemistry plot of $\text{FeO-Cr}_2\text{O}_3\text{-MgO-V}_2\text{O}_3$ vs. $\text{FeO} + \text{TiO}_2 + \text{Ga}_2\text{O}_3$ for Muling light blue and deep blue sapphire. Modified after Giuliani et al. (2015).

Vis spectra with distinctly different features in the near-infrared range (see figures 22 and 23), which reveal different growth environments. Angular color zoning has never been observed in red, light blue, and yellow samples but is common in deep blue samples, also indicating different formation environments. Therefore, additional study is needed to explore the true origin of Muling sapphire.

CONCLUSIONS

This study presented a comprehensive set of gemological data on a deposit of fine-quality sapphire beneath the fertile soils of northeastern China. Gemological characteristics including color, clarity, and carat weight indicate the quality of Muling sapphire. The samples showed a full range of hues and saturations, and clarity ranged from transparent to

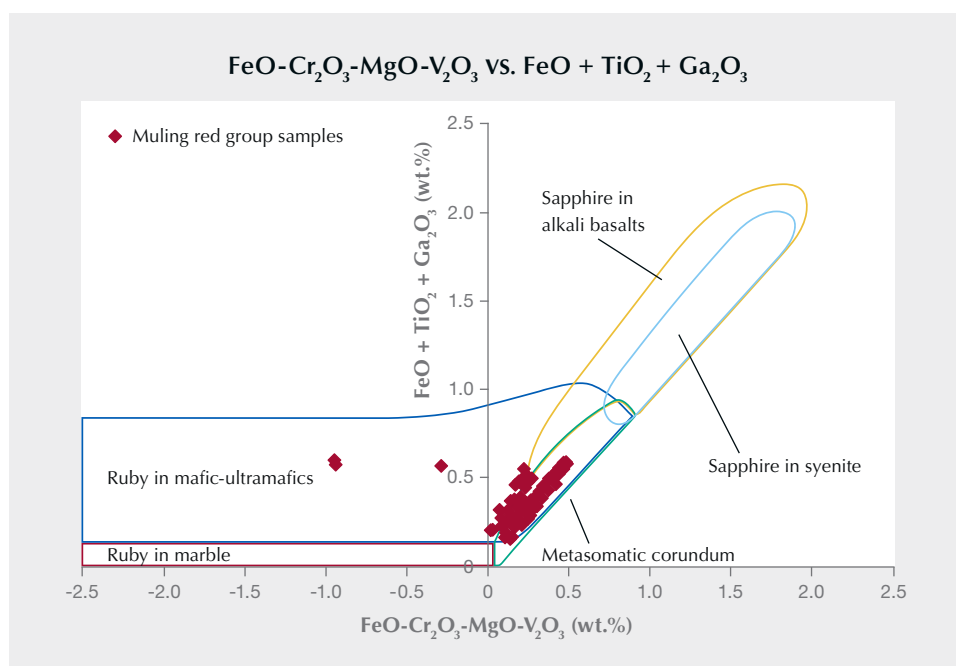


Figure 30. Chemical distribution plot of $\text{FeO-Cr}_2\text{O}_3\text{-MgO-V}_2\text{O}_3$ vs. $\text{FeO} + \text{TiO}_2 + \text{Ga}_2\text{O}_3$ for red group samples from Muling. Modified after Giuliani et al. (2015).

semitransparent. Most samples weighed 1–3 ct, with the largest rough sample reaching 51 ct. Microscopic observation revealed rutile needles, tubes, hexagonal zoning, and twinning, along with mineral inclusions (such as anorthite and zircon) as typical internal features in Muling sapphire.

Quantitative analyses with spectroscopy and trace element chemistry determined correlations between chromophore mechanisms and trace elements for each color group of samples. The spectra of blue sapphire material also indicated a mixture of geological formation environments, which were evidenced by their different appearances. Analyses of chemical data utilizing multiple discrimination models further demonstrated that Muling has a more diverse geological environment than typical magmatic or metamorphic settings. Deep blue samples showed dispersed

chemical fingerprints across magmatic and metamorphic sapphire. Light blue samples were more consistent with chemical compositions of metamorphic (or metasomatic) sapphire. Red group samples mainly showed metasomatic features with high iron contents. Muling sapphire, known for being of predominantly basaltic origin, produced wide color varieties from a rather limited geographic area. This deposit is a rare example that is distinctly different from common alkali basaltic deposits (e.g., Australia or Shandong, China).

The study of Muling sapphire enriched our knowledge of basalt-related gem corundum with various gemological and geological characteristics. The geological formation origin of Muling sapphire is a subject that deserves further study, and the exploration of their aesthetic qualities will continue as well.

ABOUT THE AUTHORS

Ms. Liu (yim2015@163.com) is a PhD student, and Dr. Lu (renlu.cc@gmail.com) is a distinguished professor, at the Gemmological Institute, China University of Geosciences in Wuhan.

ACKNOWLEDGMENTS

The authors would like to thank the reviewers and editors for their thoughtful suggestions that substantially improved this manuscript. We especially thank Aijun Yi for his help on the field trips and sample collection. We also express our gratitude to lifelong friend Leiguang Zheng for his enthusiastic support on our field trips and his telling of the region's history and natural heritage.

REFERENCES

- Abduriyim A., Kitawaki H. (2006) Determination of the origin of blue sapphire using laser ablation inductively coupled plasma mass spectrometry (LA-ICP-MS). *Journal of Gemmology*, Vol. 30, No. 1-2, pp. 23–36.
- Beran A., Rossman G.R. (2006) OH in naturally occurring corundum. *European Journal of Mineralogy*, Vol. 18, No. 4, pp. 441–447, <http://dx.doi.org/10.1127/0935-1221/2006/0018-0441>
- Chen T., Ai H., Yang M., Zheng S., Liu A.Y. (2011) Brownish red zircon from Muling, China. *G&G*, Vol. 47, No. 1, pp. 36–41, <http://dx.doi.org/10.5741/GEMS.47.1.36>
- Chen T., Liu Y., Yin Z., Liu N. (2013) Gemology and spectra characterization of gem garnet from Muling City, Heilongjiang Province. *Spectroscopy and Spectral Analysis*, Vol. 33, No. 11, pp. 2964–2967, [http://dx.doi.org/10.3964/j.issn.1000-0593\(2013\)11-2964-04](http://dx.doi.org/10.3964/j.issn.1000-0593(2013)11-2964-04) [in Chinese].
- Cheng Y., Wang J., Tian L.G., Zhang H., Li J. (2009) Application of ion implantation technique in optimization treatment of Shandong sapphire. *Journal of Synthetic Crystals*, Vol. 38, No. 6, pp. 1472–1476. Chinese with English abstract, <http://dx.doi.org/10.16553/j.cnki.issn1000-985x.2009.06.002> [in Chinese].
- Dubinsky E.V., Stone-Sundberg J., Emmett J.L. (2020) A quantitative description of the causes of color in corundum. *G&G*, Vol. 56, No. 1, pp. 2–28, <http://dx.doi.org/10.5741/GEMS.56.1.2>
- Editorial Committee of Muling (1989) *The County Chronicle of Muling*. Chinese Cultural and Historical Press, Beijing, 11 pp.
- Emmett J.L., Douthit T.R. (1993) Heat treating the sapphires of Rock Creek, Montana. *G&G*, Vol. 29, No. 4, pp. 250–272, <http://dx.doi.org/10.5741/GEMS.29.4.250>
- Emmett J.L., Scarratt K., McClure S.F., Moses T., Douthit T.R., Hughes R., Novak S., Shigley J.E., Wang W., Bordelon O., Kane R.E. (2003) Beryllium diffusion of ruby and sapphire. *G&G*, Vol. 39, No. 2, pp. 84–135, <http://dx.doi.org/10.5741/GEMS.39.2.84>
- Emmett J.L., Stone-Sundberg J.L., Guan Y., Sun Z. (2017) The role of silicon in the color of gem corundum. *G&G*, Vol. 53, No. 1, pp. 42–47, <http://dx.doi.org/10.5741/GEMS.53.1.42>
- Emori K., Kitawaki H., Okano M. (2014) Beryllium-diffused corundum in the Japanese market, and assessing the natural vs. diffused origin of beryllium in sapphire. *Journal of Gemmology*, Vol. 34, No. 2, pp. 130–137.
- Feng Z.-Q., Liu Y.-J., Li L., Jin W., Jiang L.-W., Li W.-M., Wen Q.-B., Zhao Y.-L. (2019) Geochemical and geochronological constraints on the tectonic setting of the Xinlin ophiolite, northern Great Xing'an Range, NE China. *Lithos*, Vol. 326–327, pp. 213–229, <http://dx.doi.org/10.1016/j.lithos.2018.12.018>
- Ferguson J., Fielding P.E. (1971) The origins of the colours of yellow, green and blue sapphires. *Chemical Physics Letters*, Vol. 10, No. 3, pp. 262–265, [http://dx.doi.org/10.1016/0009-2614\(71\)80282-8](http://dx.doi.org/10.1016/0009-2614(71)80282-8)
- (1972) The origins of the colors of natural yellow, blue, and green sapphires. *Australian Journal of Chemistry*, Vol. 25, No. 7, pp. 1371–1385, <http://dx.doi.org/10.1071/ch9721371>
- Galibert O., Hughes R.W. (1995) Chinese ruby and sapphire - a brief history. *Journal of Gemmology*, Vol. 24, No. 7, pp. 467–473.

- Giuliani G., Ohnenstetter D., Fallick A.E., Groat L.A., Fagan A.J. (2014) The geology and genesis of gem corundum deposits. In L.A. Groat, Ed., *Geology of Gem Deposits*, Mineralogical Association of Canada (MAC), pp. 29–112.
- Giuliani G., Pivin M., Fallick A.E., Ohnenstetter D., Song Y., Demaiffe D. (2015) Geochemical and oxygen isotope signatures of mantle corundum megacrysts from the Mbuji-Mayi kimberlite, Democratic Republic of Congo, and the Changle alkali basalt, China. *Comptes Rendus Geoscience*, Vol. 347, No. 1, pp. 24–34, <http://dx.doi.org/10.1016/j.crte.2014.12.003>
- Gu Z., Xie Y., Gao Y., Ren X., Cheng C., Wang S. (2018) Quantitative assessment of soil productivity and predicted impacts of water erosion in the black soil region of northeastern China. *Science of the Total Environment*, Vol. 637–638, pp. 706–716. <http://dx.doi.org/10.1016/j.scitotenv.2018.05.061>
- Gübelin E.J., Koivula J.I. (1986) *Photoatlas of Inclusions in Gemstones*. Opinio Verlag, Basel, Switzerland.
- Guo J., Wang F., Yakoumelos G. (1992) Sapphires from Changle in Shandong Province, China. *G&G*, Vol. 28, No. 4, pp. 255–260, <http://dx.doi.org/10.5741/GEMS.28.4.255>
- Hänni H.A. (1994) Origin determination for gemstones: Possibilities, restrictions, and reliability. *Journal of Gemmology*, Vol. 24, No. 3, pp. 139–148.
- Hsu T., Lucas A., Kane R.E., McClure S.F., Renfro N.D. (2017) Big Sky country sapphire: Visiting Montana's alluvial deposits. *G&G*, Vol. 53, No. 2, pp. 215–227, <http://dx.doi.org/10.5741/GEMS.53.2.215>
- Hu L., Pan S., Lu R., Zheng J., Dai H., Guo A., Yu L., Sun H. (2022) Origin of gem-quality megacrysts in the Cenozoic alkali basalts from the Muling area, northeastern China. *Lithos*, Vol. 422–423, article no. 106720, <http://dx.doi.org/10.1016/j.lithos.2022.106720>
- Huang W., Ni P., Shui T., Pan J., Fan M., Yang Y., Chi Z., Ding J. (2021) Trace element geochemistry and mineral inclusions constraints on the petrogenesis of a marble-hosted ruby deposit in Yunnan Province, China. *Canadian Mineralogist*, Vol. 59, No. 2, pp. 381–408, <http://dx.doi.org/10.3749/canmin.2000054>
- Jochum K.P., Nohl U., Herwig K., Lammel E., Stoll B., Hofmann A.W. (2005) GeoReM: a new geochemical database for reference materials and isotopic standards. *Geostandards and Geo-analytical Research*, Vol. 29, No. 3, pp. 333–338, <http://dx.doi.org/10.1111/j.1751-908x.2005.tb00904.x>
- Keller A.S., Keller P.C. (1986) The sapphires of Mingxi, Fujian Province, China. *G&G*, Vol. 22, No. 1, pp. 41–45, <http://dx.doi.org/10.5741/GEMS.22.1.41>
- Keller P.C., Wang F. (1986) A survey of the gemstone resources of China. *G&G*, Vol. 22, No. 1, pp. 3–13, <http://dx.doi.org/10.5741/GEMS.22.1.3>
- Koivula J.I., Fryer C.W. (1987) Sapphirine (not sapphire) in a ruby from Bo Rai, Thailand. *Journal of Gemmology*, Vol. 20, No. 6, pp. 369–370.
- Lafuente B., Downs R.T., Yang H., Stone N. (2015) 1. The power of databases: The RRUFF project. In T. Armbruster and R.M. Danisi, Eds., *Highlights in Mineralogical Crystallography*. De Gruyter, Berlin, pp. 1–30.
- Lannes B., Zhang C. (2020) China's unstoppable 2020 luxury market. Bain & Company, December 16, <https://www.bain.com/insights/chinas-unstoppable-2020-luxury-market/>
- Li Y., Xu W.-L., Zhu R.-X., Wang F., Ge W.-C., Sorokin A.A. (2020) Late Jurassic to early Cretaceous tectonic nature on the NE Asian continental margin: Constraints from Mesozoic accretionary complexes. *Earth-Science Reviews*, Vol. 200, article no. 103042, <http://dx.doi.org/10.1016/j.earscirev.2019.103042>
- Ling Y.-Y., Zhang J.-J., Liu K., Ge M.-H., Wang M., Wang J.-M. (2017) Geochemistry, geochronology, and tectonic setting of Early Cretaceous volcanic rocks in the northern segment of the Tan–Lu Fault region, northeast China. *Journal of Asian Earth Sciences*, Vol. 144, pp. 303–322, <http://dx.doi.org/10.1016/j.jseas.2016.12.025>
- Liu Y., Lu R. (2016) Gem News International: Ruby and sapphire from Muling, China. *G&G*, Vol. 52, No. 1, pp. 98–100.
- Liu Y., Hu Z., Gao S., Günther D., Xu J., Gao C., Chen H. (2008) In situ analysis of major and trace elements of anhydrous minerals by LA-ICP-MS without applying an internal standard. *Chemical Geology*, Vol. 257, No. 1–2, pp. 34–43, <http://dx.doi.org/10.1016/j.chemgeo.2008.08.004>
- Lu R. (2012) Color origin of lavender jadeite: An alternative approach. *G&G*, Vol. 48, No. 4, pp. 273–283.
- Lu R., Shen A.H. (2011) Lab Notes: Unusually high beryllium in three blue sapphires. *G&G*, Vol. 47, No. 3, pp. 232–233.
- Miquelle D., Darman Y., Seryodkin I. (2011) *Panthera tigris* ssp. *Altaica*. The IUCN Red List of Threatened Species, <https://www.iucnredlist.org>
- Palke A.C., Breeding C.M. (2017) The origin of needle-like rutile inclusions in natural gem corundum: A combined EPMA, LA-ICP-MS, and nanoSIMS investigation. *American Mineralogist*, Vol. 102, No. 7, pp. 1451–1461.
- Palke A.C., Wong J., Verdel C., Ávila J.N. (2018) A common origin for Thai/Cambodian rubies and blue and violet sapphires from Yogo Gulch, Montana, USA? *American Mineralogist*, Vol. 103, No. 3, pp. 469–479.
- Palke A.C., Saesaw S., Renfro N.D., Sun Z., McClure S.F. (2019a) Geographic origin determination of blue sapphire. *G&G*, Vol. 55, No. 4, pp. 536–579, <http://dx.doi.org/10.5741/GEMS.55.4.536>
- (2019b) Geographic origin determination of ruby. *G&G*, Vol. 55, No. 4, pp. 580–613, <http://dx.doi.org/10.5741/GEMS.55.4.580>
- Pan S., Zheng J., Griffin W.L., Xu Y., Li X. (2015) Nature and evolution of the lithospheric mantle beneath the eastern Central Asian Orogenic Belt: Constraints from peridotite xenoliths in the central part of the Great Xing'an Range, NE China. *Lithos*, Vol. 238, pp. 52–63, <http://dx.doi.org/10.1016/j.lithos.2015.09.013>
- Pardieu V. (2013) Blue sapphires and Beryllium: An unfinished world quest. *InColor*, Vol. 23, pp. 36–43.
- Peucat J.J., Ruffault P., Fritsch E., Bouhnik-Le Coz M., Simonet C., Lasnier B. (2007) Ga/Mg ratio as a new geochemical tool to differentiate magmatic from metamorphic blue sapphires. *Lithos*, Vol. 98, No. 1–4, pp. 261–274, <http://dx.doi.org/10.1016/j.lithos.2007.05.001>
- Powell R.C. (1998) *Physics of Solid-State Laser Materials*. Springer-Verlag, New York, 423 pp.
- Qiu Z., Yang J., Yang Y., Yang S., Li C., Wang Y., Lin W., Yang X. (2007) Trace element and hafnium isotopes of Cenozoic basalt-related zircon megacrysts at Muling, Heilongjiang province, northeast China. *Acta Petrologica Sinica*, Vol. 23, No. 2, pp. 481–492. Chinese with English abstract, <http://dx.doi.org/10.3969/j.issn.1000-0569.2007.02.024>
- Rankin A.H., Greenwood J., Hargreaves D. (2003) Chemical fingerprinting of some East African gem rubies by laser ablation ICP-MS. *Journal of Gemmology*, Vol. 28, No. 8, pp. 473–482.
- Renfro N.D., Palke A.C., Berg R.B. (2018) Gemological characterization of sapphires from Yogo Gulch, Montana. *G&G*, Vol. 54, No. 2, pp. 184–201, <http://dx.doi.org/10.5741/GEMS.54.2.184>
- Roedder E. (1962) Ancient fluids in crystals. *Scientific American*, Vol. 207, No. 4, pp. 38–47, <http://dx.doi.org/10.1038/scientificamerican1062-38>
- Schmetzer K., Bank H. (1981) The colour of natural corundum. *Neues Jahrbuch Fur Mineralogie-Monatshefte*, Vol. 11, No. 2, pp. 59–68.
- Schwarz D., Pardieu V., Saul J.M., Schmetzer K., Laurs B.M., Giuliani G., Klemm L., Malsy A.-K., Erel E., Hauzenberger C., Du Toit G., Fallick A.E., Ohnenstetter D. (2008) Rubies and sapphires from Winza, central Tanzania. *G&G*, Vol. 44, No. 4, pp. 322–347, <http://dx.doi.org/10.5741/GEMS.44.4.322>
- Smith G. (1978) Evidence for absorption by exchange-coupled Fe²⁺-Fe³⁺ pairs in the near infra-red spectra of minerals. *Physics and Chemistry of Minerals*, Vol. 3, No. 4, pp. 375–383, <http://dx.doi.org/10.1007/bf00311848>

- Sorokin A., Owens P., Láng V., Jiang Z.-D., Michéli E., Krasilnikov P. (2021) "Black soils" in the Russian soil classification system, the US Soil Taxonomy and the WRB: Quantitative correlation and implications for pedodiversity assessment. *CATENA*, No. 196, pp. 104824, <http://dx.doi.org/10.1016/j.catena.2020.104824>
- Sorokina E.S., Rassomakhin M.A., Nikandrov S.N., Karampelas S., Kononkova N.N., Nikolaev A.G., Anosova M.O., Som-sikova A.V., Kostitsyn Y.A., Kotlyarov V.A. (2019) Origin of blue sapphire in newly discovered spinel-chlorite-muscovite rocks within meta-ultramafites of Ilmen Mountains, South Urals of Russia: Evidence from mineralogy, geochemistry, Rb-Sr and Sm-Nd isotopic data. *Minerals*, Vol. 9, No. 1, pp. 36, <http://dx.doi.org/10.3390/min9010036>
- Su L. (1990) Sapphires from east of Heilongjiang Province. *Geology of Building Materials*, No. 2, pp. 11+10. Chinese with English abstract.
- Sun J.X. (1995) Basalts related to ruby and sapphire in eastern Heilongjiang and reconstruction of Paleovolcanic mechanism. *Acta Petrologica et Mineralogica*, No. 14, pp. 126–132. Chinese with English abstract.
- Sun J.X., Li F., Dang Y.S., Cui G., Zhou Y.B. (2005) Mineralogical features of ruby and sapphire from Heilongjiang Province. *Acta Petrologica et Mineralogica*, Vol. 24, No. 1, pp. 62–66. Chinese with English abstract, <http://dx.doi.org/10.3969/j.issn.1000-6524.2005.01.007>
- Sutherland F.L., Abduriyim A. (2009) Geographic typing of gem corundum: a test case from Australia. *Journal of Gemmology*, Vol. 31, No. 5-8, pp. 203–210.
- Sutherland F.L., Hoskin P.W.O., Fanning C.M., Coenraads R.R. (1998) Models of corundum origin from alkali basaltic terrains: a reappraisal. *Contributions to Mineralogy and Petrology*, Vol. 133, No. 4, pp. 356–372, <http://dx.doi.org/10.1007/s004100050458>
- Tatian B. (1984) Fitting refractive-index data with the Sellmeier dispersion formula. *Applied Optics*, Vol. 23, No. 24, pp. 4477–4485, <http://dx.doi.org/10.1364/AO.23.004477>
- Wang C., Yang Y., Li G. (1992) Oxidation treatment of the sapphires from Shandong Province, China. *Journal of Gemmology*, Vol. 23, No. 4, pp. 195–197.
- Wang C., Liu J., Zhang H., Ge J., Xi Z., Wang H. (2019) Mineralogical features and petrogenetic significance of the clinopyroxene and hornblende of the Wuhaolai mafic complex in northern North China Craton, Inner Mongolia. *Earth Sciences Research Journal*, Vol. 23, No. 2, pp. 133–146.
- Wang F. (1988) The sapphires of Penglai, Hainan Island, China. *G&G*, Vol. 24, No. 3, pp. 155–160, <http://dx.doi.org/10.5741/GEMS.24.3.155>
- Wang X.-K., Qiu S.-W., Song C.-C., Kulakov A., Tashchi S., Myasnikov E. (2001) Cenozoic volcanism and geothermal resources in northeast China. *Chinese Geographical Science*, Vol. 11, No. 2, pp. 150–154, <http://dx.doi.org/10.16509/j.georeview.1999.s1.147>
- Wang Y., Dou L.R. (1997) Formation time and dynamic characteristics of the northern part of the Tan-Lu fault zone in east China. *Seismology and Geology*, Vol. 19, No. 2, pp. 186–194.
- Wilhem C., Windley B.F., Stampfli G.M. (2012) The Altaids of Central Asia: A tectonic and evolutionary innovative review. *Earth-Science Reviews*, Vol. 113, No. 3-4, pp. 303–341, <http://dx.doi.org/10.1016/j.earscirev.2012.04.001>
- Wong J., Verdel C., Allen C.M. (2017) Trace-element compositions of sapphire and ruby from the eastern Australian gemstone belt. *Mineralogical Magazine*, Vol. 81, No. 6, pp. 1551–1576, <http://dx.doi.org/10.1180/minmag.2017.081.012>
- Zaw K., Sutherland F.L., Dellapasqua F., Ryan C.G., Yui T.F., Mernagh T.P., Duncan D. (2006) Contrasts in gem corundum characteristics, eastern Australian basaltic fields: trace elements, fluid/melt inclusions and oxygen isotopes. *Mineralogical Magazine*, Vol. 70, No. 6, pp. 669–687, <http://dx.doi.org/10.1180/0026461067060356>
- Zhang J., Zhou C., Hu C. (2003) Mineralization characteristics of gems in Ailaoshan structural belt, Yunnan Province. *Journal of Gems & Gemology*, Vol. 5, No. 3, pp. 27–30. Chinese with English abstract, <http://dx.doi.org/10.15964/j.cnki.027jgg.2003.03.010>
- Zhang Y.Q., Shi W., Dong S.W. (2003) Cenozoic deformation history of the Tancheng-Lujiang fault zone, North China, and dynamic implications. *The Island Arc*, Vol. 12, No. 3, pp. 281–293, <http://dx.doi.org/10.1046/j.1440-1738.2003.00395.x>
- Zhang Z., Ding H., Dong X., Tian Z., Mu H., Li M., Qin S., Niu Z., Zhang N. (2018) The eocene corundum-bearing rocks in the Gangdese arc, south Tibet: Implications for tectonic evolution of the Himalayan orogen. *Geoscience Frontiers*, Vol. 9, No. 5, pp. 1337–1354, <http://dx.doi.org/10.1016/j.gsf.2017.12.011>
- Zwaan J.C., Buter E., Mertz-Kraus R., Kane R.E. (2015) The origin of Montana's alluvial sapphires. *G&G*, Vol. 51, No. 4, pp. 370–391, <http://dx.doi.org/10.5741/GEMS.51.4.370>



Join our growing G&G Facebook group of more than 30,000 members, connecting gem enthusiasts from all over the world!



GEMS ON CANVAS: PIGMENTS HISTORICALLY SOURCED FROM GEM MATERIALS

Britni LeCroy

Pigments have been sourced from gemstones and gem materials for centuries. These colors have been applied to ancient cave drawings, classical canvas paintings, and modern artworks, revealing the evolution of the human creative experience as well as the history and progression of studies such as anthropology and chemistry. Red ochre, sourced from hematite, is one of the oldest pigments, used by early humans and even Neanderthals. Azurite was the backbone of blue pigments during the medieval and Renaissance periods. Malachite's use as a colorant can be traced back to 6000 BCE in Egyptian cosmetics and as late as the nineteenth century in Impressionist paintings. Certain colors, such as the red of cinnabar, diminished in popularity with the invention of more affordable synthetics. Other pigments, such as bone black, continue to be manufactured and used today. The most noble of all pigments, ultramarine sourced from lapis lazuli, was so costly and valuable that only the wealthiest members of society could afford it, and its use in paintings was reserved for these patrons. Lastly, an inference can be drawn that pigment evolution correlates with the rise of significant art movements, each causing a fundamental shift in the history of art.

The wearing and collecting of gems mark their bearers with powerful symbols of status and allure. Because of their high value, gems are researched with nondestructive methods to feed growing public interest in areas such as geographic origin, synthesis, and treatment. For a gemologist, causing damage to a stone is a cardinal sin. For a painter in the past, gem materials were coveted for their pigment potential. For centuries, perfectly viable gemstones met their fate between a mortar and pestle before becoming immortalized as paint on a canvas, mural, or cave wall. These pigments commemorated color as a means of communication beyond the limits of written or spoken language. Gem materials such as hematite, azurite, malachite, lapis lazuli, bone, ivory, and cinnabar have all played roles as pigments throughout history—for some, a role assumed long before their use as gem materials (figure 1). Pigment research is an important field encompassing geologists, artists, anthropologists, historians, and even gemologists who contribute their knowledge and expertise to a subject where these disciplines converge.

Pigment can be defined as the component of paint that contributes color (Siddall, 2018). Natural inorganic pigments are derived from rocks or minerals that have been processed to extract and concentrate the material's coloring agent (figure 2). Synthetic pigments are often chemically identical to their natural coun-

In Brief

- Gem materials have been used as pigments by artists for thousands of years. These colors can be seen in ancient cave paintings and modern canvas works alike.
- Historically, many of these pigments were very expensive and therefore only available to wealthy consumers such as churches and royal families.
- A correlation can be seen between pigment technology and historical art movements.

terparts but have been produced artificially. This distinction in a pigment's origin might seem negligible, but that is hardly the case. Synthetics strive to be chemically pure, and their crystal sizes are highly uniform. Natural pigments are never compositionally homogeneous, as rocks and minerals do not form in sterile environments. These slight imperfections in a natural pigment's particle size and structure after pro-

See end of article for About the Author and Acknowledgments.

GEMS & GEMOLOGY, Vol. 58, No. 3, pp. 318–337,

<http://dx.doi.org/10.5741/GEMS.58.3.318>

© 2022 Gemological Institute of America

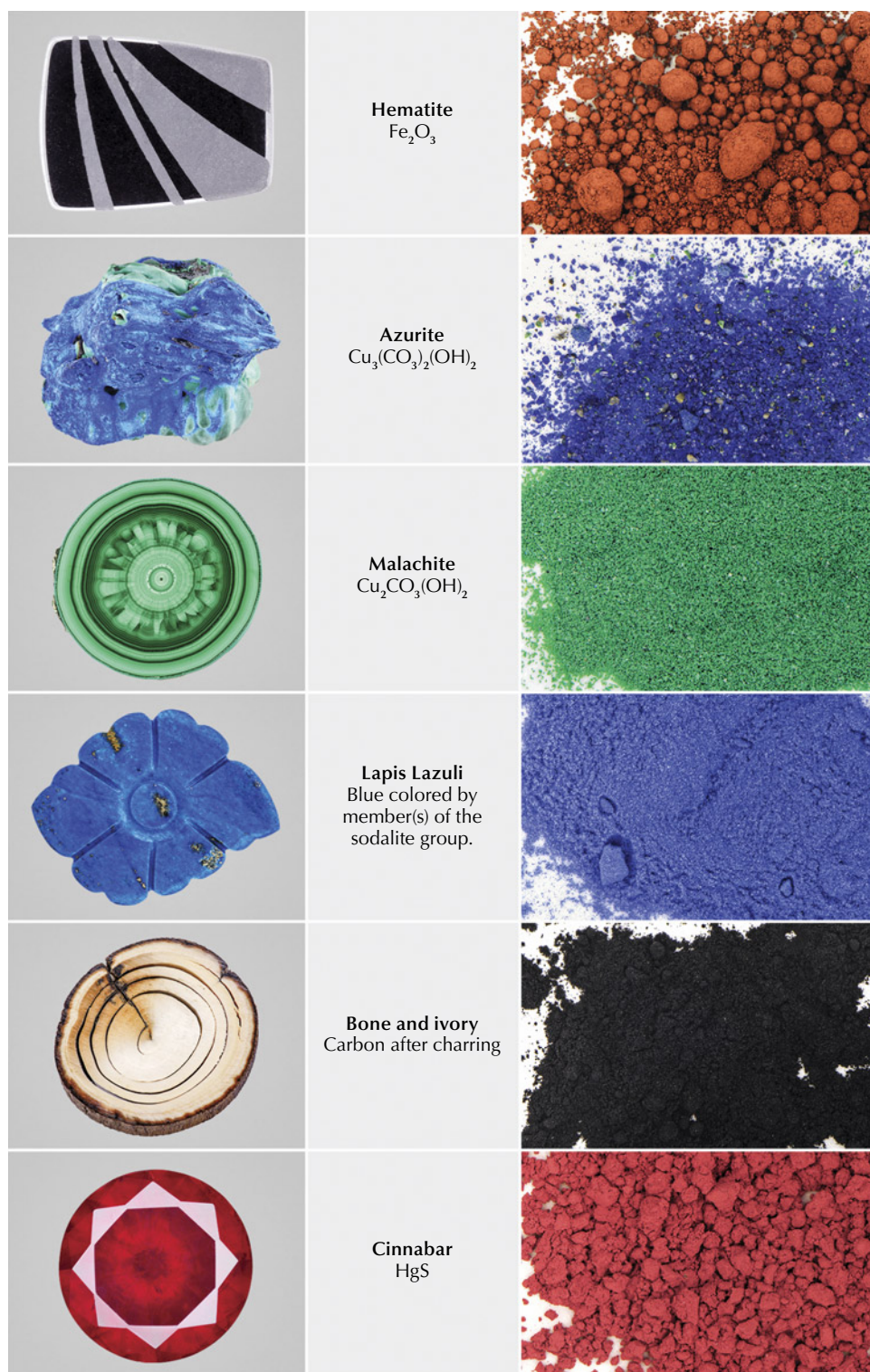


Figure 2. Gem materials and their corresponding pigments. The faceted cinnabar is courtesy of the Dr. Edward J. Gübelin Collection, and the polished hematite is courtesy of the GIA Collection. The other gem materials were gifted to GIA by Vincent Manson (polished malachite slice), Bill Pinch (polished azurite rough), Ebert & Company (lapis lazuli carving), and Richard Marcus (mammoth ivory slice). The malachite and azurite pigments are of coarse variety. Gem photos by Diego Sanchez and Dylan Hand. Pigment photos by Nathan Renfro.

processes, can also be inferred by comparing the first cave drawings with the acrylic paintings seen in art museums today. The former consists of natural pigments such as ochres (derived from iron oxides), charcoal, and simple organic colors, while today's

paintings very often contain 100% lab-created coloring agents. The advent of affordable, mass-produced synthetic pigments is the culmination of hundreds of years of research. Prior to this revolutionary development, creating paint was expensive

BOX A: ART CONSERVATION AND RESTORATION



Figure A-1. Raman analysis is conducted on Raphael's Scuola di Atene (The School of Athens). © Renishaw plc.

A more recent application of pigment research is in the area of art conservation and restoration. The practice is more of a science than an art, with pieces undergoing exposure to a variety of testing methods that are also commonplace in gemological laboratories. These include visible and Raman spectroscopy, as well as fluorescence techniques including infrared, ultraviolet, and X-ray. First, ultraviolet fluorescence reveals the presence and condition of organic materials and varnishes. X-ray fluorescence gives information about the elemental composition, while infrared can uncover the original un-

derdrawing and areas with paint loss. Raman spectroscopy (figure A-1) is used to identify minerals within the paint.

But the real magic is in the visible spectroscopy, which reveals the exact visible spectrum produced by the pigment. The spectrum is then matched to known pigments through an established database. This allows for exact color replicas to be used during the restoration process, thereby ensuring significant works of art remain compositionally correct for future generations to admire.

and highly laborious—each hue had to be mixed by hand, either by the artist or an assistant. Minerals needed for color often traveled great distances from the original source before reaching the artist, increasing the cost. The act of painting itself was reserved for those who could afford this luxury or those fortunate enough to be employed by royal fam-

ilies, the wealthy class, or the church. This is why most historical paintings are religious depictions or portraits of royalty and aristocrats.

The overlap of the scientific and historically artistic realms of gemstones (see box A) is a conversation not often encountered. The monetary worth and cultural significance of gems can be far inferior compared



Figure 3. Red hematite crystals in quartz. Photomicrograph by Nathan Renfro; field of view 7.22 mm.

to the value of the artworks they contribute to as pigments. Hematite, azurite, malachite, lapis lazuli, bone, ivory, and cinnabar have all been significant contributors to fine art throughout history (figure 2). While most of these pigments have been replaced by synthetic equivalents, some are still used to this day.

HEMATITE

One of the earliest gemstones known to have been used as pigment is hematite. The dark, metallic color associated with gem-quality hematite is a result of densely stacked deep red microscopic crystals that ultimately absorb most visible-color wavelengths. Hematite's red color can be seen when the mineral exists as either pulverized powder or thin crystals that allow light to pass through (figure 3). As one of the few gemstones with metallic luster, the iron oxide hematite crystallizes in the trigonal crystal system with the simple chemical formula of Fe_2O_3 . Its height of popularity as a gem was likely in the Victorian era, when it was used extensively in mourning jewelry.

Within the realm of art, the powdered pigment form is referred to as red ochre and has been used from the dawn of artistic expression. Red ochre can also be produced by heating the mineral goethite (FeOOH , yellow ochre), most commonly sourced from limonite rock (Siddall, 2018). The use of red ochre as a pigment has been recorded in works of art from all periods and traditions around the world, from the Pleistocene to the present day (Siddall, 2018). The first use of red ochre was likely in cave paintings and

as body paint. It was later used to represent blood in burial and fertility rites (Leonida, 2014), in addition to applications in sun protection, medicine, adhesives, and ceramic paint (Siddall, 2018).

The influence of red ochre on pigments is unparalleled. From the prehistoric art era (before 500 BCE) to the contemporary era, red ochre is pervasive. The earliest cave paintings from every habitable continent on Earth, revealing humans at their most primitive artistic abilities, feature red ochre. One well-known and researched example featuring this color is the cave art of Lascaux in France, dated to roughly 19,000 years ago (Musée d'Archéologie Nationale, n.d.), depicting wildlife such as bison and horses (figure 4). A younger example is the eerie Cueva de las Manos in Argentina, created 13,000 to 9,500 years ago (UNESCO World Heritage Convention, n.d.), which shows painted hand silhouettes (figure 5). It has become widely accepted by scholars that the adoption of red ochre is synonymous with the beginnings of art and therefore human intellectual evolution. In fact, the use of ochre and tool-making are two significant advances in human evolution, with the latter universally acknowledged as an indicator of humankind's intellectual, social, and cultural development (Wreschner et al., 1980). It can be theorized that the uniting of art and science began to take form with the use of red ochre.

The Blombos Cave archaeological site along the southern Cape coastline of South Africa has proved to be a major anthropological discovery related to red ochre. The pigment uncovered exists not as an application but as raw red ochre contained in abalone shells that slowly became buried by sands as they lay abandoned on the cave floor over thousands of years. Other materials found with the shells and ochre include cobbles, bones from seals and antelope, and stone tools. Together, these objects are believed to constitute prehistoric artistic "tool kits" dated to roughly 100,000 years old. Henshilwood and van Niekerk (2012) documented these materials and interpreted their significance: "What these findings tell us, is that the artisans who lived in Blombos Cave 100,000 years ago had the capacity for abstract thought, multi-tasking, long-term planning and an elementary knowledge of chemistry."

Until recently it was believed that cave painting was an exclusive trait of *Homo sapiens*. In 2018, a team of paleoanthropologists published data on uranium-thorium dating of a series of simple drawings found inside three Spanish caves. The works examined in that study consisted of dots, lines, discs, and



Figure 4. The famous Hall of the Bulls in the Lascaux Caves contains early cave paintings rendered in red ochre. Photo by JoJan/CC BY 4.0.

hand stencils, all created by red ochre (Netburn, 2018). All three were found to be at least 64,800 years old, which predates the arrival of humans in Europe by at least 20,000 years (Hoffmann et al., 2018). Neanderthals exclusively populated this region of modern-day Europe at the time, implying that the artists were indeed Neanderthals. Proof of their ability to create art helps dispel the popular misconception that Neanderthals were mentally inferior to *Homo sapiens*.

Nearly every canonized artist has used red ochre at some point. The color was also a traditional ingredient in sanguine, a type of chalk colored by red ochre (figure 6). Leonardo da Vinci grew fond of the material,

featuring it in numerous drawings during the Renaissance period. Da Vinci is credited with being the first



Figure 5. The entrance of Cueva de las Manos reveals red ochre hand stencils created by ancient Argentinian tribe members. Photo by Pablo A. Gimenez/CC BY SA 2.0.



Figure 6. Elisha Kirkall's mezzotint print in sanguine (chalk colored by red ochre) from the early eighteenth century is a reproduction of Raphael's *The Holy Family of Francis I* (1518). Photo courtesy of the National Gallery of Art, Washington, DC.

major artist to use this ochre variety (Millidge, 2003), and Michelangelo continued its reach. This period also popularized the use of red ochre in fresco murals. Paul Gauguin, one of the most famous painters of the Post-Impressionist movement, made it a staple of his palette. Red ochre's importance to modern artworks is incalculable. Twentieth-century masters such as Pablo Picasso, Mark Rothko, and Andy Warhol created works featuring the color, bringing it full circle. While most natural pigments have been far surpassed by synthetic pigments, red ochre is the exception. Red ochre paints continue to be predominantly made with

natural hematite or heated goethite due to the abundance and low cost of these materials.

AZURITE AND MALACHITE

Malachite, $\text{Cu}_2(\text{CO}_3)(\text{OH})_2$, is perhaps the first vivid green pigment (Bergslien, 2012). A basic carbonate of copper, it is the weathered form of the blue parent mineral azurite, $(\text{Cu}_2^{3+}(\text{CO}_3)_2(\text{OH})_2)$, and possesses a similar chemical formula. Azurite and malachite are rarely found exclusive from one another and form in exposed areas of copper ore. Both minerals have a monoclinic crystal structure and a low Mohs hard-



Figure 7. Pacino di Bonaguida's The Martyrdom of Saint Lawrence from the *Laudario of Sant'Agnese*, circa 1340. This page from an illuminated manuscript features a brilliant blue azurite tempera background as well as gold leaf appliqué. Photo courtesy of the Getty Open Content Program.

ness of 3.5–4.0. Malachite has been used extensively as a decorative material since antiquity. Azurite's decorative use has been far more limited by its low durability and high likelihood of breaking along cleavage planes. It has mainly been reserved for pigments.

Possibly the earliest application of azurite and malachite came in the form of cosmetics. Malachite pigment can be traced to ancient Egypt, where it was used as an eye paint during the predynastic period, spanning from 6000 BCE to 3100 BCE (Gettens and FitzHugh, 1993b). Likewise, high-purity, coarsely ground azurite particles have been traced to Neolithic female and infant burial sites at the Central Anatolian site of Çatalhöyük (modern-day Turkey) and dated to 6700 BCE (Siddall, 2018), where the mineral was also likely used as a cosmetic material. The same era saw both minerals used in the Middle East to color soapstone ornaments, beginning around 4500 BCE (Ball, 2002).

Although azurite is far less abundant than malachite, azurite pigment has been utilized more widely. It was the most important blue pigment in Europe throughout the medieval period (figure 7) and en-

joyed peak use during the Renaissance (Gettens and FitzHugh, 1993a). This is because of its dual role as not only a royal color but also as an underpaint for the lavish ultramarine (a pigment from lapis lazuli). Both pigments were used for centuries in Japan, in Ukiyo-e style paintings (sixteenth through nineteenth centuries; Gettens and FitzHugh, 1993a,b) and malachite in screen and scroll paintings to the present day (figure 8). Historical Chinese artworks also feature the two extensively, spanning hundreds of years.

Copper and copper-containing metals are most commonly associated with bright green patina, a color and pigment material known as verdigris. Chinese history reveals one cunning application of malachite in imitation of verdigris. Beginning around 1000 CE, patina—the surface discoloration of certain metals from long periods of oxidation—became associated with ancient bronzes unearthed in China (Craddock, 2003). This feature became a sought-after trait among antique bronze collectors, offering a sense of authenticity. Bronze statues excavated and collected during the Song (960–1279 CE), Ming (1368–1644 CE), and Qing (1644–1911 CE) dynasties



Figure 8. Irises at Yatsubashi (Eight Bridges) by Ogata Korin, from the early eighteenth century. These famous screens feature a flat malachite green and deep azurite blue on gold foiled paper. The two minerals also coexist in nature. Photo courtesy of the Metropolitan Museum of Art.

were often imitated by carefully painting replicas with malachite pigment to achieve a faux patina effect. Blue azurite patina is less prevalent but still possible in specific conditions.



In European easel painting, malachite was vitally important from the fourteenth to seventeenth centuries, until the rise of copper greens such as verdigris and copper resinate (Eastaugh et al., 2004). Synthetic green pigments replaced malachite around 1800 (Bergslien, 2012). Malachite experienced a brief resurgence later in the nineteenth century, and it was during this period that Pierre-Auguste Renoir painted *Chrysanthemums* (figure 9). Renoir helped solidify the Impressionist movement along with contemporaries such as Monet, Cézanne, Degas, and Manet. Impressionism is distinguished by short, coarse brushstrokes creating a spontaneous unfinished appearance, vibrant color palettes, and themes of nature. The movement was bolstered by readily available premade oil paints in tubes (Newman et al., 2019). This brought unprecedented mobility, allowing pioneering artists to take their work outdoors. The movement thrived from the mid- to late nineteenth century and is considered the most important influence on modern art, since it did not follow established conventions.

Figure 9. Renoir's *Chrysanthemums* (1881–1882, oil on canvas) utilizes green malachite pigment and exemplifies the Impressionist style. Photo courtesy of the Art Institute of Chicago.

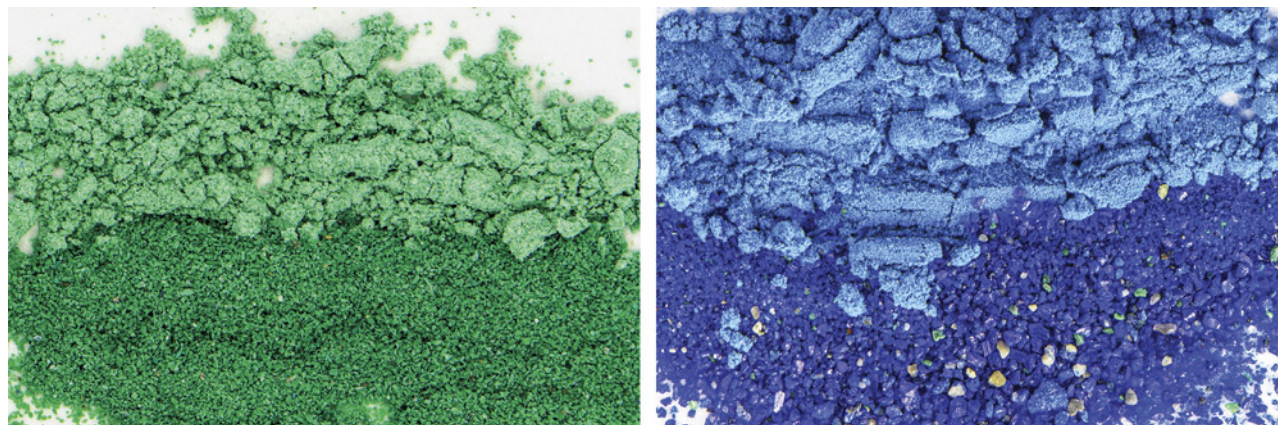


Figure 10. Malachite (left) and azurite (right) display contrasting saturations resulting from different particle sizes. The soft pastel saturation shown at the top of each photo is a result of very fine pigment grains measuring an average of 30 μm (malachite) and 20 μm (azurite). The vibrant, strongly saturated variety shown at the bottom of each photo is due to larger, coarser particles averaging 100 μm and 220 μm , respectively. Photomicrographs by Nathan Renfro; field of view 14.10 mm.

One inconvenience drove malachite and azurite into obscurity as pigments: the fact that their color is dependent on particle size (figure 10). Finely ground material offers a preferable texture for canvases but reduces the color to an undesirable milky pastel. Coarse particles offer a radiant hue but are difficult to paint in layers. Azurite became obsolete in the nineteenth century with the invention of the artificial pigment Prussian blue (Gettens and FitzHugh, 1993a).

LAPIS LAZULI

Lapis lazuli is a complex metamorphic rock consisting of a variety of minerals, often including calcite, pyrite, diopside, amphibole, and feldspathoid silicates, among others. The blue color source within lapis remains an open question. Lazurite is commonly believed to be the blue constituent, but several publications have credited the mineral haüyne. The two minerals, along with sodalite and nosean, are members of the sodalite group. Several studies have shown that haüyne (sulfate member) rather than lazurite (sulfide member) is consistently the dominant species in lapis from Sar-e-Sang in Afghanistan and Baffin Island in Canada (Hassan et al., 1985; Fleet et al., 2005; Moore and Woodside, 2014). Meanwhile, specimens from the Coquimbo region of Chile have been characterized as lazurite-dominant (Coenraads et al., 2000).

Of all the natural pigments created throughout history, ultramarine, a blue derived from lapis lazuli,

reigned supreme. Cennino Cennini was a fifteenth-century Italian painter and author of *The Craftsman's Handbook* (1437), an artist's manual on methods and techniques that remains remarkably relevant today. Cennini held the pigment in the highest regard: "Ultramarine blue is a color illustrious, beautiful, and most perfect, beyond all colors; one could not say anything about it, or do anything with it, that its quality would not still surpass." During its prime, the blue was deemed so sacred that it was reserved for the most important works and only the holiest of religious figures. Ultramarine was said to be as expensive as an equal weight of gold. Its high cost was due to the inconvenience of only one source location supported by the arduous procedure required to process the rock into pure pigment. Lapis lazuli's life as a pigment can be traced to the origins of human civilization itself.

While blue seems abundant in nature given the color of the sky and sea and other smaller examples, none of these actually contain a blue pigment. Instead, the blue color of the sky is a result of light scattering off the molecules in the atmosphere, called Rayleigh scattering. Sea water is blue due to the preferential absorption of long-wavelength (red) light. The cause of blue in both cases is a result of light physics rather than chemical properties. Only a handful of plants and animals possess a genuine blue pigment. This left few options for artists of the past. Azurite was predominant from the medieval period to the Renaissance (Plesters, 1993). Its limitation is a typically green undertone that cannot be removed. In contrast, ultramarine often contains a violet to purplish undertone

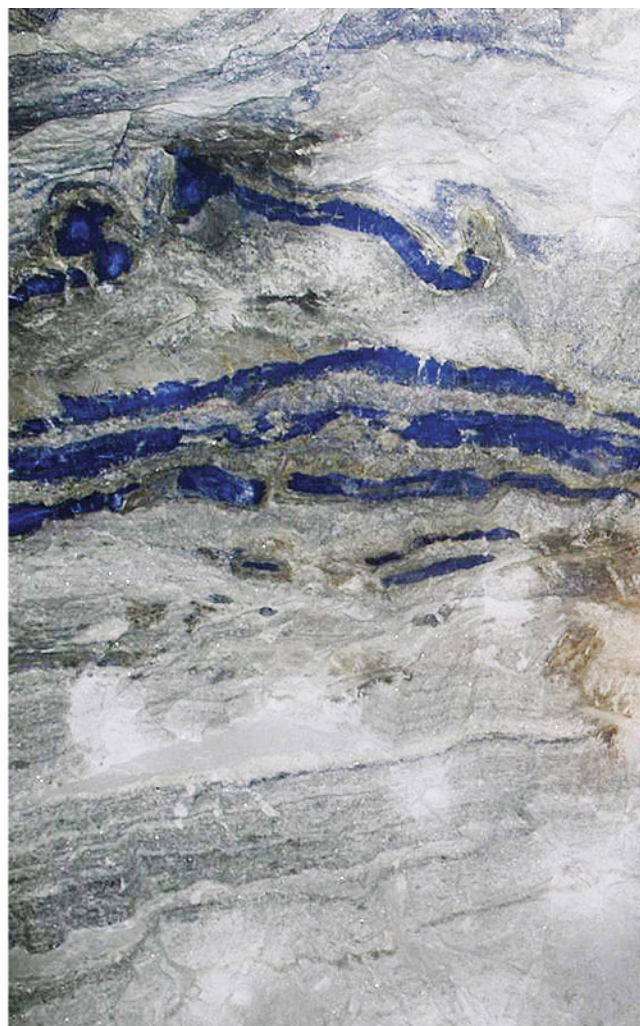


Figure 11. Left: A miner at the Sar-e-Sang mines in Afghanistan. Right: Veins of blue lapis lazuli stand out in contrast to its carbonate host rock. Photos by Gary Bowersox.

(figure 2), creating an unequivocal color that came to be associated with divinity.

Due to its geological rarity, lapis lazuli sourced in antiquity originated from a single location—the Sar-e-Sang mines in the Badakhshan Mountains of north-eastern Afghanistan (Siddall, 2018) (figure 11). Lapis mining at Sar-e-Sang began in the Stone Age, with lapis jewelry found in graves of the Mehrgarh people (a Neolithic settlement located in present-day south-west Pakistan) dated to 7000 BCE.

Lapis was exported to the ancient Sumer civilization of Mesopotamia around 3000 BCE before arriving in Egypt during predynastic times and becoming prevalent by the First Dynasty (ca. 3100–2900 BCE) (Moore and Woodside, 2014). Egyptians utilized lapis in jewelry and decorative inlays, medicinal preparations, and cosmetic pigments. Perhaps the most famous artifact of ancient Egypt, the funerary mask of

the pharaoh Tutankhamun, features a variety of inlaid gems: obsidian, white quartz, lapis lazuli, turquoise, amazonite, carnelian, and other stones (Reeves, 2015). A portion of the lapis inlay serves as Tutankhamun's eyeliner, a representation of the cosmetic pigment worn by the elite.

The earliest discovery of ultramarine was in oil paintings on cave walls in Bamiyan, Afghanistan, likely created in the late sixth century and consisting of Buddhist subjects drawn in semi-Indian, semi-Persian style (Gettens, 1938). Significantly, this finding also revealed the oldest known use of oil as a binder (Cotte et al., 2008). Ultramarine emerged in Europe during the early medieval period (Siddall, 2018) and rose in popularity into the fourteenth to mid-fifteenth centuries, when it was used heavily in panel paintings and illuminated manuscripts (Plesters, 1993). In paintings from the fourteenth to sixteenth



Figure 12. Illuminated manuscripts were one-of-a-kind, ornately illustrated books typically devoted to Christian scripture or themes. They often featured the Virgin Mary and Christ in robes of ultramarine blue that became synonymous with their image. This page from Georges Trubert's Book of Hours (1480–1490) combines tempera colors, gold leaf, inks, and metallic paints on parchment. Photo courtesy of the Getty Open Content Program.

centuries, the highest-quality ultramarine was reserved for the cloaks of Christ and the Virgin Mary (Plesters, 1993) (figure 12). Ultramarine was the most expensive pigment during its prime, meaning it could only be used sparingly (Plesters, 1993).

Ultramarine's popularity was bolstered by the mass publication of the process required to extract pigment from lapis lazuli. Because lapis lazuli is a rock containing various accessory minerals such as calcite and pyrite, the measures used in the preparation of azurite such as simple milling, washing, and

sieving were not sufficient (Plesters, 1993). The accessory minerals, especially pyrite, would darken and discolor ultramarine's brilliant blue if not extracted. Cennini documented the extraction process in *The Craftsman's Handbook*, and his method is still used today. It involves repeatedly crushing and sieving the highest-quality lapis. The powder is then worked into a dough with various waxes and kneaded under a liquid solution of lye. The fine blue particles slowly precipitate out of the dough and into the solution, while heavier materials such as pyrite are retained. Once the liquid has evaporated, one is left with ultramarine. The process can take up to several months—another factor influencing its high cost. The ensuing centuries saw ultramarine blue ascend to unequalled prestige in Europe, and works featuring the color went on to achieve everlasting fame (figures 13 and 14).

Figure 13. This blue drapery around the arms of the Virgin Mary is perhaps the most vivid example of ultramarine in classical art, in Giovanni Battista Salvi da Sassoferrato's *The Virgin in Prayer* (1640–1650, oil on canvas). Photo courtesy of the National Gallery, London.





Figure 14. Girl with a Pearl Earring (ca. 1665, oil on canvas), Johannes Vermeer's most celebrated painting, depicts a girl wearing an ultramarine turban and an exceptionally large pearl earring. Pearl was the most valuable of gems at the time. Other pigments include cinnabar (lips) and bone black (background and the turban's shadows). Photo courtesy of the Mauritshuis, The Hague.



Figure 15. A meeting of Greek mythological figures is imagined in Titian's *Bacchus and Ariadne* (1523, oil on canvas). Ariadne (far left) wears a robe in ultramarine and a red vermillion sash. Ultramarine is also featured in the sky and distant landscape. Malachite is used in the green foliage to the right of Bacchus. The sea and greener areas of the distant landscape are composed of azurite. Photo courtesy of the National Gallery, London.

While ultramarine most often appeared in Christian art, it was sometimes used to create a picturesque sky on canvas. The sky's features mimicked those of lapis lazuli, whose scintillating pyrite and globules of calcite in a sea of deep blue resemble stars and clouds. This hallmark is seen in *Bacchus and Ariadne* (figure 15), one of Titian's most famous works, which also incorporates azurite, malachite, and cinnabar.

For a color as fabled as ultramarine, it is only fitting that its decline would also be chronicled. In 1824, France's Society for the Encouragement of National Industry announced a contest for synthesizing artificial ultramarine, with a prize of 6,000 francs (Plesters, 1993). Four years later, a process was discovered and Jean Baptiste Guimet was named the winner. This synthetic, often referred to as "French ultramarine," sold for approximately one-tenth the cost of the natural material. In the mid-nineteenth century, it was manufactured throughout Europe and quickly outsold the natural variant, as it still does today.

BONE AND IVORY

For centuries, bone and ivory have been used to create black pigments. These materials are complex, consisting of both organic and inorganic compounds. Most recent studies have identified the composition as carbonate hydroxylapatite (Eastaugh et al., 2004). When bone or ivory is heated in the absence of oxygen via a closed crucible, black pigment is produced. The carbon source is primarily the protein collagen (Winter and FitzHugh, 2007), which is incorporated in the matrix of the material.

Bone is one of the oldest known gem materials. Recently, archaeologists discovered a more than 46,000-year-old aboriginal nose ring made of bone at a site in Western Australia, the oldest bone implement found on the continent (Langley et al., 2016). A variety of animal bones have been used as pigment source material throughout history, including cattle and lamb and possibly even human remains in earlier centuries (Finlay, 2002). Documents from the current largest producer of bone black pigment in the United States, Ebonex Corporation, specify charcoaled cow

bone as their source material (Ebonex Corporation Activity Report, 2018).

The Roman naturalist Pliny the Elder credited the development of ivory black to Apelles, the most notable painter of ancient Greece, though none of his

Figure 16. A single piece of carved ivory, ca. 1390–1352 BCE, holds six pigment cakes and is inscribed with the name “Amenhotep III,” the ninth pharaoh of the Eighteenth Dynasty of Egypt. Photo courtesy of the Metropolitan Museum of Art.



works have survived (Pliny, 77 CE). As the name implies, genuine ivory black was created from ivory wastes. These wastes were in relative abundance from the fifteenth to nineteenth centuries, as ivory was widely traded throughout many parts of the world. It was fashioned into jewelry, tools, weapons, containers, musical instruments, billiard balls, and other novelties (Smithsonian National Museum of African Art, 2019). Ivory black pigment was manufactured until the end of World War II (Kremer Pigmente, 1985). Due to species protection measures, all ivory black sold on the market today must be sourced solely from old stock (Kremer Pigmente, 1985) or be composed of high-grade bone black (Winter and FitzHugh, 2007). Ivory black is reportedly more intensely black than bone black, but this is arguably due to the pigment simply being more carefully made, since ivory has always been more scarce than bone (Winter and FitzHugh, 2007). Ivory was also used for paint palettes in previous centuries (figure 16).

Bone black has been found in prehistoric, Egyptian, Greek, Roman, medieval, and Renaissance art (Coles, 2018). Optical microscopy revealed its use on gravestones in ancient Greece from the third to second century (Winter and FitzHugh, 2007). Ivory and bone black have been scientifically identified in western European art dating from at least the fifteenth century into the twentieth century, including works by Tintoretto, Rubens, Rembrandt, Manet, and Renoir (Winter and FitzHugh, 2007). An extensive analysis of works in the Museum of Pablo Picasso in Paris concluded that 62 of his paintings contained either ivory or bone black (Winter and FitzHugh, 2007). Modern artist Kazimir Malevich, who founded the Suprematism movement and (along with Picasso) helped propel and popularize abstract art, featured ivory black in his signature geometric style (figure 17).

The process for creating white pigment from bone can be duplicated in the presence of oxygen. Essentially the ash that remains after all organic material has been destroyed, bone white was first used in the Neolithic period (Coles, 2018), primarily as a paper preparation in metalpoint drawing. In this technique, a soft metal writing utensil (silver, gold, or copper) grazes across a paper that has been primed, usually with bone white pigment mixed with rabbit skin glue. Bone ash possesses a slightly abrasive quality, allowing the metal to exfoliate and adhere to the primed surface, similar to a modern graphite pencil against paper. Graphite eventually became more popular because it was easier to use, causing metalpoint to fade into ob-

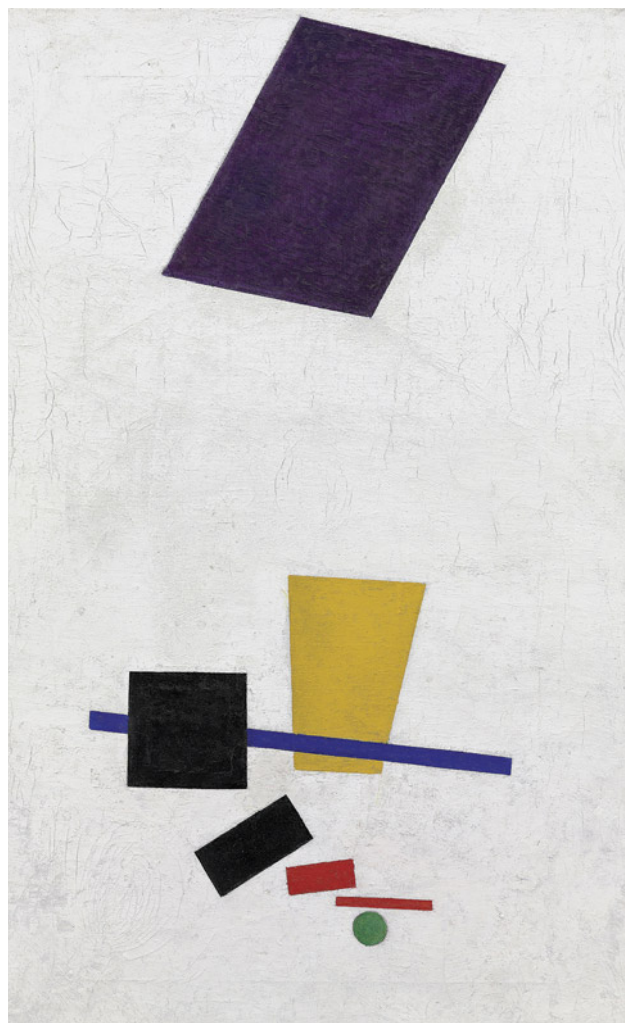


Figure 17. Kazimir Malevich's *Painterly Realism of a Football Player—Color Masses in the 4th Dimension* (1915, oil on canvas) features ivory black, artificial ultramarine blue, and vermilion red. The work is painted in the Suprematist style, a movement focused on geometric shapes and a limited range of colors. Photo courtesy of the Art Institute of Chicago.

scurity. While bone ash has little use as a modern-day pigment, bone black is still sold at art stores.

CINNABAR

Cinnabar (HgS) is an intensely colored mercury sulfide mineral and the principal ore of mercury. It is not abundant in the earth's crust, and only a handful of important deposits occur in Europe, the Middle East, and Asia. It is usually found with a massive habit, though well-formed, gem-quality single crystals are occasionally discovered (figure 2). Its hue is a strikingly vivid red with a strong orange component, unlike the comparatively dark and common red

ochre. In its simplest form, cinnabar's color is derived from simply crushing and grinding the mineral in a stone mortar. A synthetic form, commonly referred to as vermilion, has existed for several centuries and is obtained from synthesizing mercury and sulfur. After ultramarine, cinnabar was historically the most valuable and prestigious pigment in the trade, with Spanish and Chinese sources being the most significant (Siddall, 2018).

One of the earliest uses of cinnabar as pigment was in the Middle East in Çatalhöyük, an early human settlement from 7100 BCE to 5700 BCE, where it has been found in paintings and burial contexts (Çamurcuoğlu, 2015). Of the more than 800 Dead Sea Scrolls discovered in Israel and considered the world's earliest copies of biblical books, four fragments have been shown to contain red ink composed of cinnabar (Nir-El and Broshi, 1996). Ancient Romans indulged in the use of the pigment in wall paintings, assigning it great importance and sacred associations (Spindler, 2018) (figure 18). Pure cinnabar pigment could turn black when exposed to light, prompting the Roman scholars Vitruvius and Pliny the Elder to use a coating of oil or wax in their work (Eastaugh et al., 2004). Recent studies have shown that this discoloration is actually associated with cinnabar that has either been exposed to halogen or contains traces of chlorine (Eastaugh et al., 2004).

Cinnabar also experienced a widespread cultural diffusion in China. During the Shang and Zhou dynasties (1600–256 BCE), it was used for strewing of remains in grave burials, presumably to preserve the dead (Gettens et al., 1993). Treasured in Chinese alchemy, cinnabar was an important ingredient in recipes for preparing the philosopher's stone (a mythical substance believed to turn common metals into gold) and medieval pharmaceutical elixirs (Gettens et al., 1993). Traditional Chinese medicine prescribed powdered cinnabar to treat a variety of medical conditions including skin infections and intestinal disorders (Liu et al., 2008). Many of these cinnabar remedies are still used in Chinese medicine.

Cinnabar pigment was used considerably in Chinese lacquerware—a material that dates to 7000 BCE and is still produced today (Siddall, 2018). Lacquer is a resin primarily sourced from the tree species *Toxicodendron vernicifluum*. When exposed to oxygen and dried, it transforms into a natural plastic that is resistant to heat and water. Lacquerware is created from a base of turned wood with 30 to 200 layers of lacquer applied (Metropolitan Museum of Art, 2009). Once hardened, lacquer can be elaborately carved into geo-



Figure 18. This Roman fresco features what is believed to be a Macedonian queen or princess (seated) playing a gilded kithara beside her daughter or younger sister. Both are adorned with gold bracelets, earrings, and headbands with a central medallion, suggesting royalty. The background features a profuse display of expensive cinnabar pigment. Wall painting from Room H of the Villa of P. Fannius Synistor at Boscoreale, ca. 50–40 BCE. Photo courtesy of the Metropolitan Museum of Art.

metric motifs or extraordinary representations of earth, water, or sky (figure 19). These items were most often colored red and became known as “cinnabar lacquer.”

Vermilion is an artificially created cinnabar that can be produced through either a wet or dry process. The dry process may have been invented in China before spreading west through Arab traders, with the first documentation of this process originating in the eighth century (Gettens et al., 1993). Medieval recipes for dry-process vermillion involve combining mercury with molten sulfur and heating until the compound sublimes and condenses. The final product is a red crystalline modification of mercury sulfide. It is then treated with an alkali solution to remove free sulfur, washed, and ground under water in preparation as pigment. The wet process, discovered in the seventeenth century, calls for the combination of mercury sulfide and a heated solution of ammonium or potassium sulfide. This process was more cost efficient and became the favored method of vermillion production in the West. Obscure in the eighth century, vermillion had become mainstream by the fourteenth century (Gettens et al., 1993). Unlike malachite and azurite, cinnabar and vermillion are strong light absorbers whose colors are preserved at all particle sizes.

Vermilion was an important color in illuminated manuscripts as it was used to paint the *rubricae* (text written/printed in red ink for emphasis) and imagery. It became a staple from the fourteenth century onward (Gettens et al., 1993), appearing in the works of Vermeer (figure 14), Titian (figure 15), and Degas (figure 20). In the early nineteenth century, cadmium red was introduced and began to take the place of vermillion (Melo and Miguel, 2010), which had already surpassed cinnabar in production and usage. Cadmium pigments have since become the standard for brilliant, lightfast, and weather-resistant yellow, red, and orange paints.

CONCLUSIONS

Many historical pigments led double lives as gem materials, and both commodities have retained value over time. While the beauty of gems is appreciated by society, art viewers are often unaware that acclaimed paintings from the prehistoric to postmodern eras feature colors obtained from ornamental materials. Pigments and gems are further intertwined by their ability to reveal anthropological information about humankind’s comprehension of the natural world. With a better understanding of chemistry, the synthesis of both pigments and gemstones



Figure 19. Objects carved from cinnabar lacquer. Left: A stem cup with lychee and vines, from late-fifteenth/early-sixteenth century China. Right: A covered box with butterflies, gourds, and scrolling vines, from eighteenth-century China. Photos courtesy of the Art Institute of Chicago.

inevitably followed. The availability of a variety of gem materials shaped the development of pigments, which in turn shaped the history of art. As art is

merely a psychological reflection of and reaction to our environment, the conversation of art has contributed to the shaping of humankind itself.

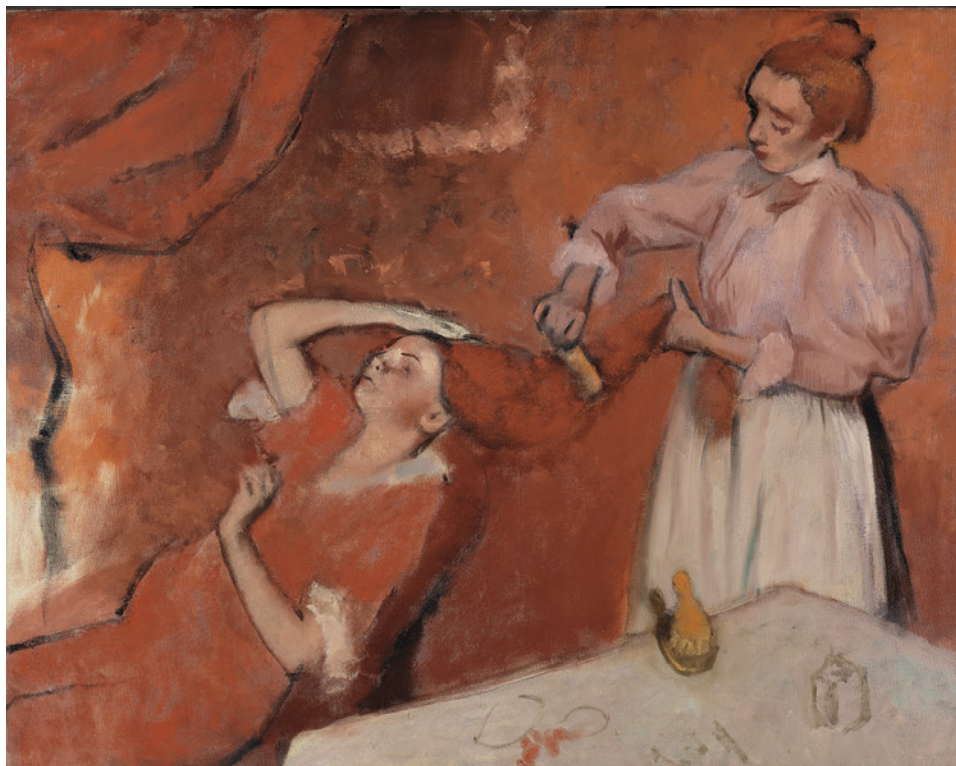


Figure 20. Combing the Hair (La Coiffure) by Edgar Degas (1896, oil on canvas) is a near-mono-chromatic celebration of red, showcasing vermillion, red ochre, and red lead pigments. Photo courtesy of the National Gallery, London.

ABOUT THE AUTHORS

Britni LeCroy is a staff gemologist at GIA in Carlsbad, California

ACKNOWLEDGMENTS


The author is grateful to GIA's Nathan Renfro for advising on this project. Many thanks to colleagues from GIA's Richard T. Liddicoat Library: Judy Colbert, for her expertise on image use and copyright; Augustus Pritchett, for help sourcing books and aca-

demic articles; and Robert Weldon, for providing an original photo. The author is also grateful for the support of McKenzie Santimer from the GIA Museum. Special thanks to these museums for images featured in this article: the Mauritshuis, the National Gallery of Art, the J. Paul Getty Museum, the Metropolitan Museum of Art, and the Art Institute of Chicago. Gary Bowersox and Renishaw plc are thanked for permission to use their images. All pigments pictured in this article are from Sinopia Pigments.

REFERENCES

- Ball P. (2002) *Bright Earth: Art and the Invention of Color*. Penguin, UK.
- Bergslien E. (2012) *An Introduction to Forensic Geoscience*. Wiley-Blackwell, Hoboken, New Jersey, p. 302.
- Çamurcuoğlu D.S. (2015) The wall paintings of Çatalhöyük (Turkey): Materials, technologies and artists. University College London, p. 233.
- Carr R.J. (2002) Evaluation of adhesive binders for the preservation of in-situ aboriginal surface finishes at Mesa Verde National Park. Master's thesis, University of Pennsylvania, Philadelphia.
- Cennini C. (1437) *The Craftsman's Handbook*. Reprinted by Dover Publications Inc., New York, 1954, pp. 25, 36–39.
- Coenraads R.R., de Bon C.C. (2000) Lapis lazuli from the Coquimbo region, Chile. *G&G*, Vol. 36, No. 1, pp. 28–41, <http://dx.doi.org/10.5741/GEMS.36.1.28>
- Coles D. (2019) *Chromatopia: An Illustrated History of Color*. Thames and Hudson, New York, pp. 23–25.
- Cotte M., Susini J., Solé V.A., Taniguchi Y., Chillida J., Checroun E., Walter P. (2008) Applications of synchrotron-based micro-imaging techniques to the chemical analysis of ancient paintings. *Journal of Analytical Atomic Spectrometry*, Vol. 23, No. 6, pp. 820–828, <http://dx.doi.org/10.1039/B801358F>
- Craddock P.T. (2003) Patina. Oxford Art Online: Grove Dictionary of Art, <http://dx.doi.org/10.1093/gao/9781884446054.article.T065767>
- Eastaugh N., Walsh V., Chaplin T., Siddall R. (2004) *Pigment Compendium: A Dictionary of Historical Pigments*. Elsevier Butterworth-Heinemann, Oxford, UK, pp. 57–58, 387.
- Ebonex Corporation Activity Report (2018) Michigan Department of Environmental Quality, http://www.deq.state.mi.us/aps/downloads/srn/P0871/P0871_SAR_20180725.pdf
- Finlay V. (2002) *Color: A Natural History of the Palette*. Random House, New York.
- Fleet M.E., Liu X., Harmer S.L., Nesbitt H.W. (2005) Chemical state of sulfur in natural and synthetic lazurite by S K-Edge XANES and X-ray photoelectron spectroscopy. *Canadian Mineralogist*, Vol. 43, No. 5, pp. 1589–1603, <http://dx.doi.org/10.2113/gscanmin.43.5.1589>
- Gettens R.J. (1938) The materials in the wall paintings of Bamiyan, Afghanistan. *Technical Studies in the Field of the Fine Arts*. Vol. 6, No. 3, pp. 186–193.
- Gettens R.J., FitzHugh E.W. (1993a) Azurite and blue verditer. In A. Roy, Ed., *Artists' Pigments: A Handbook of Their History and Characteristics, Volume 2*. National Gallery of Art, Washington, DC, and Archetype Publications, London, pp. 23–35.
- (1993b) Malachite and green verditer. In A. Roy, Ed., *Artists' Pigments: A Handbook of Their History and Characteristics, Volume 2*. National Gallery of Art, Washington, DC, and Archetype Publications, London, pp. 183–202.
- Gettens R., Feller R., Chase W.T. (1993) Vermilion and cinnabar. In A. Roy, Ed., *Artists' Pigments: A Handbook of Their History and Characteristics, Volume 2*. National Gallery of Art, Washington, DC, and Archetype Publications, London, pp. 159–182.
- Hassan I., Peterson R.C., Grundy H.D. (1985) The structure of lazurite, ideally $\text{Na}_6\text{Ca}_2(\text{Al}_6\text{Si}_6\text{O}_{24})\text{S}_{12}$, a member of the sodalite group. *Acta Crystallographica Section C*, Vol. 41, No. 6, pp. 827–832, <http://dx.doi.org/10.1107/S0108270185005662>
- Henshilwood C.S., Van Niekerk K.L. (2012) Middle Stone Age chemists: A 100,000 year old pigment processing workshop at Blombos Cave, South Africa. *The Digging Stick*, Vol. 29, No. 3, pp. 1–5.
- Hoffman D.L., Standish C.D., García-Díez M., Pettitt P.B., Milton J.A., Zilhão J., Alcolea-González J.J., Cantalejo-Duarte P., Collado H., de Balbín R., Lorblanchet M., Ramos-Muñoz J., Weniger G.-Ch., Pike A.W.G. (2018) U-Th dating of carbonate crusts reveals Neandertal origin of Iberian cave art. *Science*, Vol. 359, No. 6378, pp. 912–915, <http://dx.doi.org/10.1126/science.aap7778>
- Kremer Pigmente (1985) Ivory Black, <https://www.kremer-pigmente.com/elements/resources/products/files/11200e.pdf>
- Langley M.C., O'Connor S., Aplin K. (2016) A >46,000-year-old kangaroo bone implement from Carpenter's Gap 1 (Kimberley, northwest Australia). *Quaternary Science Reviews*, Vol. 154, pp. 199–213, <http://dx.doi.org/10.1016/j.quascirev.2016.11.006>
- Leonida M.D. (2014) Pigments. In *The Materials and Craft of Early Iconographers*. SpringerBriefs in Materials. Springer, Cham, Switzerland, pp. 15–40.
- Liu J., Shi J.-Z., Yu L.-M., Goyer R.A., Waalkes M.P. (2008) Mercury in traditional medicines: Is cinnabar toxicologically similar to common mercurials? *Experimental Biology and Medicine*, Vol. 233, No. 7, pp. 810–817, <http://dx.doi.org/10.3181/0712-MR-336>
- Melo M.J., Miguel C. (2010) The making of vermilion in medieval Europe: Historically accurate reconstructions from *The book on how to make colours*. NOVA University Lisbon. Available at researchgate.net
- Metropolitan Museum of Art (2009) Cinnabar: The Chinese art of carved lacquer, <https://www.metmuseum.org/exhibitions/listings/2009/cinnabar>
- Millidge S. (2003) Chalk. Oxford Art Online: Grove Dictionary of Art, <http://dx.doi.org/10.1093/gao/9781884446054.article.T015736>
- Moore T.P., Woodside R.M. (2014) The Sar-e-Sang lapis mines. *Mineralogical Record*, Vol. 45, No. 3, pp. 280–336.
- Musée d'Archéologie Nationale (n.d.) Dating the figures at Lascaux, <https://archeologie.culture.fr/lascaux/en/dating-figures-lascaux>
- Netburn D. (2018) Case closed: Oldest known cave art proves Neanderthals were just as sophisticated as humans. *Los Angeles Times*, <https://www.latimes.com/science/sciencenow/la-sci->

- sn-neanderthals-were-artists-20180222-htmistory.html
 Newman G., McNair A., Goswamy B., Bloom J., Blair S., Okediji M., Brittenham C. (2019) Colour. Oxford Art Online: Grove Dictionary of Art, <http://dx.doi.org/10.1093/gao/9781884446054.article.T018806>
- Nir-El Y., Broshi M. (1996) The red ink of the Dead Sea Scrolls. *Archaeometry*, Vol. 38, No. 1, pp. 97–102, <http://dx.doi.org/10.1111/j.1475-4754.1996.tb00763.x>
- Pliny (77 CE) *Natural History*, Book XXXV, p. 293, https://www.loebclassics.com/view/pliny_elder-natural_history/1938/pb_LCL394.293.xml
- Plesters J. (1993) Ultramarine blue, natural and artificial. In A. Roy, Ed., *Artists' Pigments: A Handbook of Their History and Characteristics, Volume 2*. National Gallery of Art, Washington, DC, and Archetype Publications, London, pp. 37–65.
- Reeves N. (2015) Tutankhamun's mask reconsidered. *Bulletin of the Egyptological Seminar*, Vol. 19, pp. 511–526. Available at https://www.academia.edu/7415055/Tutankhamuns_Mask_Reconsidered_2015
- Siddall R. (2018) Mineral pigments in archaeology: Their analysis and the range of available materials. *Minerals*, Vol. 8, No. 5, article no. 201, <http://dx.doi.org/10.3390/min8050201>
- Smithsonian National Museum of African Art (2019) Ivory: Significance and protection, <https://africa.si.edu/collection/conservation/protect-ivory/>
- Spindler E. (2018) The story of cinnabar and vermilion (HgS) at The Met. The Metropolitan Museum of Art, <https://www.metmuseum.org/blogs/collection-insights/2018/cinnabar-vermilion>
- UNESCO World Heritage Convention (n.d.) Cueva de las Manos, Río Pinturas, <https://whc.unesco.org/en/list/936/>
- Winter J.W., FitzHugh E.W. (2007) Pigments based on carbon. In B.H. Berrie, Ed., *Artists' Pigments: A Handbook of Their History and Characteristics, Volume 4*. National Gallery of Art, Washington, DC, and Archetype Publications, London, pp. 1–37.
- Wreschner E.E., Bolton R., Butzer K.W., Delporte H., Häusler R., Heinrich A., Jacobson-Widding A., Malinowski T., Masset C., Miller S.F., Ronen A., Solecki R., Stephenson P. H., Thomas L. L., Zollinger H. (1980) Red ochre and human evolution: A case for discussion [and comments and reply]. *Current Anthropology*, Vol. 21, No. 5, pp. 631–644, <http://dx.doi.org/10.1086/202541>


2022

CONGRATULATIONS, G&G Challenge Winners

This year, readers from all over the world took the 2022 Gems & Gemology Challenge. Participants tested their knowledge by answering questions from the Spring 2022 issue. Those who earned a score of 75% or higher received a GIA Certificate of Completion. Participants who scored a 92% or higher are listed below.

Australia
Barbara Wodecki

India
Raju Jain

Malaysia
Arnold Cheong

Ukraine
Nataliya Vovk

United States
Krystal Barker
Robert Campbell
Kenneth Fogelberg
Jessica Kramer
Tim Richardson
Teresa Tolbert
Geraldine Vest
Kate Waterman
Thomas Wendt
Clifton Young

Answers
See pages 60–61 of the Spring 2022 issue for the questions.

1 (d), 2 (a), 3 (d), 4 (b), 5 (a), 6 (d), 7 (c), 8 (b), 9 (b), 10 (a), 11 (a), 12 (c), 13 (d), 14 (c), 15 (b), 16 (b), 17 (c), 18 (a), 19 (d), 20 (b), 21 (b), 22 (c), 23 (a), 24 (a), 25 (c)

Congratulations to the following participants who were randomly selected to receive a free one-year subscription to G&G:

Shawn Hall (Dallas) • Lucia Gori (Milan) • Yinxin (Caesar) Zhang (Toronto)

COLOR MECHANISM AND SPECTROSCOPIC THERMAL VARIATION OF PINK SPINEL REPORTEDLY FROM KUH-I-LAL, TAJIKISTAN

Yicen Liu, Lijian Qi, Dietmar Schwarz, and Zhengyu Zhou

The color mechanism of pink spinel from Kuh-i-Lal in the Pamir Mountains of Tajikistan was studied using photoluminescence, mid-infrared, and ultraviolet/visible spectroscopy. This included studying the variations in spectra after heating to a series of temperatures ranging from 300° to 1000°C. Laser ablation–inductively coupled plasma–mass spectrometry was used to measure the trace elements present. The results reveal that the color is caused by the combined effect of spin-allowed transitions of Cr^{3+} , Fe^{3+} , V^{3+} , and Fe^{2+} – Fe^{3+} intervalence charge transfer mechanisms. The photoluminescence spectra show that during heat treatment, the intensity of the N_1 peak (687 nm) and the full width half maximum of the R-line and N-lines increase with temperature. Following heating in the range of 750°–825°C, there is a linear relationship between temperature and the ratio of integral areas of the R-line and N-lines. The mid-infrared spectra indicate that the band at 581 cm^{-1} (ν_3) gradually disappears during the heating process, which is likely related to the variation of octahedral M–O and tetrahedral T–O bond length in the spinel lattice.

Spinel is a series of metal oxides with the general formula $(\text{A}_{1-i}\text{B}_i)^{\text{IV}}(\text{A}_i\text{B}_{2-i})^{\text{VI}}\text{O}_4$, in which A represents divalent cations such as Mg^{2+} , Fe^{2+} , Zn^{2+} , Mn^{2+} , Co^{2+} , or Ni^{2+} , while B represents trivalent cations such as Al^{3+} , Cr^{3+} , V^{3+} , or Fe^{3+} , IV and VI represent the tetrahedral site and octahedral site respectively, and i is the degree of distortion. Gem-quality spinel is composed mainly of MgAl_2O_4 . Due to the different chromophoric ions contained within the lattice, spinel comes in a diverse range of colors. For example, spinel containing Co^{2+} is commonly blue (Shigley and Stockton, 1984; Fregola et al., 2014; Chauviré et al., 2015; Long et al., 2018). Iron-rich spinel appears blue, green, or pink when iron is the dominant minor element. When iron largely replaces magnesium in the main lattice, spinel appears black (De Souza et al., 2001; Taran et al., 2005; Lenaz and Lughi, 2013; Andreozzi et al., 2019). Cr^{3+} - and V^{3+} -bearing spinel is typically orange, red, or magenta (Malsy and Klemm, 2010; Widmer et al., 2015; Giuliani et al., 2017; Malíčková et al., 2021). Yellowish green spinel is related to high manganese content (Andreozzi et al., 2019), while high zinc content is

commonly associated with a dark blue or dark green color (Fregola et al., 2014).

Spinel from the Kuh-i-Lal deposit in Tajikistan (figure 1) is mainly pink and purple, and it formed in the Goran metamorphic series of southwest Pamir Plateau. The lithology of the Golan area is high-grade metamorphic rock, and spinel occurs in the forsterite

In Brief

- Spin-allowed transitions of Cr^{3+} , Fe^{3+} , V^{3+} , and Fe^{2+} – Fe^{3+} intervalence charge transfer lead to the color of pink spinel.
- The intensity of the R-line and N-lines at 680–692 nm in the PL spectrum are independent of the Cr^{3+} content.
- Thermal treatment widens the FWHM of R-line and N-lines, corresponding to changes in the classes of Cr^{3+} ions in spinel.
- The disappearance of the ν_3 band at 581 cm^{-1} with heating is likely related to the increasing M–O and decreasing T–O bond lengths.

See end of article for About the Authors and Acknowledgments.

GEMS & GEMOLOGY, Vol. 58, No. 3, pp. 338–353,
<http://dx.doi.org/10.5741/GEMS.58.3.338>

© 2022 Gemological Institute of America

lens of magnesian skarn. These forsterite lenses generally range in length from 10 cm to 5 m, with a maximum of 30 m (Hubbard et al., 1999). At Kuh-i-Lal, spinel often coexists with enstatite, magnesite, phlo-

gopite, pyrrhotite, pyrite, rutile, uvite, and graphite, in the mining area (Grew, 1994). Its formation is related to the tertiary collision between the Eurasia plate and the Indian Subcontinent in the Himalayan Orogenic Belt (Garnier et al., 2006; Malsy and Klemm, 2010).

While there has been no systematic and specialized spectroscopic research on samples from Kuh-i-Lal, spinel has been investigated for decades. Wood and Imbusch (1968) calculated the crystal field parameters of Cr^{3+} in spinel. Stręk et al. (1988) analyzed the ultra-violet/visible (UV-Vis) spectra and photoluminescence (PL) spectra, concluding that MgAl_2O_4 spinel was affected by the spin-allowed transitions ${}^4\text{A}_{2g} \rightarrow {}^4\text{T}_{2g}$ and ${}^4\text{A}_{2g} \rightarrow {}^4\text{T}_{1g}$ of Cr^{3+} ions. Dickson and Smith (1976) analyzed the combination of UV-Vis and Mössbauer spectra of spinel at room temperature, explaining the effect of iron on the optical spectra. Hålenius et al. (2010) used the Racah B parameter, which can be calculated from the energies of bands on UV-Vis spectra, to prove that the number of Cr-O bonds was related to Cr^{3+} content. Taran et al. (2005) and Fregola et al. (2014) studied the spectra of Fe^{2+} and Fe^{3+} in gahnite-hercynite and found that the $d-d$ absorption spectra of Fe^{2+} in the near-infrared region are related to pressure. Andreozzi et al. (2019) classified two categories of color: (1) iron-poor orange, red, and magenta spinel and (2) iron-rich pink, blue, and green spinel. The former group of colors is mainly caused by the spin-allowed transition of Cr^{3+} and V^{3+} ions, while the latter group is due to the function of Fe_{tot} and Fe^{3+} .

A topic of particular importance to the gem and jewelry trade is the heat treatment of spinel to improve its appearance. We already have some knowledge about the heating process used: Mohler and White (1995) studied the PL spectrum of Cr^{3+} of spinel and found that the change of temperature invariably affects the phonon line structure of Cr^{3+} . Neutron diffraction, Raman spectroscopy, single-crystal diffraction, and other methods were used to explore the change of cation distribution and lattice parameters of spinel during the heating process (Peterson et al., 1991; Cynn et al., 1992; Redfern et al., 1999; Médugin et al., 2004; Minh and Yang, 2004; Uchida et al., 2005; Slotznick and Shim, 2008). Widmer et al. (2015) analyzed the changes in the PL spectrum and Raman spectrum of red spinel under heating conditions. It was found that the lattice parameters changed with temperature and pressure, resulting in a sudden change of intensity and full width at half maxima (FWHM) of peaks in the PL spectrum.

Spinel is a traditionally popular gem featuring high transparency and desirable colors. Since 2000,












Figure 1. This faceted spinel was mined in the Kuh-i-Lal deposit of Tajikistan and weighs slightly more than 20 ct. Photo by Vincent Pardieu/Gübelin Gem Lab (2008); courtesy of Edigem.

it has seen a large price increase in China. The mines of Kuh-i-Lal have been an important source for centuries (the famous Black Prince's ruby from the British Imperial State Crown is said to have been mined there). To date, however, there has been no systematic study on the characteristic spectroscopy of spinel from this mining area. In this paper, the spectroscopic thermal variations and chromophoric mechanism of pink spinel reportedly from Kuh-i-Lal were studied using UV-Vis spectroscopy, PL spectroscopy, and mid-infrared spectroscopy, combined with laser ablation-inductively coupled plasma-mass spectroscopy (LA-ICP-MS) and heat treatment, to reveal the structural changes following different heat treatment temperatures and the function of internal chromophoric elements.

MATERIALS AND METHODS

In this study, we collected 20 gem-quality pink spinel samples reportedly from the Kuh-i-Lal region. The samples were purchased by author DS during field trips to the Namak Mandi gem market in Peshawar (Pakistan) in 2000 and 2001 and from Tajik, Afghan, and Pakistani dealers in Bangkok between 2014 and 2019. Samples ranged from 0.781 to 4.360 ct. Refractive index measurements were acquired with a desktop refractometer on all samples, and hydrostatic specific gravity values were obtained on the same samples. Each crystal had either one or two polished windows, ensuring that internal characteristics could be clearly observed and spectral testing could be carried out. The sample details are listed in table 1.

TABLE 1. Description and gemological characteristics of pink spinel from Kuh-i-Lal, Tajikistan.

Sample no.	Photo	Color	Weight (ct)	Refractive index	Specific gravity
SP-01		Deep pink	1.866	1.714	3.56
SP-02		Pink	1.265	1.713	3.55
SP-03		Light pink	1.260	1.712	3.57
SP-04		Pink	1.178	1.714	3.57
SP-05		Deep pink	1.900	1.711	3.58
SP-06		Pink	0.971	1.710	3.57
SP-07		Light pink	0.781	1.712	3.57
SP-08		Pink	1.995	1.712	3.56
SP-09		Deep pink	1.909	1.713	3.57
SP-10		Pink	0.849	1.713	3.55

Spectroscopy was performed at the Laboratory of Gem and Technological Materials, Tongji University in Shanghai. PL spectra were obtained between 560 and 850 nm using a confocal Raman spectrometer (Horiba Jobin Yvon LabRAM HR Evolution). All spectra were measured using an excitation wave-

length of 532 nm. The acquisition time was 5 s, and two scans with the 50× objective of the microscope were performed. All spectra were collected using a power of 50 mW and a confocal aperture of 50 μm.

Twenty samples for UV-Vis absorbance spectra were cut and polished on two parallel sides. Each sam-

TABLE 1 (continued). Description and gemological characteristics of pink spinel from Kuh-i-Lal, Tajikistan.

Sample no.	Photo	Color	Weight (ct)	Refractive index	Specific gravity
SP-13		Pink	2.101	1.713	3.57
SP-29		Deep pink	3.345	1.713	3.56
SP-30		Light pink	2.220	1.711	3.55
SP-34		Pink	4.360	1.712	3.57
SP-36		Deep pink	2.870	1.710	3.55
SP-37		Light pink	0.823	1.710	3.58
SP-42		Light pink	1.930	1.712	3.55
SP-43		Light pink	1.218	1.711	3.58
SP-47		Deep pink	1.141	1.711	3.58
SP-50		Deep pink	2.760	1.713	3.55

ple had a thickness of 1.52 to 2.54 mm. UV-Vis absorption spectra were obtained with a UV-Vis spectrometer (PerkinElmer Lambda 650s). The spectra were obtained with a resolution of 1 nm, a scan speed of 266.75 nm/min, a photomultiplier (PMT) response of 0.4 s, and a scan range of 300–800 nm.

Mid-infrared reflectance spectra were measured with a Bruker Tensor 27 FTIR spectrometer equipped with a reflectance accessory. The spectra were recorded with a resolution of 4 cm⁻¹ and 32 scans. The scan speed was 10 kHz with a raster of 6 mm in the range of 400–4000 cm⁻¹. The absorbance of the

TABLE 2. Transition metal element contents of pink spinel from Kuh-i-Lal, obtained by LA-ICP-MS (the range of values for each sample is based upon three spots).

Sample	MgO (wt.%)	Al ₂ O ₃ (wt.%)	V (ppmw)	Cr (ppmw)	Mn (ppmw)	Fe (ppmw)	Co (ppmw)
SP-01	29.9–30.1	68.9–69.0	201–205	753–894	108.4–116.2	3577.8–3577.8	1.0–1.5
SP-02	29.6–29.9	69.1–69.4	317–355	426–444	123.9–123.9	2411.1–2488.9	0.7–9.6
SP-03	29.8–30.1	68.8–69.3	331–347	242–272	123.9–131.7	2411.1–2488.9	0.6–1.0
SP-04	30.2–30.3	68.7–68.9	354–391	457–501	108.4–123.9	2411.1–2722.2	0.6–1.2
SP-05	29.9–30.1	68.9–69.2	286–300	432–699	123.9–123.9	2411.1–2566.7	0.5–0.9
SP-06	30.2–30.3	68.5–68.8	314–347	469–873	123.9–131.7	2333.3–2644.4	0.7–1.4
SP-07	29.9–30.1	68.9–69.3	232–314	384–766	123.9–123.9	2255.6–2488.9	0.6–1.2
SP-08	30.3–30.5	68.7–68.8	286–311	290–338	123.9–131.7	2100.0–2488.9	0.8–1.1
SP-09	29.8–29.9	69.1–69.1	187–192	630–699	108.4–108.4	3577.8–3733.3	0.8–1.5
SP-10	29.1–30.1	69.0–69.9	268–283	371–412	108.4–116.2	2644.4–2722.2	0.3–0.5
SP-13	30.1–30.4	69.0–69.3	283–288	182–365	116.2–116.2	2488.9–2644.4	0.6–0.9
SP-29	29.8–30.1	68.9–69.2	271–273	669–695	108.4–108.4	2722.2–3188.9	0.7–0.8
SP-30	30.3–30.7	68.6–68.8	293–446	253–421	108.4–116.2	1944.4–2333.3	0.8–1.2
SP-34	30.4–30.5	68.4–68.6	318–332	368–446	123.9–131.7	2644.4–2877.8	0.3–0.8
SP-36	29.5–29.8	69.2–69.6	378–394	397–551	116.2–116.2	2566.7–2722.2	0.7–0.8
SP-37	30.7–31.0	68.2–68.5	358–373	136–178	100.7–108.4	1633.3–2177.8	0.3–1.0
SP-42	30.5–30.7	68.4–68.4	254–340	365–426	123.9–123.9	2722.2–2800.0	0.6–1.3
SP-43	29.6–30.4	68.6–69.6	265–339	318–464	108.4–116.2	2100.0–2566.7	0.6–0.9
SP-47	30.0–30.5	68.4–68.9	153–165	701–920	100.7–108.4	3655.6–3655.6	0.8–1.0
SP-50	29.8–30.1	69.0–69.3	262–269	303–364	116.2–116.2	2488.9–2722.2	0.5–1.0
Detection limits	0.0015	0.0032	0.5	52.9	5.4	124.4	0.7
Pink samples (Andreozzi et al., 2019)	—	—	68–815	68–1436	154.9–542.1	2722.2–27377.8	—
Magenta samples (Andreozzi et al., 2019)	—	—	476–952	1505–7115	0–154.9	1011.1–4900.0	—

Note: ppmw = parts per million by weight.

samples was calculated from the reflectance data through Kramers-Kronig analysis.

Trace element analyses were performed on all 20 samples using LA-ICP-MS at Wuhan Sample Solution

Analytical Technology Co., China, using an Agilent 7900 mass spectrometer with a GeoLas HD coherent excimer laser ablation system (193 nm ablation wavelength and 5 Hz frequency with an energy of 80 mJ).

Three measuring points (64 μm diameter) were selected for each sample. The data were calibrated using multiple external standards: NIST SRM 610, NIST SRM 612, BCR-2G, BHVO-2G, and BIR-2G. The ICPMSDataCal 10.8 software was used for data processing. Detailed information on the instrument setting and data processing follows the description of Liu et al. (2008).

Because spinel contains many crevices, it is easy for samples to fracture during the heating process. Two samples with sufficient clarity (SP-05 and SP-34) were selected for heat treatment, one of which (SP-34) was cut into four small pieces of about $2 \times 2 \times 1$ mm. These five pieces of crystal (SP-05, SP-34.1, SP-34.2, SP-34.3, and SP-34.4) were heated to temperatures of 300°, 500°, 600°, 650°, 700°, 750°, 775°, 800°, 825°, 850°, 875°, 900°, and 1000°C at a heating rate of 10°C/min. After reaching the target temperature, the samples were annealed for one hour, and then the pieces were cooled to room temperature at a rate of 20°C/min in the switched-off furnace. Unfortunately, sample SP-34.4 broke apart during the heating process, so data will only be reported for the remaining four samples. The PL and mid-infrared spectra were recorded after heating to different temperatures, and the spectral measurement parameters were the same as those for samples with no heating.

The peak fitting process was evaluated using PeakFit version 4.12 (Systat Software Inc., Palo Alto, California), with the shape and width of the peaks varied. According to Taran et al. (2005), we assume that band shapes are Gaussian, and a combination of Gaussian and Lorentzian curves was used to fit these spectra. The peak analysis (FWHM and integration of R-line and N-lines) in PL spectra were calibrated using OriginPro 2018 (OriginLab, Northampton, Massachusetts).

RESULTS

Chemical Composition. Spinel with the ideal structure MgAl_2O_4 is allochromatic, and therefore pure spinel is colorless. Color is caused by transition metal elements in the crystal lattice. One detailed study (Andreozzi et al., 2019) divided spinel of different colors into two groups:

1. Iron-poor orange, red, and magenta spinel: colored by the combined effect of iron, chromium, and vanadium
2. Iron-rich pink, blue, and green spinel: attributed to the increase of Fe_{tot} and Fe^{3+} (Andreozzi et al., 2019).

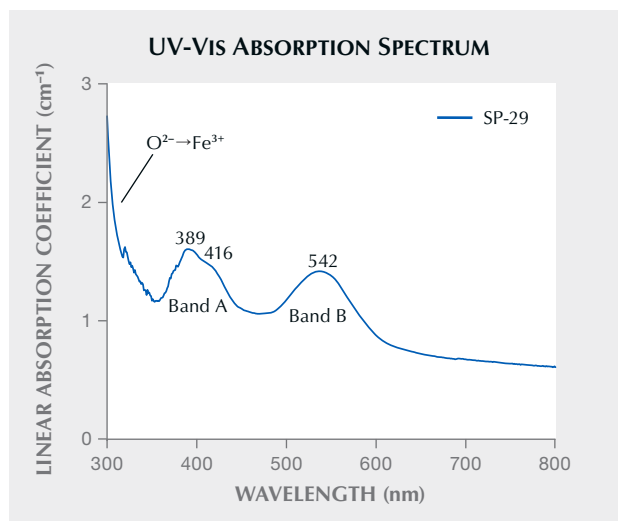


Figure 2. A typical UV-Vis absorption spectrum of pink spinel from Kuh-i-Lal.

In the present study, the main transition metal element of Kuh-i-Lal pink spinel was iron, ranging from 1633.3 to 3733.3 ppm. The samples also contained small amounts of chromium and vanadium. Chromium varied from 136.0 to 920.0 ppmw, and vanadium content ranged from 153.0 to 446.0 ppmw. In addition, there were other transition metal elements such as manganese (100.7–131.7 ppmw) and cobalt (0.3–9.6 ppmw). The LA-ICP-MS test results of all samples are presented in table 2.

UV-Vis Absorbance Spectra. A representative UV-Vis absorbance spectrum of pink spinel from Kuh-i-Lal is shown in figure 2. In general, the UV-Vis absorbance spectrum of spinel from this locality can be divided into three zones:

1. an absorption band at 389 nm, with a shoulder at 416 nm (band A)
2. a wide absorption band with absorption maxima at 542 nm (band B)
3. a set of weak and narrow absorption bands at around 700 nm with absorbance fluctuations

The detailed characteristics of the absorption peak at 685 nm in the third zone could not be observed with the UV-Vis spectrometer, so the peak was recorded by the photoluminescence spectrometer and described in detail below.

The deuterium lamp's emission at 319.2 nm causes the noise at 319 nm, while the noise from 319 to 370 nm is caused by the signal instability of the deuterium lamp. (The light source for the rest of the range was a tungsten lamp.)

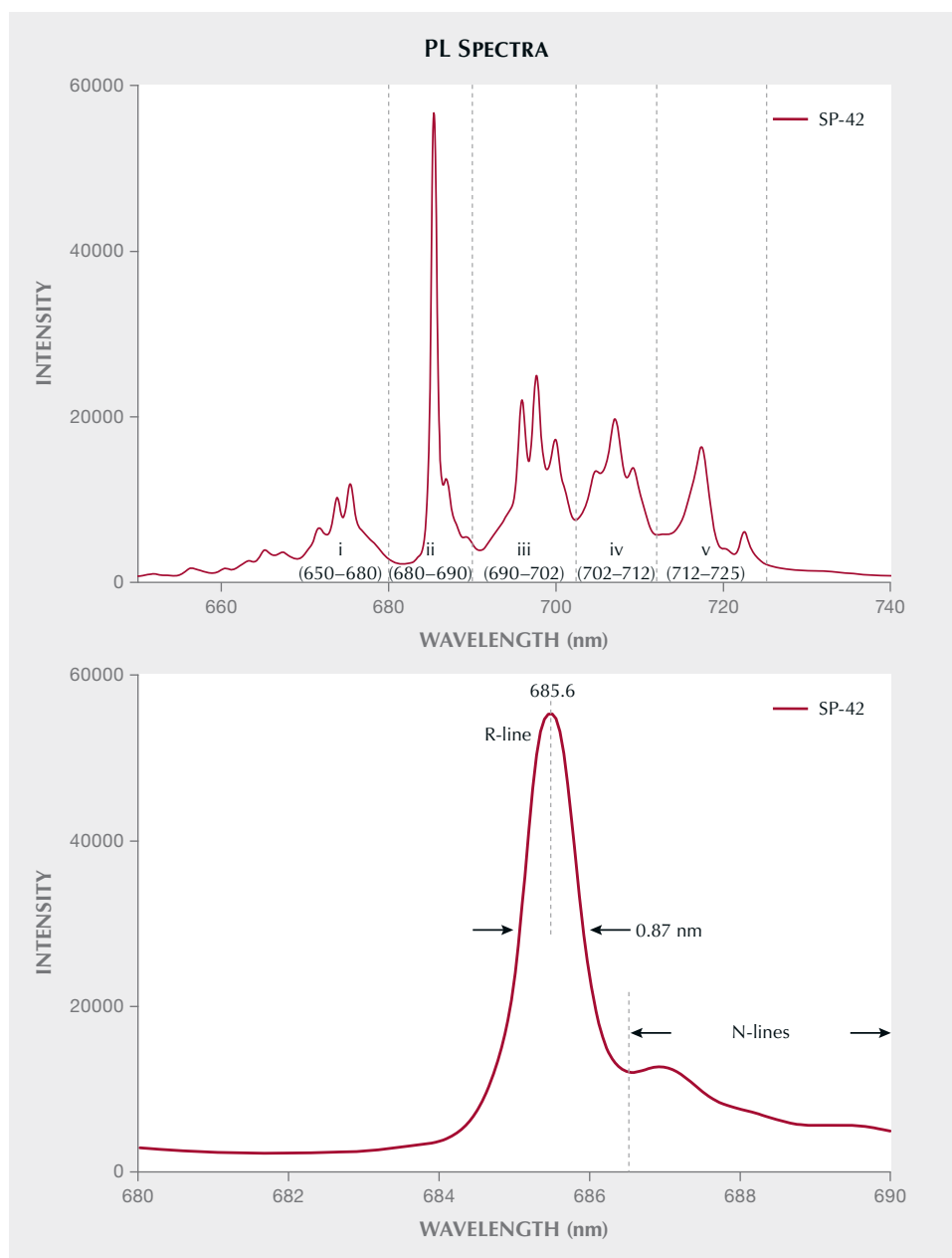


Figure 3. Top: A representative photoluminescence spectrum of Kuh-i-Lal pink spinel SP-42 at room temperature. Bottom: In region ii, the FWHM of the R-line is 0.87 nm.

The iron-poor orange, red, and magenta spinel examined by Andreozzi et al. (2019) have absorption patterns similar to those from the present study. Meanwhile, the iron-rich pink, blue, and green spinel from that earlier study have an obvious absorption band at around 458 ± 18 nm.

PL Spectra. A typical photoluminescence spectrum of Kuh-i-Lal spinel is shown in figure 3. The PL spectra of all the samples displayed the same pattern of emission lines but with different intensities. The PL spectra of spinel from Kuh-i-Lal and Myanmar are

very similar and can be divided into five regions (Malíčková et al., 2021):

- i. a group of emission lines in the area of 650–680 nm (with the strongest intensities at 672, 674, and 675 nm)
- ii. 680–690 nm (with the sharpest and highest emission line at 685.6 nm)
- iii. 690–702 nm (including a group of emission lines of 695, 698, and 700 nm, with the strongest intensity at 698 nm)
- iv. 702–712 nm (including a group of emission

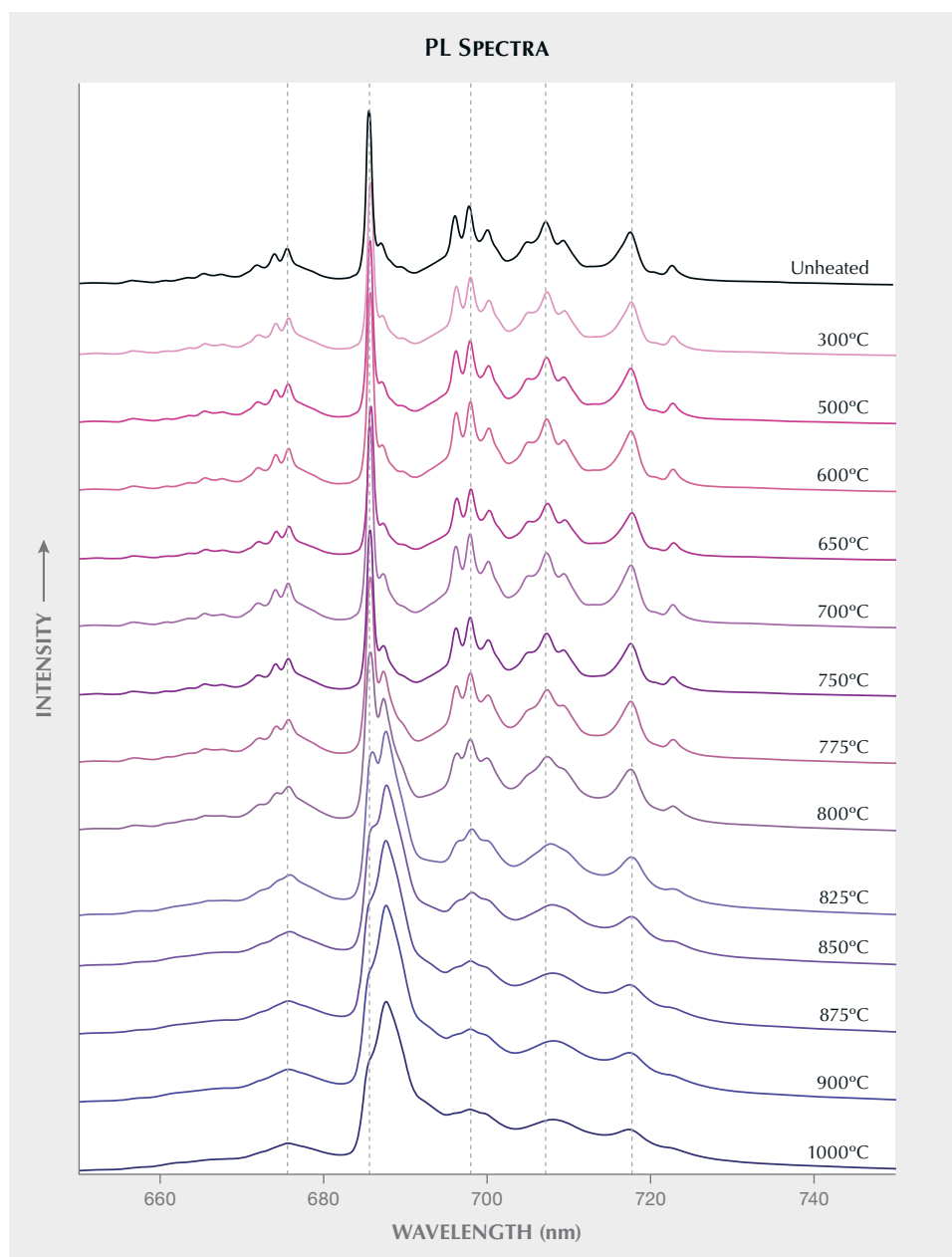


Figure 4. Photoluminescence spectra of pink spinel sample SP-05 after heating at the specified temperatures. The dashed lines represent the maxima for each peak from the different PL regions. N_1 exceeds the emission line at 685.6 nm (R-line) after heating to about 825°C, while the FWHM of these emission lines gradually widened following heating at higher temperatures.

- lines of 705, 707, and 709 nm, with maxima at 707 nm)
- v. 712–725 nm (including two emission lines at 717 and 722 nm)

In the PL spectra of Cr^{3+} -bearing spinel at room temperature, the R-line, a very strong and sharp emission line located at 685.6 nm (figure 3, top), is formed by the spin-forbidden transition ${}^2\text{E}({}^2\text{G}) \rightarrow {}^4\text{A}_2({}^4\text{F})$ of Cr^{3+} (Phan et al., 2004; Widmer et al., 2015). The strength of the R-line is related to the different classes of substitutional Cr^{3+} ions, and its generation reflects the ex-

istence of ideal coordinated Cr^{3+} (Phan et al., 2004; Widmer et al., 2015), which is recorded as Cr [ideal]. Saeseaw et al. (2009) first investigated the effect of heat treatment on PL spectra of pink spinel. According to that study, the FWHM is an important parameter to identify unheated spinel, which ranges from 0.82 to 1.12 nm. The FWHM of samples in this research ranges from 0.85 to 0.93 nm. In addition to the R-line, there are also N-lines in region ii (figure 3, bottom).

The effects of heat treatment on the PL spectra of spinel sample SP-05 (figure 4) are shown in the following two respects:

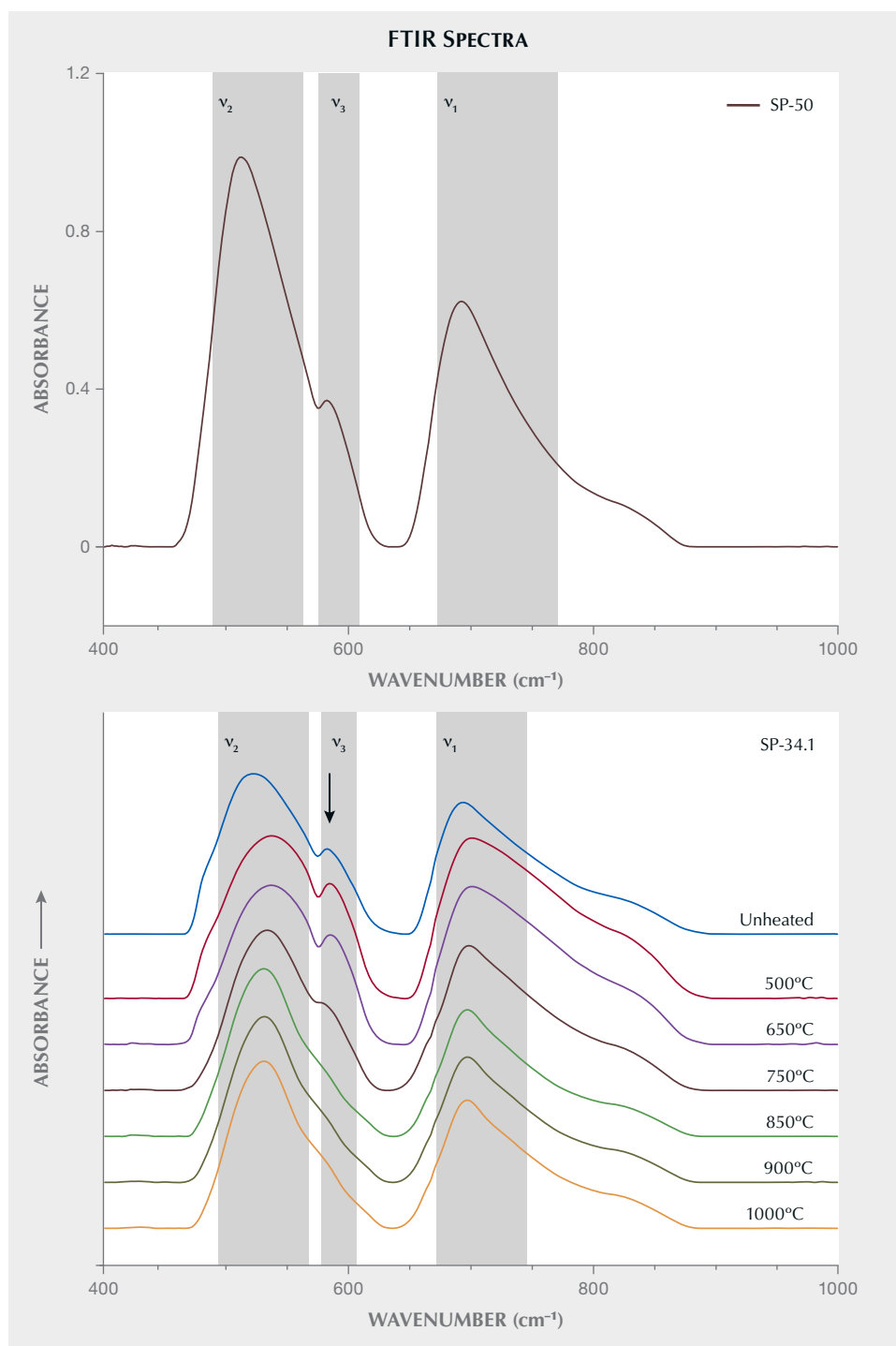


Figure 5. Top: A representative absorption spectrum (converted reflectance data) of Kuh-i-Lal unheated pink spinel. Bottom: The thermal variation of the infrared spectra (SP-34.1) following heating at the indicated temperatures. Spectra are offset vertically for clarity.

1. After heating to 750°C, the luminescence intensity at 687 nm (N_1) in region (ii) gradually increased. N_1 exceeds the emission line at 685.6 nm (R-line) after heating to about 825°C and prevails after heating up to 1000°C. The FWHM indicate a significant increase with heating. This change is no longer obvious after 850°C.
2. The baseline in parts (i), (iii), (iv), and (v) strengthened slightly following increasing heating temperature, and the FWHM of the original emission lines gradually widened simultaneously. After heating to 850°C, the spectra only display emission lines with the highest intensity at 675, 696, 698, 700, 708, and 717

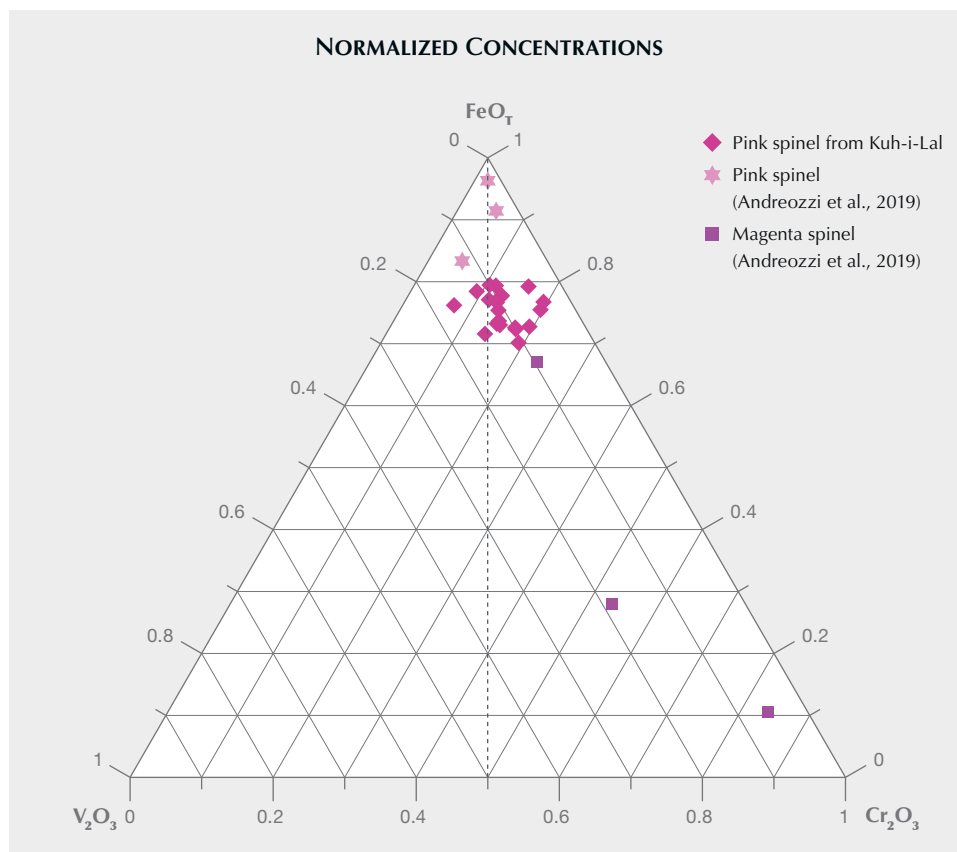


Figure 6. Normalized concentrations of FeO_T (total content of iron oxide), V_2O_3 , and Cr_2O_3 for Kuh-i-Lal spinel samples (modified from Andreozzi et al., 2019). Hexagrams and squares represent samples from Andreozzi et al. (2019), while the diamonds represent pink spinel from the present study.

nm, while other lines are not distinguishable. Following heating at 1000°C , only wide emission bands at 675, 698, 708, and 717 nm are still observable.

Mid-Infrared Spectroscopy. This study only discusses the mid-infrared spectra of Kuh-i-Lal spinel in the range of $400\text{--}1000\text{ cm}^{-1}$, because there is no absorption after 1000 cm^{-1} . A typical mid-infrared spectrum is shown in figure 5 (top). With no heating, there are two characteristic bands, centered near 686 cm^{-1} (ν_1) and 513 cm^{-1} (ν_2). Additionally, a shoulder can be observed at 581 cm^{-1} (ν_3). After heating to 650°C , this shoulder becomes less intense with rising temperature, and it disappears completely at 850°C (figure 5, bottom).

DISCUSSION

Coloration Mechanism. The color of spinel is assigned by the chromophoric elements in its lattice. The LA-ICP-MS results show that pink spinel from Kuh-i-Lal contains a variety of trace transition metal elements, but not all transition metal elements contribute to color. Iron-rich pink, blue, and green spinel are mainly influenced by iron, while orange, red, and

magenta (including iron-poor pink) spinel are colored by the combined effect of iron, chromium, and vanadium (Andreozzi et al., 2019). In Andreozzi's electron probe microanalysis (EPMA) results, the iron content of pink and magenta spinel are similar (see table 2), but the contents of chromium and vanadium in their sample sets vary greatly because of limited samples (three samples in light pink, purplish pink, and reddish pink respectively). Compared with their samples, our samples have a lower concentration of chromium and vanadium.

As shown in figure 6, the ternary diagram reflects that the distributions of iron, chromium, and vanadium in our samples are close to those from Andreozzi for both the pink samples and one of the magenta samples. Based solely on chemical composition, it is hard to declare that the color mechanism of pink spinel in Kuh-i-Lal is caused by one of the categories mentioned by Andreozzi et al. (2019).

The UV-Vis absorption spectra reveal the chromophoric mechanism of chromium and vanadium, and the UV spectral patterns of all samples were nearly the same (see figure 2 for an example spectrum). According to Taran et al. (2014), the absorption bands of $\sim 18,500\text{ cm}^{-1}$ (540.54 nm) and $\sim 25,400\text{ cm}^{-1}$ (393.70

nm) can be attributed to Cr^{3+} spin-allowed transition ${}^4\text{A}_{2g} \rightarrow {}^4\text{T}_{2g}$ and ${}^4\text{A}_{2g} \rightarrow {}^4\text{T}_{1g}$. However, the absorption bands of V^{3+} also exist in this region, very close to the absorption bands of Cr^{3+} . The two strong absorption bands of V^{3+} at $\sim 18,500\text{ cm}^{-1}$ and $\sim 25,400\text{ cm}^{-1}$ are assigned to the $d-d$ spin-allowed transitions ${}^3\text{T}_1(\text{F}) \rightarrow {}^3\text{T}_1(\text{P})$ and ${}^3\text{T}_1(\text{F}) \rightarrow {}^3\text{T}_2(\text{F})$, respectively (Andreozzi et al., 2019).

Following a peak-fitting procedure outlined by Andreozzi et al. (2019) in order to separate (deconvolute) the overlapping absorption bands, six fitted peaks were distinguished using PeakFit 4.12, as shown in figure 7 (sample SP-42). Three absorption peaks at around 389 nm (1), 418 nm (2), and 456 nm (3) were obtained by deconvoluting the band A. Peaks (1) and (2) can be attributed to the $d-d$ spin-allowed transition ${}^4\text{A}_{2g} \rightarrow {}^4\text{T}_{1g}({}^4\text{F})$ of Cr^{3+} , and peak (3) is caused by spin-forbidden transition ${}^6\text{A}_1 \rightarrow {}^4\text{A}_1$, ${}^4\text{E}$ of Fe^{3+} ions. Two other absorption peaks are obtained by fitting band B, located near 527 nm (4) and 567 nm (5), respectively. Peak (4) was assigned to ${}^4\text{A}_{2g} \rightarrow {}^4\text{T}_{2g}({}^4\text{F})$ of Cr^{3+} , while peak (5) was caused by the spin-allowed transition ${}^3\text{T}_1({}^3\text{F}) \rightarrow {}^3\text{T}_2({}^3\text{F})$ of V^{3+} (Hålenius et al., 2010; Malsy and Klemm, 2010; Taran et al., 2014; Andreozzi et al., 2019). The last

peak is at 674 nm (6), which can be attributed to $\text{Fe}^{2+}\text{-Fe}^{3+}$ intervalence charge transfer, possibly strengthened by exchange-coupled pair (ECP) interactions in $\text{Fe}^{3+}\text{-Fe}^{3+}$ clusters (Andreozzi et al., 2001). The UV-edge absorption near 300 nm is attributed to the charge transfer transition of $\text{O}^{2-} \rightarrow \text{Fe}^{3+}$ (Malsy and Klemm, 2010; Taran et al., 2014; Andreozzi et al., 2019).

Therefore, the color of pink spinel from Kuh-i-Lal is caused not only by Cr^{3+} and V^{3+} , but also by Fe^{3+} and $\text{Fe}^{2+}\text{-Fe}^{3+}$ intervalence charge transfer.

Spectroscopic Thermal Variation Characteristics.

The PL spectra of spinel mainly reflect the environment of Cr^{3+} ions (Widmer et al., 2015). The PL spectrum of Kuh-i-Lal pink spinel consists of an R-line, N-lines, and their phonon sidebands (PSB). The R-line located at 685.6 nm is formed by the spin forbidden transition ${}^2\text{E}({}^2\text{G}) \rightarrow {}^4\text{A}_2({}^4\text{F})$ of ideal coordinated Cr^{3+} . It shows a very sharp emission line at room temperature (Phan et al., 2004; Widmer et al., 2015). Cr^{3+} generates a spectrum in each different class (i.e., position in the spinel lattice), including its own zero phonon line and its associated phonon sidebands. Cr^{3+} in the ideal class will also produce a phonon

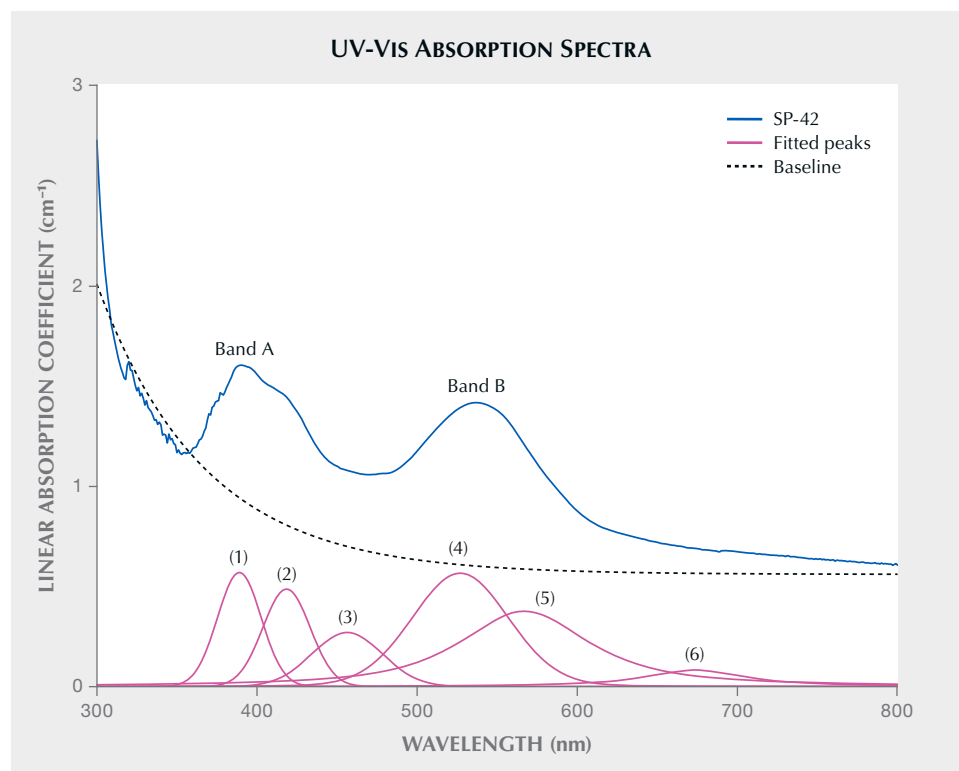


Figure 7. Curve-fitting spectra of two bands in the UV-Vis absorption spectra of sample SP-42. Results of deconvolution (pink lines) of the two bands in the absorption spectrum (blue line) of sample SP-42. The dashed line is the baseline for curve-fitting. The goodness of fit (GOF) is 0.97.

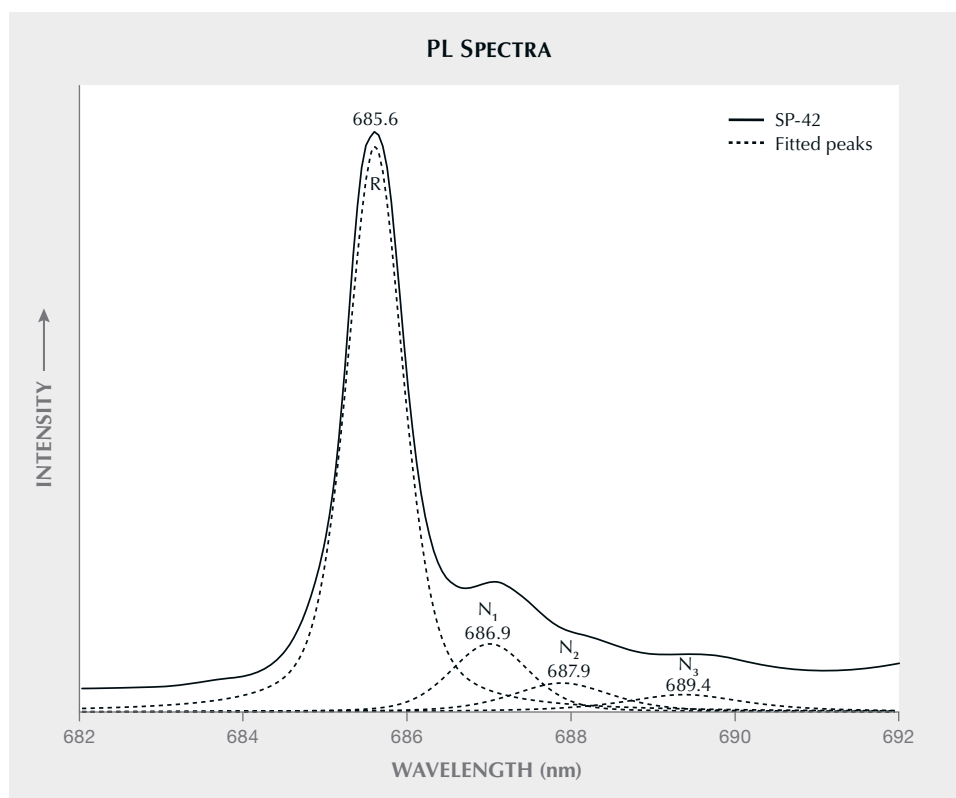


Figure 8. Curve-fitting results of PL spectra (collected at room temperature). The solid line is the PL spectrum of SP-42, and the dashed lines are the deconvoluted peaks of this unheated sample.

sideband known as R-PSB, which are phonon sidebands of the R-line. However, the anti-Stokes line of R-PSB cannot be observed at room temperature (Mikenda and Preisinger, 1981a). Lines that are neither R-line nor R-PSB are called N-lines. Due to the high intensity of the R-line at room temperature, N-lines are not as obvious. According to Widmer et al. (2015), the curve-fitting results of our samples show that three N-lines—N₁ (686.9 nm), N₂ (687.9 nm), and N₃ (689.4 nm)—can be identified in the PL spectrum in the range of 680–692 nm at room temperature, as shown in figure 8. The result of our samples matched those from Widmer et al. (2015).

The tetrahedral position of standard spinel is usually occupied by divalent cations, and the octahedral position is usually occupied by trivalent cations. For the ideal CrO₆ octahedron in spinel, six B³⁺ ions occupy the octahedral cation positions of the adjacent octahedra and six A²⁺ ions occupy the tetrahedral cation positions of the adjacent tetrahedra. The Cr³⁺ in ideal CrO₆ octahedron can also be written as Cr {ideal}. The PL spectrum of Cr {ideal} contains the R-line (685.6 nm) and R-PSB (phonon sideband) lines only. However, the substitutional Cr³⁺ ions can occupy the A and B positions at the same time in unheated spinel. The cation distribution of the

substitutional Cr³⁺ ions results in a number of different Cr³⁺ classes. There are 48 classes besides Cr {ideal}, and the distortion of [CrO₆] is described by the degree of inversion (*i*), which is the ratio of A²⁺ in tetrahedral positions and A²⁺ in both tetrahedral and octahedral positions. Mikenda and Preisinger (1981b,c) established the curve of the degree of inversion (*i*) and different Cr³⁺ classes. The degree of inversion of unheated spinel is usually below 0.1. Within this threshold, the greater the *i* value, the lower the proportion of Cr {ideal}, the higher the degree of lattice disorder, the stronger the intensity of N-lines, and the lower the R-line intensity.

There are two causes of the formation of N-lines: the content of impurity ions (type I) and the defect of the main lattice (type II). The N-lines caused by type I do not change with the lattice parameters of the host crystal but are only affected by the Cr³⁺ content in spinel. Therefore, in order to identify the attribution of N-lines, we only need to determine whether the strength of N-lines changes with chromium content.

According to the comparison between the Cr³⁺ ion content obtained by LA-ICP-MS and the integral of normalized R-line and N-lines (680–692 nm), it was found in this study that the increase of Cr³⁺ ion content in the sample has no effect on the strength of the

R-line and N-lines (figure 9). Therefore, we can exclude type I as the cause of N-lines in the PL spectrum of Kuh-i-Lal spinel. Therefore, we determined that the N-lines are caused by lattice defects. The normalized R-line integral does not change with the increase of Cr^{3+} ions, indicating that the proportion of Cr {ideal} and the degree of distortion vary little with heating.

With no heating, the PL spectrum at 680–692 nm mainly shows the R-line at 685.6 nm and the N_1 line at 686.9 nm, which gradually becomes dominant after heating (see figure 4). This is because heating disturbs the lattice of the host spinel, which leads to the original Cr {ideal} transfer to other non-ideal classes.

The FWHM is calculated based on the position of N_1 since it is dominant among the N-lines. The temperature dependence of the FWHM of sample SP-05 upon heat treatment is presented in figure 10. The FWHM of the R-line and N-lines did not change significantly at first; it increased slightly after heating at 600°C. After heating to 750°C, the FWHM of the R-line and N_1 continued to widen. After heating to 825°C, these two peaks were overlapping and difficult to separate. The total FWHM increased slightly when the sample was heated to 900° and 1000°C, and the corresponding PL spectra show a wide and overlapping band. Most of the original emission lines in figure 8 are difficult to distinguish after heating above 825°C.

High-temperature conditions significantly affect the classes of Cr^{3+} ions in spinel. Figure 11 shows the temperature dependence of the integral ratio of the R-line and N-lines (in the range of 680–692 nm). After

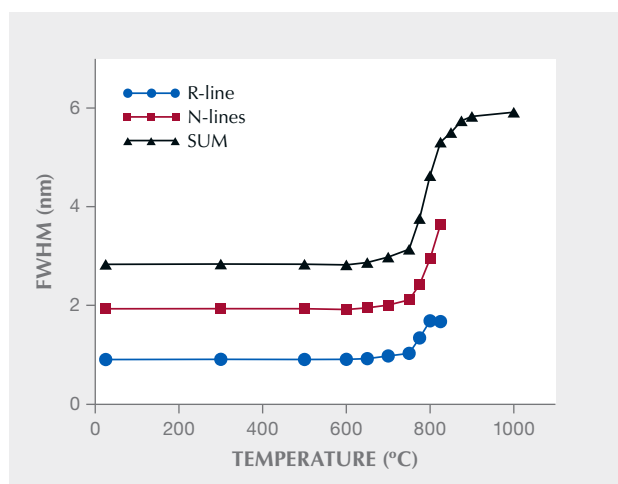


Figure 10. The trend of FWHM of the R-line and N-lines (680–692 nm) for sample SP-05 during the heating process, where SUM represents the sum of FWHM of the R-line and all N-lines.

heating to temperatures less than 600°C, the ratio of the integral areas of the R-line and N lines increased slightly. At 600°C, the ratio of integral areas of the R-line to N-lines decreased slightly, dropping significantly after heating to 750°C and decreasing slightly again after heating above 825°C. In this interval of 75°C, the ratio of integral areas of the two is almost linear. The equation between temperature and the ratio of integral areas of the two in this range can be derived:

Figure 9. After integration of the normalized R- and N-lines, the impact of chromium content is more easily observed.

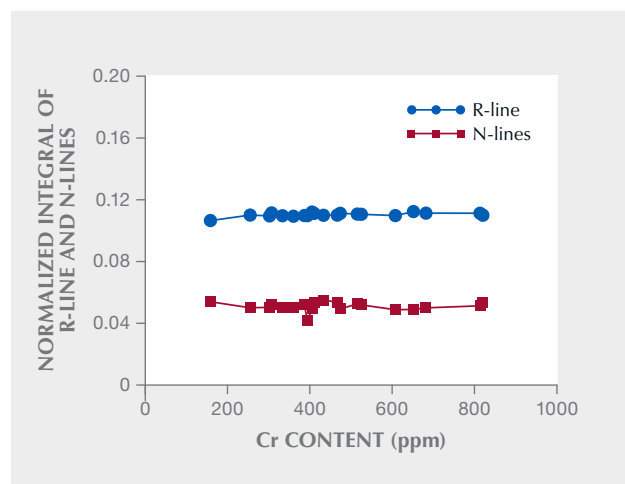


Figure 11. Temperature dependence of the ratio of integral areas of the R-line and N-lines (680–692 nm).

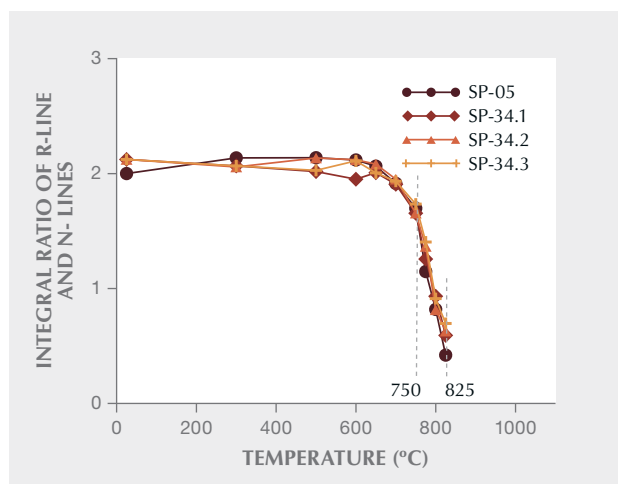




Figure 12. This pink spinel crystal in matrix from Kuh-i-Lal measures 13.82×12.54 mm, while the faceted gem from the same locality weighs 22.76 ct. Photo by Robert Weldon/GIA; courtesy of Pala International.

$$\text{SP-05: } R = -0.01665T + 14.131 \quad (1) \quad R^2 = 0.989$$

$$\text{SP-34.1: } R = -0.01405T + 12.172 \quad (2) \quad R^2 = 0.998$$

$$\text{SP-34.2: } R = -0.01453T + 12.559 \quad (3) \quad R^2 = 0.967$$

$$\text{SP-34.3: } R = -0.01443T + 12.554 \quad (4) \quad R^2 = 0.981$$

where R symbolizes the value of the ratio of integral areas of the R-line and N-lines, and T is the temperature. The linear change of the ratio of integral areas can explain the transition of Cr^{3+} ions from ideal to non-ideal classes in similar amounts in the temperature range of $750^\circ\text{--}825^\circ\text{C}$. After heating to temperatures above 825°C , the ratio of integral areas changes less dramatically than in the $750^\circ\text{--}825^\circ\text{C}$ range. At 850°C and above, the R-line and N-lines cannot be deconvoluted.

The mid-infrared spectra of spinel can be characterized by two bands at around 686 cm^{-1} (ν_1) and 513

cm^{-1} (ν_2), which are related to the bond energy between cations and oxygen in the octahedral lattice. The band at around 581 cm^{-1} (ν_3) is assigned to the complex vibration of the octahedral and tetrahedral lattices, especially the octahedral lattice vibration (Preudhomme and Tarte, 1971a,b,c, 1972).

Figure 5 (bottom) shows that ν_3 changes markedly during the heating process: The intensity of ν_3 begins to decrease with rising temperature after heating up to 650°C and almost disappears after heating to 850°C . This could provide additional evidence to distinguish between heat-treated and untreated spinel. However, the frequency of ν_1 and ν_2 fluctuate with increasing temperature, and no obvious change pattern can be observed.

Widmer et al. (2015) measured the crystal parameters of spinel before and after heat treatment using sin-

gle crystal X-ray diffraction. When heated from room temperature to 1100°C, the octahedral M-O bond length changed from 1.9226 to 1.9333 Å, and the tetrahedral T-O bond length changed from 1.9361 to 1.9130 Å. At a temperature of 650°C, the M-O and T-O bond lengths were equal at 1.927 Å (Widmer et al., 2015).

During the heating process, the difference between the two bond lengths decreases gradually. In this study, ν_3 starts to change at 650°C, which indicates that the strength and frequency of ν_3 are related to the relative length of M-O and T-O bonds. When the length of the M-O bond grows longer than that of T-O, ν_3 gradually decreases and finally disappears.

CONCLUSIONS

The main trace element of pink spinel from Kuh-i-Lal in Tajikistan (figure 12) is iron, though it also contains small amounts of chromium, vanadium, manganese, and cobalt. The chromium content is higher than that of vanadium in most samples, but in some light pink samples the chromium content is lower than that of vanadium. Pink spinel from Kuh-i-Lal owes its color to the presence of Cr^{3+} , V^{3+} , Fe^{3+} , and Fe^{2+} - Fe^{3+} intervalence charge transfer. The characteristic band A can be attributed to the spin-allowed

transition ${}^4\text{A}_{2g} \rightarrow {}^4\text{T}_{1g}({}^4\text{F})$ in Cr^{3+} and spin-forbidden transition ${}^6\text{A}_1 \rightarrow {}^4\text{A}_1, {}^4\text{E}$ of Fe^{3+} ions, while band B in the visible region is caused by spin-allowed $d-d$ transition ${}^4\text{A}_{2g} \rightarrow {}^4\text{T}_{2g}({}^4\text{F})$ of Cr^{3+} and ${}^3\text{T}_1({}^3\text{F}) \rightarrow {}^3\text{T}_2({}^3\text{F})$ of V^{3+} . The edge of the spectra at 674 nm can be attributed to Fe^{2+} - Fe^{3+} intervalence charge transfer.

With no heating, the PL spectrum of Kuh-i-Lal pink spinel is a group of emission lines characterized by the R-line and N-lines produced by Cr^{3+} ions. The intensity of the R-line and N-lines is independent of the Cr^{3+} ion content. After heating to 750–825°C, the intensity of the N_1 peak increases gradually, and the FWHM of the R-line and N-lines (in the range of 680–692 nm) increases continuously. There is a strong linear relationship between the ratio of integral areas of the R-line and N-lines (680–692 nm) and temperature in this 75° range, and Cr {ideal} changes to other non-ideal chromium classes at an almost constant rate.

Reflectance mid-infrared spectra showed that when heated to 650°C, ν_3 gradually starts to disappear before disappearing completely after heating at 850°C, which provide additional evidence for distinguishing heat-treated spinel. The disappearance of ν_3 at high temperature is probably related to the change of M-O and T-O bond lengths in the spinel lattice.

ABOUT THE AUTHORS

Ms. Liu is a postgraduate student, Dr. Qi is a professor of mineralogy and gemology, and Dr. Zhou is a professor of mineralogy and tectonics, at Tongji University in Shanghai. Dr. Schwarz is a visiting professor at Tongji Zhejiang College in Jiaxing, China.

ACKNOWLEDGMENTS

This research was supported by special funding from the Shanghai Science and Technology Commission (15DZ2283200, 18DZ2281300) and the Gem Discipline Development Fund. LA-ICP-MS tests were completed with the assistance of staff from Wuhan SampleSolution Analytical Technology Co., Ltd. We greatly thank the peer reviewers for providing suggestions and improving the manuscript.

REFERENCES

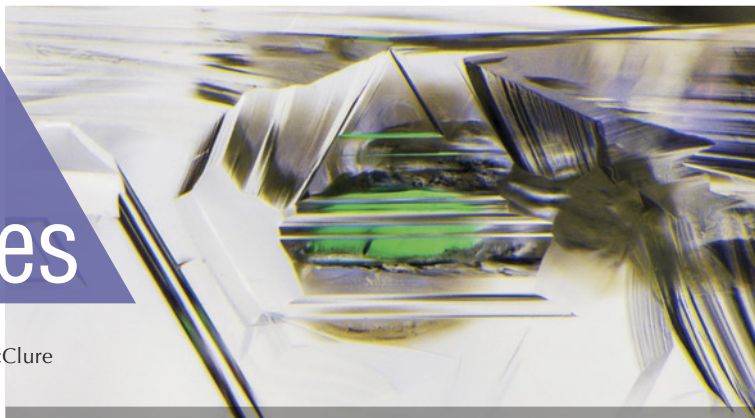
- Andreozzi G.B., Hälenius U., Skogby H. (2001) Spectroscopic active ${}^{\text{IV}}\text{Fe}^{3+}$ - ${}^{\text{VI}}\text{Fe}^{3+}$ clusters in spinel-magnesioferrite solid solution crystals: A potential monitor for ordering in oxide spinels. *Physics and Chemistry of Minerals*, Vol. 28, No. 7, pp. 435–444, <http://dx.doi.org/10.1007/s002690100178>
- Andreozzi G.B., D'Ippolito V., Skogby H., Hälenius U., Bosi F. (2019) Color mechanisms in spinel: A multi-analytical investigation of natural crystals with a wide range of coloration. *Physics and Chemistry of Minerals*, Vol. 46, No. 4, pp. 343–360, <http://dx.doi.org/10.1007/s00269-018-1007-5>
- Chauviré B., Rondeau B., Fritsch E., Ressigeac P., Devidal J.L. (2015) Blue spinel from the Luc Yen District of Vietnam. *G&G*, Vol. 51, No. 1, pp. 2–17, <http://dx.doi.org/10.5741/GEMS.51.1.2>
- Cynn H., Sharma S.K., Cooney T.F. (1992) High-temperature Raman investigation of order-disorder behavior in the MgAl_2O_4 spinel. *Physical Review B*, Vol. 45, No. 1, pp. 500–502, <http://dx.doi.org/10.1103/PhysRevB.45.500>
- De Souza S.S., Ayres F., Blak A.R. (2001) Simulation models of defects in MgAl_2O_4 : Fe^{2+} , Fe^{3+} spinels. *Radiation of Effects and Defects in Solids*, Vol. 156, No. 1, pp. 311–316, <http://dx.doi.org/10.1080/10420150108216911>
- Dickson B.L., Smith G. (1976) Low-temperature optical absorption and Mössbauer spectra of staurolite and spinel. *Canadian Mineralogist*, Vol. 14, pp. 206–215.
- Fregola R.A., Skogby H., Bosi F., D'Ippolito V., Andreozzi G.B., Hälenius U. (2014) Optical absorption spectroscopy study of the causes for color variations in natural Fe-bearing gahnite: Insights from iron valency and site distribution data. *American Mineralogist*, Vol. 99, No. 11–12, pp. 2187–2195, <http://dx.doi.org/10.2138/am-2014-4962>

- Garnier V., Giuliani G., Maluski H., Ohnenstetter D., Schwarz D. (2006) Ar-Ar and U-Pb ages of marble-hosted ruby deposits from Central and Southeast Asia. *Canadian Journal of Earth Science*, Vol. 43, No. 4, pp. 509–532, <http://dx.doi.org/10.1139/E06-005>
- Giuliani G., Fallick A.E., Boyce A.J., Pardieu V., Pham V.L. (2017) Pink and red spinels in marble: Trace elements, oxygen isotopes, and sources. *Canadian Mineralogist*, Vol. 55, No. 4, pp. 743–761, <http://dx.doi.org/10.3749/canmin.1700009>
- Hålenius U., Andreozzi G.B., Skogby H. (2010) Structural relaxation around Cr^{3+} and the red-green color change in the spinel (sensu stricto)-magnesiochromite (MgAl_2O_4 - MgCr_2O_4) and gahnite-zincochromite (ZnAl_2O_4 - ZnCr_2O_4) solid-solution series. *American Mineralogist*, Vol. 95, No. 4, pp. 456–462, <http://dx.doi.org/10.2138/am.2010.3388>
- Hubbard M.S., Grew E.S., Hodges K.V., Yates M.G., Pertsev N.N. (1999) Neogene cooling and exhumation of upper-amphibolite-facies ‘whiteschists’ in the Southwest Pamir Mountains, Tajikistan. *Tectonophysics*, Vol. 305, No. 1–3, pp. 325–337, [http://dx.doi.org/10.1016/S0040-1951\(99\)00012-8](http://dx.doi.org/10.1016/S0040-1951(99)00012-8)
- Lenaz D., Lughì V. (2013) Raman study of MgCr_2O_4 - $\text{Fe}^{2+}\text{Cr}_2\text{O}_4$ and MgCr_2O_4 - $\text{MgFe}_2^{3+}\text{O}_4$ synthetic series: The effects of Fe^{2+} and Fe^{3+} on Raman shifts. *Physics and Chemistry of Minerals*, Vol. 40, No. 6, pp. 491–498, <http://dx.doi.org/10.1007/s00269-013-0586-4>
- Liu Y.S., Hu Z.C., Gao S., Günther D., Xu J., Gao C.G., Chen H.H. (2008) In situ analysis of major and trace elements of anhydrous minerals by LA-ICP-MS without applying an internal standard. *Chemical Geology*, Vol. 257, No. 1–2, pp. 34–43, <http://dx.doi.org/10.1016/j.chemgeo.2008.08.004>
- Long P.V., Giuliani G., Fallick A.E., Boyce A.J., Pardieu V. (2018) Trace elements and oxygen isotopes of gem spinels in marble from the Luc Yen - An Phu Areas, Yen Bai Province, North Vietnam. *Vietnam Journal of Earth Sciences*, Vol. 40, No. 2, pp. 165–177, <http://dx.doi.org/10.15625/0866-7187/40/2/12241>
- Malíčková I., Bačík P., Fridrichová J., Hanus R., Illášová L., Štubna J., Furka D., Furka S., Škoda R. (2021) Optical and luminescence spectroscopy of varicolored gem spinel from Mogok, Myanmar and Luc Yen, Vietnam. *Minerals*, Vol. 11, No. 2, pp. 1–13, <http://dx.doi.org/10.3390/min11020169>
- Malsy A., Klemm L. (2010) Distinction of gem spinels from the Himalayan Mountain Belt. *Chimia*, Vol. 64, No. 10, pp. 741–746, <http://dx.doi.org/10.2533/chimia.2010.741>
- Malsy A.K., Karampelas S., Schwarz D., Klemm L., Armbruster T., Tuan D.A. (2012) Orange-red to orange-pink gem spinels from a new deposit at Lang Chap (Tan Huong-Truc Lau), Vietnam. *Journal of Gemmology*, Vol. 33, No. 1, pp. 19–27.
- Médecin F., Redfern S.A.T., Godec Y.L., Stone H.J., Tucker M.G., Dove M.T., Marshall W.G. (2004) Study of cation order-disorder in MgAl_2O_4 spinel by in situ neutron diffraction up to 1600 K and 3.2 GPa. *American Mineralogist*, Vol. 89, No. 7, pp. 981–986, <http://dx.doi.org/10.2138/am-2004-0708>
- Mikenda W., Preisinger A. (1981a) N-lines in the luminescence spectra of Cr^{3+} -doped spinels (I) Identification of N-lines. *Journal of Luminescence*, Vol. 26, No. 1–2, pp. 53–66, [http://dx.doi.org/10.1016/0022-2313\(81\)90169-1](http://dx.doi.org/10.1016/0022-2313(81)90169-1)
- (1981b) N-lines in the luminescence spectra of Cr^{3+} -doped spinels (II) Origins of N-lines. *Journal of Luminescence*, Vol. 26, No. 1–2, pp. 67–83, [http://dx.doi.org/10.1016/0022-2313\(81\)90170-8](http://dx.doi.org/10.1016/0022-2313(81)90170-8)
- (1981c) N-lines in the luminescence spectra of Cr^{3+} -doped spinels (III) Partial spectra. *Journal of Luminescence*, Vol. 26, No. 1–2, pp. 85–98, [http://dx.doi.org/10.1016/0022-2313\(81\)90171-X](http://dx.doi.org/10.1016/0022-2313(81)90171-X)
- Minh N.V., Yang I.S. (2004) A Raman study of cation-disorder transition temperature of natural MgAl_2O_4 spinel. *Vibrational Spectroscopy*, Vol. 35, No. 1–2, pp. 93–96, <http://dx.doi.org/10.1016/j.vibspec.2003.12.013>
- Mohler R.L., White W.B. (1995) Influence of structural order on the luminescence of oxide spinels: Cr^{3+} -activated spinels. *Journal of the Electrochemical Society*, Vol. 142, No. 11, pp. 3923–3927, <http://dx.doi.org/10.1149/1.2048435>
- Peterson R.C., Lager G.A., Hitterman R.L. (1991) A time-of-flight neutron powder diffraction study of MgAl_2O_4 at temperatures up to 1273 K. *American Mineralogist*, Vol. 76, No. 9–10, pp. 1455–1458.
- Phan T.L., Yu S.C., Phan M.H., Han T.P.J. (2004) Photoluminescence properties of Cr^{3+} -doped MgAl_2O_4 natural spinel. *Journal of Korean Physical Society*, Vol. 45, No. 1, pp. 63–66.
- Preudhomme J., Tarte P. (1971a) Infrared studies of spinels-I. A critical discussion of the actual interpretations. *Spectrochimica Acta Part A: Molecular and Biomolecular Spectroscopy*, Vol. 27, No. 7, pp. 961–968, [http://dx.doi.org/10.1016/0584-8539\(71\)80179-4](http://dx.doi.org/10.1016/0584-8539(71)80179-4)
- (1971b) Infrared studies of spinels-II. The experimental bases for solving the assignment problem. *Spectrochimica Acta Part A: Molecular and Biomolecular Spectroscopy*, Vol. 27, No. 6, pp. 845–851, [http://dx.doi.org/10.1016/0584-8539\(71\)80163-0](http://dx.doi.org/10.1016/0584-8539(71)80163-0)
- (1971c) Infrared studies of spinels-III. The normal II-III spinels. *Spectrochimica Acta Part A: Molecular and Biomolecular Spectroscopy*, Vol. 27, No. 9, pp. 1817–1835, [http://dx.doi.org/10.1016/0584-8539\(71\)80235-0](http://dx.doi.org/10.1016/0584-8539(71)80235-0)
- (1972) Infrared studies of spinels-IV. Normal spinels with a high-valency tetrahedral cation. *Spectrochimica Acta Part A: Molecular and Biomolecular Spectroscopy*, Vol. 28, No. 1, pp. 69–79, [http://dx.doi.org/10.1016/0584-8539\(72\)80013-8](http://dx.doi.org/10.1016/0584-8539(72)80013-8)
- Redfern S.A.T., Harrison R.J., O'Neill H.S.C., Wood D.R.R. (1999) Thermodynamics and kinetics of cation ordering in MgAl_2O_4 spinel up to 1600°C from in situ neutron diffraction. *American Mineralogist*, Vol. 84, No. 3, pp. 299–310, <http://dx.doi.org/10.2138/am-1999-0313>
- Saeseaw S., Wang W., Scarratt K., Emmett J.L., Douthit T.R. (2009) Distinguishing heated spinels from unheated natural spinels and from synthetic spinels: A short review of on-going research. *GIA Research News*, <https://www.gia.edu/doc/distinguishing-heated-spinels-from-unheated-natural-spinels.pdf>, April 2.
- Shigley J.E., Stockton C.M. (1984) ‘Cobalt-blue’ gem spinels. *G&G*, Vol. 20, No. 1, pp. 34–41, <http://dx.doi.org/10.5741/GEMS.20.1.34>
- Slotznick S.P., Shim S.H. (2008) In situ Raman spectroscopy measurements of MgAl_2O_4 spinel up to 1400°C. *American Mineralogist*, Vol. 93, No. 2–3, pp. 470–476, <http://dx.doi.org/10.2138/am.2008.2687>
- Stręk W., Dereni P., Jezowska-Trzebiatowska B. (1988) Optical properties of Cr^{3+} in MgAl_2O_4 spinel. *Physica B: Physics of Condensed Matter*, Vol. 152, No. 3, pp. 379–384, [http://dx.doi.org/10.1016/0921-4526\(88\)90006-3](http://dx.doi.org/10.1016/0921-4526(88)90006-3)
- Taran M.N., Koch-Müller M., Langer K. (2005) Electronic absorption spectroscopy of natural (Fe^{2+} , Fe^{3+})-bearing spinels of spinel s. s.-hercynite and gahnite-hercynite solid solutions at different temperatures and high-pressures. *Physics and Chemistry of Minerals*, Vol. 32, No. 3, pp. 175–188, <http://dx.doi.org/10.1007/s00269-005-0461-z>
- Taran M.N., Parisi F., Lenaz D., Vishnevskyy A.A. (2014) Synthetic and natural chromium-bearing spinels: An optical spectroscopy study. *Physics and Chemistry of Minerals*, Vol. 41, No. 8, pp. 593–602, <http://dx.doi.org/10.1007/s00269-014-0672-2>
- Uchida H., Lavina B., Downs R.T., Chesley J. (2005) Single-crystal X-ray diffraction of spinels from the San Carlos Volcanic Field, Arizona: Spinel as a geothermometer. *American Mineralogist*, Vol. 90, No. 11–12, pp. 1900–1908, <http://dx.doi.org/10.2138/am.2005.1795>
- Widmer R., Malsy A.K., Armbruster T. (2015) Effects of heat treatment on red gemstone spinel: Single-crystal X-ray, Raman, and photoluminescence study. *Physics and Chemistry of Minerals*, Vol. 42, No. 4, pp. 251–260, <http://dx.doi.org/10.1007/s00269-014-0716-7>
- Wood D.L., Imbusch G.F. (1968) Optical spectrum of Cr^{3+} ions in spinels. *Journal of Chemical Physics*, Vol. 48, No. 11, pp. 5255–5263, <http://dx.doi.org/10.1063/1.1668202>

Lab Notes

Editors

Thomas M. Moses | Shane F. McClure



DIAMOND

Exceptional Natural-Color Fancy Red Diamond

The Carlsbad laboratory recently received a 1.21 ct Fancy orangy red round brilliant cut diamond (6.62–6.84 × 4.14 mm; figure 1) for a colored diamond grading and identification report. Results of standard gemological testing and microscopic observation confirmed it had a natural color and no color treatment or clarity enhancement. The stone displayed faint fluorescence under long-wave UV and none under short-wave UV. Fourier-transform infrared spectroscopy indicated a type IaB diamond, while ultraviolet/visible (550 nm band and H3 [503.2 nm] center) and photoluminescence (PL) spectroscopy indicated natural color without any treatment. The 550 nm absorption band is closely linked to plastic deformation, which is clearly reflected in the broad emission features in the PL results. Due to the extensive plastic deformation, some fractures could have developed.

The rarity and high value of red diamonds has resulted in many attempts to reproduce this color through treatment or even laboratory growth procedures with post-growth treatment (S. Eaton-Magaña and J.E. Shigley, “Observations on CVD-grown synthetic diamonds: A re-

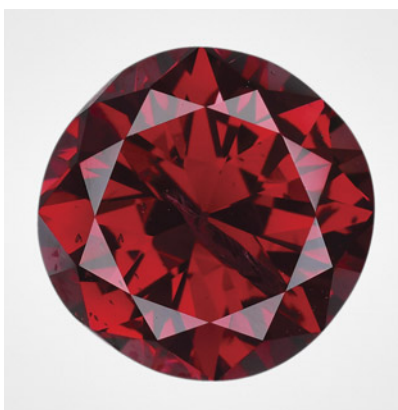


Figure 1. This 1.21 ct round brilliant diamond is notable for its size and natural Fancy orangy red color.

view,” Fall 2016 *G&G*, pp. 222–245; S. Eaton-Magaña and J.E. Shigley, “Observations on HPHT-grown synthetic diamonds: A review,” Fall 2017 *G&G*, pp. 262–284). However, treated red diamonds are often accompanied by purplish or brownish color components that are not desirable and are different from the purer hues of naturally red diamonds (W. Wang et al., “Treated-color pink-to-red diamonds from Lucent Diamonds Inc.,” Spring *G&G* 2005, pp. 6–19). Natural-color red diamonds are so rare that only around a couple dozen true red diamonds are known to exist, and most of these are under half a carat.

The exceptional natural-color 1.21 ct Fancy orangy red diamond examined here is a fine example of natural-color red diamond. It has yet to be named.

Maryam Mastery Salimi

Treated “Nickel-Rich” Green Diamond

Natural-color green diamonds are extremely rare. The cause of color for most green diamonds is attributed primarily to radiation damage resulting from exposure to radioactive elements over geologic time (W. Wang et al., “Natural type Ia diamond with green-yellow color due to Ni-related defects,” Fall 2007 *G&G*, pp. 240–243). The New York laboratory recently received a 2.12 ct pear-shaped diamond measuring 9.52 × 7.24 × 4.27 mm that was graded as Fancy yellow-green (figure 2), and testing attributed the color to several mechanisms.

Figure 2. This 2.12 ct Fancy yellow-green diamond owes its color to both the nickel-related absorption band and the artificially introduced GR1 absorption.



Editors' note: All items were written by staff members of GIA laboratories.

GEMS & GEMOLOGY, Vol. 58, No. 3, pp. 354–363.

© 2022 Gemological Institute of America

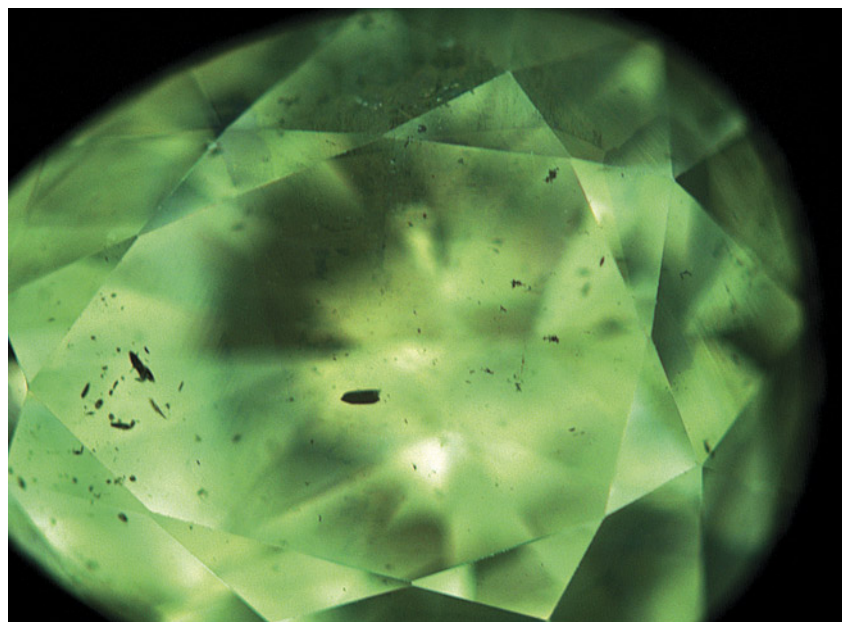
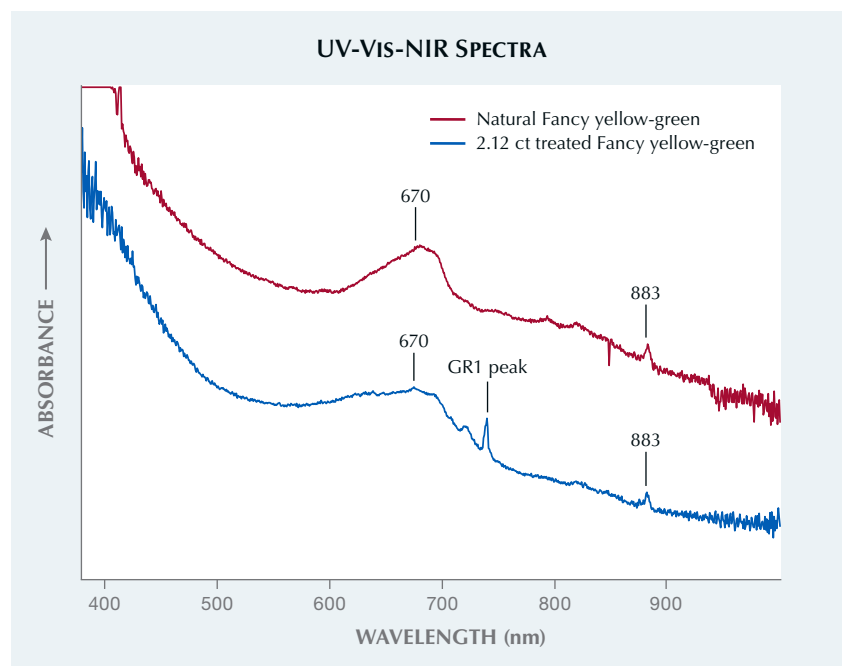


Figure 3. DiamondView imaging reveals greenish yellow fluorescence that is typical for nickel-rich diamond.

Microscopic examination revealed dark crystals and clouds throughout the stone, and infrared spectroscopy confirmed it was a type

Ia diamond. DiamondView imaging showed greenish yellow fluorescence (figure 3), typical for “nickel-rich” diamond.

Figure 4. UV-Vis-NIR spectra show the nickel-related absorption band and 883 peak in both a natural diamond from the GIA database and the 2.12 ct treated diamond. In addition, the spectrum for the treated diamond shows the GR1 peak around 740 nm. Spectra are offset vertically for clarity.



The ultraviolet/visible/near-infrared (UV-Vis-NIR) absorption spectrum showed a nickel-related absorption band at around 670 nm, a peak at 883 nm (an attributed peak in “nickel-rich” diamonds), and a GR1 (general radiation damage) peak at about 740 nm (figure 4). This is an uncommon combination of spectral features in diamond. The Ni-related absorption band is usually responsible for the green color in this type of diamond (Fall 2013 Lab Notes, pp. 173–174; Spring 2022 Lab Notes, pp. 50–51). In this particular diamond, the yellow-green color saturation can be attributed to both the nickel-related absorption band and the GR1 absorption. We have not observed these two features together in natural-color green diamond. Additional testing and gemological observations confirmed that the GR1 peak was artificially introduced, and we concluded that the color was treated. The color was likely a lighter and less saturated green before treatment.

This stone illustrates the importance of combining gemological observations with spectroscopic characteristics to separate natural- and treated-color green diamonds.

Luthfia Syarbaini and Paul Johnson

Gota de Aceite-Like Effect in a Brazilian EMERALD

Internal optical effects can provide useful information to help identify gemstones and understand their nature and geographic origin. For example, *gota de aceite*, a roiled or “drop of oil” appearance seen in Colombian emeralds, is considered to be caused by irregularities in the crystal structure due to rapid growth triggered by alteration of the growth conditions (e.g., R. Ringsrud, “*Gota de aceite*: Nomenclature for the finest Colombian emeralds,” Fall 2008 *GeG*, pp. 242–245; Winter 2017 Lab Notes, pp. 460–461).

Recently, GIA’s Tokyo laboratory examined a 2.99 ct step-cut emerald measuring $10.17 \times 8.12 \times 5.50$ mm (figure 5) for geographic origin determination. This stone exhibited a unique

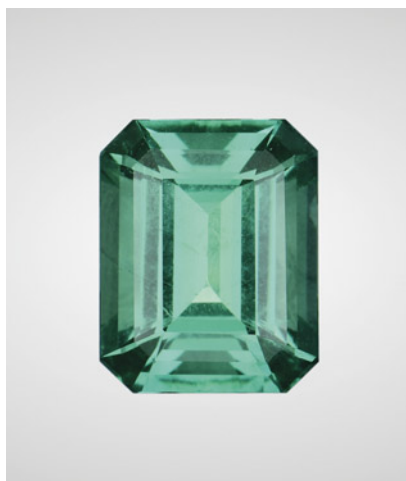


Figure 5. This 2.99 ct Brazilian emerald displayed a roiled effect similar to the *gota de aceite* phenomenon.

roiled growth structure resembling the *gota de aceite* effect (figure 6, left) at an angle nearly perpendicular to the table facet. The *gota de aceite* structure was visible parallel to the *c*-axis of the emerald based on microscopic and polariscopic observations. From other directions such as girdle to girdle, the effect was not visible and columnar growth structure was observed. The emerald also contained numerous reflective raindrop-like needles and tubes (figure 6, right) and irregular two-phase

inclusions. This stone had a refractive index range of 1.580–1.588 and showed no reaction under a Chelsea color filter. The ultraviolet/visible/near-infrared spectrum showed a significant Fe^{2+} broad band at around 810 nm. These internal and standard gemological features did not match Colombian origin, with the exception of the *gota de aceite* effect. Laser ablation–inductively coupled plasma–mass spectroscopy revealed a high iron concentration (4540–4800 ppmw) and medium potassium (230–254 ppmw) and lithium (62–68 ppmw) contents. A Brazilian origin was determined based on inclusions and trace element composition [S. Sae-seaw et al., “Geographic origin determination of emerald,” Winter 2019 *G&G*, pp. 614–646].

The *gota de aceite* optical phenomenon has been used as a characteristic feature of classic Colombian emeralds, but a similar pattern was previously reported in a Zambian emerald (Winter 2017 Lab Notes, pp. 460–461). The similarity in the growth pattern suggests that the growth conditions causing the rapid emerald crystallization were similar, although the geological origins and chemical compositions of both emeralds are different. As several microscopic studies on emerald have

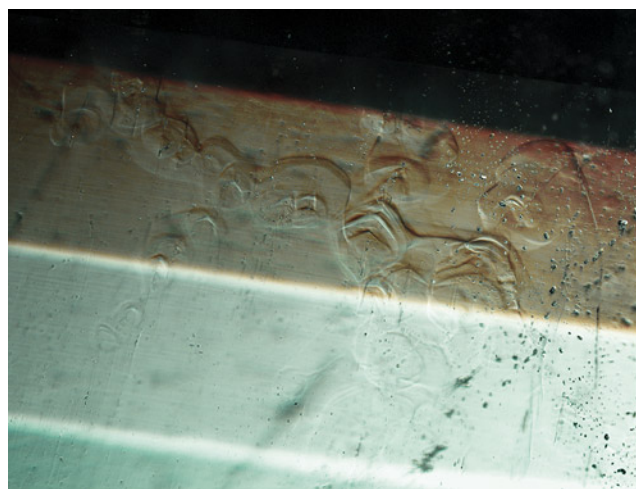
concluded (e.g., S. Sae-seaw et al., “Three-phase inclusions in emerald and their impact on origin determination,” Summer 2014 *G&G*, pp. 114–132; Winter 2017 Lab Notes, pp. 460–461), inclusions and internal features may not always be helpful in determining geographic origin, and the *gota de aceite* effect may not offer enough evidence for Colombian origin. Careful observation of other inclusions combined with advanced testing is required for origin determination of emerald.

Makoto Miura

Treated Orange and Pink CVD LABORATORY-GROWN DIAMOND

Recently, GIA received two similarly treated diamonds grown by chemical vapor deposition (CVD): a 2.00 ct Fancy Deep orange and a 3.00 ct Fancy Vivid orangy pink (figure 7). A database search revealed that the Fancy Deep orange was the first CVD-grown diamond with an unmodified orange color ever submitted to GIA. CVD-grown diamonds with an orangy pink color are far more common, and the 3.00 ct sample provided for an interesting comparison. From examination of the visible/near-infrared

Figure 6. Internal features observed in the 2.99 ct Brazilian emerald. Left: *Gota de aceite*-like optical effect with columns resembling drops of oil. Note that this image was taken at an angle parallel to the *c*-axis. Right: Numerous raindrop-like needles and tubes. Fields of view 3.10 and 2.46 mm.



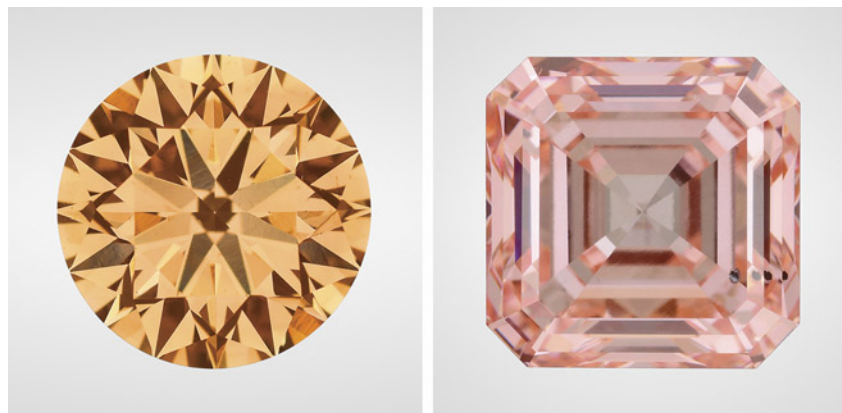
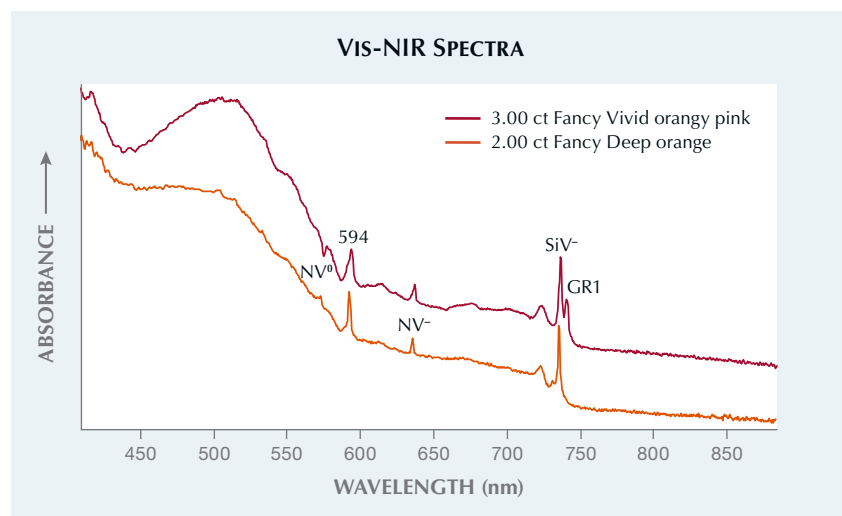


Figure 7. These 2.00 ct Fancy Deep orange (left) and 3.00 ct Fancy Vivid orangy pink (right) CVD-grown diamonds were subjected to multiple treatments including HPHT processing, irradiation, and low-temperature annealing to achieve the final color grades.

(Vis-NIR) absorption spectra, both samples had similar features and likely underwent similar treatment processes (figure 8). The subtle differences in relative peak intensities were sufficient to create the distinctly different appearances and color grades.

The Vis-NIR absorption spectra for both CVD-grown diamonds showed nitrogen vacancy centers (principal absorption for NV⁰ at 575 nm and NV⁻ at 637 nm), 594 nm peak, and the GR1 center. Both samples also displayed strong absorption of the

Figure 8. The 2.00 ct Fancy Deep orange and the 3.00 ct Fancy Vivid orangy pink CVD-grown diamonds underwent similar post-growth treatments and show similar defect centers in their Vis-NIR absorption spectra, including the NV centers, 594 nm, SiV⁻, and GR1. However, subtle differences in relative defect concentrations lead to their distinct color appearances. Although very small, the GR1 defect was also detected in the absorption spectrum of the 2.00 ct CVD-grown diamond. Spectra are offset vertically for clarity.



SiV⁻ center (737 nm). In the Fancy Deep orange sample, the NV centers exhibited lower absorption than in the orangy pink sample and also a slightly greater SiV⁻-related absorption, which helped shift the transmission window from the red (i.e., pink) toward the orange.

Based on the comparatively low value of the 468 nm emission peak determined by 457 nm photoluminescence spectroscopy, both CVD-grown diamonds showed evidence of high-pressure, high-temperature (HPHT) treatment; they were subsequently irradiated to generate the radiation-related features that included the 594 nm peak and the GR1 center. Irradiation was followed by low-temperature annealing, which was intended to generate additional NV centers without fully annihilating the GR1 center. The 594 nm center is a radiation-related defect in nitrogen-containing diamonds. In the IR absorption spectra of both CVD-grown diamonds, small peaks at 1344 cm⁻¹ were observed. From those peaks, the single nitrogen concentration could be estimated as ~1 ppm (S. Eaton-Magaña and J.E. Shigley, "Observations on CVD-grown synthetic diamonds: A review," Fall 2016 *G&G*, pp. 222–245).

Both samples presented red fluorescence when excited by the deep UV wavelengths of the DiamondView, a feature that is consistent with the strong nitrogen-vacancy centers in these CVD-grown diamonds. However, neither sample showed any noticeable photochromic effects from the deep UV exposure, something that can occur in CVD-grown diamonds due to charge transfer of the NV centers or the SiV⁻ centers (S. Eaton-Magaña et al., "Laboratory-grown diamond: A gemological laboratory perspective," *Journal of Gems and Gemmology*, 2021, Vol. 23, No. 6, pp. 25–39).

The Fancy Deep orange sample was interesting to observe, as unmodified orange colors are extremely rare among natural diamonds and, until now, laboratory-grown samples. Subtle engineering of defect concentrations during post-growth treatment



Figure 9. The 1.72 ct yellowish brown and black non-nacreous (porcelaneous) pearl with *Telescopium telescopium* shells provided by the client. The intact shell is approximately 70 × 35 mm and the sawn shell is approximately 84 × 41 mm. Inset: An enlarged image of the pearl.

can lead to vastly different results in the color grades.

Sally Eaton-Magaña and
Paul Johnson

A Non-Nacreous Pearl Reportedly from *Telescopium telescopium*

GIA's Bangkok laboratory recently examined a yellowish brown and black non-nacreous button-shape pearl weighing 1.72 ct and measuring 6.64 × 6.53 × 5.07 mm. The pearl exhibited an attractive porcelain-like luster.

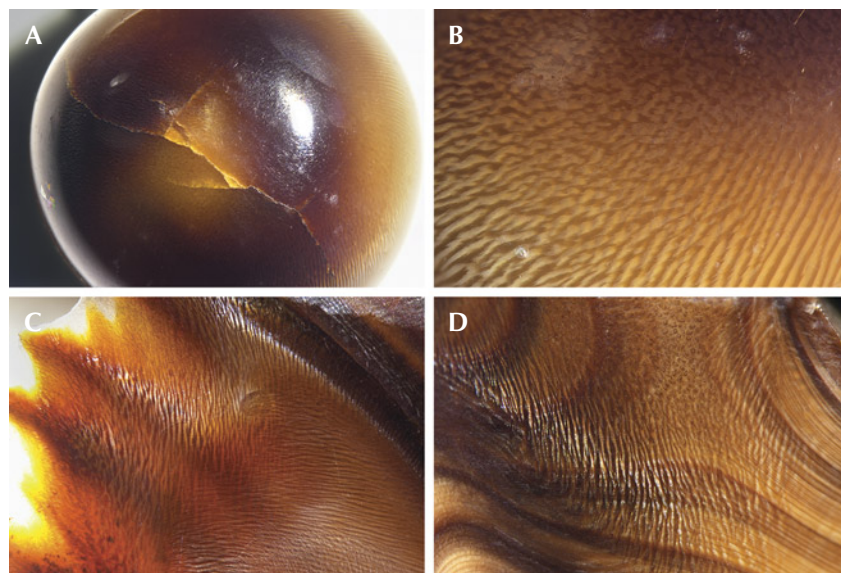
The client informed GIA that the pearl was found in a *Telescopium telescopium* shell. This edible snail (N. George et al., "DNA barcoding of gastropod *Telescopium telescopium* (Linnaeus, 1758) found at the Karachi coast, Pakistan," *Journal of Animal and Plant Sciences*, Vol. 31, No. 5, 2021, pp. 1530–1536) was retrieved from an abandoned shrimp pond near a mangrove forest in Krabi, Thailand. The story of the pearl's discovery was widely publicized in the local media. Though the client was unable to submit the shell from which the pearl was extracted, they provided us with samples of the same type of shell for further study (figure 9).

Observation through a 10× loupe and a microscope revealed long cracks traversing the darker side of the pearl (figure 10A). No polishing lines or evidence of surface or color modifica-

tion were observed, indicating that the shape and color were natural. The pearl and shells exhibited flame structures similar to those routinely observed in pearls such as those from the horse conch (Summer 2018 Lab Notes, pp. 211–212). Intersecting and overlapping flame structures typically observed in pearls from the *Cassia* genus (Fall 2012 Lab Notes, pp. 211–212) were also detected on the pearl (figure 10B) and shells (figure 10C). However, the banded structure observed on the cut shells (figure 10D) was not visible on the pearl, additional evidence that the client's item was a pearl and not an imitation fashioned from shell.

Real-time microradiography confirmed a natural whole pearl, as growth arcs close to the center and surface-reaching cracks were revealed (figure 11). As expected, energy-dispersive X-ray fluorescence analysis detected calcium as a major component in the pearl and shells, while manganese levels of less than 15 ppm and strontium levels ranging from 1005 to 2675 ppm verified a saltwater

Figure 10. A: Obvious long cracks traversing the pearl's darker side; field of view 7.20 mm. B: Intersecting flame structure on the pearl; field of view 2.40 mm. C: Intersecting flame structure on a cross section of the shell; field of view 4.80 mm. D: Banding and flame structure on a cut area of shell; field of view 4.80 mm.



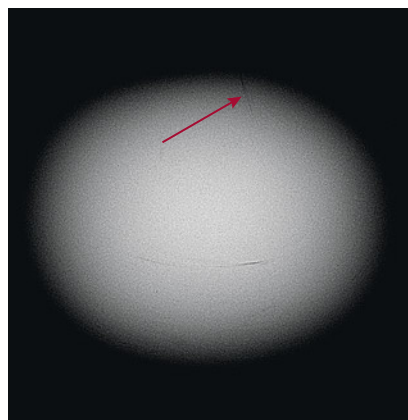


Figure 11. Real-time microradiography revealed growth arcs close to the center and surface-reaching cracks (red arrow).

formation environment. The pearl's natural color was substantiated using additional advanced spectroscopic methods. Raman spectra collected using a 514 nm argon ion laser on the pearl and shells (figure 12) revealed peaks related to the vibration modes of aragonite at 703, 1085, and 1464

cm^{-1} ; polyenic-related peaks at 1017, 1105–1120, 1297, and 1490–1500 cm^{-1} (S. Karampelas et al., "Polyacetylenic pigments found in pearls and corals," *30th International Gemmological Conference*, Moscow, 2007; L. Bergamonti et al., "The nature of the pigments in corals and pearls: A contribution from Raman spectroscopy," *Spectroscopy Letters*, Vol. 44, No. 7-8, 2011, pp. 453–458); and an additional peak at 1175 cm^{-1} that is also likely related to polyene.

Surface observations and data collected from the pearl and shells using analytical methods appeared to support the claim that the pearl formed in this mollusk species. However, this can only be confirmed by conducting DNA barcoding analysis, which is a destructive test. This report adds to the growing list of natural pearls found in edible oysters and snails described in the literature (e.g., Winter 1995 Gem News, pp. 280–281; K. Scarratt et al., "A note on a pearl attached to the interior of *Crassostrea virginica*

(Gmelin, 1791) [an edible oyster, common names, American or Eastern oyster]," *Journal of Gemmology*, Vol. 30, No. 1-2, 2006, pp. 43–50; Fall 2019 Gem News International, pp. 439–440; Fall 2020 Lab Notes, pp. 420–422; Summer 2021 Lab Notes, pp. 152–153). However, this is the first time a natural pearl has reportedly been discovered in a *Telescopium* species. Its unique appearance and characteristics provided a rare opportunity for GIA gemologists to examine and record data from a natural pearl originating from this marine snail.

Areeya Manustrong, Kwanreun Lawanwong, Ravenya Atchalak, and Nanthaporn Nilpetploy

Rare Kashmir Star SAPPHIRE

A rare star sapphire of Kashmir origin, mounted in a combination ring and pendant (figure 13), was recently examined in the New York laboratory. Kashmir has long been regarded as the

Figure 12. Raman spectra of the pearl and a shell obtained using a 514 nm argon ion laser revealed peaks related to the vibration modes of aragonite at 703, 1085, and 1464 cm^{-1} (obscured by stacking); polyenic-related peaks at 1015, 1120, 1296, and 1493 cm^{-1} ; and an additional peak at 1175 cm^{-1} that is also likely related to polyene. Spectra are offset vertically for clarity.

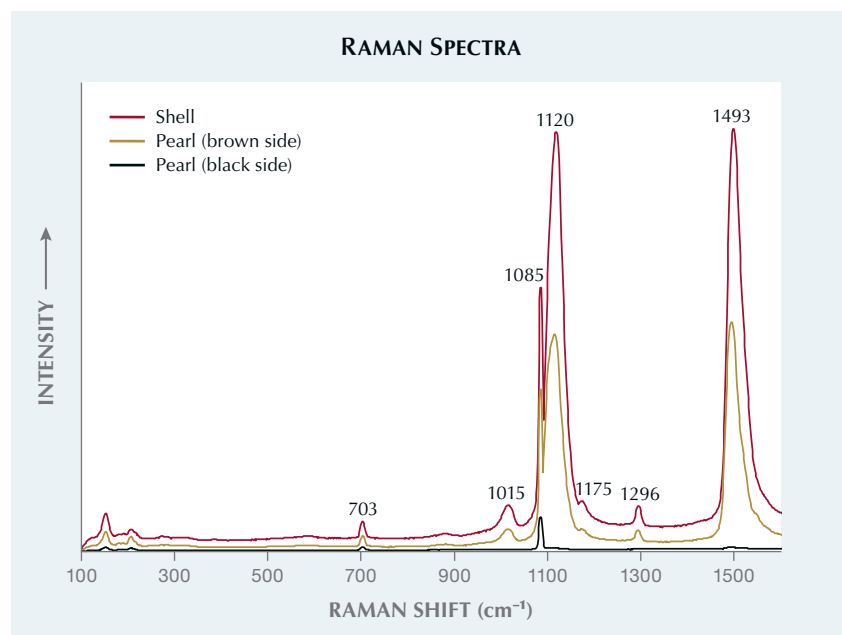


Figure 13. An approximately 15 ct blue Kashmir star sapphire set in a combination ring and pendant with near-colorless pear and marquise brilliants.



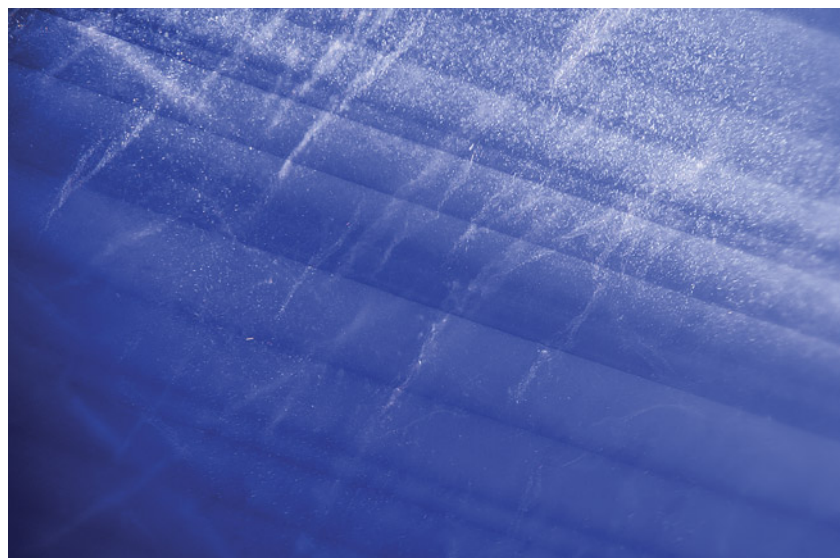


Figure 14. Wispy stringers among sharp milky bands of microscopic particles. Field of view 3.57 mm.

most sought-after source of blue sapphire since the deposit's discovery in the late nineteenth century. Words such as "sleepy" or "velvety" are often used to describe their characteristic appearance, which can be attributed to the scattering of light as it interacts with "milky" bands of microscopic particles within the stone. Due to the locality's limited production, Kashmir sapphires are scarce in the market, and star sapphires are particularly uncommon (R.W. Hughes et al., *Ruby & Sapphire: A Gemologist's Guide*, 2017, RWH Publishing/Lotus Publishing, Bangkok, p. 477).

This blue cabochon star sapphire was estimated to weigh around 15 ct. A spot reading gave an approximate refractive index of 1.76, matching corundum. Microscopic inspection revealed sharp, angular milky bands and particle streamers (figure 14), both features that are typical of Kashmir sapphires. Several sparse short silk needles were also observed (figure 15). Asterism in corundum is generally caused by the reflection of light off of exsolution rutile silk needles. This sapphire's star, however, was generated by light reflected from the crystallographically oriented bands of minute particles.

Further testing of the sapphire's spectral and chemical properties was carried out to help determine

its geographic origin. Laser ablation-inductively coupled plasma-mass spectrometry revealed a trace element chemistry consistent with stones of known Kashmir origin, based on GIA's internal reference data. This, coupled with the material's internal characteristics, confirmed that the star sapphire was in fact from Kashmir. No evidence of heat treat-

ment was detected. While the majority of corundum on the market is heated to improve color, high-quality sapphires from Kashmir are generally left untreated.

Kashmir sapphires are rare enough in their own right. Furthermore, a large star sapphire from this historic locality is truly an extraordinary sight, and certainly a first for the author.

Emily Jones

SYNTHETIC MOISSANITE

Fraudulently Inscribed Synthetic Moissanite

Stones with fraudulent GIA inscriptions are frequently reported. To verify diamond identity, GIA recently announced a diamond matching service using GIA Match iD, based on laser inscription imaging. In most cases of fraud, the inscribed material is diamond (Fall 2017 Lab Notes, p. 366), but there has also been a report involving non-diamond materials (Fall 2020 Lab Notes, pp. 424–425). A similar case was recently identified.

The Mumbai laboratory received a 1.71 ct square modified brilliant (figure

Figure 15. Several short needles of exsolution silk amid the abundant particle stringers. Field of view 1.85 mm.

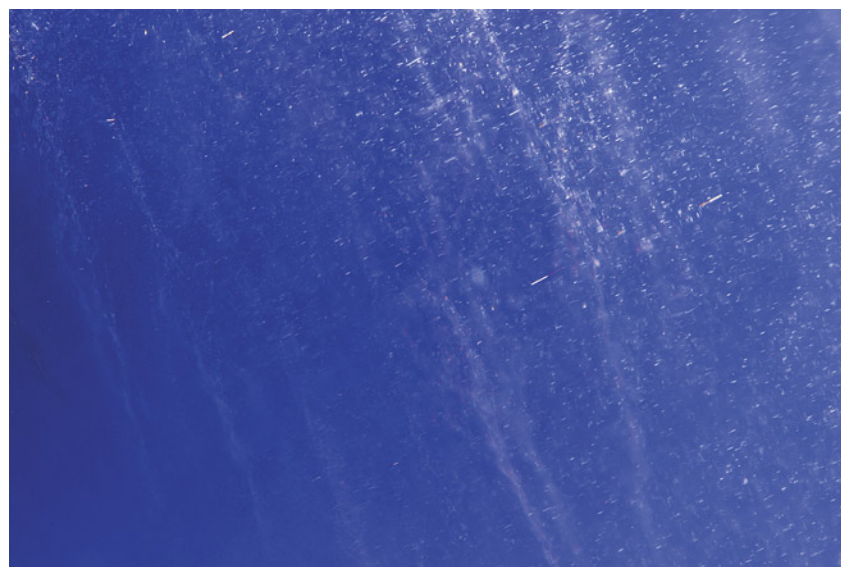




Figure 16. This 1.71 ct square modified brilliant bears a fraudulent GIA inscription.

16) for update service. The girdle was inscribed with "GIA" and a number matching an existent report, although the font was different from that of an actual GIA inscription (figure 17). The inscribed report number matched one for a natural diamond, a 1.71 ct square modified brilliant cut. Compared with a typical laser inscription from the GIA laboratory, this one was significantly different. Gemological and spectroscopic examination confirmed that the brilliant was synthetic moissanite. In addition to diamonds and synthetic moissanite, GIA has previously identified laser inscriptions on cubic zirconia, diaspore, emerald, garnet, ruby, sapphire, spinel, tanzanite, and other materials.

Shoko Odake

Figure 17. The fraudulent inscription on the synthetic moissanite.



A Synthetic Moissanite Presented As Natural Diamond Rough

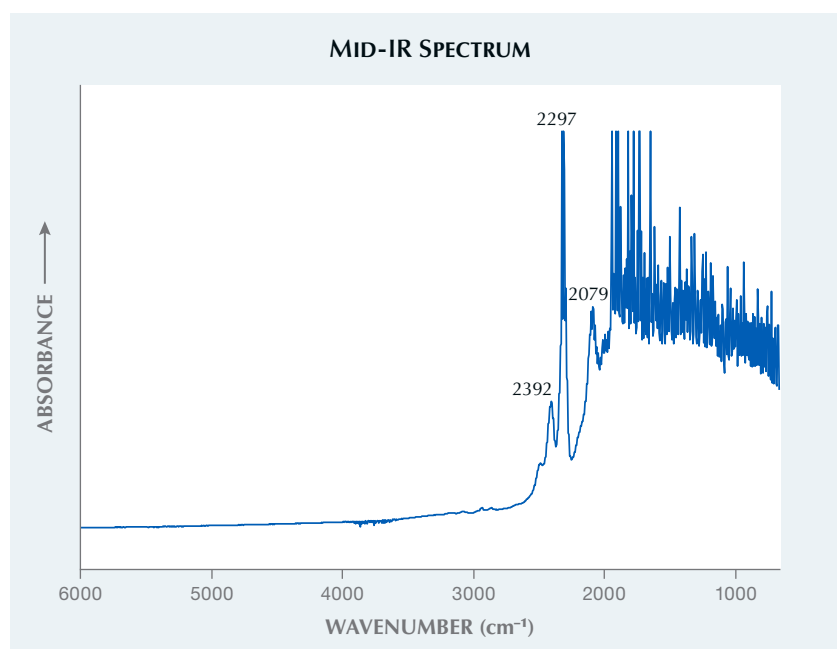
A 7.42 ct light bluish green specimen (figure 18) submitted to the New York lab for a colored diamond identification and origin report was identified as a synthetic moissanite crystal carved to resemble a natural diamond rough. Since synthetic moissanite resembles diamond at a glance and has a similar specific gravity and "heft," it could easily be mistaken for natural diamond. The sample was first identified as synthetic moissanite using Fourier-transform infrared (FTIR) spectroscopy (figure 19). The resulting data displayed a distinctive moissanite spectrum, with peaks occurring at 2079, 2297, and 2392 cm^{-1} (A.M. Hofmeister et al., "Optical constants of silicon carbide for astrophysical applications," *Astrophysical Journal*, Vol. 696, No. 2, 2009, pp. 1502–1516). This finding was confirmed with an analysis of the Raman spectrum, which showed strong 767, 788, and 798 cm^{-1} peaks, also consistent with synthetic moissanite (figure 20). Although natural moissanite does exist,



Figure 18. This 7.42 ct light bluish green synthetic moissanite, submitted as a diamond, displays triangular features on each of the octahedral faces.

crystals are tiny and fragmented. Gem-quality specimens have not yet been found (Summer 2014 Gem News International, pp. 160–161).

Figure 19. The peaks at 2079, 2297, and 2392 cm^{-1} displayed in this FTIR spectrum are consistent with synthetic moissanite.



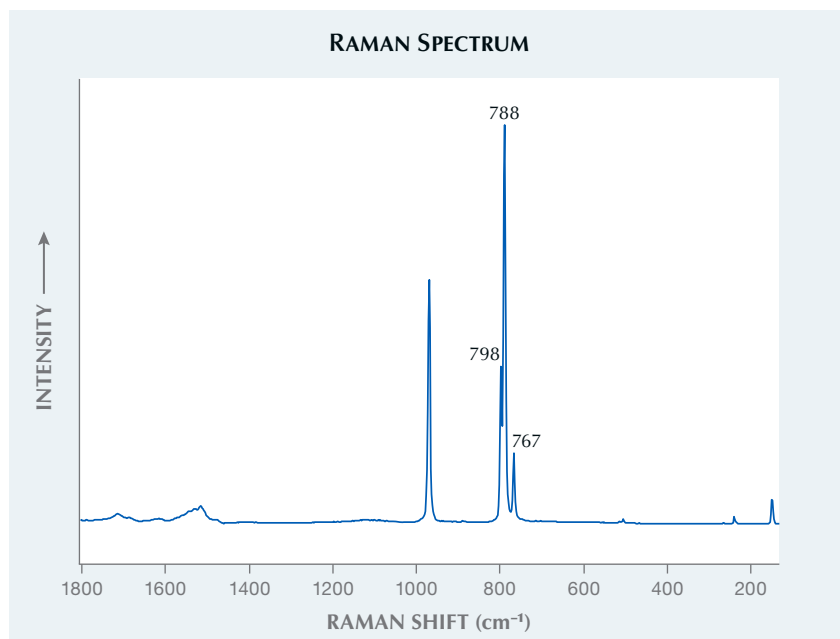


Figure 20. Raman spectroscopy confirmed the identification as synthetic moissanite, with peaks at 767, 788, and 798 cm^{-1} . (The sharp peak at 970 cm^{-1} suggests a hexagonal 6H type of silicon carbide.)

The turbid and stained 7.42 ct synthetic moissanite was shaped into a slightly rounded octahedron with prominent stepped edges. Octahedra belong to the cubic crystal class; both natural and synthetic SiC belong to the trigonal class and always display hexagonal prismatic to tabular forms. It was concluded that the synthetic moissanite rough had been carved into an octahedron, and that the detailing of the stepped edges and coarse textures were specifically chosen to imitate the appearance of a natural diamond octahedron that had been partially resorbed by kimberlitic magma, such as the natural diamond in figure 21. Although sharp and well-formed diamond octahedra are occasionally found preserved in mantle rocks entrained in kimberlitic eruptions, the vast majority of natural diamond crystals are exposed to corrosive kimberlitic fluids during their ascent through the cratonic mantle and display a wide variety of resorption textures (R. Tappert and M.C. Tappert, *Diamonds in Nature: A Guide to Rough Diamonds*, 2011, Springer Verlag, Heidelberg, Germany).

This investigation is a reminder to take caution when identifying gemstones, as intentional material processing steps such as these may be used to deceive consumers and could damage the integrity of the gem trade.

Courtney Robb and Sarah Arden

Cat's-Eye Paraíba TOURMALINE With Copper Inclusions

The Tokyo laboratory recently received a 1.33 ct greenish blue oval cabochon measuring $6.83 \times 6.17 \times 3.55$ mm (figure 22) and displaying a cat's-eye effect. Standard gemological testing yielded a refractive index of 1.620–1.640, a uniaxial optical sign, and a hydrostatic specific gravity of 3.08, all consistent with tourmaline. Ultraviolet/visible/near-infrared spectrometry showed the absorption band at 900 nm, which is greater than the one at 700 nm, indicating the greenish blue color of this sample was dominated by copper (P.B. Merkel and C.M. Breeding, "Spectral differentiation between copper and iron colorants in gem tourmaline," Summer 2009 *G&G*, pp. 112–119). This stone



Figure 21. Exposure to kimberlitic fluids rich in O_2 and H_2O creates varied shapes and textures in natural diamond octahedra. This natural green diamond, known as the "Matryoshka" (Spring 2020 Lab Notes, pp. 127–129) has resorbed points and edges as well as trigonal etching on the {111} faces.

meets the requirement for designation as a Paraíba tourmaline (Laboratory Manual Harmonisation Committee Information Sheet #6, 2012). Laser ablation–inductively coupled plasma–mass spectrometry indicated a high copper concentration of 11741–14794 ppmw. The high copper (over 10000 ppmw) is limited to Bra-

Figure 22. This 1.33 ct cat's-eye Paraíba tourmaline with copper inclusions shows a golden chatoyancy.



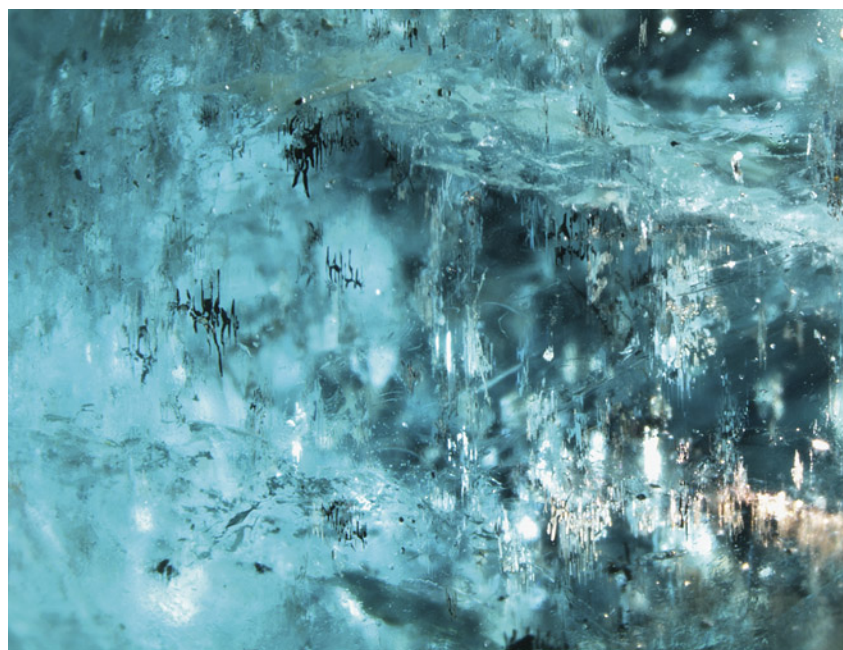


Figure 23. The copper inclusions on the lower right are partially reflecting light. Field of view 3.5 mm.

zilian origin (Y. Katsurada et al., "Geographic origin determination of Paraiba tourmaline," Winter 2019 *G&G*, pp. 648–659).

As previously reported (Winter 2018 Lab Notes, pp. 438–439), cat's-eye Paraiba tourmaline usually includes groups of parallel tube-like inclusions that create the phenomenon. However, that was not the case for this tourmaline.

Different from normal cat's-eye Paraiba tourmaline, the band of reflected light in this stone was stronger, with metallic luster. Microscopic examination revealed a fluid inclusion network, rounded metallic inclusions, and growth tubes, with many golden-colored dendritic inclusions causing the cat's-eye effect (figures 23 and 24). Raman spectroscopy could not be used to identify the in-

clusions, which were too thin and did not reach the surface. Such inclusions in Paraiba tourmaline have been reported and identified as natural copper (F. Brandstätter and G. Niedermayr, "Copper and tenorite inclusions in cuprian-elbaite tourmaline from Paraiba, Brazil," Fall 1994 *G&G*, pp. 178–183). The natural copper inclusions were aligned in the same direction, parallel to each other, and reflected the light to cause the chatoyant effect. This also explains why the reflective light band in this stone looked different from other cat's-eye Paraiba tourmaline.

While some cat's-eye Paraiba tourmalines have been examined in GIA laboratories, this is the first with chatoyancy caused by copper inclusions.

Yuxiao Li

PHOTO CREDITS

Diego Sanchez—1, 7 (left); Jian Xin (Jae) Liao—2, 18, 21; Luthfia Syarbaini—3; Shunsuke Nagai—5, 22; Makoto Miura—6; Sood Oil (Judy) Chia—7 (right); Lhapsin Nillapat and Nuttapol Kitdee—9; Ravenya Atchalak and Kwanreun Lawanwong—10, 11; Annie Haynes—13; Emily Jones—14, 15; Sushant Shinde—16; Sandesh Mali—17; Yuxiao Li—23, 24

Figure 24. The copper inclusions aligned in the same direction appear brownish and black (left) and together display golden luster when the light enters from a certain direction (right). Field of view 2.3 mm.





G&G

Micro-World

Editor: Nathan Renfro

Contributing Editors: Elise A. Skaltwold and John I. Koivula

Breyite Inclusion in Diamond

Sublithospheric or “superdeep” diamonds are rare, estimated to make up only 1–3% of mined diamonds globally. They are recognized on the basis of their mineral inclusions. Breyite (CaSiO_3) is one of the minerals sometimes encountered in this curious geological family of diamonds. Diamonds containing breyite are often interpreted to come from depths greater than 360 km, where the breyite would have initially had a high-pressure perovskite-type crystal structure. The perovskite-structured CaSiO_3 would have changed to the breyite crystal structure in response to the drastic decrease in pressure during the diamond’s journey to the surface. Alternatively, it is theoretically possible that breyite could be trapped directly in a diamond at much shallower depths, say within 150–200 km, although such an occurrence within a known lithospheric diamond has yet to be encountered.

The breyite inclusion in figure 1 was recently observed in a 1.00 ct D-color type IIa diamond submitted to GIA’s New York laboratory. Raman spectroscopy was used to identify it as breyite. This large inclusion, 450 μm in its longest dimension, is colorless and transparent. A conspicuous healed fracture surrounds it, containing graphite (black) and smaller “sub-inclusions” of breyite that appear

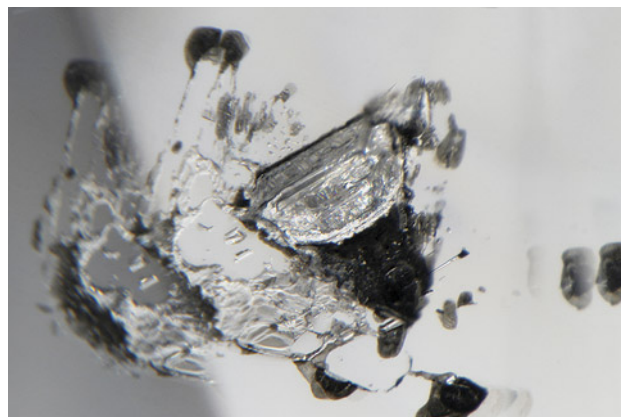
to emanate from the main inclusion. Based on this breyite inclusion, the diamond is suspected to be sublithospheric in origin.

*Evan M. Smith and Kyaw Soe Moe
GIA, New York*

Small “Surprise” in Elbaite Tourmaline

Recently, a 0.86 ct orange-yellow elbaite tourmaline cabochon was submitted to Taiwan Union Lab of Gem Research (TULAB) for identification service. The stone contained many prismatic and round xenocrysts. Among these inclusions was a prismatic crystal associated with a

Figure 1. A breyite inclusion in diffuse illumination. Doubling of some features to the right and left of the inclusion is an artifact of viewing through multiple pavilion facets. Photomicrograph by Evan M. Smith; field of view 1.58 mm.



About the banner: This topaz from Madagascar contains a negative crystal etch tube, highlighted in blue using Rheinberg illumination. Photomicrograph by Nathan Renfro; field of view 2.21 mm. Stone courtesy of the John Koivula Inclusion Collection.

GEMS & GEMOLOGY, VOL. 58, NO. 3, pp. 364–369.

© 2022 Gemological Institute of America



Figure 2. The “exclamation point” inclusions were identified as diopside crystals using Raman spectroscopy. Photomicrograph by Shu-Hong Lin; field of view 4.11 mm.

round crystal, a composition resembling an exclamation point (figure 2). The crystals were later confirmed to be diopside using Raman spectroscopy. Darkfield illumination, plane polarized light, and extended depth of field were adopted to obtain a clear microscopic image of this little “surprise” inside the gemstone.

Shu-Hong Lin
Institute of Earth Sciences,
National Taiwan Ocean University
Taiwan Union Lab of Gem Research, Taipei
Tsung-Ying Yang, Kai-Yun Huang, and Yu-Shan Chou
Taiwan Union Lab of Gem Research, Taipei



Figure 3. This 27.76 ct pear-shaped double cabochon contained several fluid inclusions with a vibrant purple component. Photo by Annie Haynes; courtesy of Mike Bowers.

Unusual Purple Fluid in Quartz

Recently the authors examined a 28.93 mm long, 27.76 ct transparent pear-shaped double cabochon rock crystal quartz that contained numerous fluid-filled negative crystals (figure 3). Oddly, some of the negative crystals also hosted a brightly colored purple liquid in addition to what appeared to be a colorless liquid, the two liquid phases being immiscible (figure 4).

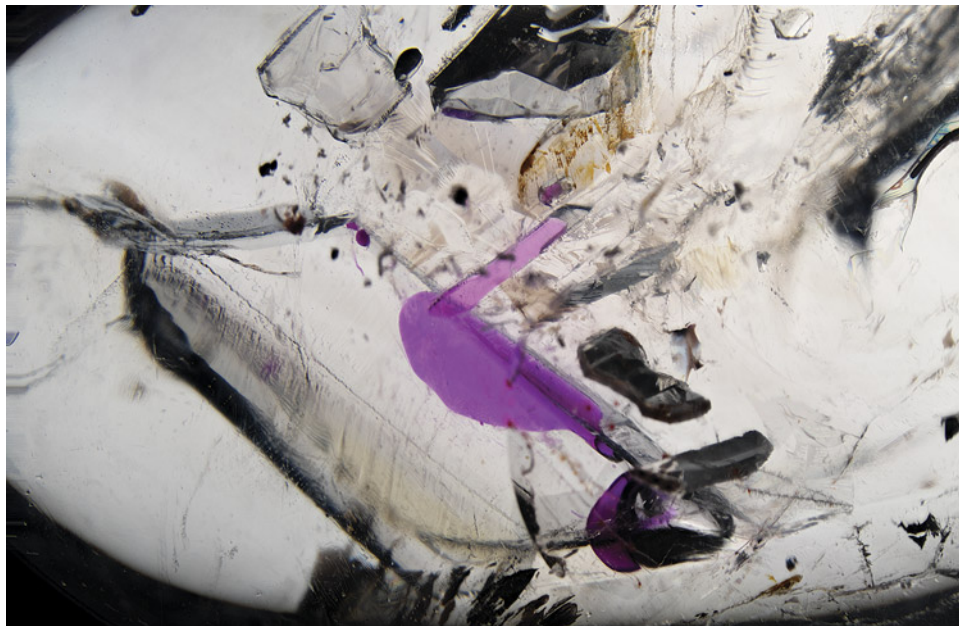


Figure 4. Several fluid-filled negative crystals were present in this rock crystal quartz cabochon, a few of which contained a highly unusual brightly colored purple liquid. Photomicrograph by Nathan Renfro; field of view 14.50 mm. Courtesy of Mike Bowers.

Not all of the fluid inclusions within this quartz contained the purple component. However, all of the purple liquid-hosting negative crystals did contain partially healed, limonite-stained fractures intersecting them. This suggests that the purple fluid may have entered the negative crystal cavities through a post-growth or secondary process rather than homogeneous entrapment during growth.

While colored fluid inclusions have been previously reported in quartz—colors that include blue, yellow, and orange (see e.g., Spring 2004 Gem News International, pp. 79–81; Spring 2006 Gem News International, p. 71)—this is the authors' first observation of a purple fluid trapped within quartz. Unfortunately, Raman spectroscopy to identify the fluid was unsuccessful, as the fluid was too deep in the crystal. While the composition of the fluid is unknown, as well as the conditions under which the fluid entered the quartz, there is no obvious indication that it resulted from an artificial process. However, the possibility of such artificial tampering cannot be ruled out entirely. This fascinating purple fluid inclusion is one of the strangest and most interesting the authors have examined.

Nathan Renfro and John I. Koivula
GIA, Carlsbad

Large Orange Rutile Inclusion in a “Chameleon” Diamond

The author recently received for analysis a 1.51 ct round brilliant diamond with very light green color and SI₂ clarity. The diamond exhibited “chameleon” properties, showing a clear color change from green to yellow upon heating

with an alcohol lamp. An ~0.2 mm orange inclusion was clearly visible on the crown (figure 5). The crystal was partially enclosed, confirming it was an actual inclusion rather than a crystal adhered to the diamond surface. It was also partially exposed, enabling simple Raman spectroscopy for identification without the spectra showing any contribution from the diamond itself. The crystal was determined to be rutile (TiO₂), suggesting an eclogitic origin.

Rutile inclusions in diamond are themselves relatively uncommon, and we rarely see such a large, eye-catching crystal. Rutile inclusions can also provide useful clues about a diamond's age. Geochemists can determine the age of rutile crystals by measuring the concentration of isotopes of various elements that are present at parts-per-million concentrations, allowing for constraints on the age of the diamond itself (see A.K. Schmitt et al., “U-Pb ages of rare rutile inclusions in diamond indicate entrapment synchronous with kimberlite formation,” *Lithos*, Vol. 350–351, 2019, article no. 105251). It will be interesting to see what scientific information this rare inclusion in diamond may reveal.

Mike Jollands
GIA, New York

“Smoke Rings” in a Non-Beryllium-Diffused Sapphire

When analyzing corundum for evidence of heat treatment, one of the most useful and standard methods for gemologists is microscopic examination (N.D. Renfro et al., “Inclusions in natural, synthetic, and treated sapphire,” Summer 2017 *G&G*, pp. 213–214). Inclusion suites can

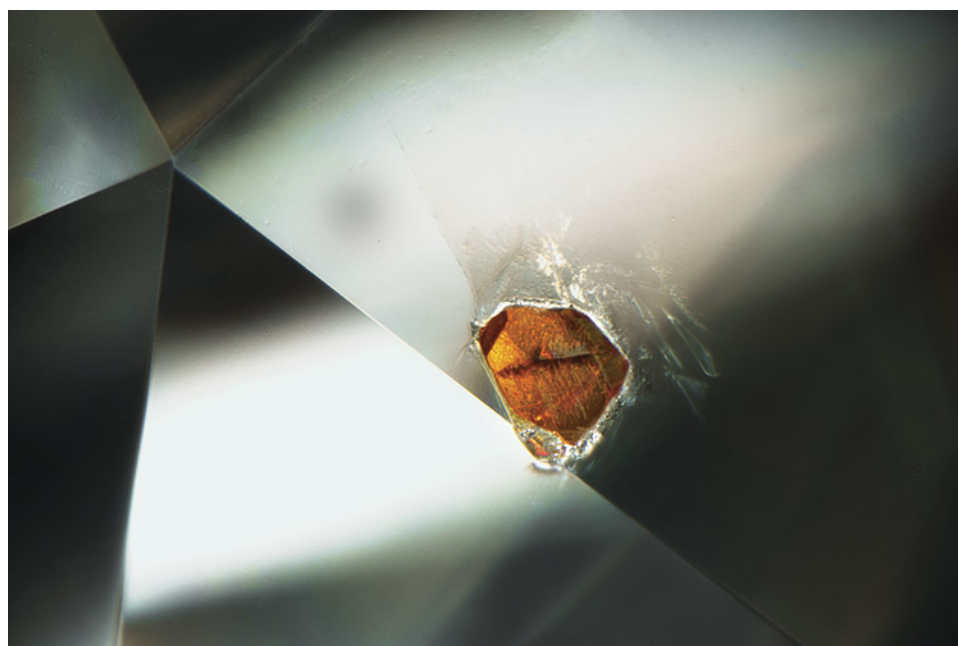


Figure 5. An orange rutile crystal partially enclosed on the crown of a faceted diamond (the sharp line from top left to bottom right is the facet junction). Photomicrograph by Tyler Smith; field of view 0.8 mm.

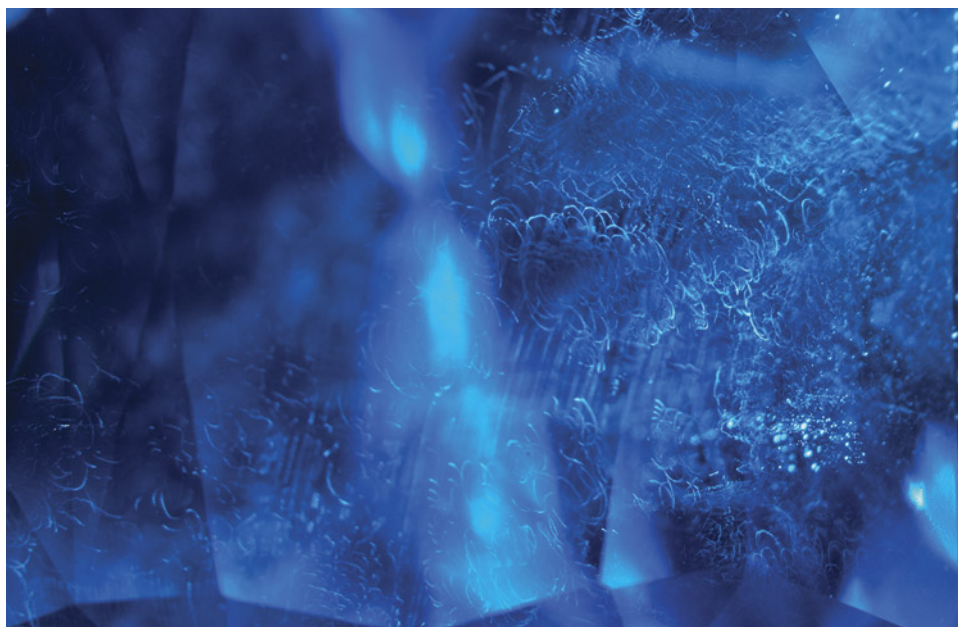


Figure 6. This “smoke ring” pattern was observed in a heat-treated blue sapphire. While this pattern is commonly associated with beryllium-diffused blue sapphires, no beryllium was detected in this stone. Photomicrograph by Nicole Ahline; field of view 7.39 mm.

start to alter at temperatures as low as 200°C. As the temperature rises, many inclusions start to show clear evidence of heat treatment, such as the internal diffusion of titanium, resulting in a spotty blue color, and discoid tension cracks with healed fringes around crystals. Standard temperature heat treatment for corundum happens between 500° and 1700°C, whereas high-temperature heat treatment, such as beryllium diffusion, occurs at temperatures above 1750°C. These high temperatures can modify inclusions in a way that renders them unidentifiable, suggesting that a stone may have undergone beryllium diffusion.

While examining a heated blue sapphire recently, the author observed “smoke ring” inclusions throughout it (figure 6) using fiber-optic illumination. Trace element chemistry analysis of the blue sapphire via laser ablation–inductively coupled plasma–mass spectrometry revealed no signs of beryllium. This came as a surprise, as this dislocation pattern is associated with beryllium-diffused corundum. These “smoke ring” dislocations are consistent with sapphires that have been heated at high temperatures, but chemistry ruled out beryllium diffusion treatment. This sapphire offers a striking example of why continuous documentation of inclusions, in both treated and untreated gemstones, is an important tool in gemstone analysis.

*Nicole Ahline
GIA, Carlsbad*

Stellate Zircon in a Paraíba Tourmaline

While examining a 1.17 ct blue-green Paraíba tourmaline with a fiber-optic light, the author observed a remarkable set of stellate inclusions (figure 7). The striking suite consisted of one larger cluster with scattered smaller needles trailing behind it. Reflective lighting revealed needles breaking the surface with a different luster from the host tourma-

line. Raman spectroscopy identified the needles as zircon.

Tourmalines form in a pegmatite environment and contain inclusions that reflect this type of growth, most notably fluid inclusions, transparent crystals, and tubular inclusions. Zircon has been observed in tourmaline as prismatic or rounded crystals. The zircons in this 1.17 ct Paraíba tourmaline were atypical as they were needles and in a stellate formation. This type of zircon morphology has been previously documented in morganite (Winter 2013 Lab Notes, pp. 253–254), but stellate inclusions, specifically those composed of zircon, are a rather unique find. The stellates in this Paraíba tourmaline make the gemstone quite unusual.

Nicole Ahline

Figure 7. Zircon needles in a stellate formation observed in a 1.17 ct blue-green Paraíba tourmaline. Photomicrograph by Nicole Ahline; field of view 2.18 mm.

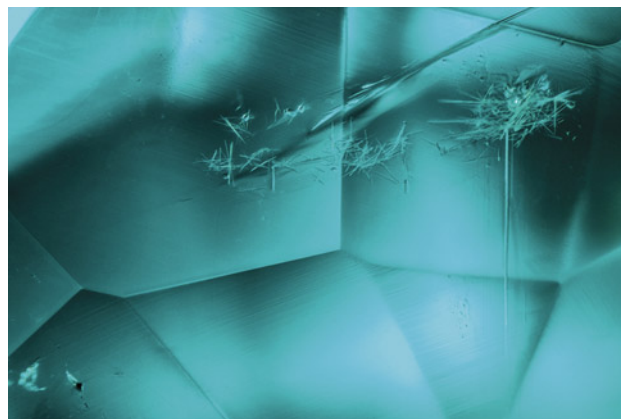




Figure 8. Weighing 751.95 ct, this parallel cluster of two quartz crystals contains a directional phantom plane composed of numerous green to near-colorless hexagonal inclusions. Photo by Adriana Gudino.

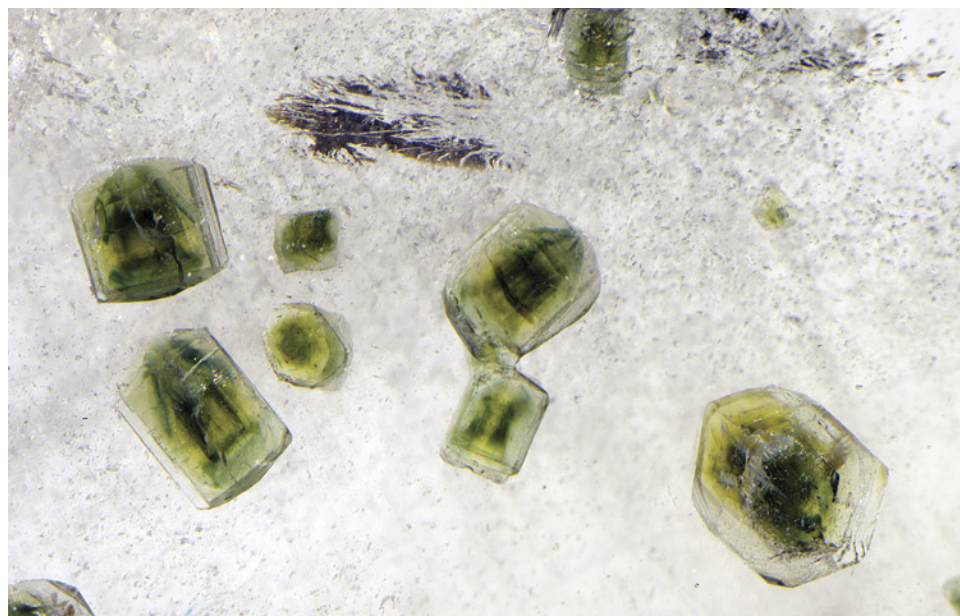


Figure 9. The translucent green-colored crystals along the phantom plane in the Portuguese quartz were identified as fluorapatite by Raman analysis. Photomicrograph by Nathan Renfro; field of view 12.47 mm.

Quarterly Crystal: Panasqueira Quartz

With its relatively high hardness and high degree of transparency, colorless rock crystal quartz is the perfect host for an abundance of fluid and mineral inclusions. As a common crustal mineral, it sometimes forms as solid single crystals and crystal clusters.

This issue's Quarterly Crystal, a 751.95 ct double crystal measuring $110.54 \times 50.30 \times 24.82$ mm from Minas da Panasqueira in Portugal (figure 8), comes from the personal collection of Jordi Fabre of Fabre Minerals in Barcelona. Examination of the two parallel quartz crystals revealed numerous colorless to green, transparent to translucent euhedral inclusions, identified by Raman

analysis as fluorapatite (figure 9). Some of these fluorapatite inclusions surrounded a much larger dark brownish orange protruding crystal confirmed as cassiterite (figure 10).

The colorless to green fluorapatite crystals show directional deposition and are along a phantom plane, situated only on one side of the quartz specimen. This suggests that they are syngenetic with the quartz host.

Quartz is relatively common at the Panasqueira mine. This "floater" quartz crystal group, which is recrystallized at its base, is an excellent host for the numerous inclusions of fluorapatite and the solitary cassiterite crystal.

John I. Koivula and Nathan Renfro

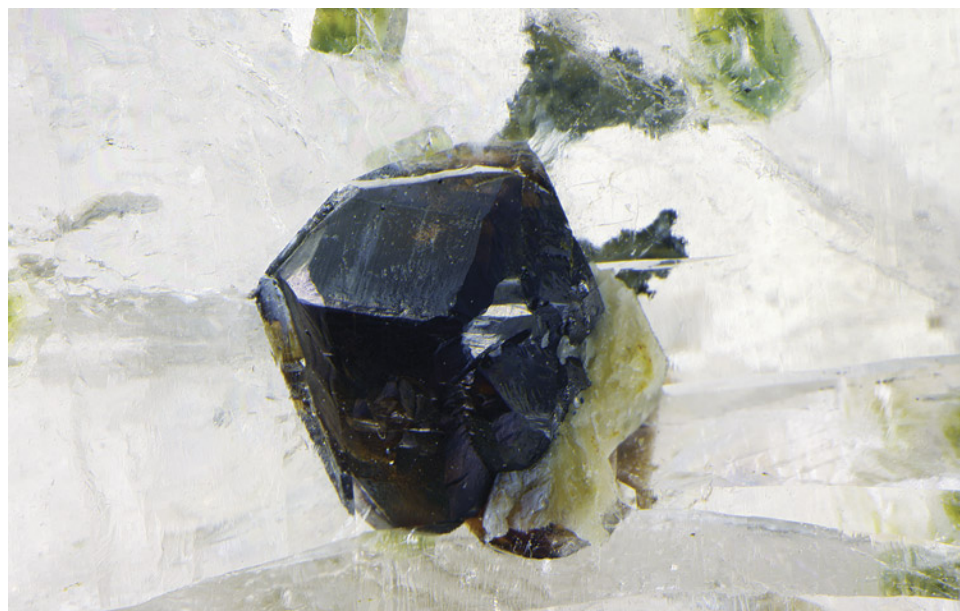


Figure 10. Using Raman microspectrometry, this single protruding dark brownish orange crystal was identified as cassiterite. Photomicrograph by Nathan Renfro; field of view 13.64 mm.



Editor: Evan M. Smith

The Liquids Lurking Inside Your Diamonds

Diamonds are dense, solid crystals of carbon. In top gem-quality form, a diamond appears to be a pristine, uniform, transparent material. It may be hard to believe, but even the highest-clarity natural diamonds are thought to contain nanometer-sized droplets of fluid. They are too small to see, even at high magnification with an optical microscope. And these are not the only kinds of fluid found in diamonds. Sometimes there are larger fluid inclusions, big enough to see with a microscope, that have either been trapped during diamond growth or have entered along small fractures that have healed and sealed themselves shut while the diamond was still deep within the earth's mantle. Some diamonds even contain colorful iridescent fluid mixtures of carbon dioxide and nitrogen. All of these fluids are reflections of the various natural processes that create and modify diamonds.

Fluids Trapped in Fibrous Diamonds

The discussion of liquid or fluid in diamond begins with something called *fibrous diamond*, which is generally not used as a gem because of its poor clarity. Fibrous diamonds contain abundant micrometer-sized inclusions (typically 0.1–1.0 μm) that render them cloudy or turbid in appearance. They often take the form of imperfect cube-shaped crystals or coatings atop octahedral diamonds (figure 1). Fibrous diamonds are thought to crystallize rapidly, and inclusions readily become trapped between their “fibers” or microscopic dendrites during growth (Kamiya and Lang, 1965; Navon et al., 1988; Sunagawa, 1990).

Editor's note: Questions or topics of interest should be directed to Evan Smith (evan.smith@gia.edu).

GEMS & GEMOLOGY, VOL. 58, NO. 3, pp. 370–374.

© 2022 Gemological Institute of America

Diamond growth in the mantle occurs at a depth of about 150–200 km and sometimes even deeper. Most forms of diamond growth, including fibrous diamond growth, occur by metasomatism, meaning the interaction between carbon-bearing fluids and preexisting host rocks (Haggerty, 1999; Stachel et al., 2005). As this fluid percolates along grain boundaries and cracks, it can undergo changes in temperature, pressure, or composition that cause its dissolved carbon to crystallize as diamond. A central aim of diamond research has been to understand what kinds of carbon-bearing fluids (or melts) contribute to diamond growth. In this respect, fibrous diamonds have offered considerable insight.

The abundant inclusions in fibrous diamonds are well-preserved samples of carbon-bearing, diamond-forming fluids (Navon et al., 1988). A range in fluid compositions has been observed, with four distinct “end-member” compositions: silicic, saline, high-magnesium carbonatitic, and low-magnesium carbonatitic (Navon et al., 1988; Israeli et al., 2001; Tomlinson et al., 2006; Klein-BenDavid et al., 2007; Weiss et al., 2009). During the time of diamond growth, the fluid being trapped as inclusions was a single phase, without bubbles or crystals. Water makes up 10–25 wt.% of this fluid, with the remainder being dissolved material (Weiss et al., 2010; Elazar et al., 2019). Considering the high initial dissolved content, they are sometimes called high-density fluid (HDF) inclusions. However, when a kimberlite or related volcanic eruption carries a fibrous diamond up to the earth's surface, the cooler and lower-pressure conditions cause daughter crystals of silicate, carbonate, and other solids to form within the inclusions. The result is an inclusion containing multiple solid daughter phases and a residual fluid phase. These watery, carbon-bearing fluid inclusions represent snapshots of the parental diamond-forming fluid for fibrous diamonds. Interestingly, similar fluids may be involved in the growth of most transparent, gem-quality diamonds (Jablon and Navon, 2016; Krebs et al., 2019).

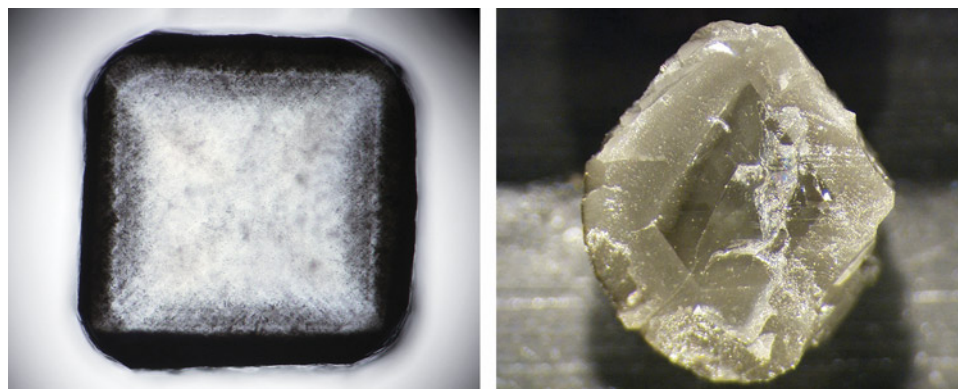


Figure 1. Examples of fibrous diamond. The polished slice (left) is roughly a {100} section through a fibrous cuboid. The broken diamond (right) is roughly a {110} section through a fibrous coat and a transparent, non-fibrous octahedral core. Photos by Evan M. Smith; fields of view 4.51 mm (left) and 5.38 mm (right).

Gem-Quality Diamonds

Why do scientists think there is a link between transparent gem-quality diamonds and the palpable cloudiness of fluid inclusions in fibrous diamonds? Part of the answer comes from macle twinned gem-quality diamonds. One study that searched for inclusions trapped along macle twin planes encountered fluid micro-inclusions in eight specimens from two localities, and the fluid compositions fell within the range of those seen in fibrous diamonds worldwide (Jablon and Navon, 2016). This finding was used to argue that fibrous and non-fibrous diamonds can form from the same kinds of parental fluids.

The second part of the answer lies in trace elements. Diamonds are made of a single major element, carbon, but also contain trace amounts of many other elements of the periodic table. The absolute and relative abundances of these elements represent a geochemical ledger that reflects the specific conditions and ingredients contributing to the growth of any given diamond. Comparing the trace element characteristics of transparent gem-quality diamonds with cloudy fibrous diamonds reveals striking similarities (Krebs et al., 2019). The similarity of trace element signatures provides an additional piece of evidence that many gem-quality diamonds crystallize from roughly the same kinds of fluids as those trapped in fibrous diamonds. Rather than occurring as substitutional or interstitial atoms in the

diamond crystal lattice, the trace element signatures measured in gem-quality, transparent diamonds are proposed to come from sub-microscopic nano-inclusions of fluid like those of fibrous diamonds, but present in lower abundance. It implies that high-clarity, optically transparent diamonds that appear to be inclusion-free are actually laced with small droplets of fluid that are simply too small to see.

Exotic Metallic Liquid

There are multiple ways diamonds can form in nature, involving different host rocks, at different depths within the earth, and different kinds of diamond-forming fluids. We are still learning about all the different kinds of diamond-forming fluids, but we know there are multiple distinct groups. The range of saline-silicic-carbonatitic fluids found in fibrous diamond is just one of these groups. Some diamonds crystallize from completely different kinds of fluids. For example, we now have compelling evidence that some diamonds crystallize from methane-rich fluid (Smit et al., 2016) or even iron-rich metallic liquid (Smith et al., 2016). The latter are mixtures of iron, nickel, carbon, and sulfur that were molten at the time of diamond growth but now exist as solid inclusions (figure 2). Inclusions like these that are solid now at the ambient conditions of the earth's surface, but were molten liquid at the time of entrapment, are sometimes called melt inclusions.



Figure 2. Left: A type IIa diamond (4.12 ct, D color) with metallic inclusions. Photo by Jian Xin (Jae) Liao. Right: The large metallic inclusion has a localized round, graphitized fracture extending from its top end. Photomicrograph by Evan M. Smith; field of view 1.42 mm.

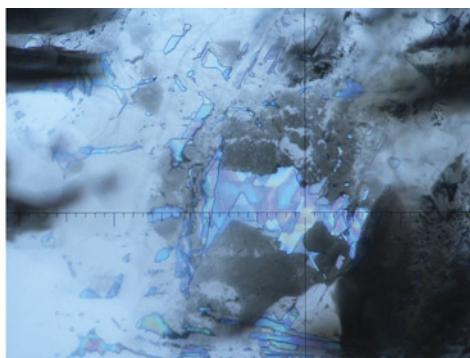


Figure 3. Left: A polished diamond slice (3.7 mm × 3.7 mm) with healed fractures and fluid inclusions. Right: The fluid inclusions display thin-film interference colors and have irregular polygonal boundaries governed by the diamond recrystallization as the fracture healed (field of view 245 μm). Photos by Evan M. Smith.

The solidified metallic liquid in figure 2 is a kind of inclusion that has been observed repeatedly in what can be called “CLIPPIR” diamonds (Smith et al., 2016, 2017). This is a variety of sublithospheric or super-deep diamond that originates from an estimated 360–750 km deep in the earth. Large, colorless (D color), type IIa diamonds often belong to this family. In fact, the initial recognition of this diamond variety stems from recurrent observations in the gem trade that larger, higher-quality diamonds have a greater tendency to be type IIa. The CLIPPIR acronym captures their distinguishing physical properties: Cullinan-like, Large, Inclusion Poor, Pure, Irregular, and Resorbed.

Out of 83 inclusion-containing CLIPPIR diamonds in one study, 67 had inclusions with metallic melt (Smith et al., 2017). The relative abundance of metallic melt inclusions is one of the features that makes these diamonds so interesting. The origin of this metal has been illuminated by measuring the isotopic composition of iron (Smith et al., 2021). The iron can be traced back to a process called serpentinization, where water chemically reacts with the rocks in oceanic tectonic plates. Iron from seafloor serpentinization was carried deep into the earth by the action of oceanic tectonic plates sinking down into the mantle, a process called subduction. After sinking down to 360–750 km, the serpentinized rocks contribute to the growth of CLIPPIR diamonds and are responsible for supplying the

exotic metallic liquid sometimes trapped as inclusions. Tracing out this deep subduction pathway for serpentinized oceanic rocks is important for our understanding of how water, carbon, and other materials get transported from the earth’s surface down into the convecting mantle over millions of years.

Healed Fractures

Fluid micro-inclusions in fibrous diamonds, invisible nano-inclusions in some gem-quality diamonds, and metallic melt inclusions in CLIPPIR diamonds are all examples of primary inclusions. This means they were trapped during diamond growth. It is also possible to trap material post-growth in fractures. If a fracture allows fluid to penetrate into a diamond and conditions allow the fracture to heal, it can trap some of the fluid as an inclusion. So-called fingerprint inclusions in corundum and other minerals also arise from secondary, post-growth fluid trapping along fractures.

A colorful instance of fluid trapped in a healed fracture in diamond is shown in figure 3. This is an alluvial diamond from the Ebelyakh River, Siberia. Alluvial diamonds from this region sometimes have discontinuous, black graphitic features inside them that trace out healed fracture networks. Under closer examination, these healed fractures regularly host fluid inclusions (Tomilenko et al.,

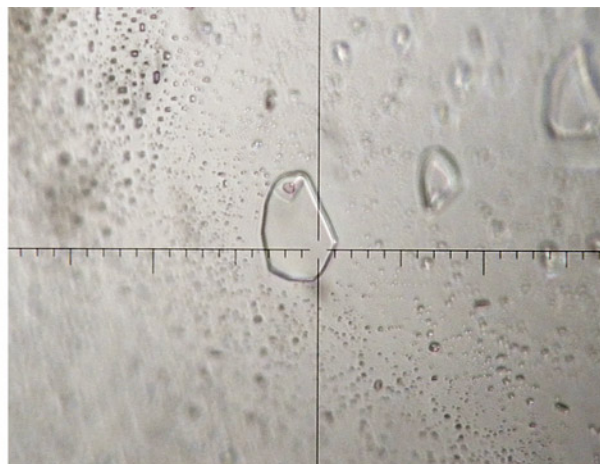


Figure 4. Left: A 3.66 ct octahedral diamond crystal (shown beside a millimeter scale) with silicate melt inclusions in healed fractures. The black and red ink marks are for planning prior to polishing for research purposes. Right: The largest inclusion (under the crosshairs) has a 4 micrometer wide pinkish bubble of nitrogen visible at the top end (field of view 180 μm). Photos by Evan M. Smith.

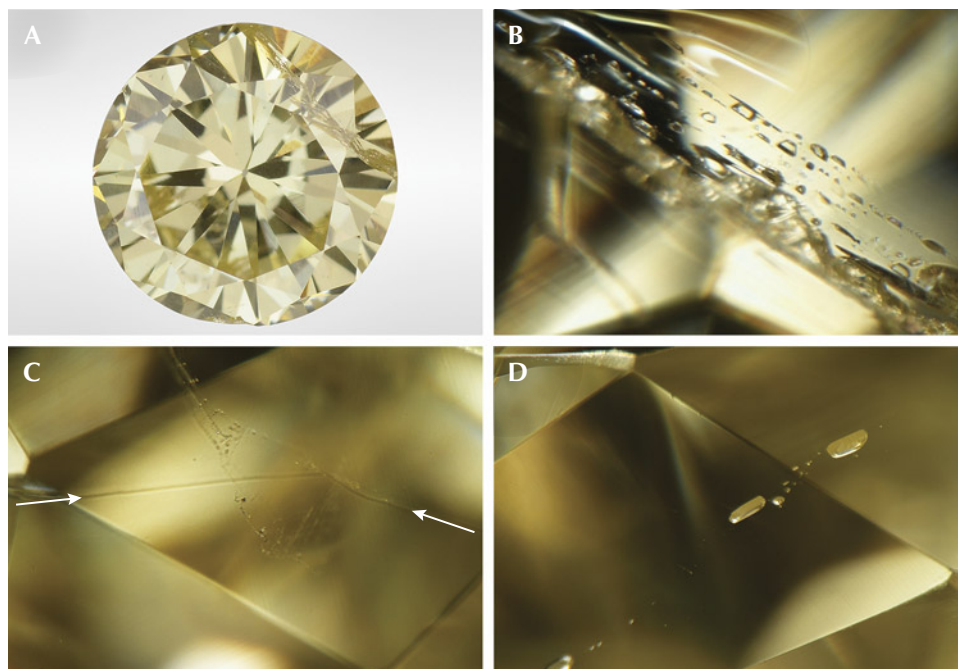


Figure 5. A 1.06 ct yellow diamond (A) containing a series of healed fractures with silicate melt inclusions (B–D). At bottom left (C), the healed fracture has interrupted the quality of polishing and appears as a surface grain line, indicated by arrows. Top left photo by Jian Xin (Jae) Liao. Photomicrographs by Evan M. Smith; fields of view 1.15 mm (B) and 1.42 mm (C and D).

1997, 2018). The inclusions in figure 3 contain a mixture of carbon dioxide (CO_2) and nitrogen (N_2), identified using Raman spectroscopy and microthermometry (Smith et al., 2015). These inclusions are often only a few micrometers thick, and thin-film interference gives them a colorful, iridescent appearance (like the colorful swirls seen in soap bubbles). The CO_2 - N_2 inclusions are a snapshot of a free-flowing fluid that could have been percolating along crevices and between grains of the solid surrounding eclogitic host rock when this diamond sat in the mantle at a depth of 150–200 km (Ragozin et al., 2002; Smith et al., 2015).

Figure 4 shows another example of fluid trapped in a healed fracture in a diamond, this one from the Democratic Republic of the Congo. In this case, the fluid is best described as an ultramafic (magnesium-rich and silica-poor) silicate melt (Smith et al., 2014). When this melt solidified, it exsolved a nitrogen-rich (N_2) fluid phase that is visible as a pinkish-colored bubble within the largest melt inclusion (figure 4, right). Similar solidified melt inclusions were observed in a diamond from the Roberts Victor mine in South Africa (Smith et al., 2014) as well as in a yellow faceted diamond of unknown origin, shown in figure 5. The yellow diamond contains numerous transparent inclusions

that lie together in an irregular planar configuration defining a healed crack. Individual inclusions are spatially confined to the plane of the crack, with larger inclusions having flattened, tabular shapes. Some inclusions are rod-like in shape or are grouped in lineaments that define the receding edge of the crack during healing. Raman spectroscopy shows that these solidified melt inclusions are dominated by olivine. The process responsible for making secondary silicate melt inclusions like these remains uncertain and requires further study.

Concluding Remarks

The fluid inclusions shown here—whether liquid, gaseous, or solidified melts—are only some of what have been encountered in natural diamonds, and future research is likely to uncover more. In the geological world, it is common to encounter fluid inclusions in minerals, but those found in diamonds have exceptional scientific value because of their deep mantle origin. Diamond is the only mineral that routinely captures and preserves fluids from great depths inside our planet and gets transported up to the earth's surface. Thanks to their gem properties, we can both admire and learn from these crystals.

REFERENCES

- Haggerty S.E. (1999) A diamond trilogy: Superplumes, supercontinents, and supernovae. *Science*, Vol. 285, No. 5429, pp. 851–860, <http://dx.doi.org/10.1126/science.285.5429.851>
- Izraeli E.S., Harris J.W., Navon O. (2001) Brine inclusions in diamonds: A new upper mantle fluid. *Earth and Planetary Science Letters*, Vol. 187, No. 3–4, pp. 323–332, <http://dx.doi.org/>

- 10.1016/S0012-821X(01)00291-6
- Jablon B.M., Navon O. (2016) Most diamonds were created equal. *Earth and Planetary Science Letters*, Vol. 443, pp. 41–47, <http://dx.doi.org/10.1016/j.epsl.2016.03.013>
- Klein-BenDavid O., Izraeli E.S., Hauri E., Navon O. (2007) Fluid inclusions in diamonds from the Diavik mine, Canada and

- the evolution of diamond-forming fluids. *Geochimica et Cosmochimica Acta*, Vol. 71, No. 3, pp. 723–744, <http://dx.doi.org/10.1016/j.gca.2006.10.008>
- Krebs M., Pearson D., Stachel T., Laiginhas F., Woodland S., Chinn I., Kong J. (2019) A common parentage-low abundance trace element data of gem diamonds reveals similar fluids to fibrous diamonds. *Lithos*, Vol. 324–325, pp. 356–370, <http://dx.doi.org/10.1016/j.lithos.2018.11.025>
- Navon O., Hutcheon I.D., Rossman G.R., Wasserburg G.J. (1988) Mantle-derived fluids in diamond micro-inclusions. *Nature*, Vol. 335, No. 6193, pp. 784–789, <http://dx.doi.org/10.1038/335784a0>
- Ragozin A., Shatsky V., Ryllov G., Goryainov S.V. (2002) Coesite inclusions in rounded diamonds from placers of the Northeastern Siberian platform. *Doklady Earth Sciences*, Vol. 384, pp. 385–389.
- Smit K.V., Shirey S.B., Stern R.A., Steele A., Wang W. (2016) Diamond growth from C–H–N–O recycled fluids in the lithosphere: Evidence from CH₄ micro-inclusions and $\delta^{13}\text{C}$ – $\delta^{15}\text{N}$ –N content in Marange mixed-habit diamonds. *Lithos*, Vol. 265, pp. 68–81, <http://dx.doi.org/10.1016/j.lithos.2016.03.015>
- Smith E.M., Kopylova M.G., Frezzotti M.L., Afanasiev V.P. (2014) N-rich fluid inclusions in octahedrally-grown diamond. *Earth and Planetary Science Letters*, Vol. 393, pp. 39–48, <http://dx.doi.org/10.1016/j.epsl.2014.02.033>
- (2015) Fluid inclusions in Ebelyakh diamonds: Evidence of CO₂ liberation in eclogite and the effect of H₂O on diamond habit. *Lithos*, Vol. 216–217, pp. 106–117, <http://dx.doi.org/10.1016/j.lithos.2014.12.010>
- Smith E.M., Shirey S.B., Nestola F., Bullock E.S., Wang J., Richardson S.H., Wang W. (2016) Large gem diamonds from metallic liquid in Earth's deep mantle. *Science*, Vol. 354, No. 6318, pp. 1403–1405, <http://dx.doi.org/10.1126/science.aal1303>
- Smith E.M., Shirey S.B., Wang W. (2017) The very deep origin of the world's biggest diamonds. *G&G*, Vol. 53, No. 4, pp. 388–403, <http://dx.doi.org/10.5741/gems.53.4.388>
- Smith E.M., Ni P., Shirey S.B., Richardson S.H., Wang W., Shahar A. (2021) Heavy iron in large gem diamonds traces deep subduction of serpentinized ocean floor. *Science Advances*, Vol. 7, No. 14, <http://dx.doi.org/10.1126/sciadv.abe9773>
- Stachel T., Brey G., Harris J.W. (2005) Inclusions in sublithospheric diamonds: Glimpses of deep earth. *Elements*, Vol. 1, pp. 73–78.
- Sunagawa I. (1990) Growth and morphology of diamond crystals under stable and metastable conditions. *Journal of Crystal Growth*, Vol. 99, pp. 1156–1161.
- Tomilenko A.A., Chepurov A.L., Pal'yanov Y.N., Pokhilenko L.N., Shebanin A.P. (1997) Volatile components in the upper mantle. *Russian Geology and Geophysics*, Vol. 38, No. 1, pp. 294–303.
- Tomilenko A.A., Bul'bak T.A., Logvinova A.M., Sonin V.M., Sobolev N.V. (2018) The composition features of volatile components in diamonds from the placers in the northeastern part of the Siberian platform by gas chromatography–mass spectrometry. *Doklady Earth Sciences*, Vol. 481, No. 1, pp. 953–957, <http://dx.doi.org/10.1134/s1028334x18070309>
- Tomlinson E.L., Jones A.P., Harris J.W. (2006) Co-existing fluid and silicate inclusions in mantle diamond. *Earth and Planetary Science Letters*, Vol. 250, pp. 581–595, <http://dx.doi.org/10.1016/j.epsl.2006.08.005>
- Weiss Y., Kessel R., Griffin W.L., Kiflawi I., Klein-BenDavid O., Bell D.R., Harris J.W., Navon O. (2009) A new model for the evolution of diamond-forming fluids: Evidence from microinclusion-bearing diamonds from Kankan, Guinea. *Lithos*, Vol. 112, Supplement 2, pp. 660–674, <http://dx.doi.org/10.1016/j.lithos.2009.05.038>

For online access to all issues of GEMS & GEMOLOGY from 1934 to the present, visit:

gia.edu/gems-gemology



**Fast.
Accurate.
Affordable.**

PASS



GIA®

The GIA iD100®

The ultimate diamond detecting triple-threat. The GIA iD100 distinguishes stones in under 2 seconds, offers 100% accuracy and has the best price in its class. Expect the confidence only GIA can offer when distinguishing natural from laboratory-grown diamonds.



GIA®



Learn More at
GIA.edu/id100

MORE ON ORANGE LUMINESCENCE IN CORUNDUM

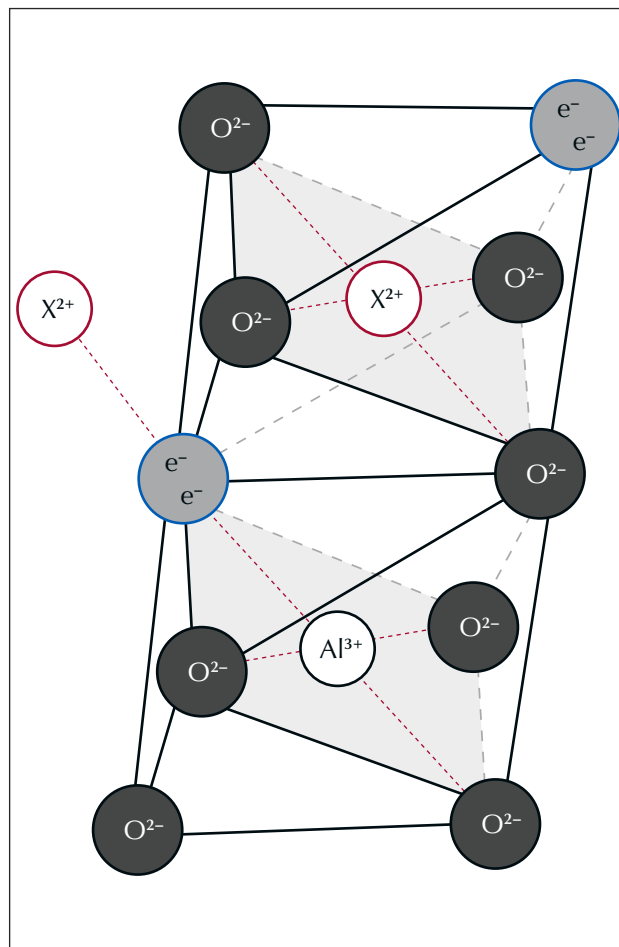
We have read with great interest the Winter 2021 article entitled “Blue sapphires from Mogok, Myanmar: A gemological review,” by Wasura Soonthorntantikul et al. (pp. 292–317). The authors conducted a fairly complete bibliographical review and a qualitative characterization using gemological, spectroscopic, and chemical techniques, improving our knowledge of Mogok’s rare and renowned blue sapphires. In the process, the authors associate the 640 nm emission band of orange luminescence with “trapped hole chromophores,” quoting Hughes et al. (2017), that section of the book being based on Segura’s gemology dissertation at the University of Nantes (Segura, 2013). We wish to add further details regarding orange luminescence in corundum, from Mogok and elsewhere. In particular, we recently conducted a rather extensive study of this luminescence, making it possible to describe in further detail the defect(s) involved.

Dr. Soonthorntantikul and her associates state that “the remainder displayed zoned orange fluorescence (with very weak or no red fluorescence) in near-colorless to light blue color zones,” as seen in their figure 12. For Mogok, orange luminescence has also been described in the yellow zone of a blue sapphire (Ho et al., 2018, pp. 128–129). Actually, for all sapphires worldwide, orange luminescence is absent from blue zones and may be found only in near-colorless or yellow domains. This behavior can be explained for all corundum. Indeed, the blue color is related to the Fe-Ti charge transfer, and thus blue zones contain iron, also as Fe^{3+} , as can be seen in their UV-visible absorption spectrum (see figure 26 of Soonthorntantikul et al.). In blue zones, the O^{2-} - Fe^{3+} charge transfer absorbs the ultraviolet range, taking away the source of energy necessary to induce luminescence. Thus, it acts as a luminescence quencher for orange and red emissions.

Regarding the nature of the defect involved with orange fluorescence, the location “trapped hole chromophore” does not describe the atomic structure in which the hole is trapped. Our team proposes a more complete description deduced from the careful characterization of a collection of nearly 100 orange-luminescing corundum (Vigier et al., 2021a,b). Based on luminescence excitation spectra and other arguments, the orange luminescence has been related to a color center or defect including two oxygen vacancies. An oxygen vacancy is a missing oxygen atom in the lattice (figure 1), which can be created by

chemical means during growth or induced by irradiation after growth, for example. Such a defect is called an F-center, or even $\text{V}_\text{O}^{\bullet\bullet}$ (Kröger-Vink notation) in the physics community. An oxygen vacancy may contain zero, one, or two unpaired electrons. Thus, when there are two vacancies from two oxygens, each containing two electrons, four

Figure 1. A schematic of the F_2 center, believed to be responsible for the orange luminescence in corundum (Vigier et al., 2021a,b). Two adjacent AlO_6 octahedra in the corundum ($\alpha\text{-Al}_2\text{O}_3$) structure are represented here. Two oxygen vacancies are present (noted with two “e⁻” each, for the two electrons). X^{2+} stands for a divalent cation, most likely Mg^{2+} .



electrons are electrically compensated in the corundum structure by the presence of two divalent cations (see also Emmett et al., 2003). This double defect is an F_2 center, compensated by two divalent ions such as Mg^{2+} , Be^{2+} , and rarely Mn^{2+} (again, see figure 1). The concentration of such defects is not known but may be very small (of the order of parts per million or less), as luminescence is a very efficient way to detect defects. The chemical results presented in Soonthorntantikul et al. (2021) explicit that there are always traces of magnesium, which is consistent with this proposed structure.

Furthermore, concerning the relation between orange luminescence and infrared absorption, the authors state: "We noted that the studied sapphires exhibiting the 3161

cm^{-1} IR feature frequently show orange zoned fluorescence..." This is true for Mogok samples and—in our experience—for some metamorphic yellow sapphires (generally from Sri Lanka). However, for other corundum (natural, synthetic, or treated), we did not note any correlation of the 3161 cm^{-1} band with orange luminescence.

We hope these additional scientific details will be helpful to better understand the little-studied orange luminescence in sapphire and will nicely complement the work of Dr. Soonthorntantikul and her colleagues.

Maxence Vigier and Emmanuel Fritsch

University of Nantes

CNRS, Institut des Matériaux Jean Rouxel, IMN

Nantes, France

REFERENCES

- Emmett J.L., Scarratt K., McClure S.F., Moses T., Douthit T.R., Hughes R., Novak S., Shigley J.E., Wang W., Bordelon O., Kane R.E. (2003) Beryllium diffusion of ruby and sapphire. *G&G*, Vol. 39, No. 2, pp. 84–135, <http://dx.doi.org/10.5741/GEMS.39.2.84>
- Ho K., Fritsch E., Rabouan J.-B., Notari F., Caplan C., Hainschwang T. (2018) *Mogok: The Valley of Precious Stones*. Glénat Livres, Grenoble, 191 pp.
- Hughes R.W., Manorotkul W., Hughes E.B. (2017) *Ruby & Sapphire: A Gemologist's Guide*. RWH Publishing, 732 pp.
- Segura O. (2013) La luminescence orange des corindons. Diplôme universitaire de gemmologie, Université de Nantes, 60 pp.

- Soonthorntantikul W., Atikarnsakul U., Vertrieest W. (2021) Blue sapphires from Mogok, Myanmar: A gemological review. *G&G*, Vol. 57, No. 4, pp. 292–317, <http://dx.doi.org/10.5741/GEMS.57.4.292>
- Vigier M., Fritsch E., Segura O. (2021a) Orange luminescence of corundum, an atypical origin for gemmologists (part one) [in French with English abstract and figure captions]. *Revue de l'Association Française de Gemmologie*, Vol. 211, pp. 12–19.
- (2021b) Orange luminescence of corundum, an atypical origin for gemmologists (part two) [in French with English abstract and figure captions]. *Revue de l'Association Française de Gemmologie*, Vol. 212, pp. 12–18.

REPLY

We truly appreciate the letter from Maxence Vigier and Dr. Emmanuel Fritsch for the detailed information on defects for orange luminescence in corundum and also for sharing their experience with this feature. Their letter is very helpful and improved our knowledge on this luminescence. We

noted the feature in a few samples but did not further explore this, since it would have taken us outside the scope of the article.

Wasura Soonthorntantikul, Ungkhana Atikarnsakul,
and Wim Vertrieest
GIA, Bangkok

For online access to all issues of GEMS & GEMOLOGY from 1934 to the present, visit:

gia.edu/gems-gemology





GEM NEWS INTERNATIONAL

Contributing Editors

Gagan Choudhary, Gem Testing Laboratory, Jaipur, India (gagan.choudhary@iigirlc.org)

Christopher M. Breeding, GIA, Carlsbad (christopher.breeding@gia.edu)

Guanghai Shi, School of Gemmology, China University of Geosciences, Beijing (shigh@cugb.edu.cn)

COLORED STONES AND ORGANIC MATERIALS

Atypical “box bead” cultured pearls. Gemologists are aware of two main types of bead cultured pearls—bead cultured (BC) and atypical bead cultured (aBC). BC pearls are cultured with the typical round, predominantly freshwater shell bead nuclei, while aBC pearls are cultured with any material that is not typical. Atypical bead nuclei include fancy-shaped shell beads, pearls of any kind, plastic beads, gemstones, or other materials of various shapes. GIA’s Bangkok laboratory received five loose undrilled pearls as research samples for examination. These were reportedly sold as “tissue box pearls” in the Indian market by a trader known to some GIA staff. Externally they exhibited a smooth surface with luster resembling that of South Sea *Pinctada maxima* cultured pearls. The samples ranged from $8.00 \times 7.26 \times 6.05$ mm to $9.93 \times 7.86 \times 5.86$ mm, weighing between 2.50 and 3.49 ct, and exhibited a baroque form with a white to cream color (figure 1).

Microradiographic examination revealed unusual box-shaped demarcation outlines uncharacteristic of traditional BC pearls (figure 2). To the author’s knowledge, this kind of internal rectangular shape is never seen in natural pearls. Sample 2 revealed an additional structural feature extending from the shorter side of the “box bead” (see red arrow in figure 2). Sample 3 possessed two distinct radio-translucent areas around the box-shaped outline; these are expected for voids or certain organic-rich features in pearls. Samples 4 and 5 also showed similar radio-translucent features, but to a lesser extent. Since the rectangular internal structures are not observed in natural pearls, the clear de-

marcation features with a box-shaped outline are enough to identify these as aBC pearls.

The box-shaped beads clearly influenced the external shapes of their pearl hosts when they formed within the mollusks, as seen in figure 1. Samples 2 and 3 were cut in half for further examination of their internal structures. Under magnification, each half showed an obvious demarcation between the box-shaped bead and the nacre overgrowth. The “box beads” appeared to be more translucent than traditional beads and exhibited platy structure and banding in some areas, proving they were fashioned from shell. Additionally, the feature in sample 2 possessed a radial structure and appeared somewhat translucent. Observation through a gemological microscope revealed that the gaps around the nucleus in sample 3 were in fact voids with areas of dark organic-rich material, likely conchiolin, present within (figure 3).

Another point of interest was the inert reaction of the shell nuclei in each half of both samples under optical X-

Figure 1. The five “box bead” cultured pearls examined ranged from $8.00 \times 7.26 \times 6.05$ mm to $9.93 \times 7.86 \times 5.86$ mm. Photo by Lhapsin Nillapat.



Editors’ note: Interested contributors should send information and illustrations to Stuart Overlin at soverlin@gia.edu or GIA, The Robert Mouawad Campus, 5345 Armada Drive, Carlsbad, CA 92008.

GEMS & GEMOLOGY, VOL. 58, NO. 3, pp. 378–398.

© 2022 Gemological Institute of America

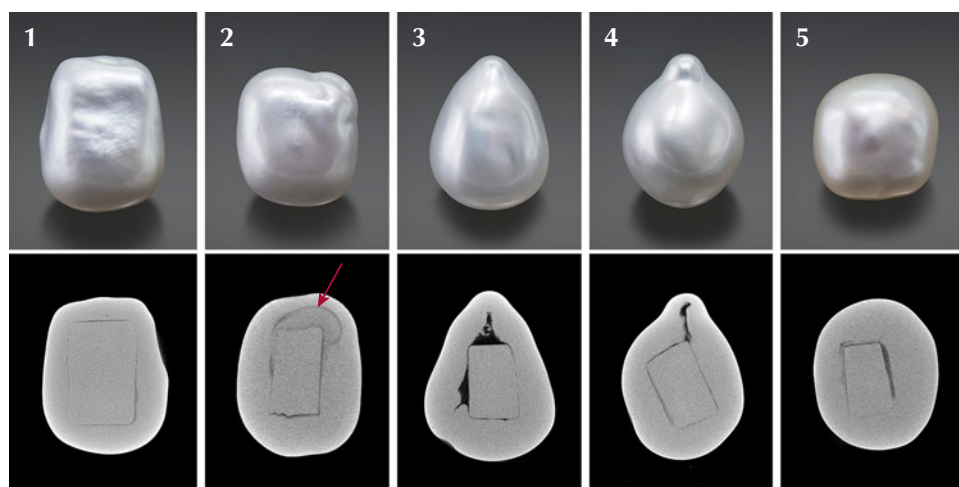


Figure 2. The five “box bead” cultured pearls (top) together with their X-ray computed microtomography (μ -CT) slices showing the obvious rectangular bead demarcations resembling a box shape (bottom). The red arrow indicates the additional structural feature observed within sample 2. Photos by Lhapsin Nillapat.

ray fluorescence. Since most freshwater bead nuclei show strong yellowish green or greenish yellow reactions, it was clear that the “box beads” were not fashioned from freshwater mussel shells.

Energy dispersive X-ray fluorescence (EDXRF) results of the “box bead” nuclei, outer nacre layers, and the radial calcitic area revealed major amounts of calcium, along with high levels of strontium ranging from 1209 to 1986 ppm, and manganese below 63 ppm. The low levels of manganese detected by EDXRF corresponded to the inert optical X-ray fluorescence reaction (figure 4), as the intensity of any reaction is directly correlated to the manganese levels (P. Kessrapong et al., “Atypical bead cultured *Pinctada maxima* pearls nucleated with freshwater non-bead cultured pearls,” *GIA Research News*, April 6, 2020,

<https://www.gia.edu/gia-news-research/atypical-bcp-nucleated-with-nbcp>). The high strontium and low manganese concentrations indicated saltwater origin.

Under long-wave ultraviolet radiation, the sawn surfaces exhibited a bluish reaction. Sample 2 showed additional very weak orangy reactions associated with the columnar feature partially surrounding the bead (figure 5).

Short-wave UV fluorescence spectra were also collected from the pearl surfaces using a GIA-developed spectrometer. The spectra showed two distinct peaks around 330 and 360 nm with counts above 10,000, indicating the surfaces were not processed using bleach or any whitening/brightening agents (C. Zhou et al., “Detection of color treatment and optical brightening in Chinese freshwater ‘Edison’ pearls,” Summer 2021 *G&G*, pp. 124–133).

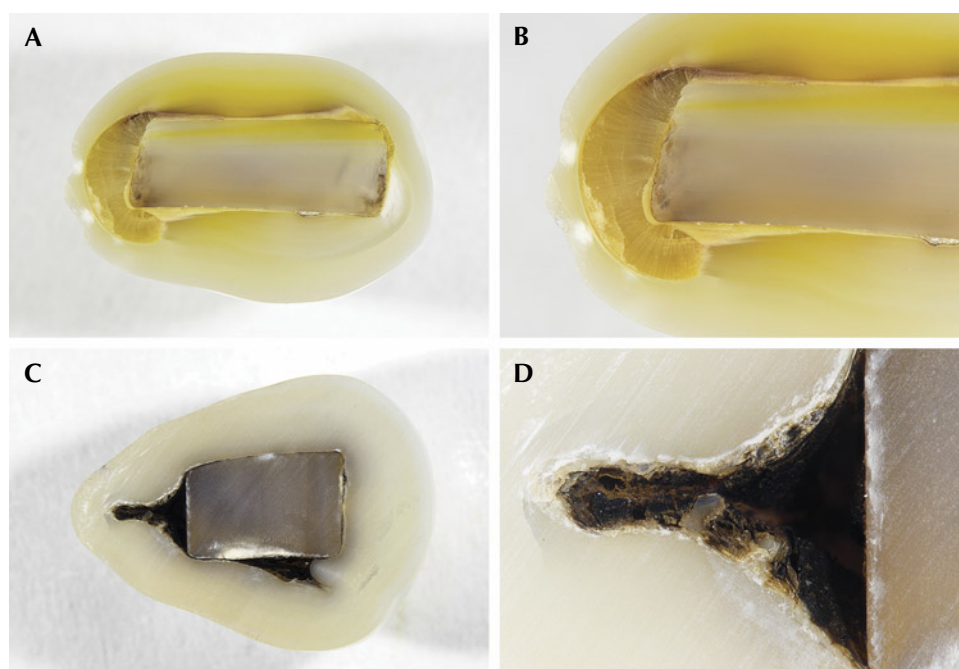


Figure 3. A: Cross section of sample 2. B: Radial columnar structures, identified as calcite by Raman, observed in an area within the nacre overgrowth covering sample 2's bead nucleus. C: Cross section of sample 3. D: Magnified view of one of the void features with dark organic-rich material attached to the inner surface. Photos by Ravenya Atchalak; fields of view 14.40 mm (A and C), 7.20 mm (B), and 2.88 mm (D).

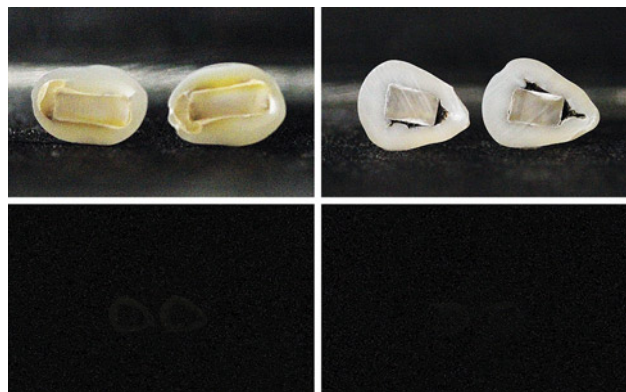


Figure 4. The cross sections of sample 2 (top left) and sample 3 (top right) under white light and their inert reactions under X-ray fluorescence (bottom). Photos by Ravenya Atchalak.

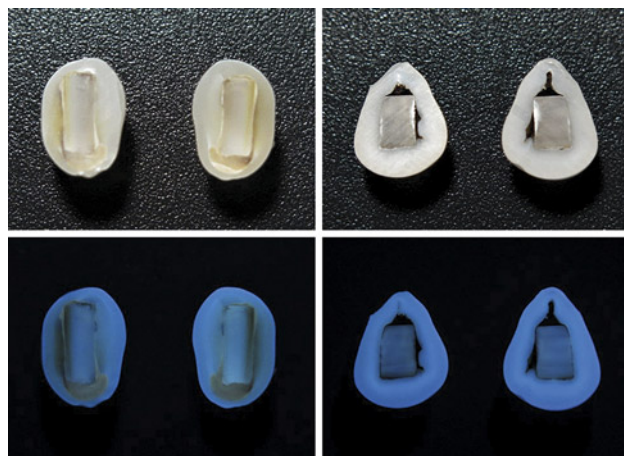


Figure 5. The cross sections of sample 2 (top left) and sample 3 (top right) under white light and their reactions under long-wave UV (bottom). Photos by Ravenya Atchalak.

Raman analysis using 514 nm laser excitation on the “box bead” surfaces and outer nacreous layers of the sawn surfaces showed typical aragonite features at around $701/704\text{ cm}^{-1}$ (doublet) and 1085 cm^{-1} . The columnar radiating area on sample 2 was also analyzed, revealing features at around $154, 281, 711,$ and 1085 cm^{-1} that were consistent with calcite (J. Urmos et al., “Characterization of some biogenic carbonates with Raman spectroscopy,” *American Mineralogist*, Vol. 76, 1991, pp. 641–646).

All the data obtained from the advanced testing methods as well as observation under magnification prove the “box bead” nuclei were fashioned from saltwater shell.

Although this is not the first time GIA has encountered saltwater cultured pearls containing non-traditional bead nuclei, the box shape of the beads in this sample group has never been documented in the gemological literature and is therefore notable.

Ravenya Atchalak
GIA, Bangkok

A type of multi-colored quartz with oriented inclusions, reportedly from Brazil. A special quartz called “Auralite 23” in the Chinese trade has recently appeared in the Donghai jewelry market in Jiangsu Province (figure 6). Sell-



Figure 6. Multi-colored quartz traded in the Donghai jewelry market in Jiangsu Province, China. Photo by Qingfeng Wu.

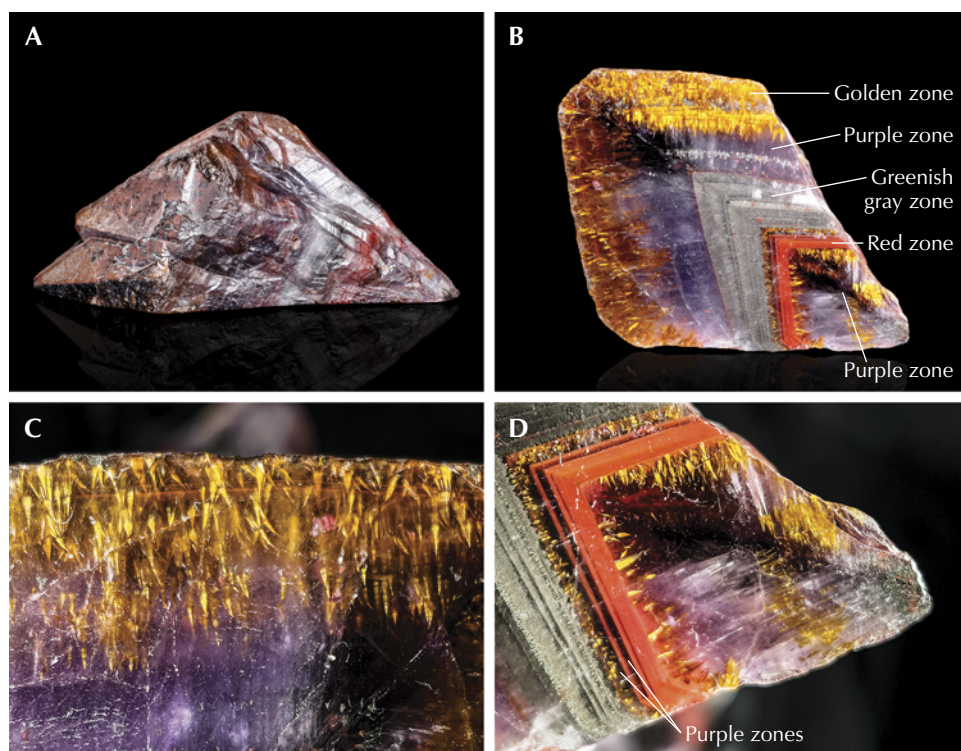


Figure 7. A: External characteristics of a piece of rough “Auralite 23” quartz measuring $8.2 \times 5.5 \times 3.7$ cm. Well-developed rhombohedrons can be found on one side of the quartz, and the other side displays an uneven pyramidal shape with parallel striations. B: Five color zones and substantial oriented inclusions. C: Golden “broom-like” inclusions form a beautiful independent zone. D: Alternating purple and red zones. Photos by Zhuoxuan Li.

ers claim the material is from Brazil. The quartz is very similar to amethyst from Minas Gerais, Brazil (B.M. Laurs and N.D. Renfro, “Amethyst from Brazil with interesting inclusion patterns,” *Journal of Gemmology*, Vol. 35, No. 6, 2017, pp. 468–469).

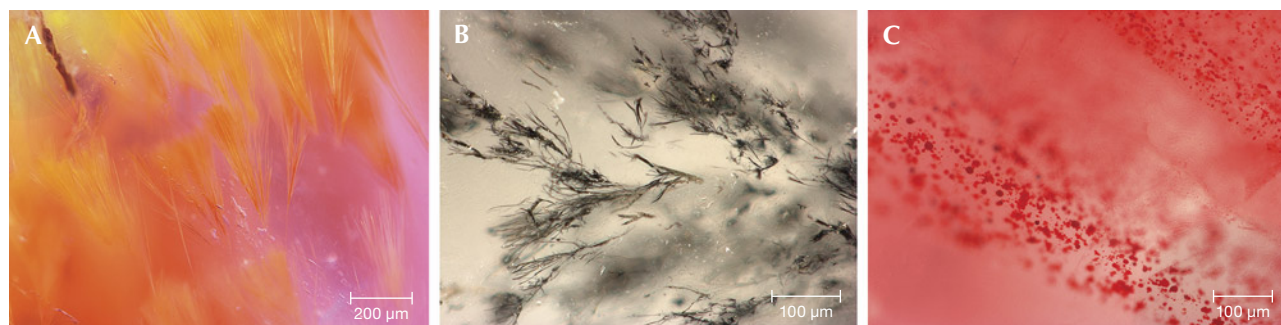
Four color zones (purple, red, greenish gray, and a second purple zone) are displayed when observed along the threefold axis. Sometimes, a separate golden zone can be formed (e.g., figure 7, B and C). The purple and greenish gray zones in the upper part of figure 7D are well defined, while the red and purple zones in the lower part show alternating growth bands. After cutting, substantial oriented inclusions can be found in each color zone. Golden “broom-like” inclusions observed in the purple zones are

regularly distributed along the growth direction. Greenish gray horsetail-like inclusions are found in the middle of the quartz. In addition, red platelet inclusions appear in the red zone (figure 8). Notably, the platelet inclusions are seemingly restricted to this red zone and thus generate an agate-like zoning.

A multi-colored quartz slice was purchased and re-searched. The Fourier-transform infrared (FTIR) transmission spectra—with weak peaks at 3584 and 2331 cm^{-1} , medium strong peaks at 2924 , 2850 , 2671 , 2597 , 2498 , and 2136 cm^{-1} , and strong peaks at 3454 and 2242 cm^{-1} —indicate that this is a natural quartz (figure 9).

Raman analysis identified the typical inclusions in the purple zones, with peaks at 246 , 300 , 387 , 415 , 550 , and

Figure 8. Three representative solid inclusions in the multi-colored quartz. A golden “broom-like” inclusion in the purple region (A), greenish gray horsetail-like inclusions in the greenish gray region (B), and red platelet inclusions in the red region (C). Photomicrographs by Huizhen Huang; fields of view 1.35 mm , 0.6 mm , and 0.71 mm .



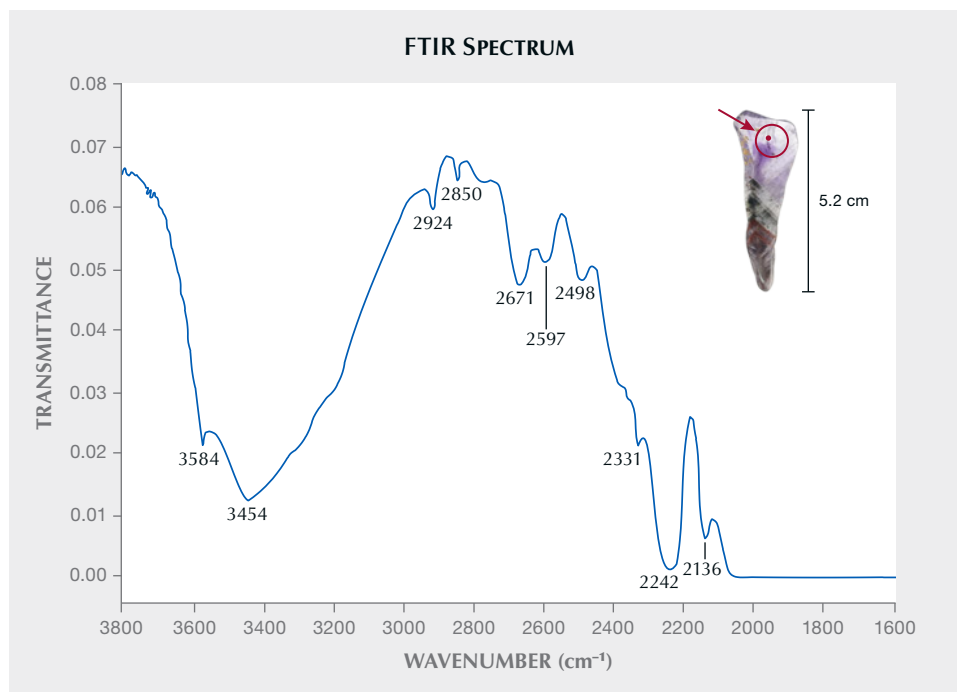
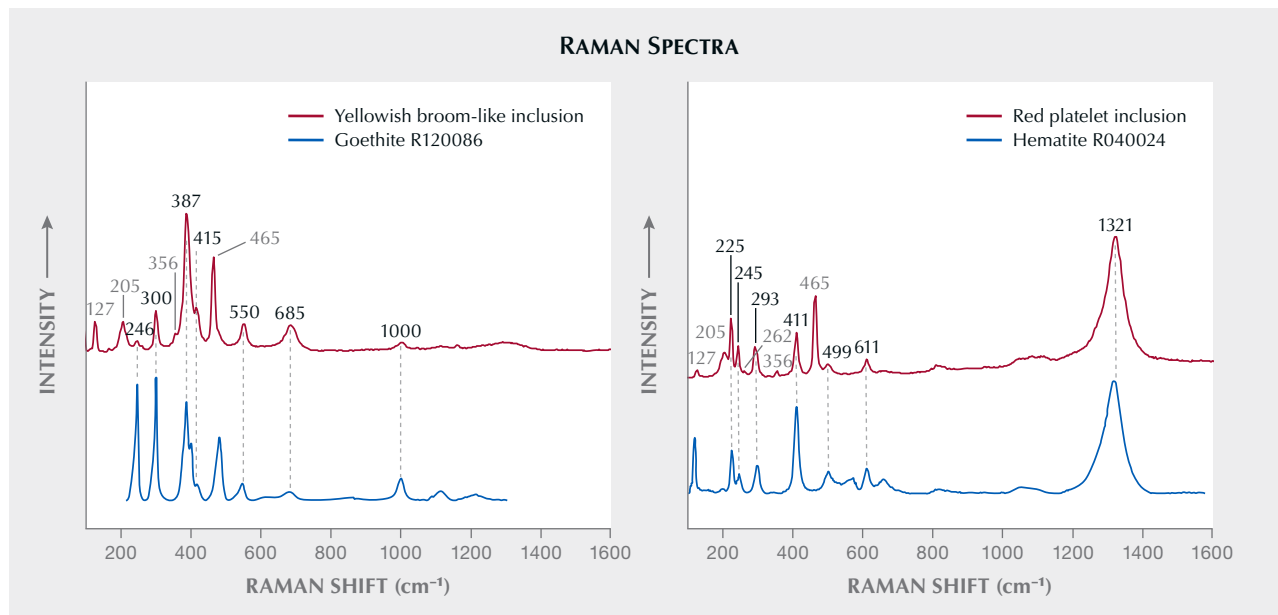


Figure 9. Fourier-transform infrared (FTIR) transmittance spectrum of the imaged quartz sample. A slice of the tested multi-colored quartz is shown in the inset.

685 cm^{-1} as goethite. The red platelet inclusions with peaks at 225, 245, 293, 411, 499, 611, and 1321 cm^{-1} are hematite (figure 10). The greenish gray horsetail-like inclusions could not be identified by Raman spectroscopy, so we car-

ried out electron probe microanalysis (EPMA). The chemical analysis of these inclusions are mainly iron (45.49–46.51 wt.%) and sulfur (51.34–51.87 wt.%), indicating that they are FeS_2 inclusions.

Figure 10. Raman spectra of representative solid inclusions are shown along with the Raman reference spectra from the RRUFF database. Left: The purple zone contained a substantial amount of golden “broom-like” inclusions that matched with goethite. Right: The red platelet inclusions produced a Raman spectrum corresponding to hematite. The black numbers in this figure indicate the Raman peaks of the inclusion, and the gray numbers indicate the peaks of the quartz.



Considering the multi-colored zones and different oriented inclusions, this quartz likely formed and crystallized in multiple stages. However, the origin of this special pattern still remains unclear and is worth further research.

Huizhen Huang, Quanli Chen, and Yan Li
Gemmological Institute,
China University of Geosciences, Wuhan

Update from Mozambique's ruby mines. Mozambican rubies have revolutionized the dynamics of the ruby trade since their debut on the global gem scene in 2009. GIA has been following the evolution of the deposits around Montepuez in the Cabo Delgado Province of northern Mozambique since the very beginning (see W. Vertriest and S. Saseaw, "A decade of ruby from Mozambique: A review," Summer 2019 *G&G*, pp. 162–183). In August 2022, a GIA field gemology team visited the mining area to document the current state of mining and to collect samples for future studies.

In less than a decade, the balance has shifted from an informal environment dominated by artisanal miners and foreign buyers to a situation that is mostly under the control of large-scale miners who bring these rubies directly to the global market.

There are currently three of these major operations working in the area east of Montepuez.

- Montepuez Ruby Mining (MRM): A partnership between Gemfields and local partner Mwiriti that has been mining rubies since 2012. Gemfields also mines Zambian emeralds at the Kagem mine.
- Fura Gems: This company has been involved in Mozambican ruby mining since 2019. Some of their

concessions were previously worked by Mustang Resources. Fura is also actively mining Colombian emerald and Australian sapphire.

- GemRock: Owned by luxury jewelry brand Dia-Color, this operation has been active on the ground since 2019.

In terms of geological formation, the ruby mineralization in the Montepuez area is not yet fully understood. The gems are generally described as amphibole-related corundum since the associated rocks are rich in amphibole. This mineral also dominates the inclusion scene of these gems.

While some primary mineralization is known and these ruby-bearing bodies are areas of interest for the mining companies, the rubies are seldom mined from the host rock. Nearly all of the mining activity is focused on the secondary deposits. These weathered gravel layers are rich in rubies and referred to locally as *camada*. This type of material is easy to mine, and the value of the ruby found here is higher than that in the primary deposits. The original host rock may contain higher volumes, but the majority of this corundum tends to be of very low grade. The exploration strategies of the mining companies focus heavily on identifying the extent, thickness, and distribution of the secondary gravels throughout their respective concessions. Understanding the geological formation of the corundum in this geological setting is a continuing process. Exploration teams are actively delineating and characterizing the ore bodies that hold the primary mineralization.

All three large-scale operations extract these ruby-rich gravels by stripping the overburden with excavators. This exposes the *camada*, which is dug up and stockpiled near the wash plants (figure 11). Local variations of the gravel



Figure 11. Mining of the gravels at Mugloto pit 3 in the MRM concession. The gravel layer is around 30 cm thick. The material on top has a distinct reddish tint that is typical for sediments in tropical environments. Under the layer of gravel, the weathered basement rock is more grayish in color. Photo by Wim Vertriest; courtesy of MRM.



Figure 12. The first step in the wash plant at Fura is the feeding bin (top left), where material enters the washing process. While the material moves down through the bins, water is added and a first screening removes large boulders. The trommel serves a dual function, breaking up clay lumps and screening out oversized materials. This image captures the first of seven steps to reduce the gravel to a concentrate rich in ruby, which is then handled in the sort house. Photo by Wim Vertriest; courtesy of Fura Gems.

layers can provide additional challenges. In some areas the sediment cover is less than 50 cm thick, which means the shallow gravel layer contains an abundance of roots, branches, and other organic material, making it harder to process further down the line. In other areas, the gravels are buried over 15 m deep, requiring serious effort and planning to strip the overburden. The ruby-rich layers themselves can vary from 10 to 150 cm; in some cases, multiple layers are present. The main one is always lying directly on the (extremely weathered) basement rock, which often consists of amphibolites, gneisses, and occasional felsic pegmatite veins.

While washing the rubies out of the gravel sounds very straightforward, this is a complex engineering process that requires careful monitoring and control. The gravels are unsorted, with quartz boulders up to 30 cm in diameter, but can also have a significant clay content. Processing them is no easy task and requires many steps of separating by size as well as various techniques to break up sediment clusters and concentrate the ore. Sizing is routine, but the other steps require considerable effort. At all of the large mining operations, logwashers, rotating trommels, and high-pressure water jets are used to break up clay clumps (figure 12). Concentration of the gravels (i.e., removal of the unwanted minerals) focuses on separating based on the specific gravities of the components of the sediment. Ruby is relatively dense compared to most other minerals such as feldspar and quartz. The most convenient method is using a pulsating jig where the waterlogged gravels move across a screen with barriers while getting pushed up vertically. This allows lighter materials to wash over the jig while denser minerals are concentrated at the bottom. While simple, this technique has its limitations, and several of the mines have progressed to more advanced techniques that allow for more precise separation and/or higher

capacity, such as dense media separators and rotating pans in which a slurry with a precisely controlled density is used to separate heavier mineral fractions.

All of these techniques require large volumes of water. Plant operators assume that every metric ton of gravel processed requires 1000 liters of clear water. This water consumption was a decisive factor for development of the wash plant. For instance, a nearby river can serve as a cheap and constant supply of water, while boreholes are a much more costly alternative. As such, considerable effort is put into recycling water using settling ponds, cyclones, and flocculants. This allows much of the water, sometimes up to 90%, to be reused in the cleaning process.

With three large-scale mines operating in the area, the volumes of gravel processed are immense. The combined washing capacity of the three mines is more than 500 metric tons per hour.

The final product coming out of the wash plant is an intensely concentrated mix of heavy minerals enriched in ruby, though considerable portions of garnet, iron oxides, and other minerals are still present. Initially simple techniques such as manual sorting were used to handpick the rubies from this mix. As these operations grew, however, more advanced technology has been applied. Optical sorting devices are able to recognize rubies by their fluorescence and separate them from the mix. Most mines use these devices nowadays, often with manual control of the rejects since the machines are not flawless. In a final step, the mix of rubies is graded based on clarity, color, and size. Some mines perform this detailed and specialized task at company headquarters, while others do so at the mine. During the final stages of concentrating the rubies, security procedures become increasingly strict. Automatic sorting and gloveboxes (figure 13) are used to avoid contact with the rubies. The final grading, which must be done manu-



Figure 13. At GemRock, the concentrate from the wash plant is fed onto a conveyor belt where teams of sorters hand-pick the rubies. The workers are using glove-boxes to prevent physical access to the stones. At the end of the shift, the rubies are collected and inspected. Photo by Wim Vertrieft; courtesy of GemRock.

ally by experienced specialists, is heavily supervised in secured spaces. This is one reason why some companies prefer to do this at their headquarters.

The further development and growing importance of these large-scale mining operations has also brought changes to the artisanal mining communities. These *garimpeiros* mined 100% of Mozambique's rubies in the first years after the discovery in 2009. Only in 2014 did the first rubies from large-scale mining reach the international market, through an auction hosted by MRM. Not all of these small-scale miners are local; many traveled from other provinces in Mozambique or even from neighboring countries such as Tanzania. In recent years, the importance of the *garimpeiro* in Mozambique's ruby market has been in decline. Legal codes were adjusted to make unlicensed mining a crime, allowing government officials to intervene with the artisanal mining activities that took place on the licenses of the large companies. As compensation, the government created *areas designadas* that were assigned to the artisanal miners. However, these are often small and nearly barren. At the moment, these areas cover an area of four square kilometers. The mining licenses secured by the large-scale mining companies cover over 2,000 square kilometers. Conflicts over mining rights have created considerable tension between established powers and the local communities. Some of these disputes are only now coming to light or are just beginning to be felt.

But the most drastic impact on the artisanal mining community has probably been the sanctions against the foreign buyers in the neighboring towns. Ruby buyers, mainly from Asia, have worked from offices near Montepuez to buy directly from the *garimpeiros* since 2008–2009, but their numbers have been drastically reduced in recent years. This has almost completely eliminated the main clientele for the artisanal ruby miners. During GIA's

visit in 2016, huge numbers of *garimpeiros* (tens of thousands of them) could be seen working and traveling throughout all the mining concessions east of Montepuez. During GIA's recent 10-day expedition in August 2022, only 37 artisanal miners were seen in the same area. Most of the artisanal activity has moved farther east toward the city of Chiure, where the *garimpeiros* are mining more recent river sediments that are rich in rubies. Many have returned to their home villages, while some of the locals have found employment with the large mining companies.

The Cabo Delgado Province is currently experiencing social and political turmoil. Religious extremist groups under the name Ahlu-Sunna wa al Jama'a have been growing more violent. This has forced many people to abandon their villages and relocate to the southern reaches of the provinces, where the mines are located. One company reported that the number of people residing on their mining license increased from 1,500 to more than 20,000 in less than one year.

The local political structure also lacks the strength to successfully empower the local communities. All large-scale miners pay significant royalties and taxes to Mozambique's central government. Unfortunately, many of these funds fail to reach the historically underprivileged communities surrounding the mines in the northern Cabo Delgado Province. This only amplifies social unrest. Many local projects have been set up by the large companies as part of their own corporate social responsibility programs, focusing on a sustainable food supply, transportation, and healthcare.

The last five years have brought dramatic change to ruby mining around Montepuez. Nowadays the dominant players are the larger operations and no longer the *garimpeiro* community with their associated trading network. These large-scale miners have immensely upgraded and professionalized



Figure 14. This bracelet containing 12 mm beads was submitted as “root amber.” Photo by Tsung-Ying Yang.

their operations since their initial exploration and early mining phases. They have integrated more sophisticated techniques in both the gravel processing and the sorting. Larger fleets of machinery and fine-tuned wash plants allow huge volumes of ruby ore to be handled. This has resulted in a more stable ruby supply to the international markets.

However, the situation on the ground remains unstable, with social unrest growing in the wider areas where the ruby mining is happening. Only time will tell how this situation will evolve.

Wim Vertriest and Sudarat Saeseaw
GIA, Bangkok

Kevin Schumacher
GIA, Carlsbad

SYNTHETICS AND SIMULANTS

Pressed amber imitation of “root amber.” Root amber, a commercial variety of burmite (amber from northern Myanmar), is popular in the Taiwanese market. As the name suggests, root amber resembles tree roots and usually has a dark brown to light yellow color with creamy swirls caused by the mixing of fine calcite particles and resin during the sedimentation of the amber (Y. Wang, *Amber Gemology*, China University of Geosciences Press, Beijing, 2018, p. 244).

Recently, a bracelet was submitted to Taiwan Union Lab of Gem Research (TULAB) as root amber (figure 14). This bracelet consisted of a string of dark brown beads with light yellow creamy swirls. The refractive index of these beads was about 1.54 by spot reading, which was consistent with the RI of amber, and the beads showed uneven medium blue to faint yellow fluorescence under long-wave UV light. Microscopic observation of the beads revealed slight differences from natural root amber. First, the yellow swirls appeared to have a coarse texture rather than smooth. Second, the brown regions seemed to show a vaguely granular structure. The beads were further investigated under a microscope with long-wave UV illumination and compared with those of natural root amber. The results of fluorescence microscopy revealed that these regions did, in fact, show a granular structure with particle sizes ranging from tens to hundreds of microns, while the natural root amber appeared relatively fine-grained and homogeneous under the same lighting (figure 15). Raman spectroscopic analysis and comparison with both the

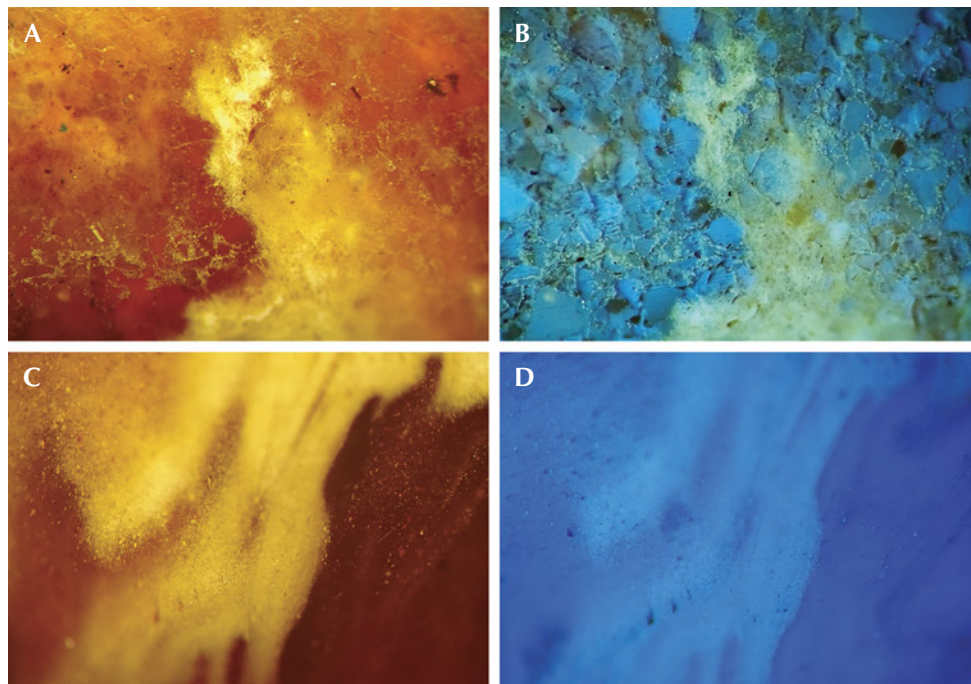


Figure 15. Pressed amber imitations and natural root amber. Under white light, the pressed amber (A) appeared less homogeneous than natural root amber (C). Granular structure of the pressed amber (B) revealed under long-wave ultraviolet light, whereas natural root amber showed relatively even fluorescence (D) under the same long-wave UV lighting. Photomicrographs by Kai-Yun Huang; field of view 4.23 mm.

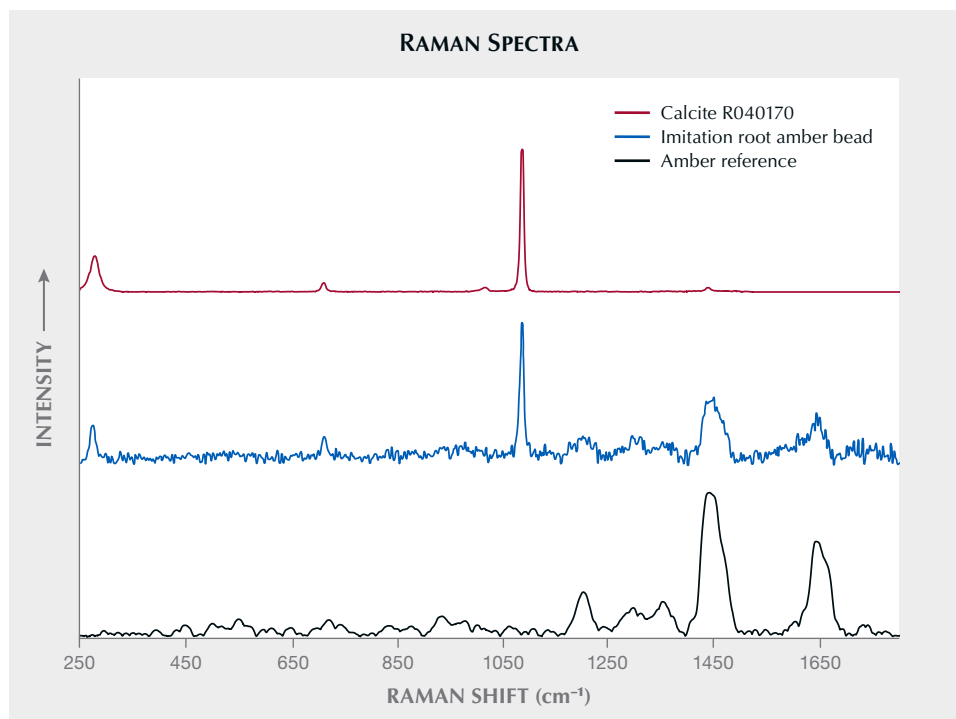


Figure 16. Raman spectra comparisons between the spectrum of the bead, amber reference (TULAB), and that of calcite from the RRUFF database suggested that the bead consisted of calcite and amber. The peaks at 1645 and 1450 cm^{-1} may be assigned respectively to $\nu(\text{C}=\text{C})$ and $\delta(\text{CH}_2)$ modes in fossil resin. The stacked spectra are baseline-corrected and normalized.

RRUFF database and the internal amber references compiled by TULAB confirmed that these beads were made of amber and calcite particles (figure 16). Previous studies also pointed out that the strongest peaks at 1645 and 1450 cm^{-1} may respectively be assigned to $\nu(\text{C}=\text{C})$ and $\delta(\text{CH}_2)$ modes in fossil resin (R.H. Brody et al., “A study of amber and copal samples using FT-Raman spectroscopy,” *Spectrochimica Acta Part A*, Vol. 57, No. 6, 2001, pp. 1325–1338). To summarize, the amber bracelet should be defined as an imitation—specifically, a pressed amber mixed with calcite powder during the manufacturing process.

Although pressed amber has long existed in the trade, the addition of calcite powder made this sample a better imitation of natural root amber and more difficult to distinguish by standard gemological testing. The best identification method for such an imitation is observation with fluorescence microscopy.

Shu-Hong Lin
Institute of Earth Sciences,
National Taiwan Ocean University
Taiwan Union Lab of Gem Research, Taipei
Tsung-Ying Yang, Kai-Yun Huang, and Yu-Shan Chou
Taiwan Union Lab of Gem Research, Taipei

Synthetic sapphire with Rose channels. The Laboratoire Français de Gemmologie (LFG) received a 15.84 ct light purplish blue corundum for identification (figure 17). Under the microscope, clouds of bubbles similar to those seen in synthetic corundum were observed (figure 18), along with twinning planes and hollow channels known as Rose channels (figures 18 and 19). The Rose channels,

which are always found at the intersection of twin lamellae, were crystallographically oriented along the edges of the rhombohedral faces and formed angles of about 90° (again, see figure 18); these features are normally seen in natural corundum (F. Notari et al., “Boehmite needles’ in corundum are Rose channels,” Fall 2018 *G&G*, p. 257).

Rose channels and twinning lamellae are common in natural corundum but seldom reported in synthetic corundum, including one instance in a Ramaura flux synthetic ruby (E. Fritsch et al., “Are boehmite needles in corundum Rose channels?” *Geophysical Research Abstracts*, Vol. 20, EGU2018-19493, 2018). This is because the twinning

Figure 17. A 15.84 ct light purplish blue synthetic sapphire measuring 15.35 × 14.05 × 8.25 mm. Photo by U. Hennebois.



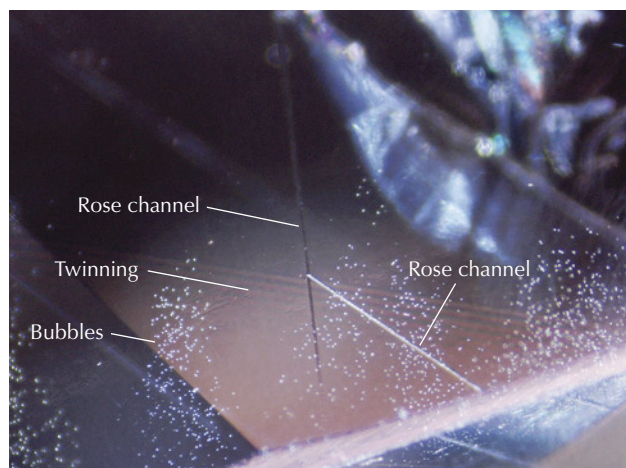


Figure 18. Clouds of bubbles, Rose channels, and twinning planes in the synthetic corundum under crossed polarizers. Photomicrograph by U. Hennebois; field of view 3 mm.

lamellae is most often formed via deformation twinning and results from post-growth events; thus, it is frequently observed in natural samples.

The sample was inert under long-wave UV and presented strong blue luminescence under short-wave UV. No gallium was detected with energy dispersive X-ray fluorescence, which further confirms that this corundum was synthetic (S. Muhlmeister et al., "Separating natural and synthetic rubies on the basis of trace-element chemistry," Summer 1998 *G&G*, pp. 80–101). DiamondView imaging showed curved growth lines, characteristic of Verneuil flame-fusion synthetic corundum (figure 20). Rose channels in corundum were linked in the past with boehmite needles and the characteristic absorptions in the 1500–

Figure 19. Clouds of bubbles, Rose channels, and twinning planes in the synthetic corundum. Photomicrograph by U. Hennebois; field of view 10 mm.

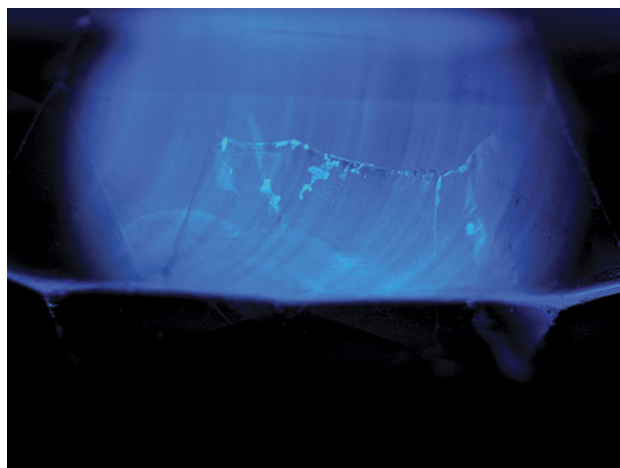


Figure 20. DiamondView imaging revealed curved growth lines characteristic of synthetic Verneuil corundum. Image by A. Herreweghe; field of view 10 mm.

4000 cm^{-1} region (Notari et al., 2018); however, no absorptions were observed in this region of the FTIR spectrum.

Although by far most common in natural corundum, the presence of Rose channels and twinning planes in synthetic corundum serves as evidence that these features alone cannot be used to confirm natural origin.

Ugo Hennebois, Aurélien Delaunay,
Annabelle Herreweghe, and Stefanos Karampelas
(s.karampelas@lfg.paris)
LFG, Paris

Emmanuel Fritsch
University of Nantes, CNRS-IMN, France

TREATMENTS

Gemological characteristics of low-temperature “gel-filled” turquoise. In the past decade, low-temperature “gel-filled” turquoise (X. Yating and Y. Mingxing, “Filling material and characteristic of polymer-impregnated turquoise in Anhui Province,” *Journal of Gems and Gemmology*, Vol. 21, No. 1, 2019, pp. 20–30) has been sold in the Chinese market. This special gel filling treatment is quite different from previous resin-filling or impregnation treatments (L. Liu et al., “Technical evolution and identification of resin-filled turquoise,” Spring 2021 *G&G*, pp. 22–35). The rough turquoise materials are soaked in a polymer composite gel at -10° to -15°C (without pressure) for filling and enhancement of appearance. According to the information obtained from a turquoise factory in Shiyan city, Hubei Province, the process can be generally summarized as follows:

1. The rough turquoise material is selected, cut, washed, and dried at about 100°C .
2. The material is immersed in a polymer composite



Figure 21. Untreated rough turquoise material produced in Zhushan County, Hubei Province, China, including one piece (indicated with the dotted line) that was selected to be cut into several square pieces. Photo by Andi Zhao.

gel solution, then put in the refrigerator and soaked at -10° to -15°C for 7–10 days.

3. The turquoise material is removed from the refrigerator and heated from room temperature to 80° at $1^{\circ}\text{C}/\text{min}$, followed by soaking at 80°C for four hours.
4. The material is further heated by ramping the temperature from 80° to 120°C at $1^{\circ}\text{C}/\text{min}$, followed by soaking at 120°C for eight to ten hours.
5. The turquoise material is then cooled from 120°C to room temperature at $3^{\circ}\text{C}/\text{min}$.
6. After removal from the furnace, the gel residue is removed by polishing off the surface layer.

The authors selected a piece of rough turquoise material (figure 21) produced in Zhushan County in Hubei Province, China, and cut it into several square pieces. According to the above treatment process, the turquoise was filled using the gel solution provided by the turquoise factory in Hubei. The material before treatment (N-1) was light whitish blue, with uneven color distribution, and black impurities were locally distributed. After treatment, the material's color deepened to a more desirable blue-green and became more uniform (figure 22), still retaining the original black impurities. After polishing, the surface of the gel-filled turquoise had a waxy luster and the hydrostatic specific gravity changed from approximately 2.32 to 2.21 due to the lower SG of the

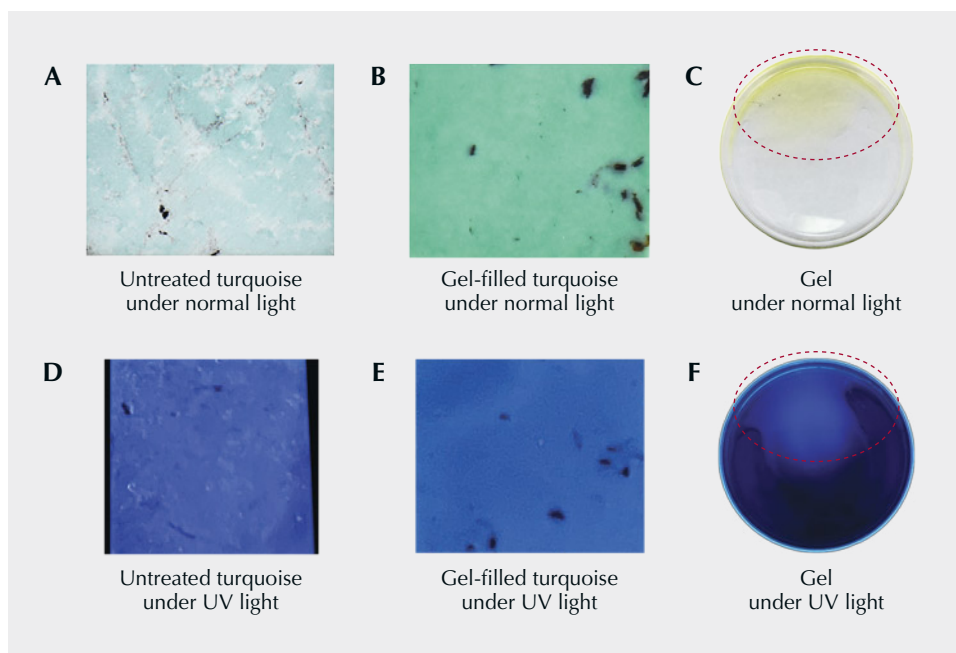


Figure 22. These images show the untreated turquoise, the gel-filled turquoise, and the gel solution in glassware under normal light (A–C) and under UV light (D–F). Photos by Andi Zhao.

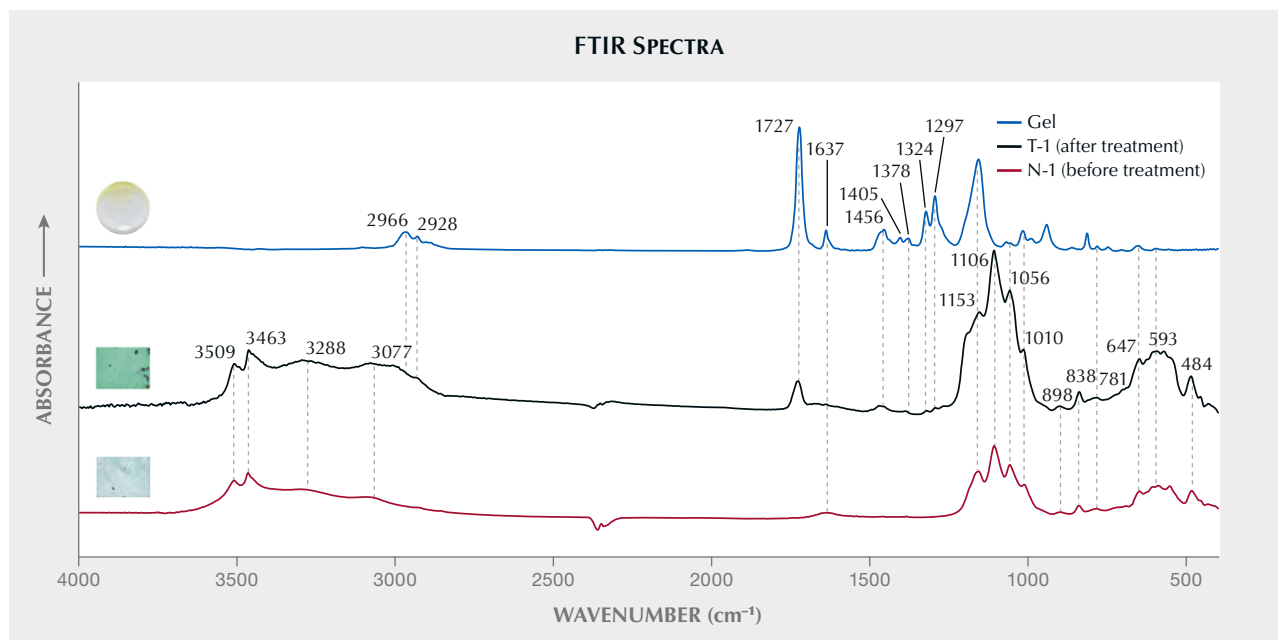


Figure 23. FTIR spectra of the gel, untreated turquoise, and low-temperature gel-filled turquoise. The characteristic peaks for gel-filled turquoise are a series of peaks at 2966, 2928, 1727, 1637, 1456, 1405, 1378, 1324, and 1297 cm^{-1} that are caused by the gel.

gel (approximately 1.00). The turquoise before treatment showed medium-light bluish white fluorescence with an abundance of white spots. After treatment, it showed uniform medium bluish white fluorescence (figure 22) under long-wave UV fluorescence. The turquoise was inert to short-wave UV before and after treatment. The light yellow gel solution showed a strong bluish white fluorescence along the edge of the glassware under long-wave UV and was inert under short-wave UV.

Fourier-transform infrared (FTIR) spectra of the gel and turquoise samples (before and after treatment) are shown in figure 23. Typical peaks for turquoise were observed, namely two absorption peaks at 3509 and 3463 cm^{-1} caused by the stretching vibration of hydroxyls (OH) (Q. Chen et al., "Turquoise from Zhushan County, Hubei Province, China," Fall 2012 *G&G*, pp. 198–204). Due to strong hydrogen bonding associated with the hydroxyl groups, the absorption peaks are relatively sharp. The absorption peaks at 3288 and 3077 cm^{-1} caused by OH stretching of water molecules are relatively flat, while the peak associated with the bending vibration of water is near 1637 cm^{-1} and the intensity of the absorption peak is relatively weak. There are four absorption peaks produced by the PO_4 stretching vibration between 1000 and 1200 cm^{-1} , which appear near 1153, 1006, 1056, and 1010 cm^{-1} . In addition, the gel-filled turquoise showed a weak absorption peak (2928 cm^{-1}) caused by a CH_2 stretching vibration and a strong stretching vibration peak (1727 cm^{-1}) caused by C=O (Yating and Mingxing, 2019). A series of weak small absorption peaks

also appeared at 1456, 1324, and 1297 cm^{-1} . These spectral peaks are consistent with the FTIR spectra of the gel. The spectral peaks can also be used to distinguish between untreated and gel-filled turquoise. Gas chromatography–mass spectrometry identified the main components of the gel as methyl isocrotonate ($\text{C}_5\text{H}_8\text{O}_2$, 46.05 wt.%), cyclooctatetraene (C_8H_8 , 35.8 wt.%), and oxirane ($\text{C}_2\text{H}_4\text{O}$, 5.93 wt.%).

Quanli Chen
Gemmological Institute,
China University of Geosciences, Wuhan
School of Jewelry, West Yunnan University of
Applied Sciences, Tengchong

Andi Zhao, Yan Li, Yanhan Wu, and Tianchang Liu
Gemmological Institute,
China University of Geosciences, Wuhan

CONFERENCE REPORTS

Inaugural Turquoise United conference. The first-ever Turquoise United conference was held August 11–13, 2022, in Albuquerque, New Mexico. This multifaceted event was organized and hosted by Joe Dan Lowry and his son Jacob, part of a fifth-generation family in the turquoise industry. All activities took place in the Turquoise Museum (www.turquoisemuseum.com), owned and operated by the family and the Albuquerque Convention Center (figure 24).

Turquoise has been treasured and used by many different cultures for thousands of years. As an aggregate gem-



Figure 24. Left: The entrance to the Turquoise Museum. Photo by Jacob Lowry/Turquoise Museum. Right: A corner in the origin display room shows rough and polished samples from Tyrone and Cerrillos, two well-known deposits in New Mexico. Photo by Tao Hsu.

stone, it also poses a challenge for traders. Possibly more so than for any other gemstone, the buying, selling, and owning of a turquoise piece can be an intensely personalized experience. A combination of factors including color, matrix pattern, specific mine origin, and the presence or absence of treatment come into play, making each piece unique. Turquoise United provides a platform for everyone involved in the trade to gather as a community and discuss important topics. About 100 delegates from different countries attended the inaugural event, including miners, cutters, treatment experts, dealers, television shopping network suppliers, collectors, jewelry designers, enthusiasts, consumers, appraisers, and scientists. GIA sent research and education representatives to connect with the turquoise community and learn from the experts. We had the opportunity to interview over 10 industry experts, including members of the domestic and international trade, miners, and artisans involved in turquoise treatment and the manufacture of imitation turquoise (figure 25). The content gathered will be highlighted in future GIA educational programs.

A wide variety of activities made this educational conference enjoyable. An evening gala and auction kicked off



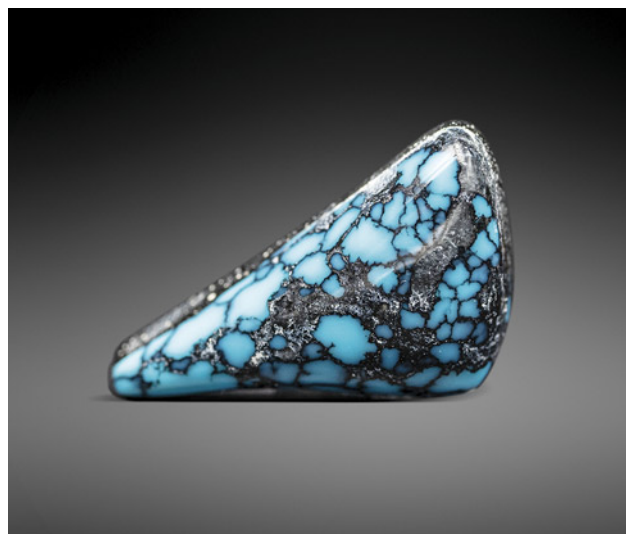
Figure 25. Russell Twiford III holds a massive resin imitation of turquoise he created, which is now displayed at the Turquoise Museum. Photo by Aaron Palke.



Figure 26. Left: Attendees enjoy a conversation about Southwestern-style jewelry design and manufacture outside the Turquoise Museum. Right: Joe Dan Lowry and son Jacob were the auctioneers at the kickoff gala. Photos by Tao Hsu.

the event (figure 26). Auction items included finished turquoise pieces, specimen and finished stone sets, and a bracelet featuring more than 200 inlay pieces designed and donated by GL Miller (Studio GL, Albuquerque). All other items were provided by the museum, and the proceeds will be allocated for future Turquoise United events. Delegates had the opportunity to view representative items from domestic and international sources such as Yungaisi, China (figure 27). All items were auctioned by the end of the gala. Each attendee received a gift bag containing a piece of turquoise, including some nice cabochons.

Figure 27. A 9.32 ct backed turquoise from Yungaisi, China, purchased during the auction at the Turquoise United conference. Photo by Aaron Palke.



During the day sessions, experts including Joe Dan Lowry, GL Miller, and author AP hosted identification panels at the Turquoise Museum (figure 28). Panelists evaluated the identity and origin of various turquoise jewelry pieces submitted by participants. The panel attracted consumers and enthusiasts who shared the stories behind their treasures. In the turquoise collector community, mine origin is an extremely important aspect. Turquoise enthusiasts often spend a lifetime putting together a collection of quality pieces from the most important turquoise mines, especially from the American Southwest. Lowry and

Figure 28. Turquoise enthusiasts and consumers brought their jewelry pieces to the identification panel experts, who shared their opinions on the pieces and answered questions from the audience. Photo by Tao Hsu.





Figure 29. Top: Joe Dan Lowry proposes a turquoise grading system alongside a panel of experts. Photo by Tao Hsu. Bottom: A look at the color scale and master stones for blue turquoise included in Lowry's grading system. Photo by Joe Dan Lowry.

Miller impressed the audience with their knowledge of historic turquoise mine characteristics, and engaged in much discussion about the complexity involved in conclusive identification and origin determination.

Two evening discussion panels took place in the Albuquerque Convention Center, with one focused on the vision and educational function of Turquoise United and the other on turquoise grading. The authors participated in

both panels along with delegates from all aspects of the industry. Author TH noted the current lack of turquoise-related educational programs and the potential industry benefit of reaching a broader audience not limited just to turquoise traders.

The second panel centered on Joe Dan Lowry's proposal for a turquoise grading system that could be applied inside and outside of the turquoise community (figure 29). Lowry's grading system is based on an unsurpassed collection of turquoise master stones of various qualities from global sources accumulated by the Lowrys over five generations. In the proposed grading system, origin is considered separately from other quality factors. A scoring system is based on a scale of 0 to 100, with the most important factor being color (70% of the final score) and additional consideration given to the aesthetics of the matrix (20%) as well as "zat" (10%), a combined description of the dynamic and boldness of both the color and the matrix patterns. Different levels of "zat" can be described as dynamic and bold in contrast to dull, flat, or uninteresting. After the quality evaluation and considering the importance of origin in many cases, the result would be combined with the condition of the piece (treated or untreated), cut, weight, and backing to give the buyer a complete picture of the stone. The panelists had a lengthy discussion on the applicability of the grading system, and author AP shared his views on consistency and potential market impact with the attendees.

In addition to the educational activities, a small-scale turquoise show took place in the courtyard of the museum. A dozen dealers participated, displaying rough and finished turquoise to attendees (figure 30). To keep the event focused, dealers could only sell turquoise stones and not finished jewelry. Turquoise from the southwestern United States, Mexico, China, and Iran were all featured at the show.

Figure 30. Left: A turquoise show attendee checks out polished pieces from multiple southwestern U.S. deposits. Photo by Tao Hsu. Right: An assortment of high-quality natural Persian turquoise cabochons; the one being held weighs about 19 ct. Photo by Aaron Palke.

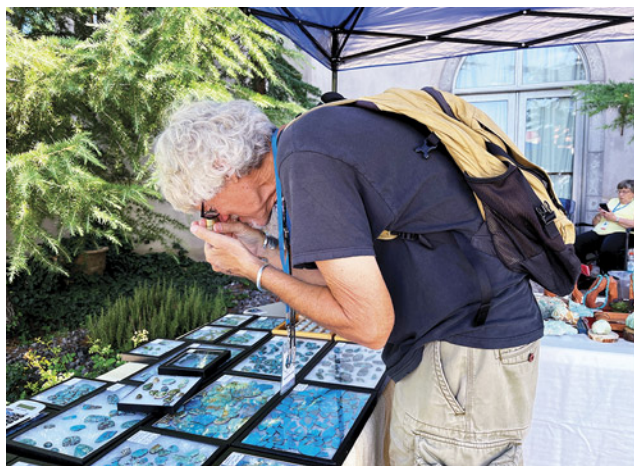




Figure 31. The historic Tiffany mine in the Cerillos mining district. This pit was mined many hundreds of years ago by Native Americans before contact with European cultures. Photos by Aaron Palke.

Surrounded by historic turquoise mines (figure 31) and Native American communities that have contributed enormously to the popularity of turquoise in the United States through their iconic turquoise jewelry designs, Albuquerque was the perfect setting for the conference. The annual Santa Fe Indian Market (SFIM), held every August, is also in close proximity. This year marks the hundredth anniversary of this famous event celebrating Native American arts and fashion, which features turquoise and turquoise jewelry. While the second Turquoise United conference is set for Albuquerque, the Lowrys are already planning future events and considering other important turquoise centers to host the conference as well.

*Tao Hsu and Aaron Palke
GIA, Carlsbad*

ANNOUNCEMENTS

Ahmadjan Abduriyim receives JAMS award for applied mineralogy. The Japan Association of Mineralogical Sciences (JAMS) has named Dr. Ahmadjan Abduriyim as the recipient of its 2021 award for applied mineralogy (figure 32). As president of Tokyo Gem Science and director of GSTV Gemological Laboratory in Tokyo, Abduriyim was recognized for his contributions to applied mineralogy.

Abduriyim holds a PhD in mineralogy and geology from Kyoto University and is a former senior manager and senior scientist at GIA's Tokyo laboratory. A longtime *G&G* contributor and editorial review board member, Abduriyim has published numerous articles on topics related to diamonds, colored stones, and organic gem materials in various journals, including *G&G*, *Journal of Gemmology*, and *Australian Gemmologist*.

Abduriyim's research has covered geographic origin determination of major gemstones, advanced testing of colored stones, and the application of laser ablation-in-

Figure 32. Dr. Ahmadjan Abduriyim (left) receives the 2021 Japan Association of Mineralogical Sciences (JAMS) award for applied mineralogy.





Figure 33. A view of the GSTV Gem Museum in Tokyo, exhibiting the extensive gem and mineral collection of the late Akira Chikayama. Photo by Ahmadjan Abduriyim.

ductively coupled plasma-mass spectrometry (LA-ICP-MS) in the gemological field. Most recently, Abduriyim has worked to integrate information obtained from the following three areas of research: the collection of geological data and gem samples from field surveys of mines worldwide, the application of high-precision analytical methods, and the construction of a database for the latest geographic origin determination and individual identification. He and his team are currently researching the usefulness of LA-ICP-MS in measuring trace elements and U-Pb isotope dating for geographic origin determination.

Meanwhile, Abduriyim recently honored Akira Chikayama, Japan's "Father of Gemology," by opening a museum featuring Chikayama's collection of rocks, minerals, and gemstones at GSTV Gemological Laboratory (figure 33). Chikayama, an esteemed gemology instructor, collected rock, mineral, and gemstone samples from

international mines and trade shows for use in his courses, eventually amassing a collection of more than 30,000 specimens. After his passing in 2007, the collection went unused until Abduriyim had the opportunity to view it in 2016 and envisioned creating a museum to share the collection with the world. In May 2022, the GSTV Gem Museum opened, displaying Chikayama's vast collection as well as several hundred books and magazines. On display are more than 600 rock specimens, 2,000 mineral specimens, 25,000 rough gemstones/gemstones in matrix (figure 34), 500 transparent crystals, 2,500 faceted stones, and 300 synthetic and imitation stones. The museum is not only an exhibition of Chikayama's collection, but also a place for visitors to learn about the fascinating world of gemology.

Erica Zaidman
GIA, Carlsbad



Figure 34. A portion of Chikayama's crystal specimens featured in the GSTV Gem Museum. Photo by Ahmadjan Abduriyim.



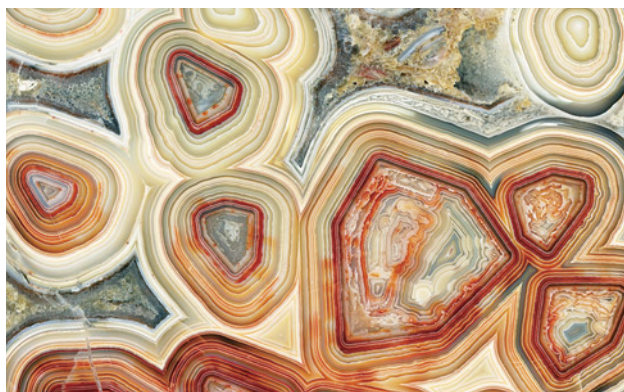
Figure 35. A gem pocket replica highlighting various gems and minerals mined in San Diego County, including tourmaline, quartz, kunzite, aquamarine, and mica. Dubbed the “Miner’s Fantasy Mine,” this replica combines various gems and minerals in the same pocket for illustrative purposes only. Photo courtesy of the San Diego Natural History Museum.

Hidden Gems at the San Diego Natural History Museum.

Known locally as The Nat, the San Diego Natural History Museum is making good use of unoccupied space with its *Hidden Gems* exhibit. Spanning the five floors of the museum, the 2,000 square foot vertical gem and mineral exhibit fills the space outside of the elevators on each floor, providing a permanent home to more than 100 specimens from the museum’s collection, many of which had not been on display prior to the exhibit’s opening. In this vertical exploration, visitors can expect to be wowed with a different experience as they reach each level of the museum.

Each floor has its own theme designed to showcase the diversity of minerals from all over the world. Fluorescent minerals are aglow under black lights on the lower level.

Figure 36. An image of quartz agate from Chihuahua, Mexico, scanned from the specimen and used to create wallpaper featured on Level 4 of the museum. Photo courtesy of the San Diego Natural History Museum.



Level 1 displays a sampling of gems from all over the world, with a special case dedicated to birthstones from GIA. Level 2 is comprised entirely of gems mined locally in San Diego County, California, including quartz, topaz, and hot pink tourmaline. This level also features a replica gem pocket full of gemstones found in the area (figure 35). Level 3 focuses on the application of minerals in the real world, including a section highlighting the minerals used to make cell phones. Finally, Level 4 covers geologic diversity, presenting a wide array of gems and minerals of different colors, shapes, and sizes. After experiencing all five floors, visitors leave with an understanding of the many roles of gems and minerals—esthetic, geological, and practical.

The walls and ceilings of the exhibit also deserve honorable mention. Large-scale murals produced by scanning various mineral specimens and printing them on the wallpaper create the feeling of walking into the featured mineral (figure 36). And a 24-foot sculpture modeled after the crystalline structure of silicate dangles from the ceiling.

Hidden Gems is a long-term exhibit and will occupy the space outside the elevators for the near future, until the museum unveils another innovative exhibit to fascinate visitors. For now, *Hidden Gems* is a vertical delight for all to see. Visit <https://www.sdnhm.org/exhibitions/hidden-gems/> to learn more.

Erica Zaidman

The Year of Mineralogy at the Perot Museum. 2022 is the International Mineralogical Association’s designated year for celebrating the history, development, and role of mineralogy, with a goal of promoting public interest in mineral studies. The association aims to emphasize mineralogy’s critical role in technology and society and to highlight the future of mineralogy through the exploration of new and environmentally



Figure 37. The Year of Mineralogy at the Perot Museum of Nature and Science in Dallas features 10 cases filled with fascinating samples demonstrating the importance of the mineral world around us. Photo courtesy of the Perot Museum of Nature and Science.

conscious methods for extracting the minerals used today. To help carry out this mission, the Perot Museum of Nature and Science in Dallas has created the *Year of Mineralogy* exhibit (figure 37) in the Lyda Hill Gems and Minerals Hall (<https://www.perotmuseum.org/exhibits/halls/lyda-hill-gems-and-minerals-hall/>).

With more than 5,700 minerals identified to date, and more added each year, there is no shortage of specimens to display. Each of the exhibit's 10 cases educates visitors

with spectacular examples to illustrate various mineral properties. The first case defines what a mineral is, showing specimens such as lapis lazuli and lazurite (figure 38). Chemical composition and crystal structure are explained in the second case, while the remainder are dedicated to the various properties of minerals, including hardness, tenacity, streak, luster (figure 39), and color.

"By understanding mineral characteristics, like hardness, magnetism, and specific gravity, we are able to find

Figure 38. This striking example of lapis lazuli, a rock composed of minerals including lazurite, pyrite, and calcite, is on display in the exhibit. From the Sar-e-Sang mine in the Kokcha River area of Badakhshan Province, Afghanistan. Photo courtesy of the Perot Museum of Nature and Science; specimen courtesy of Keith and Diane Brownlee.

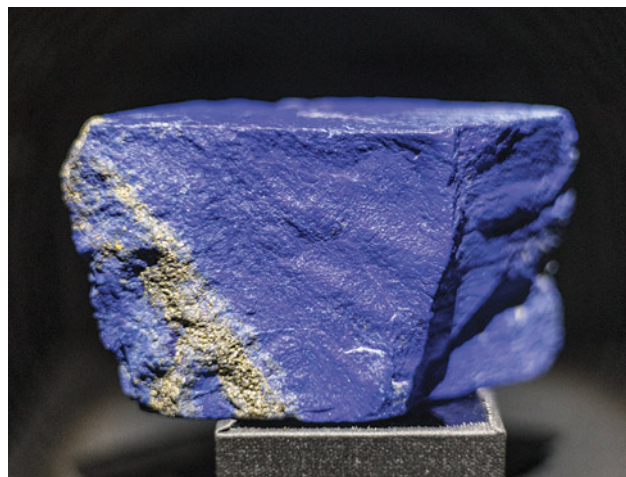


Figure 39. The resinous appearance of this sphalerite specimen highlights the mineral property of luster. From the Picos de Europa Mountains, Asturias, Spain. Photo courtesy of the Perot Museum of Nature and Science; specimen courtesy of Gail and Jim Spann.



solutions to many modern industrial problems and improve our overall well-being,” said Kimberly Vagner, director of gems and minerals at the Perot Museum.

On display until April 24, 2023, the exhibit is an opportunity for all ages to acquire a deeper understanding of the mineral world around us. Can’t make it to Dallas before April 24? Follow the museum’s Lyda Hill Gems and Minerals Hall on Instagram for posts highlighting some of the magnificent minerals on display.

Erica Zaidman

IN MEMORIAM

Andrew Cody. Australian opal leader Andrew Cody (figure 40) passed away on September 12, 2022, at the age of 71. Internationally regarded as one of Australia’s foremost opal wholesalers, cutters, and exporters, Cody was instrumental in the establishment of opal as Australia’s national gemstone and the development of standard opal nomenclature.

Collecting fossils, gemstones, and minerals since the age of 12, Cody began cutting opal in 1964 after a class trip to the famous deposit at Coober Pedy. In 1971, at the age of 20, he established Cody Opal, a wholesale opal and gem cutting business, which later began exporting worldwide. Cody was the joint founder of the National Opal Collection, an Australian opal and opal jewelry supplier with showrooms and museums located in Sydney and Melbourne.

Over the course of his career, Cody served in a number of leadership positions, including president of the Australian Gem Industry Association and president of the International Colored Gemstone Association. He was awarded honorary fellowships from the Australian Gemmological Association and the Gemmological Association of Great Britain. Also an author, Cody published two



Figure 40. Andrew Cody was one of Australia’s leading opal authorities and made numerous contributions to the industry. Photo by Tao Hsu.

books. *Australian Precious Opal – A Guide Book for Professionals* (1991) was followed by *The Opal Story: A Guidebook* (2010), written with his brother Damien and published in six languages.

For more than 50 years, Cody worked tirelessly to promote Australian opal across the global gem industry, leaving an enduring legacy. We extend our condolences to his family and friends.

For online access to all issues of GEMS & GEMOLOGY from 1934 to the present, visit:

gia.edu/gems-gemology

